The tectonic evolution of the Tibetan Plateau: insights from the deformation and erosion history of northern Tibet and the surrounding region

by

Alison R. Duvall

A dissertation submitted in partial fulfillment
of the requirements for the degree of
Doctor of Philosophy
(Geological Sciences)
in The University of Michigan
2011

Doctoral Committee:

Assistant Professor Marin K. Clark, Chair
Professor Roman D. Hryciw
Professor Rob Van Der Voo
Assistant Professor Eric A. Hetland
Assistant Professor Nathan A. Niemi

This thesis is dedicated to the millions of people affected by the devastating Wenchuan (May 12, 2008) and Yushu (April 14, 2010) earthquakes

Acknowledgements

This thesis would not be possible without the invaluable guidance of my advisor, Dr. Marin K. Clark. Throughout the PhD process, she pushed me to question thoughtfully, think critically, and analyze carefully, all while keeping the important big-picture questions in mind. I have learned these and many other valuable skills from her. Special thanks to my committee members, Dr. Roman D. Hryciw, Dr. Rob Van Der Voo, Dr. Eric A. Hetland, and Dr. Nathan A. Niemi, for helpful feedback and constructive criticism of this work. All of those involved with the "Upward and Outward: Tibetan Plateau Growth and Climate Consequences" project, including Peter Molnar, Marin Clark, Doug Burbank, Eric Kirby, Carmie Garzione, Ken Farley, Gerard Roe, Zhang Peizhen, Yuan Dao-Yang, Zheng Dewen, Li Chuanyou, Zhang Huiping, Richard Lease, Brian Hough, Bill Craddock, Sandra Penny, and Katherine Dayem, have greatly contributed to the outcomes of this dissertation as well as my personal development as a scientist. It was fantastic to work so closely with such a fine group of people. I had the pleasure of visiting China and Tibet six times in the last five years and so many people helped to make this possible. Specifically, thanks to Katherine Dayem, Karen Vasko, Sandra Penny, Nora Lewandowski, John Bershaw, Li Chuanyou, Eric Kirby, and Marin Clark for being wonderful field companions, to the drivers and employees of the Institute of Seismology, Lanzhou, who endured long hours and tough conditions while taking me to the most important (and often remote) spots within the Tibetan Plateau, and to Zhang

Peizhen and his colleagues at the China Earthquake Administration, Beijing, for allowing all of this field work to be possible. I also had the privilege of working with Ken Farley and Lindsey Hedges at the noble gas laboratory, California Institute of Technology. Special thanks to them for teaching me the ins and outs of (U-Th)/He thermochronometry. I also need to recognize many colleagues at the University of Michigan who helped me greatly with the fault-gouge dating aspect of this thesis: Ben van der Pluijm, Chris Hall, Anja Schleicher, Jim Hnat, Sam Haines, Tim O'Brien, and Charlie Verdel. Thank you to my "SCALE lab" family: Peter Yakovlev, Lydia Staisch, and most especially Alex Lechler and Boris Avdeev, for being wonderful friends and colleagues. I have learned so much from you! Without the support and encouraging spirit of my family and friends, most especially my mother and sister, I could have never come so far. I must also acknowledge my funding sources: NSF Continental Dynamics Project (EAR-0507431), University of Michigan Rackham Graduate School (Rackham Predoctoral Fellowship, Rackham International Research Award, and Rackham Conference Travel Grants), and the University of Michigan Department of Geological Sciences Scott Turner Fund. Finally, I would like to recognize the department staff, especially Nancy Kingsbury and Anne Hudon, and my fellow Michigan geology grads – thank you for the support, laughs, and good times. It was a pleasure to be involved in this department.

TABLE OF CONTENTS

LIST OF FIGURES

FIGURE

LIST OF TABLES

TABLE

Chapter I

Introduction

The Tibetan Plateau is arguably the most outstanding topographic and geologic feature on earth (Figure 1.1). With an areal extent of 2.5 million km^2, this vast landscape encompasses 82% of the world's land surface area >4 km above sea level (Fielding et al., 1994) and is underlain by continental crust twice as thick as average (>70 km; Wittlinger et al., 2004; Rai et al., 2006). Ongoing India-Eurasia continental convergence since ~55-45 Ma (Rowley, 1996; 1998 and references therein; Zhu et al., 2005; Henderson et al., 2010) is the widely accepted cause of Cenozoic deformation within Tibet and the surrounding region (Powell and Conaghan, 1973; Molnar and Tapponnier, 1975). Due to the fact that convergence is still in progress, studies of this region yield valuable insights into continental orogen development not possible in older tectonic systems. Despite decades of research and discovery, however, no consensus has yet been reached with regard to the fundamentals of orogenic evolution in response to this convergence. This is in part due to the complex nature of continental deformation. Unlike dense oceanic lithosphere, which is generally more rigid, block-like and recyclable through the process of subduction, continental lithosphere may undergo pervasive internal deformation, often distributed over broad zones near plate boundaries and, due to its buoyancy, may withstand multiple generations of deformation.

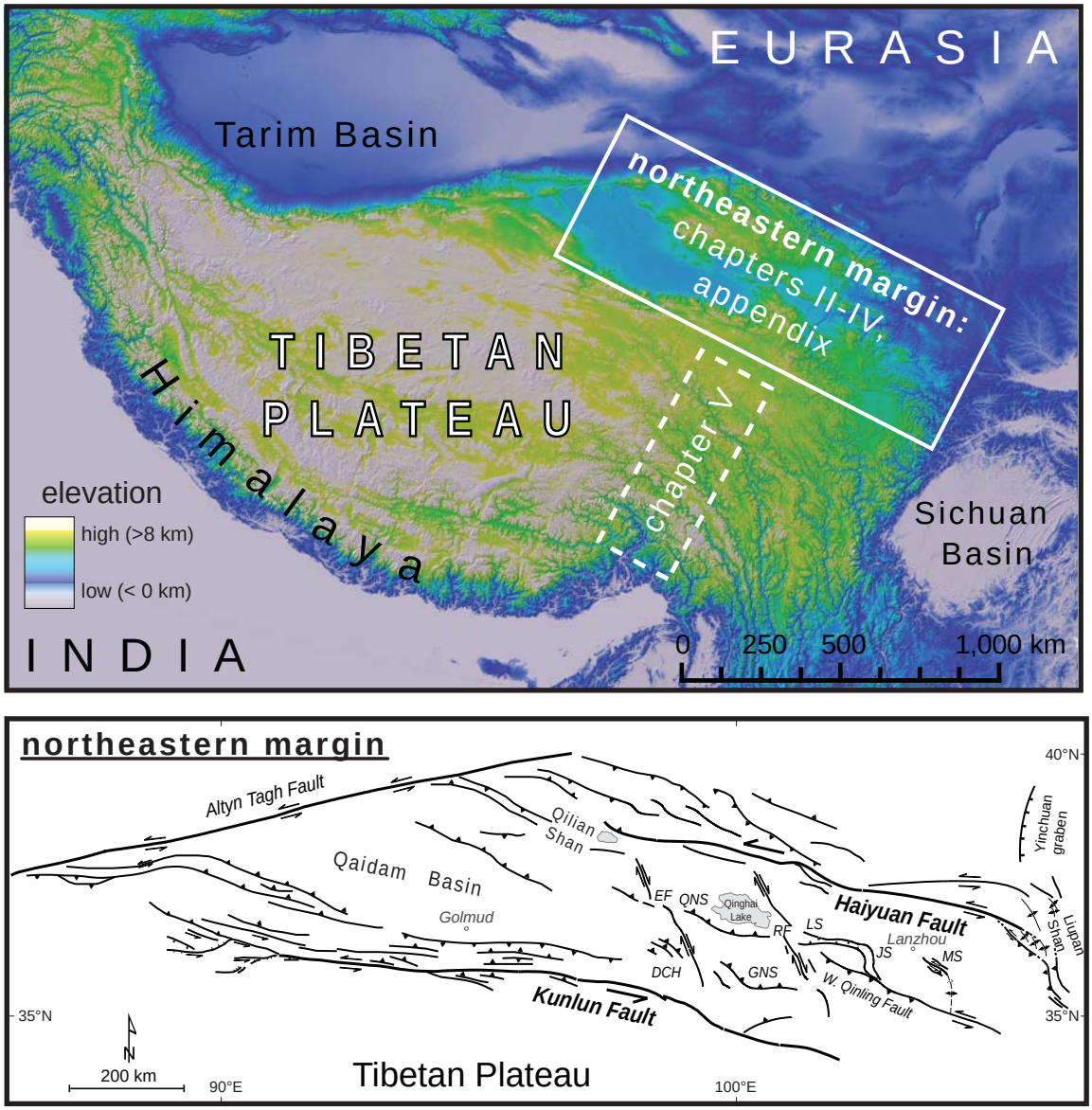

Figure 1.1. Shaded relief map of Tibetan Plateau and surrounding region. Solid white box highlights the location of detailed studies along the northeastern margin of the Tibetan Plateau (chapters II-IV and the appendix). Lower panel shows the faults of the northeastern margin of the Tibetan Plateau compled from published sources (GBGMR Gansu Province, 1989; QBGMR, 1991; Van der Woerd et al., 2002; Jolivet et al., 2003; Pan et al., 2004; Yin et al., 2002; 2007; 2008; Bovet et al., 2009; Zheng et al., 2010; Huang et al., 2011) and original field observations. Dulan-Chaka Highland (DCH); Laji Shan (LS), Jishi Shan (JS), Maxian Shan (MS); Elashan Fault (EF); Riyueshan Fault (RF); Qinghai Nan Shan (QNS); Gonghe Nan Shan (GNS). Dashed white box highlights the field location of the broader-scale plateau-wide component of the dissertation (Chapter V).

1.1 Motivation: Prototype of continent-continent collision

The Tibetan orogenic system is a prime example of complex and widespread deformation of anisotropic continental lithosphere with a long geologic past. Tibet and the surrounding area comprise terranes accreted successively to the Eurasian craton since the early Mesozoic (Dewey et al., 1988; Şengör and Natal'in, 1996). Convergence of these continents and continental fragments was accompanied by subduction of intervening Tethys oceans in a complicated process of rifting, back-arc spreading, and intra-ocean subduction (Şengör, 1984). Remnants of the Mesozoic Tethyan subduction complex are revealed by tomographic imaging of the mantle under Tibet, India, and the adjacent Indian Ocean (Van der Voo et al., 1999).

A number of competing mechanisms to explain Cenozoic crustal deformation and surface uplift due to continental collision with India have been proposed. These can be classified broadly into four main categories described below: 1) underthrusting, 2) rigid-block tectonics, 3) continuum models, and 4) crustal flow. It should be noted that debate regarding model validity often considers each as separate end members. In reality, these descriptions are not necessarily mutually exclusive of one another, and the development of the Tibetan-Himalayan orogenic system may have involved aspects of more than a single mechanism.

Underthrusting

Long before the advent of plate tectonics, Émile Argand proposed that the Tibetan Plateau resulted from the underthrusting of India (Argand, 1924). Adding to this landmark proposal, Powell (1986) suggested that wholesale subduction of buoyant Indian

continental crust led to underplating and subsequent rise of the Asian Tibetan continental crust. A variation by Zhao and Morgan (1987) suggested injection of Indian crust into weaker Tibetan lower crust was the mechanism for massive crustal thickening. Seismic experiments lend support to the underthrusting of Indian lithosphere at least in the southern part of the Plateau (Owens and Zandt, 1997; Tilmann et al., 2003; Hetényi et al., 2007; Nábelek et al., 2009) but suggest that anomalously hot, low-density upper mantle characterized by observable mantle anisotropy (Owens and Zandt, 1997) underlies northern Tibetan crust (north of the Bangong Suture). Recent surface wave tomography studies have reinvigorated this debate as results imply a high-velocity (i.e. strong and intact) lithospheric mantle beneath the whole plateau to a depth of 225-250 km (Priestley et al., 2008).

Rigid Blocks

In another seminal paper for Asian tectonics, Molnar and Tapponnier (1975) first proposed the "continental extrusion" model whereby large-scale (1000 km) eastward extrusion of Tibet was achieved by horizontal motions along major intra-continental strike-slip faults. The premise of this and other similar models (e.g., Tapponnier et al., 1982; Avouac and Tapponnier, 1993) is that Tibetan crust can be described as rigid or rigid-plastic microplates or blocks where deformation is localized on major block-bounding faults (Thatcher, 2007; Meade, 2007). In order to describe the thick crust and high-surface elevations of Tibet as well as lateral strain, Tapponnier et al. (2001) further proposed a northeasterly progressive growth of the plateau along discrete discontinuities in the crust. This description of plateau growth envisions extrusion along the major

strike-slip faults following the old suture zones, accompanied by mantle subduction at depth and thrusting, uplift, and erosion of crustal wedges.

Continuum models

In contrast to discrete deformation along rigid blocks, continuum models, such as the thin-viscous sheet model (England and McKenzie, 1982), describe deformation as distributed through a continuously deforming lithosphere driven by boundary and interior forces. Faults in the brittle crust are less significant and may simply be shallow crustal features in a more fluid-like lithosphere. A major assumption in these models is that variation in the horizontal component of velocity with depth can be ignored. In the case of Tibet, the lithosphere is predicted to deform as a continuous viscous fluid so that convergence is accommodated smoothly across the entire lithosphere by distributed thickening and shortening of Asian lithosphere (e.g., England and McKenzie, 1982; Dewey et al., 1988; England and Houseman, 1986; 1989), which may have resulted in the abrupt removal of mantle lithosphere from beneath Tibet during the late Cenozoic (Molnar et al., 1993). Strain rates and presumably crustal thickening were largest near the suture zone in southern Tibet at the beginning of continent-continent collision, increasing northward in time. Thus, like rigid-blocks, the simplest applications of thin-viscous sheet models predict a northward growth of the Tibetan Plateau (e.g., England and Houseman, 1986; England and Searle, 1986). However, more recent applications of this model framework show that far-field lithospheric deformation due to the Indian indenter shortly after collision is permissible given a strong lithosphere north of Tibet and relatively thick crust in southern Tibet at the onset of plateau building (Dayem et al., 2009).

Crustal flow

Crustal flow models of Tibet similarly predict that the lithosphere deforms as a continuous viscous fluid but differ in that convergence is accommodated through flow in the middle or lower crust. The absence of long-wavelength relief across the Tibetan Plateau inspired the idea that crustal flow occurs by power-law creep under large plateau regions underlain by thick crust and acts to level the land surface (Bird, 1991). High temperatures and/or the presence of small amounts of fluid or partial melt greatly reduce continental crustal strength (Kohlstedt et al., 1995) allowing ductile flow in the middle to lower crust in response to pressure gradients resulting from topography. Late Miocene initiation of major river incision within the easternmost margin of Tibet (Clark et al., 2005; Ouimet et al., 2010; Wilson and Fowler; 2011), a region of high topography and thickened crust (~60 km) but with no evidence of major Late Cenozoic crustal shortening, has been proposed to have experienced broad surface uplift due to crustal thickening via lower crustal flow that initiated in central Tibet and progressed outward (Clark and Royden, 2000; Kirby et al., 2002; Clark et al., 2006; Royden et al., 1997; 2008; Ouimet et al., 2010).

1.2 Motivation: Climate-tectonics links

In addition to providing important testing grounds for proposed descriptions of the mechanics of intracontinental deformation and orogenic plateau formation, the Tibetan Plateau also serves as an ideal setting for studying the coupling between the lithosphere and atmosphere, as well as the role of each in mountain-range evolution. Despite field

observations and laboratory experiments consistent with the notion that tectonics significantly impacts climate and vice versa, unequivocal evidence of such links remains elusive (e.g., Whipple, 2009).

The topographic rise of a landmass as large as the Tibetan Plateau likely affects regional and possibly global climatic and atmospheric patterns. In fact, many have postulated that accelerated erosion and weathering of silicate rock as a result of uplift of the Tibetan-Himalayan system may have led to enhanced extraction of atmospheric CO_2 and, ultimately, global atmospheric cooling in Cenozoic time (e.g., Raymo and Ruddiman, 1992; Ruddiman et al., 1997). Although more recent isotopic studies have cast some doubt upon these hypotheses (Jacobsen et al., 2002; Bickle et al., 2005), a case can still be made for a connection between Tibetan-Plateau uplift and Asian monsoonal processes.

Once even moderately high topography (~3000 m) is achieved, the Himalaya and Tibetan plateau are thought to profoundly influence Asian monsoon processes (e.g., Prell and Kutzbach, 1992; Molnar et al., 1993; Zhisheng et al., 2001; Molnar, 2005). High topography in and surrounding Tibet acts as a barrier to the circulation of cool, dry air from the north in the case of the South Asian monsoon (Boos and Kuang, 2010) and as a deflector of the jet stream in the case of the East Asian monsoon (Molnar et al., 2010). In return, Asian monsoons may significantly affect regional deformation patterns. Intense monsoonal precipitation focused on the high Himalaya, the southern boundary of the Tibetan Plateau, is thought to trigger increased erosion rates (Burbank et al., 2003), which in turn facilitate ductile extrusion of hot, weak rocks from beneath the central Tibetan Plateau in a widely cited model known as the “channel flow” hypothesis

(Beaumont et al., 2001; Hodges et al., 2001). Ultimately, understanding the true nature of such proposed monsoon-tectonics interactions requires robust measures of rates and timing of deformation and erosion events within the Tibetan Plateau orogenic system.

1.3 Thesis outline

In this dissertation, I utilize a variety of techniques including low-temperature thermochronometry, geochronology, geodesy, and analysis of geologic and geomorphic patterns from both field-based and remotely-sensed data in order to better characterize the structural and topographic evolution of the Tibetan Plateau since the time of Indo-Asia collision (~ 50 Ma). This work was undertaken at two spatial scales (Figure 1.1): detailed study along the northern plateau margin (Chapters II-IV) and a broad-scope study across the width of the east-central Tibetan Plateau (Chapter V).

Much of the interior Tibetan Plateau is a remote, arid region with relatively low relief, thus geologic studies focused on plateau margins, where accessibility and rock exposure are generally superior, offer valuable insights into plateau development. In addition, many viable descriptions of Tibetan Plateau formation, regardless of specific styles of deformation evoked, view mountain growth as a northward progression away from the collision boundary with time. As the most distal plateau margin, northeastern Tibet therefore represents a key area for detailed study. In this region, I first consider the modern deformation field using geodesy and then investigate the longer term geologic evolution using low-temperature thermochronometry and geologic and geomorphic observations. The second component of my dissertation work (Chapter V) evaluates spatial and temporal patterns in Tibetan Plateau evolution through a plateau-wide study

of fluvial erosion using detrital sediment from rivers crossing the entire width of the externally-drained portion of the east-central Tibetan Plateau (Figure 1.1). Detrital studies are best-suited for work of this scope because a single sample contains rock materials integrated from a large spatial area, thereby overcoming issues of poor accessibility and sparse bedrock outcrops. Two of these chapters are published (Chapter II,III), one is in review (Chapter V), and one is in preparation for submission (Chapter IV). The format and content of the published manuscripts match that presented in this dissertation.

Chapter II

One of the main outstanding questions in Tibetan Plateau evolution is how much of India-Eurasia convergence was absorbed by crustal shortening and thickening and how much was accommodated by lateral extrusion to the east. Central to this issue is whether fast slip on major strike-slip faults is absorbed by deformation within the plateau or if it instead extends east of the plateau to adjacent terrain. Geodetic velocities, which record motion of the present deformation field, offer one means to address these questions. Chapter II analyzes fault parallel geodetic velocities and Quaternary slip rates along strike to evaluate termination and slip transfer of the Kunlun Fault, a major left-lateral strike-slip fault in northeastern Tibet. The distribution of fault-parallel velocities across this region suggests a decrease in fault slip toward eastern fault tips and progressive dissipation of slip to the north rather than east of the Tibetan Plateau as previously suggested (e.g., Tapponnier et al., 1982; 2001). Thus, the notion of eastward extruding crustal blocks is not supported by geodetic and Quaternary slip rates in northeastern Tibet. The results of this study are published in the March 2010 issue of *Geology*: Duvall and Clark, 2010.

Chapter III

Direct dating of Eocene reverse faulting in northeastern Tibet using Ar-dating of fault clays and low-temperature thermochronometry (Chapter III) addresses the longer-term deformation of northeastern Tibet. In this study, timing of fault motion was determined using $^{40}Ar/^{39}Ar$ dating of illite in fault gouge of a major reverse fault combined with the erosional history of hanging-wall rocks from thermal data. Results from this work offer definitive evidence of Eocene-age reverse faulting within the northeastern Tibetan Plateau and suggests that compressive deformation across a significant portion of the northern margin of the plateau initiates within 10 myr of the initial collision between India and Eurasia. This work also highlights the utility of combining results from fault gouge dating with thermochronometry at the same location. Results of this study are published in the April 2011 issue of *Earth and Planetary Science Letters*: Duvall et al., 2011.

Chapter IV

Chapter IV provides minimum bounds on the onset age of the Kunlun Fault as well as the Haiyuan Fault, which is also a major left-lateral structure within the northeastern margin of the Tibetan Plateau. New low-temperature thermochronometry ages and geologic observations are used to constrain periods of exhumation associated with transpressional deformation linked to strike-slip faulting. Results suggest that Kunlun faulting initiated first during the early Miocene along the central fault segment followed by expansion along strike to the east and west. Between 15-6 Ma, structures between the Kunlun and Haiyuan Faults became active, from which I infer simultaneous Kunlun and Haiyuan faulting bounding the ~250-km-wide zone of associated transpressional shear

documented in the modern deformation field (Chapter II). Thus, left-lateral strain appears to dominate the structural landscape of the interior northeastern plateau margin beginning at ~ 15 Ma and continuing through the present.

Chapter V

Building on Part I of the dissertation, Chapter V expands upon the detailed work in northern Tibet and considers the broader, plateau-wide geologic history. This study determines patterns in erosion rates and timing of erosion-rate change across the entire width of the east-central Tibetan Plateau interior by measurements of low-temperature thermochronometry in detrital apatites collected from modern river sands. If Tibet grows by appending material to a northward expanding deformation front, then such a process will likely be recorded by a similarly migrating front of high erosion rates. Thus, the record of erosion patterns across the plateau serves as a proxy for elevation history during plateau expansion and can be used to further distinguish between models of plateau formation. Results from this study reveal that rates similarly increase by at least an order of magnitude between 11-4 Ma following a period of slow erosion across all of the studied catchments. Similar timing of accelerated erosion throughout the expanse of the Tibetan Plateau rather than a spatial or temporal progression challenges plateau evolution via a steep, northward-propagating topographic front. Although I cannot definitively distinguish between tectonic and climatic influences on the erosion record from these data alone, results are consistent with broad surface uplift, possibly due to lower-crustal flow, as the main driver of late Cenozoic erosion rate increase. This work is currently in review for publication in *Tectonics*.

The final chapter of this dissertation (Chapter VI) summarizes the main conclusions from each chapter and offers a synthesis of Cenozoic deformation along the northern plateau margin as well as implications for Tibetan Plateau development as a whole. Additional method details (Chapter II) and complete data tables (Chapters IV and V) are provided at the end of the respective chapters. The dissertation appendix includes an original geologic map and three generalized stratigraphic columns for the Maxian Shan region of northeastern Tibet (Figure 1.1).

1.4 References

An, Z., Kutzbach, J.E., Prell, W.L., and Porter, S.C., 2001, Evolution of Asian monsoons and phased uplift of the Himalaya-Tibetan plateau since Late Miocene times: Nature, v. 411, p. 62-66.

Argand, E., 1924, La tectonique de l'Asie, Proc. 13th Int. Geological Congr., 7, p. 170 372.

Avouac, J.-P., and Tapponnier, P., 1993, Kinematic model of active deformation in Central Asia: Geophysical Research Letters, v. 20, p. 895-898.

Beaumont, C., Jamieson, R.A., Nguyen, M.H., and Lee, B., 2001, Himalaya tectonics explained by extrusion of a low-viscosity crustal channel coupled to focused surface denudation: Nature, v. 414, p. 738-742.

Bickle, M.J., Chapman, H.J., Bunbury, J., Harris, N.B.W., Fairchild, I.J., Ahmad, J., and Pomiès, C., 2005, Relative contributions of silicate and carbonate rocks to

riverine Sr fluxes in the headwaters of the Ganges: Geochimica et Cosmochimica Acta, v. 69, p. 2221-2240.

Bird, P. 1991, Lateral Extrusion of Lower Crust from under High Topography, in the Isostatic Limit: J Geophys Res-Solid, v.96(B6), p. 10275-10286.

Boos, W.R., and Kuang, Z.M., 2010, Dominant control of the South Asian monsoon by orographic insulation versus plateau heating: Nature, v. 463(7278), p. 218-222.

Bovet, P.M., Ritts, B.D., Gehrels, G., Abbink, A.O., Darby, B., and Hourigan, J., 2009, Evidence of Miocene crustal shortening in the north Qilian Shan from Cenozoic stratigraphy of the western Hexi Corridor, Gansu Province, China: American Journal of Science, v. 309, p. 290-329.

Burbank, D.W., Blythe, A.E., Putkonen, J., Pratt-Sitaula, B., Gabet, E., Oskin, M., Barros, A., and Ojha, T.P., 2003, Decoupling of erosion and precipitation in the Himalayas: Nature, v. 426(6967), p. 652-655.

Clark, M.K., and Royden, L.H., 2000, Topographic ooze: Building the eastern margin of Tibet by lower crustal flow: Geology, v. 28(8), p. 703-706.

Clark, M.K., Royden, L.H., Whipple, K.X., Burchfiel, B.C., Zhang, X., and Tang, W., 2006, Use of a regional, relict landscape to measure vertical deformation of the eastern Tibetan Plateau: J Geophys Res-Earth, v. 111(F3), doi:10.1029/2005JF000294.

Dayem, K.E., Molnar, P., Clark, M.K., and Houseman, G.A., 2009, Far-field lithospheric deformation in Tibet during continental collision: Tectonics, v. 28, doi:10.1029/2008TC0002344.

Dewey, J.F., Shackleton, R.M., Chengfa, C., and Yiyin, S., 1988, The tectonic evolution of the Tibetan Plateau: Philosophical Transactions of the Royal Society of London. Series A., Mathematical and Physical Sciences, 327(1594), 379 pp.

Duvall, A.R., and Clark, M.K., 2010, Dissipation of fast strike-slip faulting within and beyond northeastern Tibet: Geology, v. 38, p. 223-226.

Duvall, A.R., Clark, M.K., van der Pluijm, B.A., and Li, C., 2011, Direct dating of Eocene reverse faulting in northeastern Tibet using Ar-dating of fault clays and low-temperature thermochronometry: Earth Planet Sci Lett., v. 304(3-4), p. 520-526.

England, P., and Houseman, G., 1986, Finite Strain Calculations of Continental Deformation .2. Comparison with the India-Asia Collision Zone: J Geophys Res-Solid, v. 91(B3), p. 3664-3676.

England, P., and Houseman, G., 1989, Extension during continental convergence, with application to the Tibetan Plateau: Journal of Geophysical Research, v. 94(B12), p. 17561-17579.

England, P., and Searle, M., 1986, The Cretaceous-tertiary deformation of the Lhasa Block and its implications for crustal thickening in Tibet: Tectonics, v. 5, p. 1-14.

Fielding, E., Isacks, B., Barazangi, M., and Duncan, C., 1994, How flat is Tibet?: Geology, v. 22, p. 163-167.

Gansu Bureau Geological and Mineral Resources (BGMR) Gansu Province, 1989, Regional Geology of Gansu Province, Geological publishing house, Beijing (in Chinese), 690 p.

Henderson, A. L., Foster, G.L., and Najman, Y., 2010, Testing the application of in situ Sm-Nd isotopic analysis on detrital apatites: A provenance tool for constraining the timing of India-Eurasia collision: Earth Planet Sci Lett, v. 297(1-2), p. 42-49.

Hetényi, G., Cattin, R., Brunet, F., Bollinger, L., Vergne, J., Nabalek, J.L., and Diament, M., 2007, Density distribution of the India plate beneath the Tibetan Plateau: Geophysical and petrological constraints on the kinetics of lower crustal eclogitization: Earth and Planetary Science Letters, v. 264, p. 226-244.

Hodges, K.V., Hurtado, J.M., and Whipple, K.X., 2001, Southward extrusion of Tibetan crust and its effect on Himalayan tectonics: Tectonics, v. 20, p. 799-809.

Huang, G., Hourigan, J.K., Ritts, B.Z., and Kent-Corson, M.L., 2011, Cenozoic multiple-phase tectonic evolution of the northern Tibetan Plateau: Constraints from sedimentary records from Qaidam Basin, Hexi Corridor, and Subei Basin, northwest China: American Journal of Science, v. 311, p. 116-152.

Jacobsen, A.D., Blum, J, D., and Walter, L.M., 2002, Reconciling the elemental and Sr isotope composition of Himalayan weathering fluxes: Insights from the carbonate

geochemistry of stream waters: Geochimica et Cosmochimica Acta, v. 66, p. 3417-3429.

Jolivet, M., Brunel, M., Seward, D., Xu, Z., Yang, J., Malavieille, J., Roger, F., Leyreloup, A., Arnaud, N., and Wu, C., 2003, Neogene extension and volcanism in the Kunlun Fault Zone: New constraints on the age of the Kunlun Fault: Tectonics, v. 22, doi:10.1029/2002TC001428.

Kirby, E., Reiners, P.W., Krol, M.A., Whipple, K.X., Hodges, K.V., Farley, K.A., Tang, W.Q., and Chen, Z.L., 2002, Late Cenozoic evolution of the eastern margin of the Tibetan Plateau: Inferences from Ar-40/Ar-39 and (U-Th)/He thermochronology: Tectonics, v. 21(1), doi:10.1029/2000TC001246.

Kohlstedt, D.L., Evans, B., and Mackwell, S.J., 1995, Strength of the lithosphere: Constraints imposed by laboratory experiments: Journal of Geophysical Research, v. 100, p. 17,587-17,602.

Meade, B.J., 2007, Present-day kinematics at the India-Asia collision zone: Geology, v. 35, p.81-84.

Molnar, P., and Tapponnier, P., 1975, Cenozoic tectonics of Eurasia: effects of a continental collision: Science, v. 189, p. 419-426.

Molnar, P., England, P., and Martinod, J., 1993, Mantle Dynamics, Uplift of the Tibetan Plateau, and the Indian Monsoon: Rev Geophys, v. 31(4), p. 357-396.

Molnar, P., 2005, Mio-pliocene growth of the Tibetan Plateau and evolution of East Asian climate: Palaeontol Electron, v. 8(1), 2A:23p.

Molnar, P., Boos, W.R., and Battisti, D.S., 2010, Orographic Controls on Climate and Paleoclimate of Asia: Thermal and Mechanical Roles for the Tibetan Plateau: Annu Rev Earth Pl Sc, v. 38, p. 77-102.

Nábelek, J., Hetényi, G., et al., 1996, Underplating in the Himalaya-Tibet collision zone revealed by the Hi-CLIMB experiment: Science, v. 325, p. 1371-1374.

Ouimet, W., Whipple, K., Royden, L., Reiners, P., Hodges, K., and Pringle, M., 2010, Regional incision of the eastern margin of the Tibetan Plateau: Lithosphere, v. 2(1), p. 50-63.

Owens, T.J., and Zandt, G., 1997, Implications of crustal property variations for models of Tibetan plateau evolution: Nature, v. 387, p. 37-42.

Powell, C.M.A., and Conaghan, P.J., 1973, Plate tectonics and the Himalayas: Earth and Planetary Science Letters, v. 20, p. 1-12.

Powell, C.M.A., 1986, Continental underplating model for the rise of the Tibetan Plateau: Earth Planet Sc Lett, v. 81(1), p. 79-94.

Prell, W. L., and Kutzbach, J.E., 1992, Sensitivity of the Indian monsoon to forcing parameters and implications for its evolution: Nature, v. 360(6405), p. 647-652.

Priestley, K., and McKenzie, D., 2008, Lithospheric structure and deep earthquakes beneath India, the Himalaya, and southern Tibet: Geophysical Journal International, v. 172, p. 345-362.

Qinghai Bureau of Geology and Mineral Resources (QBGMR), 1991, Regional Geology of Qinghai Province, Geological Publishing House, Beijing.

Rai, S., Priestley, K., Gaur, V., Mitra, S., Singh, M., and Searle, M.P., 2006, Configuration of the Indian Moho beneath the Northwest Himalaya and Ladakh: Geophysical Research Letters, v. 33, doi:10.1029/2006GL026076.

Raymo, M.E., and Ruddiman, W.F., 1992, Tectonic forcing of late Cenozoic climate: Nature, v. 359, p. 117-122.

Rowley, D. B., 1996, Age of initiation of collision between India and Asia: A review of stratigraphic data: Earth Planet Sci Lett, v. 145(1-4), p. 1-13.

Rowley, D. B., 1998, Minimum age of initiation of collision between India and Asia north of Everest based on the subsidence history of the Zhepure Mountain section: The Journal of geology, v. 106(2), p. 220-235.

Royden, L.H., Burchfiel, B.C., King, R.W., Wang, E., Chen, Z., Shen, F., and Liu, Y., 1997, Surface deformation and lower crustal flow in Eastern Tibet: Science, v. 276(5313), p. 788-790.

Royden, L. H., Burchfiel, B.C., and van der Hilst, R.D., 2008, The geological evolution of the Tibetan plateau: Science, v. 321(5892), p. 1054-1058.

Ruddiman, W., Raymo, M., Prell, M., and Kutzbach, J., 1997, The uplift-climate connection; a synthesis. In: Ruddiman, W., Editor, Tectonic uplift and climate change, Plenum Press, New York, NY, p. 417-515.

Şengör, A.M.C., 1984, The Cimmeride orogenic system and the tectonics of Eurasia: Geological Society of America Special Paper, 195, p. 1-82.

Şengör; A.M.C., and Natal'in, B.A., 1996, Paleotectonics of Asia: fragments of a synthesis, In Yin, A., and Harrison, T.M., Editors, The tectonic evolution of Asia, p. 486-641.

Tapponnier, P., Peltzer, G., Ledain, A.Y., Armijo, R., and Cobbold, P., 1982, Propagating Extrusion Tectonics in Asia - New Insights from Simple Experiments with Plasticine: Geology, v. 10(12), p. 611-616.

Tapponnier, P., Xu, Z.Q., Roger, F., Meyer, B., Arnaud, N., Wittlinger, G., and Yang, J.S., 2001, Oblique stepwise rise and growth of the Tibet plateau: Science, v. 294(5547), p. 1671-1677.

Thatcher, W., 2006, Microplate model for the present-day deformation of Tibet: Journal of Geophysical Research, v. 112 B01401, doi:10.1029/2005JB004244.

Tilmann, F., Ni, J., et al., 2003, Seismic imaging of the downwelling Indian lithosphere beneath Central Tibet: Science, v. 300, p. 1424-1427.

Van der Voo, R., Spakman, W., and Bijwaard, H., 1999, Tethyan subducted slabs under India: Earth and Planetary Science Letters, v. 171, p. 7-20.

Van der Woerd, J., Tapponnier, P., Ryerson, F.J., Meriaux, A.S., Meyer, B., Gaudemer, Y., Finkel, R.C., Caffee, M.W., Zhao, G.G., and Xu, Z.Q., 2002, Uniform postglacial slip-rate along the central 600 km of the Kunlun Fault (Tibet), form Al-26, Be-10, and C-14 dating of riser offsets, and climatic origin of the regional morphology: Geophysical Journal International, v. 148, p. 356-388.

Whipple, K.X., 2009, The influence of climate on tectonic evolution of mountain belts: Nature Geoscience, v. 2, p. 97-104.

Wilson, C.J.L., and Fowler, A.P., 2011, Denudational response to surface uplift in east Tibet: Evidence from apatite fission-track thermochronology: Bulletin of the Geological Society of America, doi:10.1130/B30331.1.

Wittlinger, G., Vergne, J., et al., 2004, Teleseismic imaging of subducting lithosphere and Moho offsets beneath western Tibet: Earth and Planetary Science Letters, v. 221, p. 117-130.

Yin, A., Rumelhart, P.E., Butler, R., Cowgill, E., Harrison, T.M., Foster, D.A., Ingersoll, R.V., Zhang, Q., Zhou, X.Q., Wang, X.F., Hanson, A., and Raza, A., 2002, Tectonic history of the Altyn Tagh fault system in northern Tibet inferred from Cenozoic sedimentation: Geological Society of America Bulletin, v. 114, p. 1257-1295.

Yin, A., Dang, Y., Zhang, M., McRivette, M.W., Burgess, W.P., and Chen, X., 2007, Cenozoic tectonic evolution of Qaidam basin and its surrounding regions (part 2): Wedge tectonics in southern Qaidam basin and the Eastern Kunlun Range: Geological Society of America Special Papers, v. 433, p. 369-390.

Yin, A., Dang, Y.Q., Wang, L.C., Jiang, W.M., Zhou, S.P., Chen, X.H., Gehrels, G.E., and McRivette, M.W., 2008, Cenozoic tectonic evolution of Qaidam basin and its surrounding regions (part 1): The southern Qilian Shan-Nan Shan thrust belt and northern Qaidam basin: Geol Soc Am Bull, v. 120(7-8), p. 813-846.

Zhao, W. L., and Morgan, W.J., 1987, Injection of Indian Crust into Tibetan Lower Crust - a Two-Dimensional Finite-Element Model Study: Tectonics, v. 6(4), p. 489-504.

Zheng, D., Clark, M.K., Zhang, P., Zheng, W., and Farley, K.A., 2010, Erosion, fault initiation and topographic growth of the North Qilian Shan (northern Tibetan Plateau): Geosphere, v. 6(6), p. 937-941.

Zhu, B., Kidd, W.S.F., Rowley, D.B., Currie, B.S., and Shafique, N., 2005, Age of initiation of the India-Asia collision in the east-central Himalaya: J Geol, v. 113(3), p. 265-285.

Chapter II

Dissipation of fast strike-slip faulting within and beyond northeastern Tibet[1]

Abstract

Structural patterns, GPS velocities, and Quaternary fault slip rates in northeastern Tibet indicate a transfer of left-lateral slip from the Kunlun Fault northeast to the Haiyuan Fault and minor crustal shortening and rotation within a 200 km wide step-over zone. Related deformation also continues at least a few hundred kilometers north of the Haiyuan Fault into a region of diffuse extensional(?) shear or rotation underlain by average thickness crust. Fast, localized slip along the central Kunlun Fault transforms into distributed deformation across a 500 km wide zone where the lower crust is weak. The distribution of fault-parallel GPS velocities across this region suggests a decrease in fault slip toward eastern fault tips and progressive dissipation of slip to the north rather than east of the Tibetan Plateau as previously suggested.

[1] Citation: Duvall, A. R. and Clark, M. K., 2010, Dissipation of fast strike-slip faulting within and beyond northeastern Tibet: Geology, v. 38, p. 223-226.

2.1 Introduction

Lateral motion and rotation of continental fragments by strike-slip faulting is a ubiquitous process in continental collisions (e.g., Tapponnier et al., 1982; Ratsbacher et al. 1991; Sengör et al., 1985). The role these faults play in accommodating plate convergence however is contentious. The Tibetan orogen, where major strike-slip faults have long been recognized as primary surface features (Molnar and Tapponnier, 1975), lies at the center of this debate. Two important questions concerning the evolution of these faults are: (1) is localized fast slip on major strike-slip faults absorbed by deformation within the plateau, or does it extend east of the plateau to adjacent terrain? and (2) when deformation is localized on one or two faults as in micro-plate or block boundaries (Thatcher, 2007; Meade, 2007), how is strain distributed from one major fault to another?

Proposed fast slip rates (>10 mm/yr) along the Kunlun, and Haiyuan left-lateral faults in northeastern Tibet are interpreted by some to continue eastward beyond the plateau margin due to the extrusion of continental fragments toward the Pacific/Philippine subduction zones (Gaudemer et al., 1995; Lasserre et al., 2002; Tapponnier et al., 1982; 2001). Alternatively, others have proposed that lateral motion terminates before reaching the eastern plateau edge (England and Molnar, 1990; Burchfiel et al., 1991; Kirby et al., 2007). This debate continues in part because we lack understanding of how fast slip is transferred from one structure to another within or beyond the plateau.

It is a challenge to document slip transfer, especially if it is distributed among many faults, because small offsets are difficult to measure in the geologic record. Geodetic measurements, which are sensitive to millimeter-scale velocities, are well suited to address this issue. In previous studies, tectonic blocks within the Tibetan orogen have been defined by the GPS velocity field (Thatcher, 2007; Meade, 2007). But such block-based approaches fail to resolve fault termination and by design, neglect smaller, minor structures that participate in slip transfer between major structures. We use fault parallel GPS velocities and Quaternary slip rates along fault strike to evaluate fault termination and slip transfer in northeastern Tibet. We also examine how minor structures participate in slip dissipation from the Kunlun Fault to the surrounding foreland.

2.2 Geologic Background and Quaternary Slip Rates

The left-lateral Kunlun Fault strikes E-W and extends ~1500 km across northeastern Tibet (Figure 2.1). The left-lateral Haiyuan Fault parallels the Kunlun Fault a few hundred kilometers to the northeast (Figure 2.1). Studies of the central and western segments of the Kunlun Fault yield measured late Pleistocene to Holocene slip rates of ~11 +/- 2 mm/yr (Van der Woerd et al., 1998; 2000; 2002) with possible reinterpreted rates as low as 6.5 – 8.7 +/- 1.8 mm/yr (Cowgill, 2007) (Figure 2.1 and 2.2). Quaternary and geodetic rates along the eastern fault segment are 2 to 6 times lower suggesting that the fault terminates within the eastern margin of the Tibetan Plateau (Kirby et al, 2007). High Quaternary slip rates (19 +/- 5 mm/yr and 11 +/- 4 mm/yr) are reported for the central segment of the Haiyuan Fault (Gaudemer et al., 1995; Lasserre et al., 1999, 2002) that decrease toward the eastern fault tip (4 – 6 mm/yr)(Li et al., 2009; Zhang et al.,

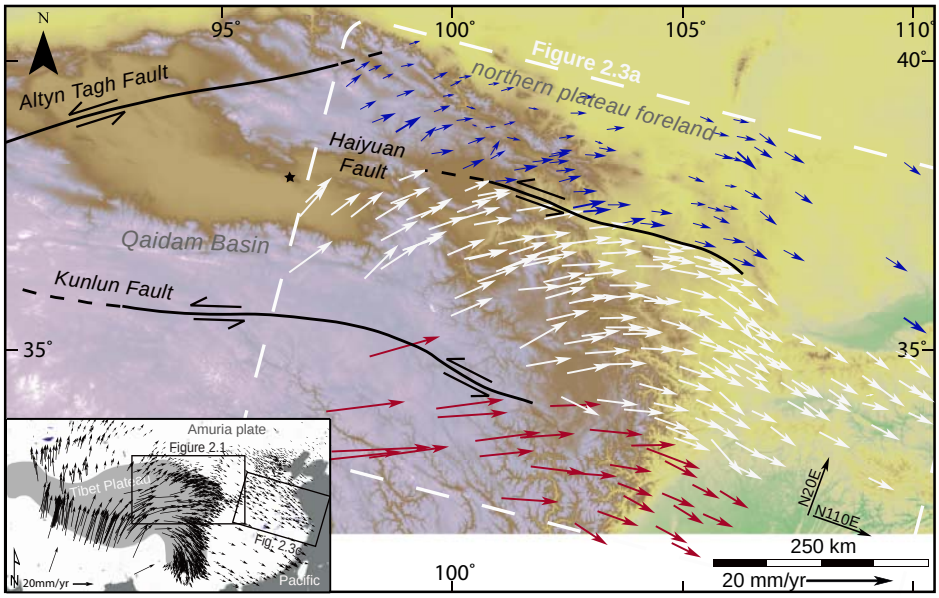

Figure 2.1. GPS velocities relative to stable Eurasia (Gan et al., 2007). Blue (northern), white (central), red (southern) represent regions with distinct N110E velocity trends. Black star shows start location for the 110° projected line. Inset map shows location of eastern China sites included in Figure 2.3.

1991). However, InSAR data suggest lower rates for the central fault segment of 4.2 – 8 mm/yr (Cavalié et al., 2008).

The intervening region between the prominent, fast-slipping Kunlun and Haiyuan Faults is a complex suite of minor faults of various types and orientations that accommodate both left and right lateral fault motion and thrusting. Faults in this region are generally smaller in length and total offset then the major bounding strike-slip faults, and how these minor faults may transfer slip from the Kunlun to the Haiyuan Fault has not been previously considered. Wang and Burchfiel (2004) interpret the right-lateral Elashan Fault (or Wenquan Fault), as a conjugate to the left-lateral Altyn Tagh Fault whereby both structures accommodate the northward indentation of the Qaidam Basin into the Qilian Shan belt. Other studies interpret the region of northeastern Tibet more simply as a wide zone of transpression (Meyer et al., 1998).

2.3 Geodetic Deformation Rates

We derive a continuous function of fault slip rate along strike of the Kunlun and Haiyuan Faults in order to evaluate the termination of these faults and the possible slip transfer between them and the surrounding foreland. Analogous to the approach of elastic dislocation models, we project strike-parallel velocities (average fault trend of N110E) from published GPS data (Gan et al., 2007) onto a line trending 110° and difference velocities across the fault to determine slip rate. Velocity in the N110E direction dominates the geodetic field in northeastern Tibet, with exception of the far western extent of our study area that overlaps with compressional deformation of the Qilian Shan

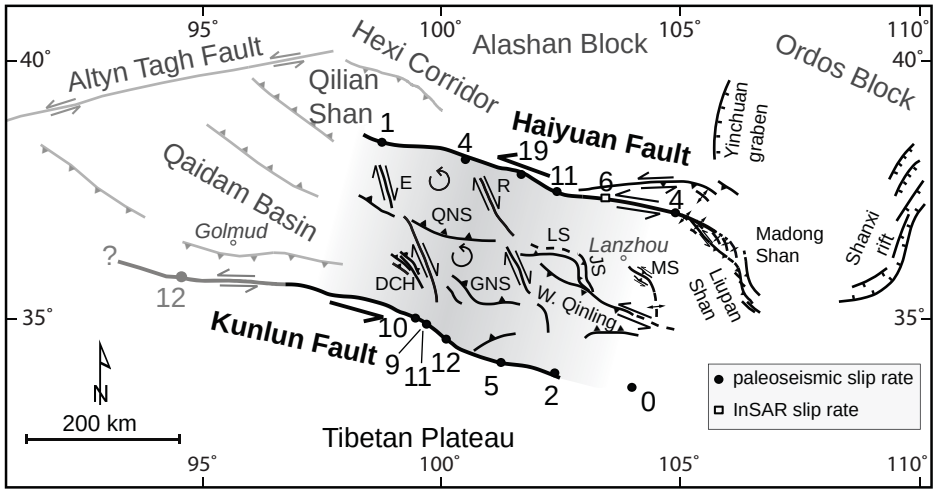

Figure 2.2. Detailed fault map of northeast Tibet (same map extent as Figure 2.1). Elashan Fault (E), Riyueshan Fault (R), Dulan-Chaka Highland (DCH), Gonghe Nan Shan (GNS), Qinghai Nan Shan (QNS), (LS) Laji Shan, (JS) Jishi Shan, and the Maxian Shan (MS) (Qinghai BGMR, 1991). Heavy lines and dark shading represent structures within the proposed Kunlun/Haiyuan stepover region with Quaternary slip rates in mm/yr.

(Figure 2.4). Block rotation between the Kunlun and Haiyuan Faults is also negligible (Thatcher, 2007).

Three distinct trends in velocity versus distance emerge: velocities south of the Kunlun Fault decrease linearly from 20 to ~6 mm/yr; between the Kunlun and Haiyuan Faults velocities initially increase and then decrease from values ranging from ~5 to 8 mm/yr; and north of the Haiyuan Fault velocities linearly increase from ~2 to 6 mm/yr (Figure 2.3). Distinct velocity trends on either side of the Kunlun and Haiyuan Faults suggest concentrated slip on these faults and scatter within each trend could result from deformation along smaller structures or may be unrelated to tectonism (e.g., movement of groundwater). Stations within 50 km (~ three locking depths based on the depths of large earthquakes in Tibet) of either fault were excluded to avoid complications related to elastic behavior within the vicinity of locked structures (Savage and Burford, 1973). We derive average velocity trends for each sub-group by fitting a line to the northern and southern data, and a parabola to the central data. These trends are equal to the average far-field velocity on either side of the Kunlun and Haiyuan Faults and the difference in velocity is equal to the slip rate (Figure 2.3; Chapter II appendix).

Kunlun geodetic and Quaternary slip rates decrease from 12 mm/yr to zero from west to east before reaching the eastern plateau margin (Kirby et al., 2007; Figure 2.3 inset). Along the same distance, Haiyuan geodetic slip rates increase from 2 mm/yr to a maximum of 4.5 mm/yr before decreasing back to zero (Figure 2.3 inset). Geodetic rates are within error of lower Quaternary and InSAR rates (<6 mm/yr) along several locations spanning 500 km along the Haiyuan Fault. High slip rates reported for the central segment of the Haiyuan Fault (Gaudemer et al., 1995; Lasserre et al., 1999; 2002) are

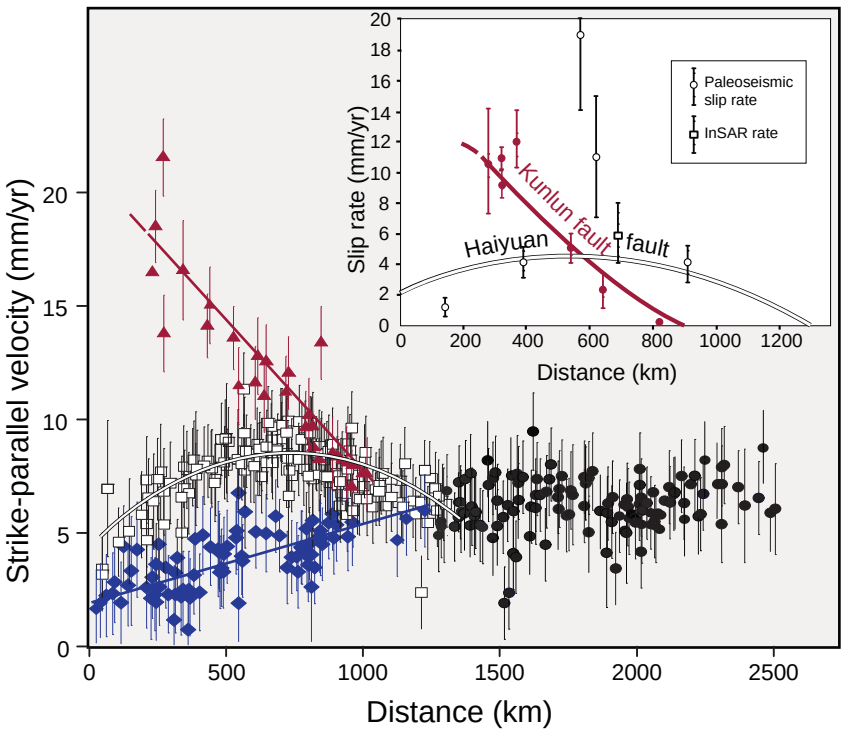

Figure 2.3. Strike-parallel velocity (N110E) versus distance. Sites south of the Kunlun fault (red), central sites between the Kunlun and Haiyuan faults (white), sites north of the Haiyuan fault (blue) and eastern China sites (black, locations Figure 2.1 inset). Inset shows geodetically determined slip rate versus projected distance for the Kunlun fault (red), calculated by subtracting trends in N110E velocities of the central data from velocities of the southern data, and Haiyuan fault (white), calculated by subtracting northern station velocities from central station velocities.

outliers to a more consistent pattern of modest slip defined by Quaternary, InSAR and geodetic rates that decrease toward the fault tips (Figure 2.3 inset).

GPS stations east and north of the plateau move eastward relative to stable Eurasia at rates of 6-10 mm/yr (Chen et al., 2000). However, velocities in the N110E direction for sites north of the Haiyuan Fault increase linearly from 2 – 6 mm/yr from west to east (Figure 2.3), which has not been recognized previously. This trend could be explained by rotation or displacement between the northern foreland and stable Eurasia. Convergence in N110E velocity at ~ 6 mm/yr occurs at roughly the eastern margin of the plateau (profile distance 1000-12000 km), which is equal to the average N110E velocities across eastern China (Figure 2.1 and 2.3). The lack of significant relative displacement in the N110E direction between the southern, central, and northern stations suggests the termination of strike-slip faulting within the eastern plateau foreland.

2.4 Discussion

Kunlun Fault to Haiyuan Fault

Between the Kunlun and Haiyuan Faults, deformation is accommodated by numerous smaller strike-slip and thrust structures that are 50 – 100 km in length (Figure 2.2). In the western part of the step-over zone, we propose that the Elashan (Wenquan) and Riyueshan Faults form antithetic right-lateral structures that accommodate shear through counterclockwise block rotation in a bookshelf or domino style (Mandl, 1987), rather than acting as a conjugate to the left-lateral Altyn Tagh Fault (Wang and Burchfiel, 2004). Rotation of smaller "blocks" of crust (50 km x 50 km) separated by right-lateral faults produces transpression and crustal thickening along ENE striking thrust and

reverse fault bounded mountain ranges, including the Qinghai Nan Shan, Gonghe Nan Shan, and Dulan-Chaka Highland (Figure 2.2). In the east, N110E directed motion is accommodated along the N-S oriented Jishi thrust fault, and oblique thrusting on the NE convergent Maxian and West Qinling Faults (Figure 2.2). The Haiyuan Fault continues farther east, beyond the tip of the Kunlun Fault, but terminates within the convergent N-S striking Liupan Shan and Madong Shan thrust and folds (Figure 2.2).

The complex deformation that we describe here is similar to other areas of continental strike-slip faulting (e.g., the Mojave block of southern California (Dokka and Travis, 1990)) and is consistent with both simple shear experiments (Freund, 1974) and general predictions of strain fields associated with systems of transcurrent faults (Sylvester, 1988). The decrease in Quaternary and geodetic fault slip rates toward the fault tips is consistent with a transfer of left-lateral motion northeast from the Kunlun to the Haiyuan Fault. However, fault slip rates suggest that not all of the Kunlun left-lateral motion is accommodated by the Haiyuan Fault alone, some of which must be absorbed by the complex deformation in the intervening region between the two faults.

North of Haiyuan Fault

GPS data from the northern plateau foreland show an unexpected linear west-to-east increase in N110E velocities with respect to Eurasia. No continuous E-W oriented fault exists north of the foreland stations; therefore we cannot simply interpret motion of the foreland stations as strike-slip faulting. Such increase in N110E velocities could represent rotation of a rigid block, such as the proposed Alashan block or Amuria microplate, although their boundaries are poorly constrained at present (Apel et al., 2006). Either distributed conjugate strike-slip faulting or east-west extension on numerous small faults

could also explain the velocity pattern. North and south-vergent transpression on WNW trending faults affects stations within the Qilian Shan/Hexi corridor (Meyer et al., 1998) (2.1 and 2.2) but cannot explain the increase in N110E velocity farther to the east. North-south trending faults of the Yinchuan Graben and Shanxi rift accommodate east-west extension within the northern foreland along the eastern extent of the profile (Zhang et al., 1991). Yet, to explain the observed velocity trend several other minor extensional structures that accommodate diffuse extensional shear must be present. Such a pattern of faulting is not yet recognized in the field but would be consistent with the geodetic data.

GPS velocities at ~6 mm/yr across eastern China sites suggest movement of this region with respect to stable Eurasia; yet the fact that rates are uniform across all stations suggests large scale regional motion of southern Eurasia, rather than extrusion of individual fault blocks. Lack of strike-slip faulting east of the plateau is noteworthy because its absence precludes the eastward escape or extrusion of tectonic blocks due to the advancing Indian plate (Tapponnier et al., 1982; Peltzer and Saucier, 1996).

Deformation by rotation or distributed faulting north of the plateau margin dissipates N110E motion. As a result, high strike-slip rates on the central Kunlun Fault (12 mm/yr) are distributed up to 500 km to the north from the high plateau into average thickness crust in the surrounding foreland. Further, this slip dissipation occurs where the Kunlun Fault extends from a region of high crustal strength (Qaidam Basin) into a diffuse plateau margin underlain by a weak lower crust (Clark and Royden, 2000), which is likely to impact faulting patterns (Roy and Royden, 2000). Models that involve an elastic upper crust underlain by low-viscosity lower crust result in broad zones of interacting faults whereas crust modeled as entirely elastic results in narrow zones of deformation focused

on single faults. Thus, weaker crust underlying the northeastern margin of Tibet may prohibit continued localized deformation along the Kunlun Fault and result in the much wider and complicated set of structures extant across this region.

2.5 Conclusions

Whereas the importance of strike-slip faulting in accommodating India-Eurasia motion is undeniable, the notion of eastward extruding crustal blocks toward a lateral "free" boundary (Tapponnier et al., 1982) is not supported by geodetic and Quaternary slip rates. Rather than continuing to the east, we demonstrate that fast slip on the left-lateral Kunlun Fault (>10 mm/yr) is transferred northward, in the direction of plate convergence. Deformation is partly accommodated by the Haiyuan Fault and intervening faults in a regional step-over, and partly by distributed extensional faults or block rotation within the northern plateau foreland. This interpretation explains both the distribution and sense of motion on faults that lie between the Kunlun and Haiyuan Faults as well as extensional faulting in the northern plateau foreland. The transfer of Kunlun Fault motion northward over 500 km suggests that a wide deforming zone develops in a region of weak lower crust.

2.6 Acknowledgements

We thank Weijun Gan, Nathan Niemi, Peter Molnar, Jeroen Ritsema and the National Science Foundation, Continental Dynamics Program (EAR-0507431) for support of this research.

2.7 References

Apel, E.V., Bürgmann, R., Steblov, G., Vasilenko, N., King, R., and Prytkov, A., 2006, Independent active microplate tectonics of northeast Asia from GPS velocities and block modeling: Journal of Geophysical Research, v. 33, doi:10.1029/2005JB004120.

Burchfiel, B.C., Zhang, P., Weiqi, Z., Fangmin, S., Qidong, D., Molnar, P., and Royden, L., 1991, Geology of the Haiyuan fault zone, Ningxia-Hui autonomous region, China, and its relation to the evolution of the northeastern margin of the Tibetan Plateau: Tectonics, v. 10, p. 1091-1110.

Cavalié, O., Lasserre, C., Doin, M.-P., Peltzer, G., Sun, J., Xu, X., and Shen, Z.-K., 2008, Measurement of interseismic strain across the Haiyuan fault (Gansu, China) by InSAR: Earth and Planetary Science Letters, v. 275, p. 246-257.

Chen, Z., Burchfiel, B.C., Liu, Y., King, R.W., Royden, L.H., Tang, W., Zhao, J., and Zhang, X., 2000, Global positioning system measurements from eastern Tibet and their implications for India/Eurasia intercontinental deformation: Journal of Geophysical Research, v. 105, p. 16215-16227.

Clark, M.K., and Royden, L.H., 2000, Topographic ooze: Building the eastern margin of Tibet by lower crustal flow: Geology, v. 28, p. 703–706.

Cowgill, E., 2007, Impact of riser reconstructions on estimation of secular variation in rates of strike-slip faulting: Revisiting the Cherchen River site along the Altyn Tagh Fault, NW China: Earth and Planetary Science Letters, v. 254, p. 239-255.

Dokka, R.K., and Travis, C.J., 1990, Late Cenozoic Strike-slip faulting in the Mojave desert, California: Tectonics, v. 9, p. 311-340.

England, P., and Molnar, P., 1990, Right-lateral shear and rotation as the explanation for strike-slip faulting in eastern Tibet: Nature, v. 344, p. 140–142.

Freund, R., 1974, Kinematics of transform and transcurrent faults: Tectonophysics, v. 21, p. 93-134.

Gan, W., Zhang, P., Shen, Z.-K., Niu, Z., Wang, M., Wan, Y., Zhou, D., and Cheng, J., 2007, Present-day crustal motion within the Tibetan Plateau inferred from GPS measurements: Journal of Geophysical Earth, v. 112, doi:10.1029/2005JB004120.

Gaudemer, Y., Tapponnier, P., Meyer, B., Peltzer, G., Shunmin, G., Zhitai, C., Huagung, D., and Cifuentes, I., 1995, Partitioning of crustal slip between linked, active faults in the eastern Qilian Shan, and evidence for a major seismic gap, the „Tianzhu gap', on the western Haiyuan fault, Gansu (China): Geophysical Journal International, v. 120, p. 599-645.

Kirby, E. Harkins, N., Wang, E., Shi, X., Fan, C., and Burbank, D., 2007, Slip rate gradients along the eastern Kunlun fault: Tectonics, v. 26, doi:10.1029/2006TC002033.

Lasserre, C., Morel, P.-H., Gaudemer, Y., Tapponnier, P., Ryerson, F. J., King, G. C. P., Métivier, F., Kasser, M,. Kashgarian, M., Liu B., Lu T., and Yuan, D., 1999, Postglacial left slip rate and past occurrence of $M \geq 8$ earthquakes on the western Haiyuan fault, Gansu, China: Journal of Geophysical Research, v. 104, p. 17,633-17,651.

Lasserre, C., Gaudemer, Y., Tapponnier, P., Mériaux, A.-S., Van der Woerd, J., Daoyang, Y., Ryerson, F.J., Finkel, R.C., and Caffee, M.W., 2002, Fast late

Pleistocene slip rate on the Leng Long Ling segment of the Haiyuan fault, Qinghai, China: Journal of Geophysical Research, v. 107, doi:10.1029/2000JB000060.

Li, C., Zhang, P., Yin, J., and Min, W., 2009, Late Quaternary left-lateral slip rate of the Haiyuan fault, northeastern margin of the Tibetan Plateau: Tectonics, v. 28, doi:10.1029/2008TC002302.

Mandl, G., 1987, Tectonic deformation by rotating parallel faults: the "bookshelf" mechanism*: Tectonophysics, v. 141, p. 277-316.

Meade, B. J., 2007, Present-day kinematics at the India-Asia collision zone: Geology, v. 35, p. 81 – 84.

Meyer, B., Tapponnier, P., Bourjot, L., Metivier, F., Gaudemer, Y., Peltzer, G., Shunmin, G., and Zhitai, C., 1998, Crustal thickening in Gansu-Qinghai, lithospheric mantle subduction, and oblique, strike-slip controlled growth of the Tibet plateau: Geophys, J. Int., v. 135, p. 1-47.

Molnar, P., and Tapponnier, P., 1975, Cenozoic tectonics of Asia: Effects of a continental collision: Science, v. 189, p. 419-426.

Peltzer, G., and Saucier, F., 1996, Present-day kinematics of Asia derived from geologic fault rates: Journal of Geophysical Research-Solid Earth, v. 101, p. 27,943–27,956, doi: 10.1029/96JB02698.

Qinghai BGMR (Bureau of Geology and Mineral Resources of Qinghai Province), 1991, Regional geology of Qinghai province: Beijing, China, Geological Publishing House (in Chinese with English abstract).

Ratschbacher, L., Frisch, W., Linzer, H.G., and Merle, O., 1991, Lateral extrusion in the Eastern Alps, structural analysis: Tectonics, v. 10, p. 257–271.

Roy, M. and Royden, L.H., 2000, Crustal rheology and faulting at strike-slip plate boundaries 2. Effects of lower crustal flow: J. Geophys. Res., v. 105, p. 5599-5613.

Savage, J.C., and Burford, R.O., 1973, Geodetic Determination of Relative Plate Motion in Central California: Journal of Geophysical Research, v. 78, p. 832-845.

Sylvester, A.G., 1988, Strike-slip faults: Geological Society of America Bulletin, v. 100, p. 1666 – 1703.

Şengör, A.M.C., Gorur, N., and Saroglu, F., 1985, Strike-slip faulting and related basin formation in zones of tectonic escape: Turkey as a case study, *in* Strike-Slip Faulting and Basin Formation, edited by Biddie, K.T. and N. Christie-Blick, Spec. Publ. Soc. of Econ. Paleontol. Mineral., v. 37, p. 227-264.

Tapponnier, P., Peltzer, G., Armijo, R., Le Dain, A.Y., and Cobbold, P., 1982, Propagating extrusion tectonic in Asia: New insights from simple experiments with plasticine: Geology, v. 10, p. 611–616.

Tapponnier, P., Zhiqin, X., Roger, F., Arnaud, N., Wittlinger, G., and Jingsui, Y., 2001, Oblique Step Wise Rise and Growth of the Tibet Plateau: Science, v. 294, p. 1671-1677.

Thatcher, W., 2007, Microplate model for the present-day deformation of Tibet: Journal of Geophysical Research, v. 112 B01401, doi:10.1029/2005JB004244.

Van der Woerd, J., Ryerson, F.J., Tapponnier, P., Gaudemer, Y., Finkel, R., Meriaux, A.S., Caffee, M., Zhao, G., Qinlin, H., 1998, Holocene left-slip rate determined by cosmogenic surface dating on the Xidatan segment of the Kunlun Fault (Qinghai, China): Geology, v. 26, p.695-698.

Van der Woerd, J., Ryserson, F.J., Tapponnier, P., Meriaux, A.S., Gaudemer, Y., Meyer, B., Finkel, R.C., Caffee, M.W., and Zhao, G., 2000, Uniform slip-rate along the Kunlun Fault: Implications for seismic behavior and large-scale tectonics: Geophysical Research Letters, v. 27, p. 2353-2356.

Van der Woerd, J., Tapponnier, P., Ryerson, F.J., Meriaux, A.S., Meyer, B., Gaudemer, Y., Finkel, R.C., Caffee, M.W., Guoguang, Z., and Zhiqin, X., 2002, Uniform postglacial slip-rate along the central 600 km of the Kunlun Fault (Tibet), from ^{26}Al, ^{10}Be, and ^{14}C dating of riser offsets, and climatic origin of the regional morphology: Geophysical Journal International, v.148, p.356-388.

Wang, E., and Burchfiel, B.C., 2004, Late Cenozoic right-lateral movement along the Wenquan Fault and associated deformation: Implications for the kinematic history of the Qaidam Basin, Northeastern Tibetan Plateau: International Geology Review, v. 46, p. 861-879.

Zhang, P. Burchfiel, B.C., Molnar, P., Zhang, W., Jiao, D., Deng, Q., Wang, Y., Royden, L., and Song, F., 1991, Rate, amount, and style of late Cenozoic deformation of southern Ningxia, northeastern margin of Tibetan Plateau: Tectonics, v. 10, p. 1111-1129.

Appendix: Chapter II

Method: Analysis of geodetic velocities

The strike-parallel velocity at each station is the component of total GPS velocity (Gan et al., 2007; Figure 2.4) in the direction N110E, the average strike of the Kunlun and Haiyuan Faults. We compare strike-parallel velocities by projecting all stations onto a line trending 110° from a start point between the two structures (black star in Figure 2.4A). We exclude stations within 3 locking depths of faults (50 km based on earthquake data for Tibet). Stations close to major faults (shown in gray, Figure 2.4) were excluded in order to avoid complications related to elastic behavior within the vicinity of locked structures. This analysis is analogous to the commonly applied method of estimating fault-slip rates where differences in far-field velocities are calculated from GPS data collected along fault-perpendicular swath profiles using a dislocation model in an elastic half-space (Savage and Burford, 1973; Figure 2.4B). A key advantage to the approach we take here is that it is possible to consider a continuum of change in fault slip rate along strike of parallel structures simultaneously; thereby enabling assessment of potential fault slip transfer.

The N20E velocity component is perpendicular to fault strike and parallel to the direction of Indian plate convergence. With exception to the far western extent of the study area that overlaps the Qilian Shan, the N20E component of velocity is small

compared to the N110E component (Figure 2.4B). As a result, we focus the detailed analysis and main points of discussion in this paper on strike-parallel velocities derived from geodetic stations across the study area.

Figure 2.4C shows plots of strike-parallel velocity versus distance for three swaths located at western, central, and eastern locations along strike of the Kunlun and Haiyuan Faults (see Figure 2.4A for locations)**.** Solid gray (Kunlun Fault) and dashed black (Haiyuan Fault) lines represent velocities predicted from a dislocation model in an elastic half-space with an assumed locking depth of 15 km (Savage and Burford, 1973). Differences in far-field velocities across faults represent approximate slip rates permitted by the data. Within the western swath (swath 1) fault slip rate along the Kunlun Fault is ~10 mm/yr and greater than twice the Haiyuan rate of 4 mm/yr. The central swath (swath 2) demonstrates a switch to higher rates along the Haiyuan Fault however rates here are less than half that of the Kunlun Fault in swath 1. Swath three, located farthest to the east, shows significantly diminished rates for both faults. Results from each of the three swaths are consistent with fault slip rates calculated from a continuous function along strike of the fault (Figure 2.3b) and highlight a transition from greater Kunlun slip rates to greater Haiyuan rates from west to east.

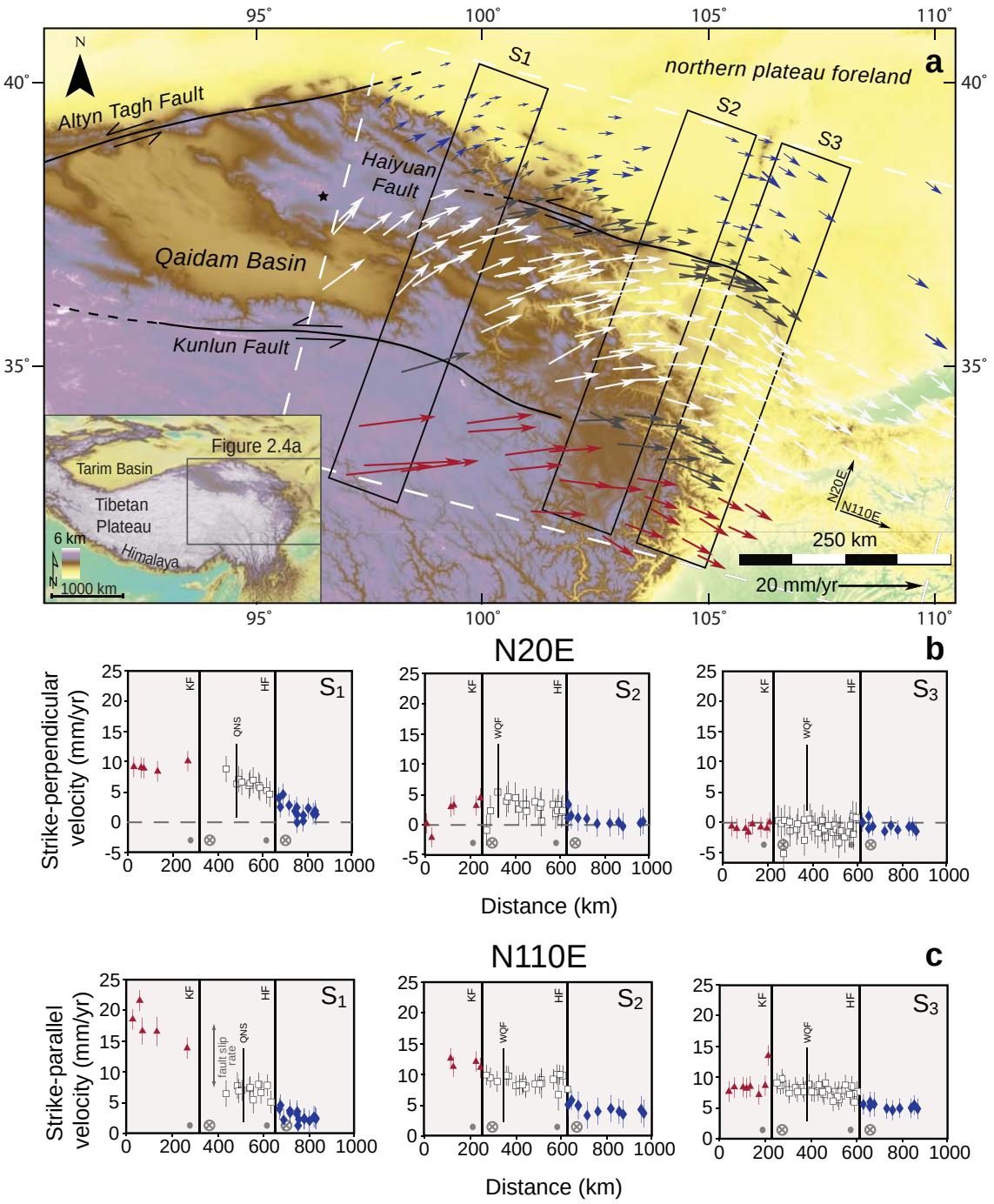

Figure 2.4. Analysis of geodetic velocities. a) GPS velocities relative to stable Eurasia (Gan et al., 2007) where blue (northern), white (central), red (southern) represent regions with distinct N110E velocity trends. Black star shows start location for the 110° projected line. Stations close to major faults, shown in gray, were excluded in order to avoid complications related to elastic behavior within the vicinity of locked structures. b and c) Plots of strike-parallel and strike-perpendicular velocity versus distance for three swaths located at western, central, and eastern locations along strike of the Kunlun and Haiyuan Faults. WQF - West Qinling Fault, QNS - Qinghai Nan Shan, KF-Kunlun Fault, HF-Haiyuan Fault. See Chapter II appendix for details.

Chapter III

Direct dating of Eocene reverse faulting in northeastern Tibet using Ar-dating of fault clays and low-temperature thermochronometry[1]

Abstract

Paired together, fault gouge dating and low-temperature thermochronometry overcome the limitations and assumptions inherent in each independent technique. Here we establish timing of brittle faulting along the West Qinling Fault of northeastern Tibet by dating several size fractions of fault gouge clay that represent variable populations of illite polytypes. Results show that the authigenic or fault-generated component of illite formed at 50 ± 8 Ma and that the detrital component formed at 236 ± 7 Ma indicating a middle Eocene age of faulting and a middle Triassic age of the wall rocks. Comparing this dataset with published thermochronology from hanging wall rocks supports the interpretation that the West Qinling Fault initiated at ~50 Ma and continued until at least middle Miocene time and that authigenic clay growth occurred at ambient temperatures of ~110°C. Lack of overprinting of younger clay ages at this site may indicate that rocks

[1] Citation: Duvall, A.R., Clark, M.K., van der Pluijm, B.A., and Li, C., 2011, Direct dating of Eocene reverse faulting in northeastern Tibet using Ar-dating of fault clays and low-temperature thermochronometry: Earth Planet Sci Lett., v. 304, p. 520-526.

were out of the thermal window for authigenic clay formation during later faulting episodes. The potential for temperature to control illite growth has implications for interpretation of authigenic illite ages and their relationship to deformation episodes within fault zones.

3.1 Introduction

Measurements of timing and rates of upper crustal deformation are central in the ongoing debate regarding the relative roles of tectonics and climate in mountain building (Willett, 1999; Whipple, 2009). However, a paucity of independent measures of fault motion, erosion, and elevation change in active orogens hinders progress in understanding the complex interaction of these competing processes (Whipple, 2009). Dating fault motion in particular is challenging because offsets of stratigraphic units useful in determining fault timing are not always preserved and stratigraphic ages are often poorly constrained. Thus, isotopic dating of clays in fault gouge provides an important alternative to directly date brittle fault motion because the energetics of faulting and fluid flow promotes growth of authigenic clay during faulting episodes within the shallow crust.

Fault gouge clays are assumed to comprise a two population mixture of mica polytypes: (1) detrital illite ($2M_1$) derived from wall rocks and (2) authigenic or *in situ* illite ($1M_d$) formed within the brittle fault zone during faulting. Isolation of pure authigenic clay for isotopic analysis is typically not possible (Pevear, 1992; Grathoff et al., 2001). As a result, ages from different clay size fractions that contain different relative percentages of each clay polytype are used to determine the age of the pure

authigenic clay assuming a two-end member mixing model (Solum et al., 2005; van der Pluijm et al., 2006; Haines and van der Pluijm, 2008).

Because fault ages calculated using the two-end member mixing model correspond to discrete events that represent either the timing of short-lived faulting or a finite period of fluid-present fault motion (Solum et al., 2005; van der Pluijm et al., 2006; Haines and van der Pluijm, 2008), determining the complete history of fault activity from a single fault-gouge age is unlikely. Illite ages determined for faults with prolonged histories are thought to represent the last major period of fault motion assuming that new authigenic illite growth occurs with each successive faulting event and the complete overprinting of illite grown during earlier phases of deformation (Solum et al., 2005; Haines and van der Pluim, 2008). Whether such assertions should apply to all cases, however, remains largely untested.

The conditions under which authigenic clay forms in a fault zone are critical to the interpretation of illite ages. Temperature is likely to be one of the key parameters controlling its growth but due to limited temperature data within fault zones dated using the illite age analysis technique, the growth temperature of authigenic illite in fault gouge is not well constrained. Early experimental work and studies of basin brines suggests the $2M_1$ polytype grows above 280ºC and that it is the most stable phase (Velde, 1965), whereas the $1M_d$ polytype is thought to form at significantly lower temperatures below 200ºC (Grathoff et al., 2001; Velde, 1965). If the window of growth temperatures of authigenic illite is relatively narrow, then the range of fault depths where formation can occur will also be limited. Importantly, in this case, there will be a relationship between depth and age of fault events and, specific periods of fault motion (i.e. first or last slip

event or some stage in between) could be targeted for sampling if exhumation history along the fault is independently known.

In this study, we determine timing of fault motion using $^{40}Ar/^{39}Ar$ dating of illite in fault gouge for a major reverse fault in northern Tibet where the erosional history from thermal data is precisely known (Clark et al., 2010). There are several advantages to combining results from fault gouge dating with thermochronometry at the same location. Cooling histories from thermochronometry place important constraints on the temperature of authigenic illite growth and thus interpretation of gouge ages. Additionally, comparison of thermal histories with gouge ages from a single or multiple faults offers independent information on the timing of discrete fault events along specific structures that relate to range growth, and may also provide separate evidence for potential erosional periods that are related to climate rather than fault motion.

3.2 West Qinling Fault site, northeastern Tibetan Plateau

Recent work in northern Tibet has shown that thrust faulting initiates at around the time of collision, which is significantly earlier than previously thought. Observations of an early, collision-age deformation history are not predicted simply by existing end-member descriptions of plateau formation (Clark, in review; Clark et al., 2010; Dayem et al., 2009; Kong et al., 1997). Although continuum (England and Houseman, 1986) and step-wise growth (Tapponnier et al., 2001) models of Tibet are widely cited as contrasting end members for plateau development, they share the view that edge forces resulting from India's northward advance into Asia (collision circa 50 Ma, Rowley (1996)) produced high strain rates and crustal thickening that first accumulates at the

plate boundary and then propagates outward in time. Mid-to-late Miocene compressive structures along the distal, northeastern plateau margin (Figure 3.1) are well documented (Lease et al., 2007; Meyer et al., 1998; Zheng et al., 2006). Additionally, regional deformation at or near collision time is implied by clock-wise rotations up to 40 degrees and onset of basin deposition between 55-52 Ma in the greater Xining Basin region (Dai et al., 2006; Dupont-Nivet et al., 2004; Horton et al., 2004) and by at least 29 Ma in the Linxia Basin (Fang et al., 2003), as well as by low-temperature thermochronology (Clark et al., 2010) and structural observations (Yin et al., 2008) that indicate Eocene activity along major northern Tibet thrust structures (Figure 3.1).

We compare the fault gouge age results with the thermal history of hanging wall rocks along a segment of the West Qinling Fault in northeastern Tibet (Figure 3.1) where the slip history likely took place along only a single strand. Eocene thrust activity is proposed along this fault, which is one of the longest and most continuous structures within the northern margin of the plateau. Recently published apatite (U-Th)/He ages (closure temperature of 60 - 70°C) from samples collected along a single depth transect show an interval of steep age/depth gradient starting at ~45 - 50 Ma and continuing through at least 12.5 Ma, which is interpreted as an increase in erosion rate of hanging wall rocks due to thrusting along the West Qinling Fault (Clark et al., 2010). Assuming that faulting is the cause of accelerated erosion, Clark et al. (2010) proposed that initial rapid cooling at the West Qinling Fault signals the first major thrust activity in northeastern Tibet, coincident with the timing of India-Eurasia collision. Forward thermal modeling of helium data that considers radiation damage effects on helium closure temperature and regional geologic constraints suggest sedimentary cover of up to 2 km over the West

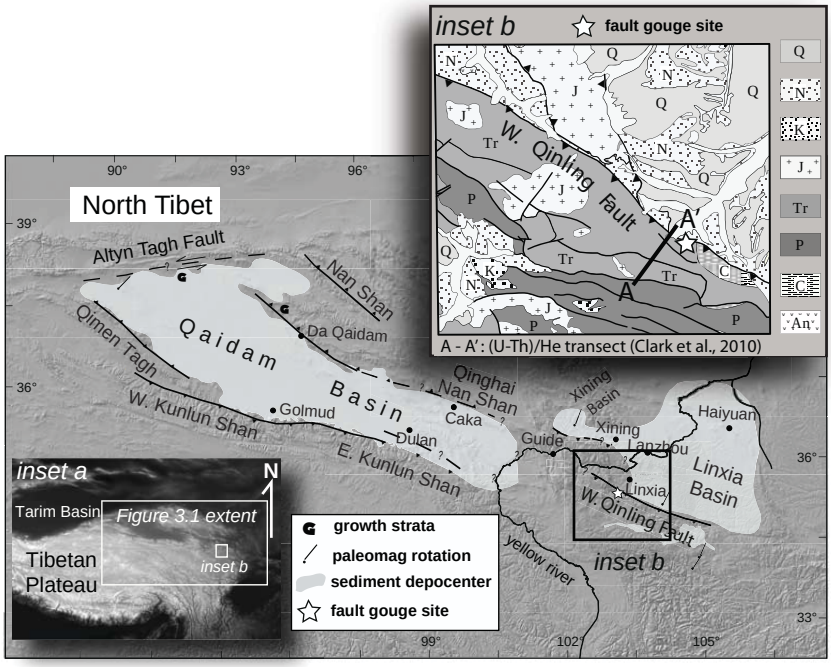

Figure 3.1. Shaded relief location map of West Qinling study area in northern Tibet. Faults and basins shown are those thought to be active during the Eocene (55.8 – 33.9 Ma). Inset a: extent of Figure 3.1 within the greater Himalaya/Tibetan Plateau region. Inset b: generalized geologic map simplified from BGMR Gansu (1989). Q-quaternary deposits, N-Neogene sandstones and shales of the Linxia Basin, K-Cretaceous sandstones and shales, Tr-Triassic flysch deposits (Songpan Ganzi complex), P-Permian rocks, C-Carboniferous rocks, An-Archean rocks. A-A' line shows the location of the (U-Th)/He vertical transect in Clark et al. (2010).

Qinling rocks during late Cretaceous through Eocene time (Clark et al., 2010). Sediment deposition during this time implies regional lowlands and basin inversion following the initiation of the West Qinling thrust fault. We sampled gouge from a site along this fault located near the helium transect (Figure 3.1). Although the fault zone is more complex to the west and east, it appears to be comparatively simple at the sample site (BGRM Gansu, 1989). Here, the moderately-dipping (~45°) reverse fault is exposed as a single strand that bounds the Linxia Basin (Figure 3.1). Hanging wall rocks are dominantly middle-late Triassic flysch deposits of the Songpan Ganzi complex and footwall rocks are primarily Neogene fine-to-coarse grained sandstones (BGRM Gansu, 1989) deposited within the Linxia Basin as a result of flexural loading (Fang et al., 2003). Subsidence patterns derived from several measured stratigraphic sections (Fang et al., 2006) indicate that the basin is flexurally loaded from the south by the West Qinling Fault (Figure 3.1). Based on detailed magnetostratigraphy, six cycles of fining upward sedimentary sequences were deposited within the Linxia Basin from at least 29 Ma through 1.7 Ma (Fang et al., 2006). Poor fossil control at the base of the deepest section prevents tighter age estimates and earlier sediment deposition may have occurred.

3.3 Illite age analysis

Fault dating is accomplished by measuring $^{40}Ar/^{39}Ar$ of clays in fault gouge. It is rarely possible to date 100% fault-formed clay as most size fractions of gouge material include both detrital and authigenic phases and thus comprise a mixture of grain ages (van der Pluijm et al., 2006). As a result, a mixing line of individual gouge clay size fractions that contain various percentages of authigenic clay is created to circumvent this

issue. The percentage of $2M_1$ polytype plotted against apparent argon age for several size fractions is extrapolated to pure authigenic and pure detrital illite end member ages assuming that these are the only two K-bearing components within the sample (Figure 3.2). Coarse (0.2 – 2.0 μm), medium (0.05 – 0.2 μm), and fine (<0.05 μm) grained clay sized fractions were prepared for analysis of gouge sampled from the fault zone (Figure 3.1). All fault-rock materials were disaggregated and separated into clay-sized fractions by first gravitational and centrifugal settling, and then drying under low-heat lamps. Carbonate minerals, which obscure peaks used for polytype quantification, were removed with a weak (~1M) acetic acid solution after separating a small aliquot of material for $^{40}Ar/^{39}Ar$ dating.

A possible complication when analyzing fine-grained crystallites is the displacement of ^{39}Ar that results from the nuclear transformation of ^{39}K. This "recoil effect" may lead to a significant loss of neutron-induced ^{39}Ar and thus produce erroneously old ages. To circumvent this issue, all clay size fractions were packaged into fused silica vials and sealed prior to irradiation, thereby retaining any ^{39}Ar expelled due to recoil (see van der Pluijm et al., 2001 for details on this glass encapsulation technique). Irradiation was performed at the McMaster University Nuclear Reactor (MNR) research facilities and Ar measurement took place at the University of Michigan. The sample vials were first broken open and the initial (recoiled) gas was analyzed followed by step-heating under a defocused laser until sample fusion occurred. Due to Ar recoil (Dong et al., 1995) and because each size fraction comprises a mixture of grain ages, the resulting age spectra from this study do not yield clear plateaus and we determine the time of faulting by

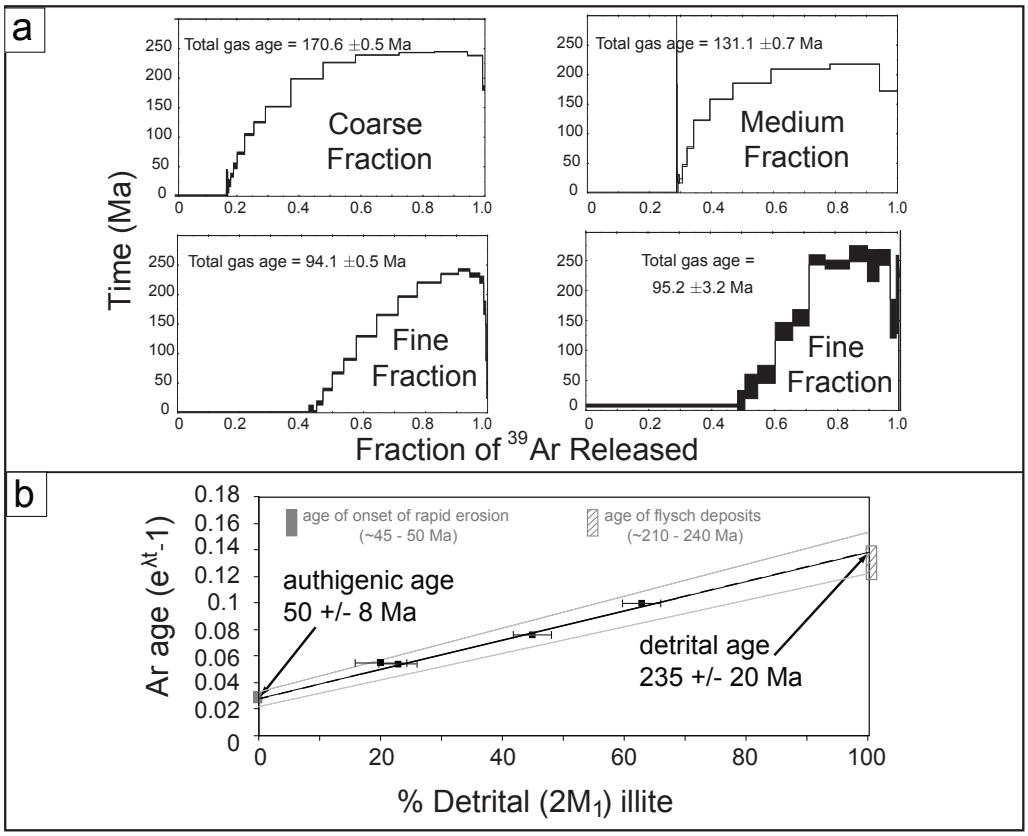

Figure 3.2. a. $^{40}Ar/^{39}Ar$ results for the coarse, medium, and two fine fractions of West Qinling fault gouge. b. Illite age analysis plot for West Qinling fault rocks. Plot displays percent detrital (2M1) illite versus the age (expressed as $e^{\lambda t} - 1$). Black symbols represent total gas ages. Horizontal error bars represent uncertainty on 2M1% (precision 3 – 5%) (Haines and van der Pluijm, 2008), vertical error on $e^{\lambda t} - 1$ is smaller than the symbol. The function $e^{\lambda t} - 1$, where λ is the decay constant of argon and t is the apparent age, is plotted rather than age because it is the decay constant of argon that is linearly proportional to the percentage of detrital mica. 0% 2M1 age on the left side of the plot represents the authigenic or fault age, and the 100% 2M1 age on the right side of the plot is interpreted as the detrital age of wall rocks. Grey lines represent errors derived using a York regression (York, 1968). Shaded boxes represent age of onset of rapid erosion from (U-Th)/He analysis (Clark et al., 2010) and age of the Songpan Ganzi wall rocks (BGMR Gansu, 1989; Weislogel, 2008).

plotting total gas ages rather than retention ages on the illite-age analysis plot (Figure 3.2).

X-ray diffraction methods were utilized to quantify the percentage of the detrital $2M_1$ and authigenic $1M_d$ illite polytypes for each aliquot. The separate size fractions of clay were step scanned from 16 – 44 2Θ with a 0.05° step size at 30 seconds per step using a Scintag X-ray diffractometer at the Electron Microbeam Analysis Laboratory (EMAL), University of Michigan. We used an end-packer device similar to that described in Moore and Reynolds (1989) in order to create near-random powder mounts for scanning, which is necessary to quantify illite polytypes accurately. The relative intensity of the (002) and (020) peaks were used to determine whether randomness was achieved (Pevear, 1992). Illite polytype quantification was accomplished by using the WILDFIRE© program (Reynolds, 1994; Grathoff and Moore, 1996). Modeling of the data entailed matching measured x-ray diffusion patterns for each clay size fraction with those generated using WILDFIRE© for variable populations of the two illite polytypes. Typical precision for this method is on the order of 3 – 5 % as determined by comparing synthetic and natural samples (Haines and van der Pluijm, 2008).

3.4 Results

Four clay size fractions were analyzed in this study. Modeling of XRD powder patterns for each aliquot indicates 23, 45, and 63% (± 3%) $2M_1$ for the fine, medium and coarse clay fractions respectively with an additional fine size fraction at 20% (± 5%) (Table 3.1). Corresponding $^{40}Ar/^{39}Ar$ total gas ages for these aliquots are 94.1 ±0.5, 131.1± 0.7, 170.6± 0.5, and 95.2± 3.2 (Table 3.1). A least squares regression (York,

Table 3.1. West Qinling fault gouge data results

Clay Size (μm)	Detrital Illite (%)	$^{40}Ar/^{39}Ar$ total gas age (Myr)	$^{40}Ar/^{39}Ar$ retention age (Myr)
fine (a)	23±3	94.1±0.5	159.3±0.8
fine (b)	20±5	95.2±3.2	172.6±5.6
medium	45±3	131.1±0.7	181.1±0.8
coarse	63±3	170.6±0.5	202.4±0.6

1968) of $2M_1$ percentage versus illite Ar age constrains a 50 ± 8 Ma (MSWD = 0.6) age of the authigenic component and a 236 ± 7 Ma (MSWD = 0.9) age of the detrital component (Figure 3.2). The larger errors (≤ 16%), calculated using a York regression (York, 1968), mostly reflect the statistics of low sample numbers compared with other similar fault gouge studies that produce repeat analyses that differ less than 2 Ma (e.g., van der Pluijm et al., 2001). Additionally, the range in percentage of illite components within the individual clay size fractions (20 – 65% $2M_1$ in the West Qinling sample) also affects the intercept errors.

Several assumptions are inherent in illite age-analysis. First, illite from fault-gouge samples is derived from a two end-member system (e.g., no late diagenesis) where these end-member polytypes have known and identifiable x-ray diffraction patterns. Second, we assume that authigenic illite is primarily a product of faulting at low-temperature conditions (<200°C) and that the authigenic age represents the time of illite formation rather than a time when the sample passed through a particular thermal window or "closure temperature". In addition, we assume negligible Ar loss from the sample in nature. We consider our results in the context of these assumptions and demonstrate their reliability.

The relationship between detrital illite percentage and Ar age is useful in assessing the two end-member assumption because the percentage of detrital illite should be linearly related to age for the different clay size populations only if two distinct polytypes exist within the mixture. If authigenic and/or detrital illite components with variable argon ages due to post-faulting diagenesis, preservation of multiple phases of detrital illite from wall rocks, or multiple phases of authigenic illite grown during different

faulting events are present within a single fault-gouge sample, then a linear relationship between illite percentage and age is highly unlikely because more than two argon-age end members comprise the mixture. The age and $2M_1$ percentage of the size fractions from the West Qinling Fault site are well fit by a linear segment and the $2M_1$ percentage correlates positively with grain size and total gas age, both of which support the two-population illite assumption (Figure 3.2). Separation of finer clay size fractions would improve the error on the linear regression used to determine the authigenic age, but gouge from the West Qinling Fault does not contain measurable quantities of super fine clay ($<<0.05$ μm). Thus, we were unable to produce a size fraction with less than 20% $2M_1$. A coarser size fraction (> 65% $2M_1$) could also improve intercept constraints, however, previous studies have shown that fractions greater in size than 2 microns are likely to be contaminated with other potassium bearing phases (e.g., potassium feldspar) and thus yield uninterpretable Ar ages (e.g., van der Pluijm et al., 2001).

The growth of authigenic illite is assumed to be lower than the closure temperature to argon loss and thus, the authigenic illite age represents the time of formation. Here, we can estimate the temperature conditions of illite growth by comparing the authigentic illite age to the temperature history of West Qinling hanging wall rocks. One-dimensional forward thermal models of West Qinling apatite helium data constrain accelerated hanging wall erosion at 45 or 50 Ma following a period of isothermal holding since 110 Ma, assuming a layered thermal structure and using the helium closure temperature from the radiation damage model (RDAMM) kinetics of Flowers et al. (2009) (Clark et al., 2010). Figure 3.3 shows the time-temperature history of West Qinling hanging wall rocks given these model results and assuming a geothermal gradient

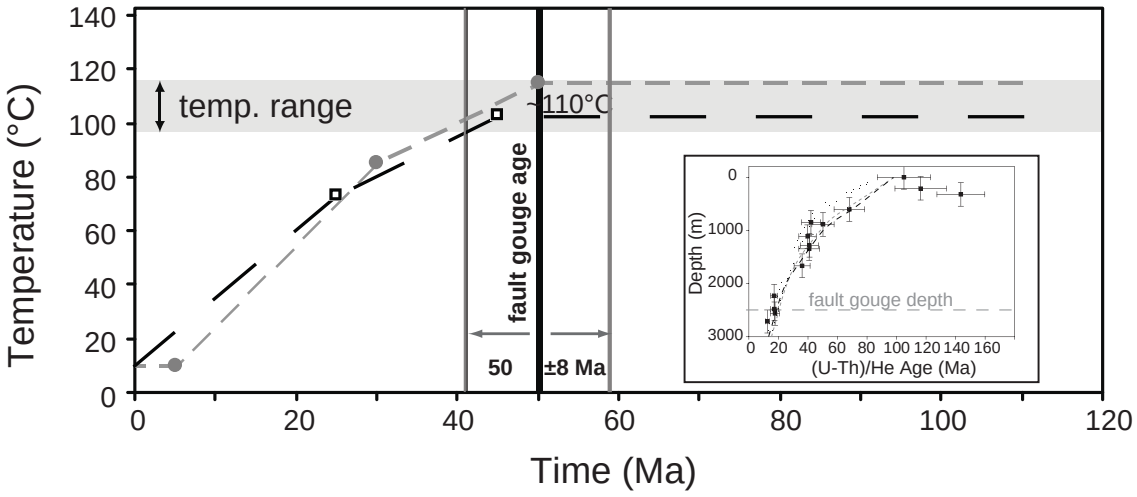

Figure 3.3. Time-temperature plot of West Qinling hanging wall rocks constructed using preferred one-dimensional forward thermal models of apatite helium age data (Clark et al., 2010) for a geothermal gradient in basement rocks of 25°C/km (grey dashed line) and 30°C/km (black dashed line). Grey box represents temperature range of authigenic illite formation estimated by superimposing fault gouge age and errors onto these cooling profiles. Dots and squares mark cooling rate changes for each profile. Inset shows apatite helium age data for West Qinling vertical transect. Horizontal error bars represent 2σ uncertainty on mean age based on single grain replicate ages and vertical error bars represent uncertainty on elevation or depth estimate below local geomorphic surface. Preferred one-dimensional forward thermal models show accelerated hanging wall erosion at 50 Ma (grey dashed line) or 45 Ma (black dashed line) following a period of isothermal holding since 110 Ma, assuming a layered thermal structure and using the radiation damage model (RDAMM) kinetics of Flower et al. (2009). Plot adapted from Clark et al., 2010.

within basement rocks of 25°C/km (grey dashed line Figure 3.3) and 30°C/km (black dashed line Figure 3.3). Using this thermal history and the fault gouge age and errors, a temperature of 108 +/- 10 °C is estimated at the time of authigenic clay formation (Figure 3.3). Though it cannot be ruled out that fluid circulation may be responsible for a different thermal regime within the fault zone, if temperatures were similar within the fault and the hanging wall rocks, then gouge formation occurred well below the approximate 250 to 350°C illite closure temperatures estimated using the equations of Dodson (1973) and recently published muscovite diffusion parameters appropriate for a cylindrical geometry (E=64 kcal/mol and D_o=4 cm^2/s; Harrison et al., 2009) for effective diffusion radii of 0.05 to 2 μm and cooling rates ranging from 1 to 10°C/Ma. This supports the notion that argon age of authigenic illite represents formation and not subsequent cooling and provides further information on temperature of authigenic illite growth.

3.5 Discussion

A fault gouge age of 50 ± 8 Ma overlaps with accelerated cooling rates of hanging wall rocks at 45- 50 Ma (Clark et al., 2010) (Figure 3.3). Correlation between these two datasets indicates that erosion of the hanging wall was commensurate with fault motion. Neogene-aged footwall rocks within the Linxia Basin in contact with the fault gouge (Fang et al., 2003; BGRM Gansu, 1989) (Figure 3.1) suggest faulting must have occurred after the Eocene Epoch, likely during Miocene time. However, correlations of these sediments to well-dated stratigraphic sections are tenuous. Continued rapid exhumation of West Qinling hanging wall rocks until at least 12.5 Ma (the age of the deepest sample

dated) supports long-lived fault activity (Clark et al., 2010). The interpolated Triassic detrital illite age also agrees well with independent geologic constraints. Footwall sandstones at the West Qinling site are likely derived from eroded Songpan Ganzi rocks in the hanging wall and thus the hanging wall and footwall have the same detrital Ar signature. middle-late Triassic sediments of the Songpan Ganzi complex were reportedly deposited in a thick package of ten to twenty kilometers (Weislogel, 2008), thick enough to likely reset muscovite argon ages during burial assuming an average crustal geothermal gradient. Later burial events significant enough to reset Ar are not known, however Late Triassic and Jurassic magmatism occurred regionally (Weislogel, 2008). Therefore, a Triassic detrital age at this site is expected regardless of dominant footwall or hanging wall contribution to the fault zone.

Despite evidence of a protracted West Qinling Fault history, post-Eocene fault motion does not appear to be reflected in the fault gouge age. Multiple episodes of fault slip that generate more than one preserved population of authigenic illite could, in theory, be difficult to resolve using fault gouge dating of illite polytypes because different populations of $1M_d$ illite are indistinguishable by XRD analysis thus producing a pseudo end member. In such cases, the 100% authigenic illite would record a mixture of ages rather than the timing of a discrete fault event. A linear relationship between illite age and percentage of detrital component, however, requires that illite polytypes are grown in the same relative proportions during each event for all size fractions. Such conditions are extremely unlikely given the wide variability in percentage of authigenic and detrital illite for same size clay fractions in previous fault gouge studies (Haines and van der Pluijm, 2010; Haines and van der Pluijm, 2008; Solum et al., 2005; Solum et al., 2007; van der

Pluijm et al., 2006). Thus, a well-defined linear relationship between Ar age and the percentage of illite polytype likely only results from a single fault episode. Based on West Qinling cooling history, geologic relationships at the fault gouge site, and the linear trend of the fault gouge data, we conclude that the estimated fault age records the earliest phase of fault motion, rather than an average of the fault duration or older and younger pulses that mix to form a 50 Ma age of faulting.

3.5.1 Implicatons for conditions of authigenic illite growth in fault zones

The absence of overprinting by younger fault motion suggests that conditions for illite growth existed only during a relatively short interval of fault activity (< 10 Myr) at this sample site compared to the longevity of the West Qinling as an active fault-bounded range (~50 Myr). High potassium (K) content, large surface area, circulating fluids, and temperatures below at least 200°C are thought to be generally appropriate for precipitation of $1M_d$ illite (Grathoff et al., 2001; Pevear, 1992). Wall rock material at the West Qinling site is predominately made up of shales and fine-grained sandstone, which commonly have high K concentrations conducive to forming clays in fault gouge. The geologic record suggests no changes in wall rock material occurred as faulting progressed, so we expect that K was also available during later faulting events. We also assume that ample surface area for clay growth during later fault episodes existed because the fault zone would have been developed after faulting initiated during the Eocene. Fluids likely play an important role in clay gouge formation; however, determining the presence and temperature of fluids circulating during the time of fault motion is outside the scope of this study.

Wall rock temperatures derived from thermochronometry (Clark et al., 2010) suggest that the purely authigenic illite component formed at ~110°C assuming that the fault and wall rock experienced similar thermal histories (Figure 3.3). One possible explanation for the lack of overprinting of younger fault ages at this site is that rocks moved outside the thermal window suitable for illite formation as thrust faulting and erosion of uplifted hanging wall rocks progressed. In this interpretation, we expect that the later fault events are recorded in gouges not yet exhumed to the surface. Unfortunately, suitable exposures of fault gouge are rare and other sites along the fault, including along more deeply exhumed segments, have not been identified. A fault gouge study from the Sierra Mazatàn extensional core complex in Mexico (Haines and van der Pluijm, 2008) with reliable, independent temperature constraints provides an important comparison to our results. At this site, onset of faulting is deduced from the timing of rapid cooling recorded by $^{40}Ar/^{39}Ar$ of K-feldspar from ductile footwall rocks (Wong and Gans, 2003). The detrital illite age ($2M_1$) matches with the approximate timing of mylonite formation whereas the authigenic age ($1M_d$) is assumed to date the later stages of faulting because it is only slightly older than an ignimbrite that caps the mylonitic carapace (Haines and van der Pluijm, 2008). Extrapolating the K-feldspar cooling data through the brittle history of faulting, the authigenic age and errors can be used to constrain the temperature of $1M_d$ illite formation at this site to between 110° and 160°C (Haines and van der Pluijm, 2008), which overlaps with the temperature constraint from the West Qinling Fault presented here.

The authigenic illite formation temperatures estimated are similar to the thermal range of two of the most commonly applied thermochronometers, apatite helium (~60 – 70 °C)

and apatite fission track (~110 °C). Thus, comparison among results from these techniques provides a powerful means to assess upper crustal deformation. Constraints on the relatively narrow temperatures of authigenic illite growth also permit targeted sampling of clays in fault gouge that correspond to particular periods of fault motion if the exhumation history of potential sample sites is reasonably well known.

3.5.2 Implications for tectonic history of the Tibetan Plateau

The depth of exhumation at the West Qinling Fault site (Clark et al., 2010) predicts that the fault age measured here should correspond with the beginning of rapid cooling of hanging wall rocks. Indeed, our results show overlap between that the 100% authigenic illite age and the beginning of accelerated exhumation, which indicates that faulting was a first-order control on erosion in this part of the orogen. Commonly, the erosional response to dip-slip fault motion inferred from low-temperature thermochronometry is employed as a proxy for fault motion (Wagner and Reimer, 1972). Increased fluvial incision occurs in response to faulting because accelerated rock-uplift rates in the hanging wall drive increased erosion by steepening river gradients, channel narrowing, or some combination of both (for the same discharge) (Whipple and Tucker, 1999; Duvall et al., 2004; Whipple, 2004). However, increased rates of erosion can occur solely with increased precipitation (Reiners et al., 2003) where relief is pre-existing, thereby complicating unique correlation of erosion events with faulting episodes. The combination of fault-gouge age and thermochronometry offers an avenue by which we can circumvent the ambiguity of precipitation versus fault driven exhumation patterns.

Together, the geologic history of the West Qinling Fault from clay gouge dating and thermochronometry shows an internally and regionally consistent fault history that begins

in the Eocene and extends through much of the Miocene. Our result offers definitive evidence of Eocene-age reverse faulting within the northeastern Tibetan Plateau and, along with reported ages on thrust faults near the Qaidam Basin (Clark et al., 2010; Yin et al., 2008), suggests that compressive deformation across a significant portion of the northern margin of the plateau initiates within 10 myr of the initial collision between India and Eurasia. Recent model results show that far-field lithospheric deformation due to the Indian indenter shortly after collision is permissible provided that Asian lithosphere can be approximated as a thin viscous sheet, given a strong lithosphere north of Tibet and relatively thick crust in southern Tibet at the onset of plateau building (Dayem et al., 2009). Alternatively, faulting in northern Tibet signifies the constant stress and strength conditions that characterize the orogen since collision (Clark, in review).

3.6. Conclusions

Dating of illite from the West Qinling Fault in northern Tibet suggests thrust fault motion at ~50 Ma. This age fits well with erosional and geologic constraints from hanging wall rocks and the adjacent foreland basin. Results from this site demonstrate that the $^{40}Ar/^{39}Ar$ age of authigenic illite represents a single interval in West Qinling Fault history rather than an amalgamation. Our results also show that the fault-formed illite age does not always represent the latest phase in fault motion (Solum et al., 2005; Haines and van der Pluijm, 2008) as in this case, we document the initiation of faulting. Instead, authigenic illite growth appears to be restricted to a thermal window of the fault history (108 +/- 10 °C), thus the stage of faulting recorded will vary among sample sites depending, at least in part, on thermal history.

3.7 Acknowledgements

We thank Chris Hall for Argon analysis in the University of Michigan's Radiogenic Isotope Geochemistry Laboratory; Sam Haines and Jim Hnat for assistance with sample preparation and data interpretation; Anja Schleicher for guidance with XRD analysis carried out at the University of Michigan Electron Microbeam Analysis Laboratory; and Karen Vasko for assistance in the field. We also acknowledge two anonymous reviewers whose comments improved this manuscript. Support for this research was provided by the National Science Foundation, Continental Dynamics Program (EAR-0507431), the National Science Foundation of China (40234040) and by the State Key Laboratory of Earthquake Dynamics (LED2008A01).

3.8 References

Bureau Geological and Mineral Resources (BGMR) Gansu Province, 1989, Regional Geology of Gansu Province, Geological publishing house, Beijing (in Chinese, 690 pp).

Clark, M.K., *in review*, Does the crust matter? A new view of post-collisional convergence rates: Nature.

Clark, M.K., Farley, K.A., Zheng, D., Zhicai, W., and Duvall, A.R., 2010, Early Cenozoic faulting of the northern Tibetan Plateau margin from (U-Th)/He ages: Earth Planet Sci Lett**.,** v. 296**,** p. 78-88.

Dai, S., Fang, X., Dupont-Nivet, G., Song, S., Gao, J., Krijgsman, W., Langereis, C., Zhang, W., 2006, Magnetostratigraphy of Cenozoic sediments from the Xining Basin: Tectonic Implications for the northeastern Tibetan Plateau: J. Geophys. Res., v. 111, doi:10.1029/2005JB004187.

Dayem, K.E., Molnar, P., Clark, M.K., and Houseman, G.A., 2009, Far-field lithospheric deformation in Tibet during continental collision: Tectonics, v. 28, doi:10.1029/2008TC002344.

Dodson, M.H., 1973, Closure temperature in cooling geochronological and petrological systems: Contrib. Mineral. Petrol., v. 40, p. 259-274.

Dong, H., Hall, C., Peacor, D., Halliday, A., 1995, Mechanism of argon retention in clays revealed by laser $^{40}Ar^{39}Ar$ dating: Science, v. 267, p. 355-259.

Dupont-Nivet, G., Horton, B.K., Butler, R.F., Wang, J., Zhou, J., and Waanders, G.L., 2004, Paleogene clockwise tectonic rotation of the Xining-Lanzhou region, northeastern Tibetan Plateau: J. Geophys. Res., v. 109, doi: 10.1029/2003JB002620.

Duvall, A.R., Kirby, E., and Burbank, D.W., 2004, Tectonic and lithologic controls on bedrock channel profiles and processes in coastal California: J. Geophys. Res., v. 109, doi: 10.1029/2003JF000086.

England, P. and Houseman, G., 1986, Finite strain calculations of continental deformation II: comparison with the India-Asia collision zone: J. Geophys. Res., v. 91, p. 3664-3676.

Fang, X., Garzione, C., Van der Voo, R., Rea, D.K., Li, J., and Fan, M., 2003, Flexural subsidence by 29 Ma on the NE edge of Tibet from the magnetostratigraphy of Linxia Basin, China: Earth Planet Sci Lett., v. 210, p. 545-560.

Flowers, R.M., Ketcham, R.A., Shuster, D.L., and Farley, K.A., 2009, Apatite (U–Th)/He thermochronometry using a radiation damage accumulation and annealing model: Geochemica et Cosmochimica Acta, v. 73, p. 2347–2365.

Grathoff, G., Moore, D., Hay, R., and Wemmer, K., 2001, Origin of illite in the lower Paleozoic of the Illinois Basin: evidence for brine migration: Geological Society of America Bulletin, v. 113, p. 1092-1104.

Grathoff , G., and Moore, D., 1996, Clays and Clay Minerals, v. 44**,** p. 835-842.

Haines, S.H., and van der Pluijm, B.A., 2008, Clay quantification and Ar–Ar dating of synthetic and natural gouge: Application to the Miocene Sierra Mazatán detachment fault, Sonora, Mexico: Joural of Structural Geology, v. 30, p. 525-538.

Haines, S.H., and van der Pluijm, B.A., 2010, Dating the detachment fault system of the Ruby Mountains, Nevada: Significance for the kinematics of low-angle normal faults: Tectonics, v. 29, doi:10.1029/2009TC002552.

Harrison, T.M., Célérier, J., Aikman, A.B., Hermann, J., and Heizler, M.T., 2009, Diffusion of ^{40}Ar in muscovite: Geochim. Cosmo. Acta., v. 73(4), p. 1039-1051.

Horton, B.K., Dupont-Nivet, G., Zhou, J., Waanders, G.L., Butler, R.F., and Wang, J., 2004, Mesozoic-Cenozoic evolution of the Xining-Minhe and Dangchang basins, northeastern Tibetan Plateau: Magnetostratigraphic and biostratigraphic results: J. Geophys. Res., v. 109, doi:10.1029/2003JB002913.

Kong, X., Yin, A., Harrison, T.M., 2007, Evaluating the role of pre-existing weakness and topographic distributions in the Indo-Asian collision by use of a thin-shell numerical model: Geology, v. 25, p. 527-530.

Lease, R.O., Burbank, D.W., and Gehrels, G.E., 2007, Signatures of mountain building: detrital zircon U/Pb ages from northeastern Tibet: Geology, v. 35(3), p. 239-242.

Meyer, B., Tapponnier, P., Bourjot, L., Metivier, F., Gaudemer, Y., Peltzer, G. Shunmin, G., Zhitai, C., 1998, Crustal thickening in Gansu-Qinghai, lithospheric mantle subduction, and oblique, strike-slip controlled growth of the Tibet plateau: Geophysics Journal International, v. 135, p. 1-47.

Moore, D.M., and Reynolds, R.C., Jr., 1989, X-ray diffraction and the identification and analysis of clay minerals: Oxford University Press, New York , 400 pp.

Pevear, D.R., 1992, Proceedings of the 7th International Symposium on Water-Rock Interaction, 1251 pp.

Reiners, P.W., Ehlers, T.A., Mitchell, S.G., and Montgomery, D.R., 2003, Coupled spatial variation in precipitation and long term erosion rates across the Washington Cascades: Nature, v. 426, p. 645-647.

Reynolds R., Jr., 1994, WILDFIRE, A Computer Program for the Calculation of Three-dimensional Powder X-ray Diffraction Patterns for Mica Polytypes and their Disordered Variations. Hanover, NH: RC Reynolds, Jr, 8 Brook Rd.

Rowley, D., 1996, Age of initiation of collision between India and Asia: A review of stratigraphic data: Earth Planet Sci Lett., v. 145, p. 1-13.

Solum, J.G., van der Pluijm, B.A., and Peacor, D.R., 2005, Neocrystallization, fabrics and age of clay minerals from an exposure of the Moab Fault, Utah: J. Struct. Geol., v. 27, p. 1563-1576.

Solum, J., and B. van der Pluijm, 2007, Reconstructing the Snake River/Hoback Canyon segment of the Wyoming thrust belt through direct dating of fault rocks, in Whence

the Mountains? Inquiries into the Evolution of Orogenic Systems: A volume in honor of Ray Price, Geol. Soc. Amer. Mem. 433, p. 183-196.

Tapponnier, P., Zhiqin, X., Roger, F., Meyer, B., Arnaud, N., Wittlinger, G., and Jingsui, Y., 2001. Oblique stepwise rise and growth of the Tibet Plateau: Science, v. 291, p. 1671-1677.

van der Pluijm, B.A., Hall, C.M., Vrolijk, P., Pevear, D.R., and Covey, M., 2001, The dating of shallow faults in the Earth's crust: Nature, v. 412, p. 172-174.

van-der-Pluijm, B., Vrolijk, P., Pevear, D., Hall, C., and Solum, J., 2006, Fault dating in the Canadian Rocky Mountains: Evidence for late Cretaceous and early Eocene orogenic pulses: Geology, v. 34, p. 837-840.

Velde, B., 1965, Experimental determination of muscovite polymorph stabilities: Amer. Mineral., v. 50, p. 436-499.

Wagner, G.A., and Reimer, G.M., 1972, Fission track tectonics: The tectonic interpretation of fission track apatite ages: Earth Planet Sci Lett., v. 14, p. 263-268.

Weislogel, A.L., 2008, Tectonostratigraphic and geochronologic constraints on evolution of the northeast Paleotethys from the Songpan-Ganzi complex, central China: Tectonophysics, v. 451, p. 331-345.

Whipple, K.X., 2004, Bedrock rivers and the geomorphology of active orogens: Annual Review and Earth and Planetary Sciences, v. 32, p. 151-185.

Whipple, K.X., 2009, The influence of climate on tectonic evolution of mountain belts: Nature Geoscience, v. 2, p. 97-104.

Whipple, K.X., and Tucker, G.E., 1999, Dynamics of the stream-power river incision model: Implications for the height limits of mountain ranges, landscape response timescales, and research needs: J. Geophys. Res., v. 104, doi:10.1029/1999JB900120.

Willett, S.D., 1999, Orogeny and orography: The effects of erosion on the structure of mountain belts: J. Geophys. Res., v. 104, doi: 10.1029/1999JB900248.

Wong, M.S. and Gans, P.B., 2003, Tectonic implications of early Miocene extensional unroofing of the Sierra Mazatàn metamorphic core complex, Sonora, Mexico: Geology, v. 31(11), p. 953-956.

Yin, A., Dang, Y., Wang, L., Jiang, W., Chen, X., Gehrels, G.E., and McRivette, M.W., 2008, Cenozoic tectonic evolution of the Qaidam basin and its surrounding regions (Part 1): The southern Qilian Shan-Nan Shan thrust belt and northern Qaidam basin: Geological Society of America Bulletin**,** v. 120, p. 813-846**.**

York, D., 1968, Least Squares fitting of a straight line with correlated errors: Earth Planet Sci Lett., v. 5, p. 320-324.

Zheng, D.W., Zhang, P.Z., and Wan, J.L., 2006, Rapid exhumation at similar to 8 Ma on the Liupan Shan thrust fault from apatite fission-track thermochronology: Implications for the growth of northeastern Tibet margin: Earth and Plan. Sci. Lett., v. 248, p. 198-205.

Chapter IV

Timing of Kunlun and Haiyuan strike-slip faulting, northeastern margin of the Tibetan Plateau[1]

Abstract

New low-temperature thermochronometry data and geologic observations date periods of exhumation associated with transpressional deformation along the Kunlun and Haiyuan left-lateral faults, two major faults within the northeastern margin of the Tibetan Plateau. Knowledge of fault slip histories including timing of fault initiation is essential to understanding the long-term role of major intracontinental strike-slip faults (>1000 km) in Tibet. We provide minimum bounds on fault ages by measure of apatite and zircon (U-Th)/He and apatite fission-track ages, which record exhumation from ~2-6 km crustal depths. Results suggest that Kunlun fault motion initiated first along the central fault segment at approximately 20 Ma and then progressed along strike to the west by 12-8 Ma and to the east by 8-5 Ma. Thermal histories from ranges associated with the active Haiyuan fault record primarily late Cretaceous cooling and suggest that exhumation associated with Cenozoic motion is less than ~2-4 km. Between 15-6 Ma, structures

[1] Citation: Duvall, A.R., Clark, M.K., Kirby, E., Farley, K.A., Craddock, W.H., Li, C., Yuan, D.-Y., *in prep*, Timing of Kunlun and Haiyuan faulting, northeastern margin of the Tibetan Plateau.

between the Kunlun and Haiyuan fault became active, from which we infer simultaneous motion of both the Kunlun and Haiyuan faults that bound an ~250 km wide zone of associated transpressional shear. Previous studies indicate that faulting along the eastern tip of the Haiyuan fault began by 10-8 Ma. Thus, collectively, these data suggest that Haiyuan fault motion propagated to the east in time. Our results suggest that strike-slip fault initiation in northeastern Tibet occurs earlier than most previous studies suggest, and that the evolution of this fault system spans more than 15 million years. Moreover, left-lateral strain appears to dominate the structural landscape of the interior northeastern plateau margin post-15 Ma. Miocene onset of Kunlun and Haiyuan faulting is also consistent with the age of initiation reported for other major Tibetan strike-slip faults (e.g., the Jiali, Karakorum, Xianshuihe, and Ganzi-Yushu faults). We propose that initiation of these faults may be a part of the evolution of the upper crust within a continental orogen during the later stages of long-term plate convergence rather than being tied to a specific event or abrupt change in orogen dynamics.

4.1 Introduction

Deformation within the interior northeastern margin of Tibet is long lived and comprises compressive as well as lateral strain throughout the Cenozoic era. Strike-slip faults, including the Kunlun, Haiyuan, and Altyn Tagh, are arguably the most important active faults as they extend for great lengths (>1000 km), have high geodetic and Quaternary slip rates (≥10 mm/yr along some fault; segments Van der Woerd et al., 1998; 2000; 2002; Zhang et al., 2007), and have produced large-magnitude earthquakes during historic times (e.g., the 1920 M ~8.6 Ningxia Province earthquake along the Haiyuan

fault, the 1997 M_w 7.6 Manyi, and 2001 M_w 7.8 Kokaxili ruptures along the Kunlun fault); yet their long-term geologic history remains unclear. Although modern, Holocene, and Quaternary slip rates are reasonably well known along these faults (Kidd and Molnar, 1988; Zhang et al., 1991; Gaudemer et al., 1995; Kirby et al., 2007; Van der Woerd et al., 1998; 2000; 2002; Lasserre et al., 1999, 2002; Zhang et al., 2004; Cowgill, 2007; Cavalié et al., 2008; Li et al., 2009; Harkins et al., 2010), robust estimates of the age of left-lateral strike-slip inception are lacking due to few piercing points in well-dated geologic units along fault traces.

Utilizing predominately remote-sensing data, Fu and Awata (2007) estimate fault initiation at 10 ± 2 Ma based on ~100 km of maximum displacement of Cretaceous sedimentary rocks and an average long-term slip rate of ca. 10 mm/yr. The Cretaceous clastic deposits of northern Tibet are rarely precisely dated and commonly include multiple intervals of regular repeating lithofacies. Thus, correlating these units on either side of the fault is inherently unreliable without tracking additional diagnostic marker horizons. In addition, applying a long-term slip rate of 10 mm/yr universally along the entire length of the fault is also problematic as slip rates have been shown to decrease eastward along the fault (Kirby et al., 2007; Harkins et al., 2010). For these reasons, the estimated 10 Ma onset of strike-slip faulting along the entire fault length is questionable.

To the west, within the Jingyu splay of the Kunlun fault zone (Figure 4.1), Jolivet et al. (2003) suggest that left-lateral motion initiated much earlier, possibly in late Eocene times, and occurred either episodically or continuously to the present. They also find evidence for recent initiation of new strike-slip fault strands within the fault zone and conclude that potential eastward propagation of the fault with time (Meyer et al., 1998;

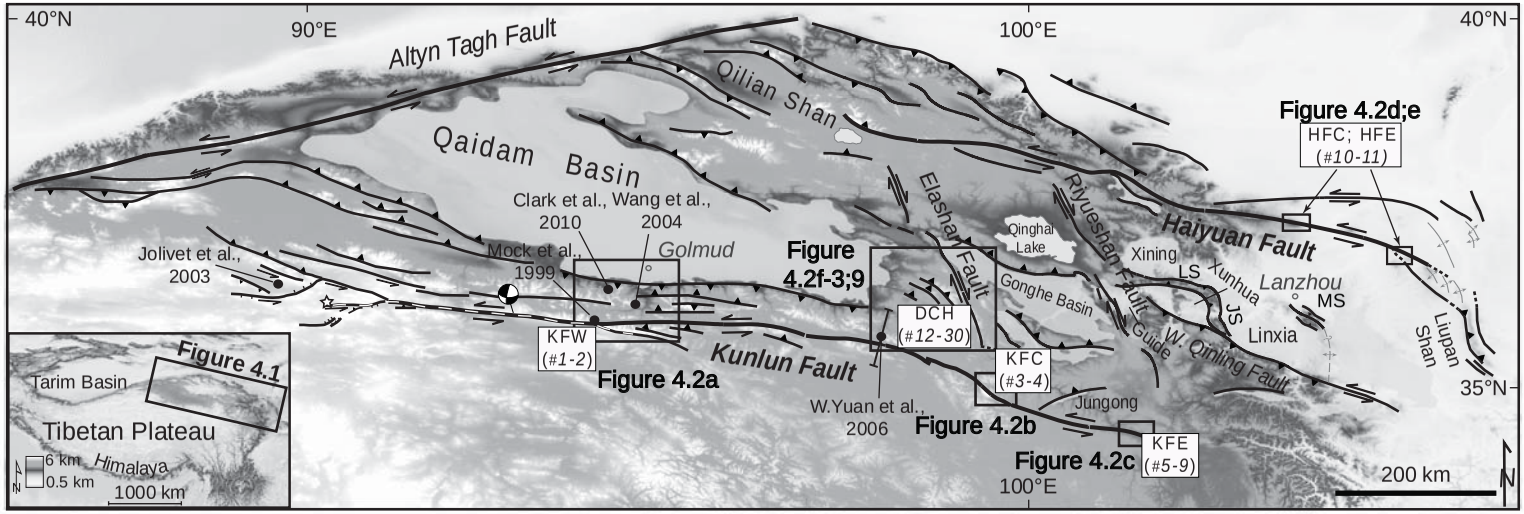

Figure 4.1. Shaded relief map of study area with faults and sample locations (sample ID numbers in parentheses) created from 90 m SRTM elevation data. Generalized faults of northern Tibetan Plateau margin compiled from published sources (GBGMR Gansu Province, 1989; QBGMR, 1991; Van der Woerd et al., 2002; Jolivet et al., 2003; Pan et al., 2004; Yin et al., 2002; 2007; 2008; Bovet et al., 2009; Zheng et al., 2010; Huang et al., 2011) and original field observations. The rupture length of the Mw ~7.8 Kokoxili earthquake (14 November 2001) is shown by a white dashed line, with centroid focal sphere (Harvard) and small white star at the hypocenter (USGS). Inset shows broader Tibetan Plateau region. Kunlun fault west (KFW), Kunlun fault central (KFC), Kunlun fault east (KFE), Dulan-Chaka Highland (DCH); Haiyuan fault central (HFC); Haiyuan fault east (HFE), Laji Shan (LS), Jishi Shan (JS), Maxian Shan (MS).

Métivier et al., 1998) must not be a simple process. Geologic mapping and thermochronometry supports Eocene to Oligocene SW-NE compression in the western Kunlun Shan (Jolivet et al., 2003). Compression apparently ceased prior to 20 Ma followed by extension, strike-slip faulting, and volcanism along the Kunlun fault during the Miocene, which is attributed to the initiation of subduction of the Tarim-Qaidam lithosphere under the Kunlun Shan (Jolivet et al., 2003). Assuming that compressional deformation near to the modern trace of the Kunlun fault relates to strike-slip motion, Jolivet et al. (2003) suggest left-lateral motion began at the onset of Kunlun Shan compression and topographic relief generation during the Eocene. Linking early compressional deformation directly with Kunlun strike-slip faulting is challenging within this region because recent studies show that compression was widespread across the length and width of the Kunlun Shan (Yin et al., 2007; Wu et al., 2009; Clark et al., 2010). As a result, it is difficult to decipher the initiation of strike-slip faulting from compressional events that may have occurred irrespective of left-slip motion.

Fewer constraints on timing of fault initiation exist along the left-lateral Haiyuan fault. Burchfiel et al. (1989; 1991) suggested a late Pliocene onset age based on estimates of only 10.5- 15.5 km total offset of clastic sedimentary rocks with poor age constraints. On the other hand, Gaudemer et al. (1995) concluded an older onset age of 10 Ma from an estimated 95 km of total displacement and assuming a slip rate of 10 mm/yr. Strike-slip deformation along the eastern Haiyuan fault tip is kinematically linked with ~ E-W directed thrusting in the Liupan Shan (Zhang et al., 1991). Based on late-Miocene rapid cooling within the Nanhua, Yeuliang Shan, and Liupan Shan thrust belts (Zheng et al., 2006; Lin et al., 2011) and sedimentation patterns in the adjacent Sikouzi basin (W.Wang

et al., 2011), motion along the eastern-tip of the Haiyuan fault is thought to initiate by 10-8 Ma. However, earlier fault initiation along more central and western parts of the fault is possible.

A growing dataset that includes sedimentation rates, low-temperature thermochronometry, stable isotopes, and paleomagnetic rotations suggests that deformation within the northern plateau margin began shortly after the initiation of Indo-Eurasian collision at ~50 Ma (Rowley, 1996; 1998). Deformation at this time involved mainly contractional structures oriented favorably to accommodate NNE-SSW convergence (Jolivet et al., 2001; Sobel et al., 2001; Yin et al., 2002; Horton et al., 2004; Dupont-Nivet et al., 2004; Dai et al., 2006; Yin et al., 2008a; Dayem et al., 2009; Clark et al., 2010; Duvall et al., 2011; X. Wang et al., 2011; Lin et al., 2011; Huang et al., 2011). Studies also suggest that faulting continued, and in some cases, initiated during Neogene time (Fang et al., 2003; 2005; Pares et al., 2003; Zheng et al., 2003; 2006; Yan et al., 2006; Lease et al., 2007; 2011; Hough et al., 2011; Yuan et al., 2011; Zhang et al., 2011; W.Wang et al., 2011; X.Wang et al., 2011; Lin et al., 2011; Craddock et al., in review).

At present it is unclear how the Kunlun and Haiyuan faults fit into this emerging geologic history. These faults represent two of the most important structural features within the northeastern margin of the Tibetan Plateau. As a result, assessing timing of their onset is essential to our understanding of the kinematic development of this region and potentially, the role of major intracontinental strike-slip faults in the long-term development of this orogenic system. Fault timing is necessary to consider outstanding questions with regard to lateral strain across Tibet such as whether strike-slip faulting initiated abruptly or gradually and/or occurred in a spatial progression or randomly. The

Kunlun and Haiyuan faults lie near to the northern plateau limit, thus timing of their onset is especially relevant to evaluating such spatial and temporal patterns.

In this study, we provide minimum bounds on the age of initiation of left-lateral Kunlun and Haiyuan fault motion by dating periods of exhumation associated with transpressional deformation along both the main fault strands and related structures (Figures 4.1-4.3). Exhumation histories are described from new low-temperature thermochronometry results including apatite and zircon helium and apatite fission-track, as well as published $^{40}Ar/^{39}Ar$ data (Mock et al., 1999). We target multiple sites along each fault in order to consider potential fault propagation.

4.2 Geologic setting

The left-lateral Kunlun fault extends roughly E-W for ~1500 km marking the boundary between the low-relief Tibetan Plateau highland to the south and basins and ranges of the plateau margin to the north (Figure 4.1). The Qaidam basin, which is located ~ 75 km north of the Kunlun fault (Figure 4.1), contains ~ 15 km of Cenozoic sediment (Bally et al., 1986; Zhou et al., 2006; Yin et al., 2008a). Internal deformation within this basin is documented (Yin et al., 2008b), although in general, it is thought to be underlain by strong basement (Zhou et al., 2006; Zhu et al., 1995) and remains a relatively intact depocenter (Figure 4.1). To the east and in sharp contrast, the northeastern plateau margin is characterized by several small to intermediate size rhomb-shaped terrestrial basins (e.g., Linxia, Xining, Xunhua, Guide, and Gonghe basins) separated from one another by intervening N-S and E-W oriented mountain ranges above reverse faults (Figure 4.1). Sediments within these basins include alternating

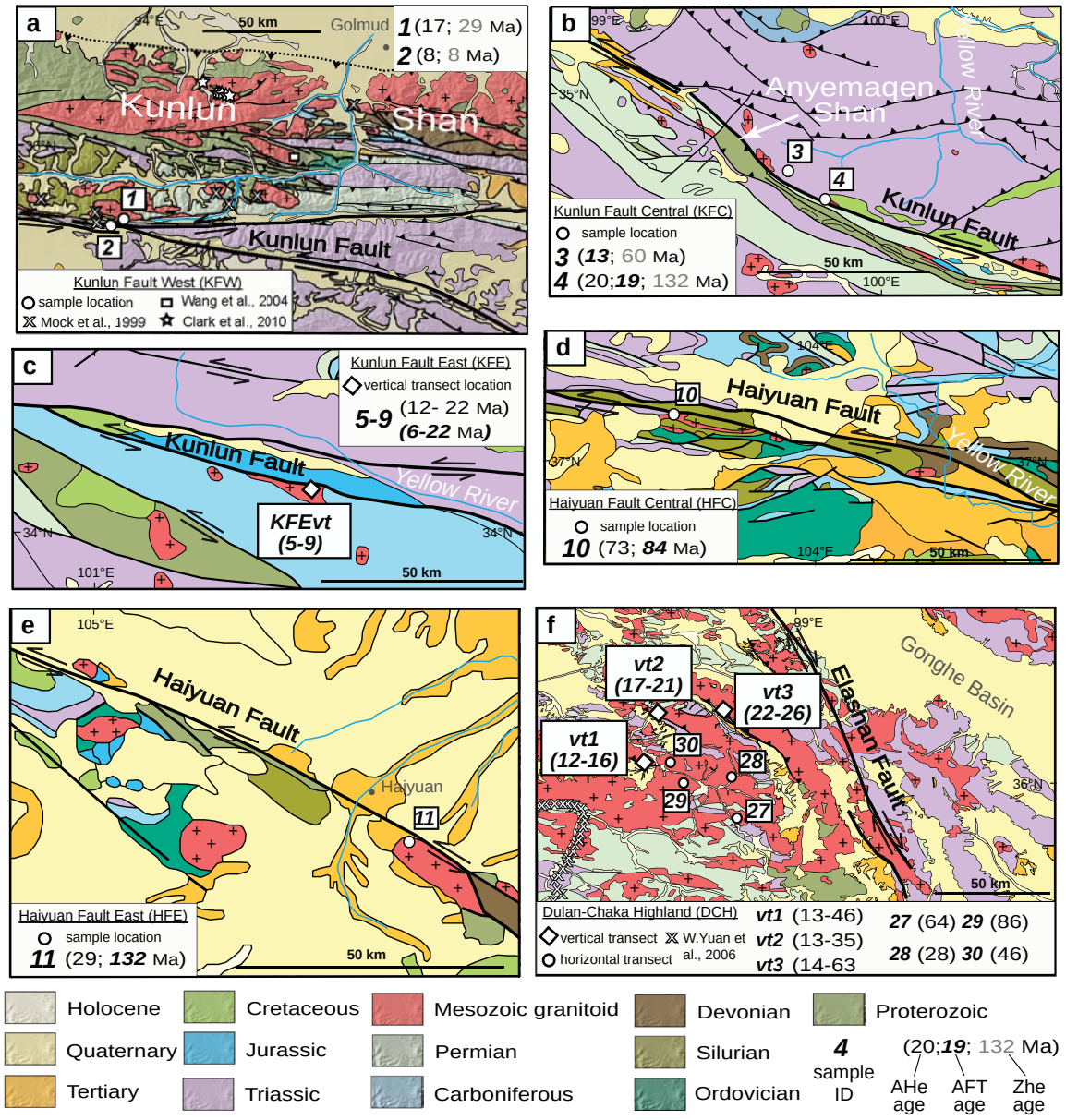

Figure 4.2. Generalized geologic maps of sample-site locations. (a) Kunlun fault west (KFW) site. Geology compiled from Kidd and Molnar, 1988; QBGMR, 1991; Pan et al., 2004; Wu et al., 2009. Apatite (black text) and zircon (gray text) helium ages shown for each sample location (#1 – 2). Sample locations from previous studies shown by x (40Ar/39Ar - Mock et al., 1999), star (AHe - Clark et al., 2010), and square (AFT - Wang et al., 2004, site approximately located) symbols. (b) Kunlun fault central (KFC) site. Geology compiled from GBGMR, 1989; Pan et al., 2004 and personal field observations. Apatite fission track (bold italic black text) and zircon helium (gray text) ages shown for each sample location (#3 – 4). (c) Kunlun fault east (KFE) site. Geology compiled from Pan et al., 2004 and Harkins et al., 2010. Youngest through oldest apatite helium (black text) and fission-track (bold italic black text) ages shown for a vertical transect (samples #5-9). (d) and (e) Haiyuan central and east fault sites (HFC and HFE respectively). Geology compiled by Pan et al., 2004 and original field observations. Apatite helium (black text) and fission-track (bold italic black text) ages shown for each sample (#10-11). (f) Dulan-Chaka highland (DCH) field site. Geology compiled from original geologic mapping and QBGMR, 1991. Youngest through oldest apatite helium ages (black text) shown for three vertical transects (vt1 #12-16; vt2 #17-21; vt3 #22-26) and one horizontal transect (~4100 m elevation #27-30). Sample locations from previous AFT study shown by x (Yuan et al., 2006).

conglomerates, sandstones, and finer-grained lake deposits that are mainly Cenozoic in age, although Cretaceous sediment is exposed in several localities throughout this region (Pan et al., 2004). Based on sedimentology, stable isotopes, structural arguments, and paleomagnetic data, it has been suggested that these individual basins were linked in a larger basin system (Zhai and Cai, 1984; Horton et al., 2004) that then became isolated from one another by deformation and topographic development as recently as the middle-to-late Miocene (Zheng et al., 2003; Fang et al., 2005; Yan et al., 2006; Lease et al., 2007; Hough et al., 2011; Lease et al., 2011; Zhang et al., 2011; Craddock et al., in review). To the northeast, the Haiyuan left-lateral strike-slip fault, which is oriented parallel to the Kunlun fault and also of great length (~1000 km), marks the boundary between the basins and ranges of the greater Linxia area and a vast region of Cenozoic folding, thrust, and strike-slip faulting to the north and west known as the Qilian Shan (Figure 4.1).

4.3 Approach

Due to a lack of precisely-measured offsets of rocks of well-known and variable ages for most of the length of the Kunlun and Haiyuan faults, we rely on indirect methods to estimate the timing of fault motion. Exhumation of deep rocks is more commonly associated with dip-slip rather than purely strike-slip fault motion. However, both uplift and subsidence often occur along major strike-slip faults due to fault geometry (i.e. restraining and releasing bends and ―stepovers" from one fault strand to another), the distribution of slip rates along the fault trace (Bilham and King, 1989), and secondary compressional and extensional structures related to distributed strain around the main

fault strand. Here we target regions of topographic growth related to transpressional deformation and assume that local erosion rates increase in response to associated changes in base level. In order to ascertain the timing of increased erosion rate and by proxy, the age of faulting, we use low-temperature thermochronometry, which provides a measure of how fast rocks move through the shallow crust from effective closure depths to the surface (Reiners and Ehlers, 2005 and references therein). Some delay between the initiation of faulting and the creation of topography could occur depending on fault-slip rates and rock strength. Lags in the erosional response to fault-induced base-level change are also possible in cases with less-erosive climates and/or erosion-resistant rocks. As a result, we consider our estimates minimum ages of fault onset.

We utilize apatite and zircon (U-Th)/He and apatite fission-track thermochronometry, which have relatively low effective closure and annealing temperatures (~55 – 75°C, ~200°C, and ~100-120°C, respectively depending on grain size, cooling rate, and effective uranium concentration (Gleadow and Duddy, 1981; Wolf et al., 1996; Farley, 2000; Reiners et al., 2002; Ketcham et al., 2007; Flowers et al., 2009)). Given average continental geothermal gradients, cooling ages of these systems typically record exhumation from ~2-6 km depths, thus are useful in studying upper-crustal processes (Zeitler et al., 1987; Wolf et al., 1996; 1998; Ehlers and Farley, 2003). In cases where rocks cool as a consequence of erosional exhumation, thermochronometry provides a means to assess timing and rates of denudation events. Thermochronometry has been utilized successfully to assess the timing of fault initiation (e.g., Wagner and Reimer, 1972) as denudation rates commonly increase in response to relief generation by faulting.

Our approach entails two different sampling strategies depending on site-specifics. In locations with high relief and well-exposed apatite- and zircon-bearing rocks, samples were collected along steep vertical transects. Age-elevation data along such transects reveals rates of cooling and potentially, changes in cooling rate through time. In ideal circumstances, ages correlate with elevation such that higher-elevation samples are older and variable and lower-elevation samples are younger and relatively invariant. Such a marked transition from a shallower to steeper gradient along the profile (i.e. "break in slope" e.g., Fitzgerald and Gleadow, 1990) is interpreted to reflect an increase in denudation rate, with older ages representing pre-faulting slow erosion or stasis in the partial retention zone (PRZ) and younger ages defining a rapid-cooling interval. Regions of low relief, poor accessibility to higher altitudes, limited rock exposure, and/or lack of apatite or zircon-bearing rocks at variable elevations, required a different approach. In these cases, multiple thermochronometers with different closure temperatures were employed on a single sample to reveal the site's cooling history. This approach is effective as long as denudation sufficiently exposes reset ages for multiple thermochronometry systems.

4.4 Sample Site Descriptions and Results

We targeted several sites (Figure 4.1-4.2; Table 4.1) along both the Kunlun and Haiyuan faults as well as within an area north of the Kunlun fault linked kinematically to strike-slip motion (Duvall and Clark, 2010), referred to informally as the Dulan-Chanka Highland (Figure 4.3). Multiple sites are essential to assess fault propagation, both along strike of the faults individually and more broadly across northeastern Tibet by comparing

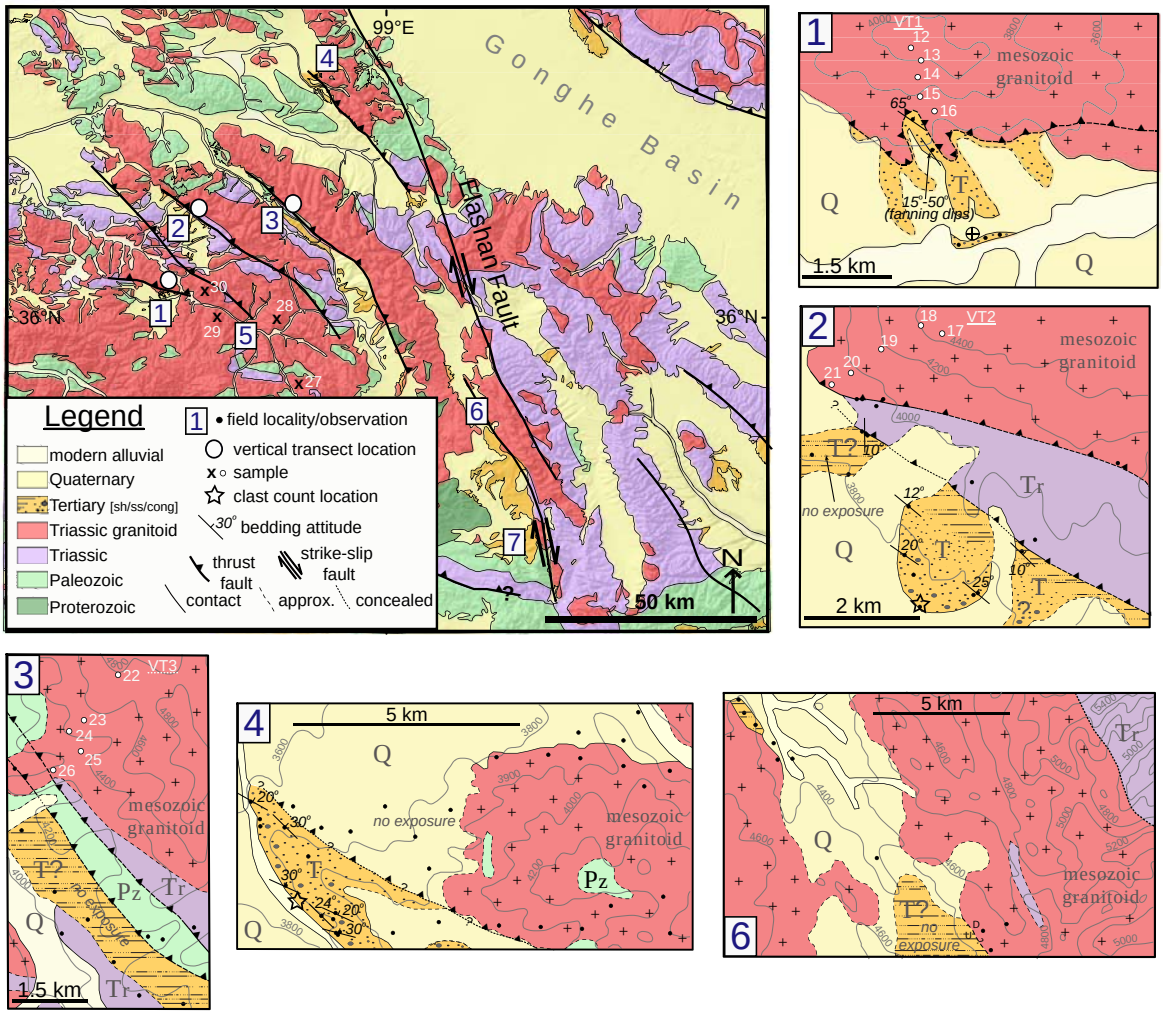

Figure 4.3. Geologic map of the Dulan-Chaka Highland draped over shaded relief. Map compiled from original geologic mapping and GBGMR (1989). Field localities visited shown by large white squares with site-locality numbers. See map key for other symbols. Larger-scale maps show details of sites 1-4 and 6. We found no Tertiary units exposed at sites 5 and 7. Digital image of site 5 landscape (Figure 4.6f) shows the low-relief surface carved in bedrock across much of the southern DCH.

TABLE 4.1: Sample Descriptions

Location	Sample ID	Rock Type	Latitude	Longitude	Elev (m)	Thermchronometers	Ap He rep*	Ap FT rep†	Zr He rep‡
Kunlun Fault West	KFW1	Granitoid	35.724	93.933	4755	AHe, ZHe	3	-	2
	KFW2	Granitoid	35.699	93.884	4935	AHe, ZHe	3	-	2
Kunlun Fault Central	KFC3	Flysch	34.717	99.679	3877	AFT, ZHe	-	39	3
	KFC4	Diorite	34.609	99.814	3944	AHe, AFT, ZHe	4	39	3
Kunlun Fault East	KFE5	Granitoid	34.094	101.508	4428	AHe, AFT, ZHe[a]	4	24	-
	KFE6	Granitoid	34.095	101.505	4259	AHe, AFT, ZHe	4	25	-
	KFE7	Granitoid	34.096	101.502	4091	AHe, AFT, ZHe	4	24	-
	KFE8	Granitoid	34.098	101.499	3841	AHe, AFT, ZHe	4	23	-
	KFE9	Granitoid	34.103	101.497	3659	AHe, AFT, ZHe	4	25	-
Haiyuan Fault Central	HFC10	Granitoid	37.114	103.66	2766	AHe, AFT	4	39	-
Haiyuan Fault East	HFE11	Granitoid	36.52	105.554	2308	AHe, AFT	4	37	-
Dulan-Chaka Highland	DCH12	Granitoid	36.073	98.405	4302	AHe[b]	4	-	-
	DCH13	Granitoid	36.071	98.407	4198	AHe	4	-	-
	DCH14	Granitoid	36.069	98.406	4093	AHe	4	-	-
	DCH15	Granitoid	36.066	98.406	3986	AHe	4	-	-
	DCH16	Granitoid	36.064	98.409	3867	AHe	4	-	-
Dulan-Chaka Highland	DCH17	Granitoid	36.256	98.472	4598	AHe[c]	4	-	-
	DCH18	Granitoid	36.258	98.467	4473	AHe	4	-	-
	DCH19	Granitoid	36.254	98.46	4276	AHe	4	-	-
	DCH20	Granitoid	36.25	98.454	4100	AHe	4	-	-
	DCH21	Granitoid	36.248	98.45	3924	AHe	4	-	-
Dulan-Chaka Highland	DCH22	Granitoid	36.28	98.719	4808	AHe[d]	4	-	-
	DCH23	Granitoid	36.277	98.712	4548	AHe	3	-	-

	DCH24	Granitoid	36.27	98.708	4407	AHe	3	-	-
	DCH25	Granitoid	36.267	98.711	4328	AHe	4	-	-
	DCH26	Granitoid	36.263	98.705	4160	AHe	4	-	-
Dulan-Chaka Highland	DCH27	Granitoid	35.856	98.769	4143	AHe[e]	4	-	-
	DCH28	Granitoid	36.015	98.751	4083	AHe	4	-	-
	DCH29	Granitoid	35.992	98.566	4123	AHe	4	-	-
	DCH30	Granitoid	36.067	98.513	4106	AHe	4	-	-

[*]Number of apatite (U-Th)/He replicate analyses per sample

[†]Number of apatite grains measured for fission tracks per sample

[‡]Number of zircon (U-Th)/He replicate analyses per sample

[a]KFE vertical transect: KFE5-9

[b]DCH vertical transect 1: DCH12-16

[c]DCH vertical transect 2: DCH17-21

[d]DCH vertical transect 3:DCH22-26

[e]DCH horizontal transect:DCH27-30

to one another. Rocks sampled for thermochonometry in all locations were crushed and sieved using standard crushing techniques. Apatite and zircon separates were derived by exploiting density and magnetic susceptibility differences. Individual apatite and zircon grains were handpicked at the University of Michigan and Caltech (respectively) and analyzed for (U-Th)/He ages at the Noble Gas Laboratory at Caltech using standard procedures (Farley and Stockli, 2002; Reiners et al., 2002). All apatite fission-track analyses were performed by Apatite to Zircon, Inc. and ages were determined using a modified decay equation that includes calibration for the LA-ICP-MS using the Durango fluorapatite standard (fission-track age of 30.6 Ma) (Donelick et al., 2005).

We present new apatite (U-Th)/He, apatite fission track, and zircon (U-Th)/He ages as well as one-dimensional modeled thermal histories found using HeFTy v. 1.6.7.43 software (Ketcham, 2005). Typically 4 single-grain analyses were used to calculate mean helium ages and standard error (2σ) and 40 individual grains were measured to estimate a pooled fission-track age and 2σ analytical error (Appendix Table 4.1). Grains that yielded helium upon a second reheating step (~~re~~-extract") following the initial laser heating and degassing of individual apatite grains were excluded on the basis of likely inclusions of a different radiogenic phase. In addition to low-temperature thermochronometry results, we also summarize geological and geomorphic observations from within the Dulan-Chaka Highland.

In cases with multiple thermochronometers from a single sample site, simple Monte Carlo inversion was utilized to determine viable thermal histories. Models were run until 100 acceptable (0.05) or good (0.5) randomly-generated thermal histories were found (worse-fit probability designation for the thermal history envelopes calculated with a

Kuiper's statistical test, Ketcham, 2005). Apatite fission-track densities and c-axis projected track length distributions were modeled using a modification of the fanning Arrhenius model (Ketcham et al., 2007; 2009), and apatite and zircon helium data were modeled with diffusion properties of Flowers et al. (2009) and Reiners et al. (2004), respectively. Thermal models were further constrained by surface temperatures of ~10ºC and, in the case of the KFW samples, high-temperature $^{40}Ar/^{39}Ar$ thermochronometry (Mock et al., 1999). Sub-segment spacing of cooling paths was allowed to vary randomly and monotonic cooling was not assumed. In cases with elevation transects, we utilize the forward-modeling function in HeFTy to compare modeled helium ages to our observed data. Reported model results correspond with simple tectonic/geomorphic scenarios most consistent with the observed age/elevation data. We recognize that more complicated scenarios not considered may also satisfy the data.

Kunlun Fault (KF)

We sampled Mesozoic rocks at three separate locations over a distance of ~ 750 km along the Kunlun fault (Figure 4.1; Table 4.1). The western segment site (KFW), which is located south and west of Golmud (Figure 4.2), is also one of the sample localities in Mock et al.'s (1999) ^{40}Ar-^{39}Ar thermochronology study (Figure 4.1). Two Triassic granitoid samples from this location (KFW1 and KFW2, Figure 4.2a), were analyzed for zircon and apatite helium. Approximately 500 km along strike to the east, the central segment sites (KFC) are located near to the Kunlun fault restraining bend resulting in the Anyemaqen massif (Figure 4.2b). Within this region of transpression, we collected two samples from approximately 3900 m elevation - fine-grained sandstone of the Songpan

Garze flysch deposit (KFC3) and diorite (KFC4). Farthest to the east (KFE) within the greater Anyemaqen Shan region of high topography (Kirby et al., 2007; Harkins et al., 2007), Triassic granitoid rocks were collected along an elevation transect spanning 800 m of relief (KFC 5-9; Figure 4.1-4.2c). Samples from this transect were analyzed for apatite helium and fission track.

Low-Temperature Thermochronometry Results

Samples from the western Kunlun fault segment yield zircon and apatite helium ages of 28.62±0.12 Ma and 17.45±1.97 for KFW1 and 7.78±2.22 Ma and 7.52±0.74 Ma for KFW2 (Figure 4.2a, Table 4.2). Overlapping KFW2 apatite and zircon helium ages indicates rapid cooling during this time interval. Biotite and K feldspar $^{40}Ar/^{39}Ar$ data and modeling results from an earlier study of samples from this same region (Figure 4.1-4.2; Mock et al., 1999) indicate temperatures between 160°C and 400°C from 140 to 30 Ma followed by a cooling event (9-15°C/m.y.) beginning around 30 Ma. Here we model cooling histories for each of the individual KFW samples using our helium ages as well as $^{40}Ar/^{39}Ar$ results as higher-temperature constraints. Models show that sample KFW1 underwent ~ 170°C of cooling to the surface starting between 30 and 25 Ma and lasting until 20-15 Ma, following a less well-constrained Cretaceous interval of slower cooling or isothermal holding (Figure 4.4, Table 4.3). This thermal history yields cooling rates of ~11-34ºC/m.y. and apparent erosion rates of ~ 0.4-1.4 mm/yr (assuming a range in average geothermal gradient of 25-30ºC/km in this and all following cases). In contrast, KFW2 model results suggest a younger cooling interval beginning at ~ 10 Ma lasting through ~ 5 Ma following slow cooling or isothermal holding from at least Cretaceous

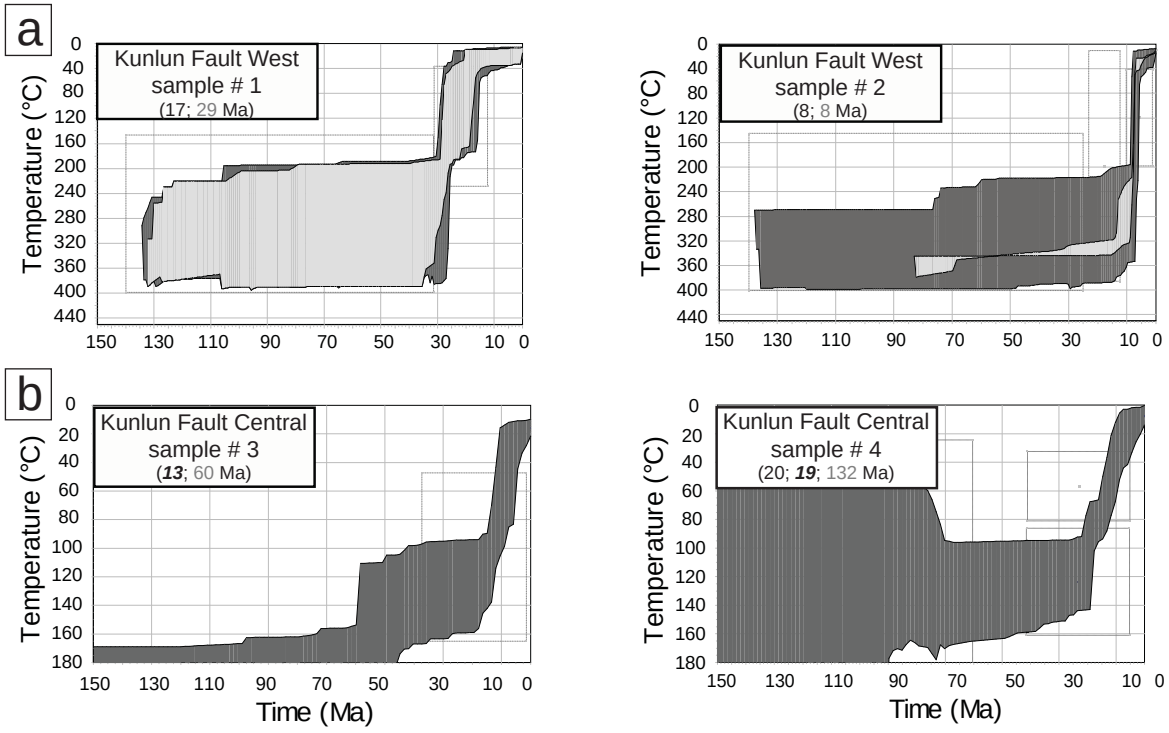

Figure 4.4a-b. Thermochronometry results for the Kunlun Fault. Time (Ma) versus temperature (°C) plots for samples along the western fault segment (a) and the central fault segment (b). Swaths represent randomly generated cooling paths that fit the data to an acceptable (dark gray) and good (light gray) standard (Ketcham, 2005; see text for details). All models constrained by at least two thermochronometric ages (shown in parentheses for each sample). AHe (black text), AFT (bold italic black text), and ZHe (light gray). Biotite and potassium feldspar 40Ar/39Ar data (Mock et al., 1999) provide additional higher-temperature constraints for samples 1 and 2 (KFW).

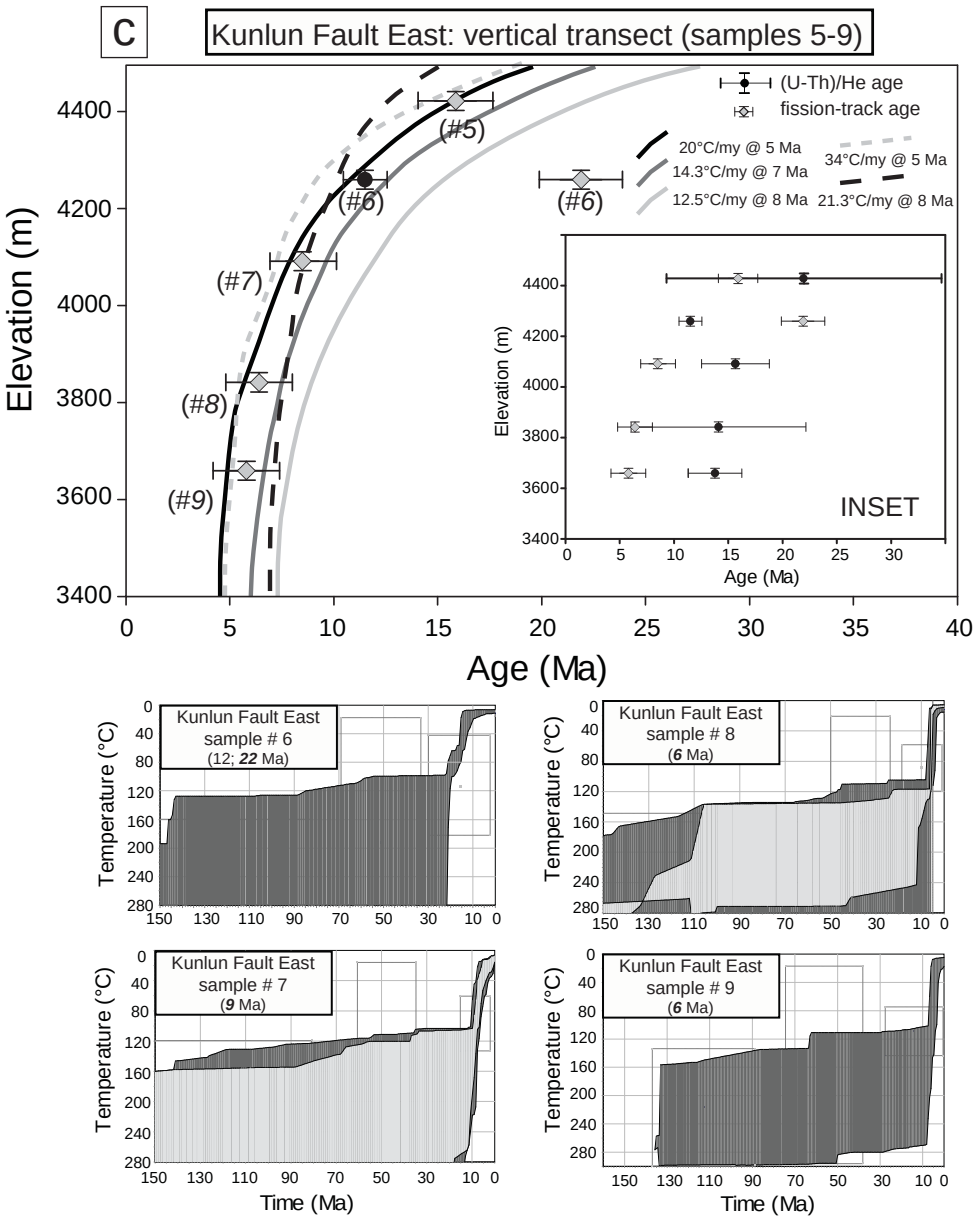

Figure 4.4c. Thermochronometry results for the Kunlun Fault. Inverse and forward thermal-modeling accomplished using HeFTy v. 1.6.7 software. Time (Ma) versus temperature (°C) plots for samples along the western fault segment. Top panel shows age/elevation plot of hte eastern Kulun Fault vertical transect (#5-9). Horizontal error bars of helium ages (black circles) represent 2σ uncertainty of mean age based on single-grain replicate ages from each sample and of fission-track ages (gray diamonds) represent 2σ uncertainty of pooled age based on analytical error. Vertical error bars represent uncertainty on elevation (Table 4.2; Appendix Table A4.1). Inset shows the entire suite of helium and fission-track data. Main plot shows a subset of reliable ages and time-temperature forward model results (solid and dashed lines). Helium samples with poor reproducability and ages older than the fission-track age from the same sample (KFE5, 7-9) are not included. Bottom four panels show results of HeFTy thermal modeling for samples KFE6-9.

time (Figure 4.4; Table 4.3). Approximately 185ºC of cooling during this interval yields rates of ~ 37ºC/m.y. and apparent erosion rates of 1.2-1.5 mm/yr.

Results from sample KFC3 from the central segment of the Kunlun fault show a mean zircon helium age of 59.65±10.07 Ma and an apatite fission-track pooled age of 12.9±1.4 Ma (Table 4.2). Apatite of the appropriate size and quality for helium analysis was not available from this sample. Sample KFC4, which is located ~ 40 km to east of KFC3 along strike (Figure 4.2b), has a zircon helium age of 132±3.6 Ma, an apatite fission-track pooled age of 19.1±1.2, and an apatite helium age of 20±0.93 Ma (Table 4.2). Overlapping KFC4 apatite helium and fission-track ages indicates rapid cooling during this time interval. Model results for sample KFC3 show ~110ºC of cooling beginning between 15 and 12 Ma and slowing by ~5 Ma (Figure 4.4, Table 4.3), which equates to a cooling rate of ~11ºC/m.y. and apparent erosion rates of ~0.37-0.44 mm/yr. In addition, model results for this sample also suggest a possible earlier interval of increased cooling beginning in the Eocene, however the rate, magnitude, and onset of such an event is poorly constrained. Model results suggest sample KFC4 underwent ~110ºC of cooling beginning at ~20 Ma and lasting through the present, which equates to a cooling rate of 5°C/m.y. and apparent erosion rates of ~0.17-0.2 mm/yr. This interval of increased cooling followed a period of slower cooling or isothermal holding from at least 70 Ma (Figure 4.4; Table 4.3).

The KFE elevation transect generally shows a positive age/depth gradient for both the apatite helium (black circles) and apatite fission-track (gray diamonds) data, with a steep gradient in fission-track ages between 10 and 5 Ma suggesting an interval of rapid cooling during this time (Figure 4.4 inset). However, most of the apatite helium are older

TABLE 4.2: Thermochronometric analyses results

KFW		Mean Ahe		Pooled AFT		Mean AFT		Mean Zhe	
Sample ID	**Elev (m)**	**age[a] (Ma)**	**Error (2σ)**	**Age[b] (Ma)**	**Error (1σ)**	**length (μm)**	**Error (1σ)**	**age[c] (Ma)**	**Error (2σ)**
KFW1	4755	17.45	1.97	-	-	-	-	28.62	0.12
KFW2	4935	7.52	0.74	-	-	-	-	7.78	2.22
KFC									
KFC3	3877	-	-	12.9	1.4	13.43	0.26	59.65	10.07
KFC4	3944	20	0.93	19.1	1.2	13.4	0.14	132	3.6
KFE: vertical transect									
KFE5	4428	21.93	12.66	15.9	0.9	14.1	0.16	-	-
KFE6	4259	11.51	1.06	21.9	1	14.07	0.13	-	-
KFE7	4091	15.66	3.12	8.5	0.8	14.08	0.17	-	-
KFE8	3841	14.12	8.05	6.4	0.7	14.67	0.16	-	-
KFE9	3659	13.78	2.46	5.8	0.8	14.87	0.2	-	-
HFC									
HFC10	2766	72.77	3.29	83.9	3.3	14.12	0.11	-	-
HFE									
HFE11	2308	29.06	9.72	132.7	7.2	12.28	0.2	-	-
DCH: vertical transect 1									
DCH12	4302	45.49	19.1	-	-	-	-	-	-
DCH13	4198	37.15	11.72	-	-	-	-	-	-
DCH14	4093	15.2	2.96	-	-	-	-	-	-
DCH15	3986	16.18	0.78	-	-	-	-	-	-
DCH16	3867	12.7	1.09	-	-	-	-	-	-
DCH: vertical transect 2									
DCH17	4598	35.26	2.41	-	-	-	-	-	-
DCH18	4473	26.81	5.95	-	-	-	-	-	-

DCH19	4276	21.02	2.19	-	-	-	-	-	-
DCH20	4100	13.88	2.17	-	-	-	-	-	-
DCH21	3924	12.55	1.99	-	-	-	-	-	-
DCH: vertical transect 3		**Mean Ahe**		**Pooled AFT**		**Mean AFT**		**Mean Zhe**	
Sample ID	**Elev (m)**	**age[a] (Ma)**	**Error (2σ)**	**Age[b] (Ma)**	**Error (1σ)**	**length (μm)**	**Error (1σ)**	**age[c] (Ma)**	**Error (2σ)**
DCH22	4808	45.22	8.95	-	-	-	-	-	-
DCH23	4548	18.7	5.85	-	-	-	-	-	-
DCH24	4407	62.97	13.17	-	-	-	-	-	-
DCH25	4328	14.16	4.11	-	-	-	-	-	-
DCH26	4160	28.09	7.86	-	-	-	-	-	-
DCH: horizontal transect									
DCH27	4143	64.2	3.6	-	-	-	-	-	-
DCH28	4083	27.66	7.98	-	-	-	-	-	-
DCH29	4123	86.08	7.83	-	-	-	-	-	-
DCH30	4106	45.39	6.7	-	-	-	-	-	-

[a]Average of replicate ages. See Appendix Table A4.1 for individual ages.

[b]See Appendix Table A4.1 for individual fission-track ages.

[c]Average of replicate ages. See Appendix Table A4.1 for individual ages.

than the apatite fission-track ages (Table 4.2), which is unexpected given the difference in closure temperatures between the two systems (~55-70°C and ~100-110°C respectively). Large errors in apatite helium age due to poor replicate reproducibility as well as the occurrence of anomalous ages (a replicate with age greater than 30% different from the other three) among three of the five apatite helium samples (Appendix Table 4.1) may help explain the apparent discrepancy between the helium and fission-track ages. Scatter of sample replicate ages that exceeds analytical uncertainty possibly relates to inclusions of a non-apatite uranium-bearing phase or zonation of U and Th (Farley et al., 2011).

We compare the observed data to calculated model helium ages along a depth section based on prescribed cooling histories using a one-dimensional thermal model (Clark et al., 2010; Lease et al., 2011). Except for sample KFE6, we exclude the helium ages from this comparison because of poor reproducibility and incompatible ages. Using HeFTy, monotonic t-T histories were derived given a range of rapid-cooling onset times, cooling rates, and changes in rates through time. Temperature histories prior to the onset of a prescribed erosion rate are modeled as isothermal holding, which is indistinguishable from slow erosion or slow deposition within error of the age measurements. A range in geothermal gradient from 25-30°C/km and removal of 0.5 to 3 km of overburden provided fits most consistent with the observed data. A geotherm approximated as constant is likely appropriate in this setting because a combination of maximum possible erosion rates (<1.5 mm/yr) and cooling duration (≤10 m.y.) yields <25% increase in thermal gradient (Ehlers, 2005).

TABLE 4.3: Thermochronometry results summary

Location	Sample(s)	Onset of increased cooling[†]
Kunlun Fault West	KFW1	30-25 Ma
	KFW2	12-8 Ma
Kunlun Fault Central	KFC3	20 Ma
	KFC4	15-12 Ma
Kunlun Fault East	KFE5-9	8-5 Ma
Haiyuan Fault Central	HFC10	–
Haiyuan Fault East	HFE11	–
Dulan-Chaka Highland	DCH12-30	17-12 Ma

[†]During Cenozoic era

Thermal model results that reasonably describe the suite of reliable ages suggest ~100 -170°C of cooling (Figure 4.4c solid and dashed lines respectively) related to erosion of hanging wall rocks starting at 8-5 Ma after a prolonged period of isothermal holding since the Cretaceous. This range in cooling histories equates to an interval of increased cooling of 13-34°C/m.y. and apparent erosion rates of 0.4-1.4 mm/yr. In addition, we inversely modeled fission-track age and length data for each sample individually using HeFTy (Figure 4.4c lower panels). The modeled thermal histories for samples KFE9, 8, and 7 suggest cooling ~100-150°C beginning at 8-5 Ma (Figure 4.4c lower panels), which is consistent with the preferred forward-modeled cooling histories. Inverse model results for sample KFE6 suggest a thermal history with increased cooling beginning earlier at ~20-15 Ma. It is unclear why this sample would have experienced a different thermal history than the others. One possibility is that unmapped structural complexity exists along the elevation profile. No acceptable paths were found for KFE5, the highest sample on the elevation transect, potentially due to incompatibility between the fission track age and track-length results for this sample.

Haiyuan Fault (HF)

To the north, the Haiyuan fault dissects a highly arid, loess-draped landscape. Sample-site options are more limited than along the Kunlun fault due to generally less structural relief along the fault (Figure 4.1) and fewer granitoid rocks in close fault proximity (Figure 4.2). We collected Mesozoic granitoid rocks at two localities along the Haiyuan fault (HFC10, HFE11; Figure 4.1) for apatite helium and fission-track analysis. The HFC sample site sits at an elevation of ~ 2800 m along the central fault segment and the HFE

sample site is located 175 km east along strike at an elevation of ~ 2300 m within the eastern fault segment (Figure 4.2d-e).

Low-Temperature Thermochronometry Results

Sample HFC10 from the central Haiyuan fault segment yields an apatite fission-track pooled age of 83.9±3.3 Ma and an apatite helium age of 72.77±3.29 Ma (Table 4.2). Model results for this sample indicate that HFC10 underwent ~10ºC of cooling from ~85 Ma to ~75 Ma and then 65ºC of faster cooling to the surface by ~70 Ma (Figure 4.5a; Table 4.3). This model result yields a cooling rate of 13°C/m.y. and apparent erosion rates of ~0.4-0.5 mm/yr. Because this sample appears to have resided at or close to the surface since the late Cretaceous and was not reset during the Cenozoic, it is not useful in assessing Cenozoic Haiyuan fault activity, though we can conclude that it was not buried significantly (≥2 km) post-Cretaceous time.

Sample HFC11 from the eastern Haiyuan fault segment yields an apatite fission-track pooled age of 132.7±7.2 and an apatite helium age of 29.06±9.72 Ma (Table 4.2). Late Cenozoic cooling events associated with the possible onset of Haiyuan faulting are poorly constrained by this sample. Overall, model cooling pathways record slow cooling from the Cretaceous through present, with a possible rate increase (albeit to still low rates) at ~90 Ma (Figure 4.5b). This cooling history suggests that the sample experienced ~60ºC of cooling in 90 m.y., which equates to a cooling rate of 0.66ºC/m.y. and apparent erosion rates of ~0.02-0.03 mm/yr. However, alternative cooling scenarios with short intervals of rapid cooling, including during the middle-to-late Miocene or early Pliocene, are permissible but not required (Figure 4.5b).

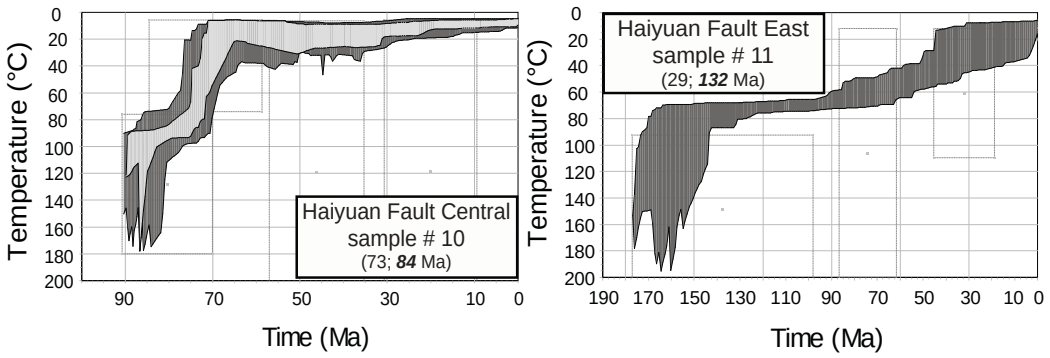

Figure 4.5. Thermochronometry results for the Haiyuan Fault. Two panels show results of thermal-history modeling using HeFTy software for the Haiyuan Fault central (#10) and east (#11) locations. Swaths of time (Ma) versus temperature (°C) represent randomly generated cooling paths that fit the data to an acceptable (dark gray) and good (light gray) standard (Ketcham, 2005; see text for details). Models from both sites constrained by AHe (black text) and AFT (bold italic black text).

Dulan Chaka Highland (DCH)

The Dulan-Chaka Highland (DCH), a region underlain by ~ 60 km thick crust (Meyer et al., 1998) and with an average elevation of ~ 4400 m, stands as a topographic divide between the Qaidam basin to the west and the rhomb shaped basins of the greater-Linxia region to the east (Figure 4.1). The DCH is locally bound by the left-lateral Kunlun fault to the south and the right-lateral Elashan fault (also known as Wenquan fault) to the east (Figure 4.1). En-echelon reverse faults within the DCH region are thought to relate to right-lateral Elashan fault activity (Wang and Burchfiel, 2004), though some of the deformation within the southern DCH may also relate more directly to Kunlun fault motion. Based on age and offset estimates of terrace risers displaced by the Elashan fault, Yuan et al. (2011) determine average slip rates of 1.1±0.3 mm/yr and a fault initiation age of 9±3 Ma using 9 – 12 km of measured offset within Triassic granitoid rocks and assuming constant long-term slip rates during late Cenozoic time. The parallel Elashan and Riyueshan faults (Figure 4.1) are thought to be antithetic right-lateral structures that accommodate shear in between the Kunlun and Haiyuan faults through counterclockwise block rotation in a bookshelf or domino style (Duvall and Clark, 2010). Thus, estimating the timing of deformation and range growth within the DCH provides an important constraint on the timing of concurrent Kunlun and Haiyuan fault activity.

Three vertical transects spanning ~700 m of relief over minimal horizontal distance (≤ 2km) were collected within hanging walls of steeply-dipping reverse faults (within the DCH (DCHVT1-VT3, Figure 4.2f). Granitoid rocks of the Triassic Kunlun Arc (Pan et al., 2004; Pullen et al., 2008) comprise all samples from this region. In the absence of structural or geomorphic horizons in the vicinity of sample transects, we assume vertical

hanging wall movement with little to no internal deformation and interpret elevation as a proxy for depth. We also collected a horizontal transect comprising individual samples collected at constant elevation (~4100 m: DCH27-30) away from mapped faults and mountain ranges in order to determine if increases in exhumation relate directly to fault motion.

Geological field investigations within several localities (Figure 4.6), mainly in the northern and central parts of the DCH, provide a regional structural context. We targeted accessible areas indicated by previous studies to have preserved Tertiary sediments (QBGMR, 1991; Wang and Burchfiel, 2004), though rock exposure turned out to be poor or nonexistent at sites 3,5,6, and 7 (Figure 4.3).

Geologic and geomorphic observations

The DCH consists of two topographically distinct regions, both with high average elevation (~4400 m) but with variable relief. The northern region is characterized by en-echelon NW trending mountain ranges above southeast-vergent reverse faults and intervening narrow, high-elevation basins, which contain terrestrial sediments overlain by Quaternary deposits (QBGMR, 1991). Basin strata can be divided generally into two lithofacies: orange-to-pink conglomerates with mudstone and sandstone interbeds and interbedded gray-to-orange mudstones and fine-grained sandstones. The majority of well-exposed basin deposits in the DCH are classified as gravel (site 1) or pebble-to-cobble (sites 2 and 4) polymict orthoconglomerates (Figure 4.6) interpreted to be alluvial-fan deposits in origin. These conglomerates are well-cemented with muddy matrices, variable clast composition (Figure 4.7) and have no obvious imbrications. The degree of grading within beds ranges from poor (site 2 and 4) to moderate (site 1). The mudstone and fine-

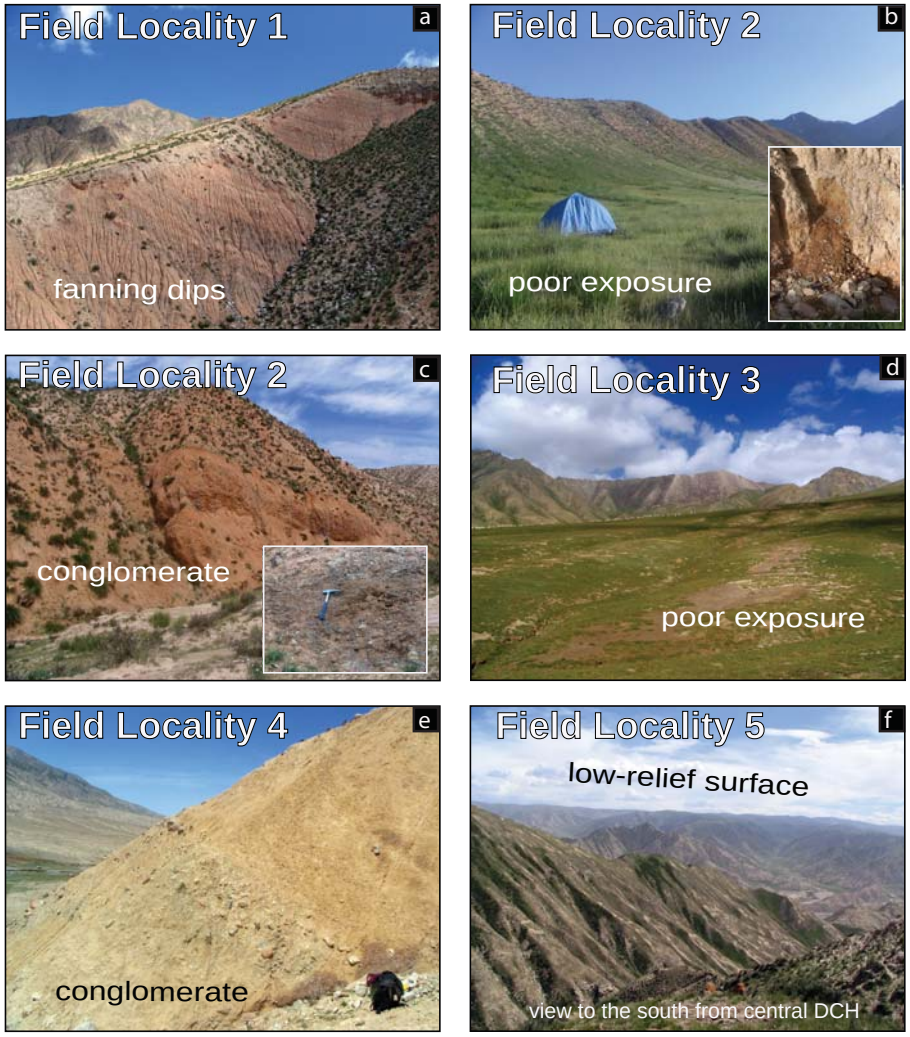

Figure 4.6. Digital images showing the geology and landscape of field localities visited within the Dulan-Chaka Highland.

grained sandstones are poorly exposed or mantled by rust-colored soil (Figure 4.6b and d). Finer-grained units likely were deposited in fluvial, flood-plain, or lake paleoenvironments. The clastic deposits of the DCH are thought to be late Miocene to Pliocene in age based on regional lithostratigraphic correlation to rocks within the Qaidam basin (QBGMR, 1991; Wang and Burchfiel, 2004). Poor exposure and/or preservation and the coarse nature of rocks commonly found in outcrop preclude better age constraints from magnetostratigraphy.

Ranges are of modest relief (< 800 m) and composed of high-grade metamorphic rocks of early Proterozoic age and sedimentary and low-grade metamorphic rocks of Paleozoic and Triassic age which are intruded by numerous granitoid bodies of large extent (QBGMR, 1991) (Figure 4.3). In general, the southern flanks of ranges are bound by steep, northeast-dipping reverse faults that place Paleozoic and Mesozoic basement over Tertiary sedimentary rocks. Range-bounding fault surfaces are not exposed but we infer steep dips (50-70°) from the linear morphology of mountain fronts and the dip of minor outcrop-scale faults within Triassic rocks proximal to the range front. Fault offsets and sub-surface fault geometries were not directly constrained. Basin deposits are generally gently to moderately deformed striking roughly parallel to range fronts and dipping 10º – 30º to the NE. Dips of beds in the footwall at locations 1 (Figure 4.6a) and 2 appear to shallow upsection (―fanning dips"), which suggests that sediment was deposited during progressive fault motion. Syntectonic deposition is also suggested by proximity of Tertiary deposits to fault-bounded ranges (Figure 4.3). Moreover, the large size and angular nature of the clasts supports a relatively local origin. However, it is notable that the composition of clasts in outcrop (counted and described at sites 2 and 4,

see Figure 4.3 for locations) differs significantly from that of the local streams draining the surrounding bedrock, especially with regard to granitoid percentage (Figure 4.7). As a result, we propose that conglomerate clasts represent geologic unit(s) eroded from overtop the currently exposed granitoids as faulting, range growth, and erosion progressed.

In contrast to the topography and geology of the north, the southern DCH is devoid of distinct ranges and basins and is characterized primarily by a low-relief landscape (Figure 4.8). Although patchy exposures of mudstones, sandstones, and conglomerates are also preserved in this region, its plateau-like character cannot be accounted for by simple infilling of basin sediments. Instead, exposed Triassic-aged units comprise the majority of this region (QBGMR, 1991; Figure 4.2f-3) with well-preserved erosion surfaces beveled across the bedrock (Figure 4.6f).

Low-Temperature thermochronometry results

Two of the three DCH elevation transects (VT1 and VT2; Figure 4.3) show regular positive age/depth gradients (Figure 4.9; Table 4.2) from which we interpret monotonic cooling histories. Age/elevation data for VT1 and VT2 are defined by a gentle gradient from ~ 45 to 15 Ma, which is indicative of slow exhumation or stasis in the PRZ for helium diffusion during this interval (Figure 4.9a,b). In contrast, a steeper trend in age data beginning at ~15 Ma indicates an interval of increased cooling during this time (Figure 4.9a,b).

Age data from VT3 do not show simple positive correlation with elevation (Figure 4.9c). Two replicates from this transect had to be excluded due to helium re-extracts and in general, samples along this transect had poorer-than-average reproducibility (Appendix

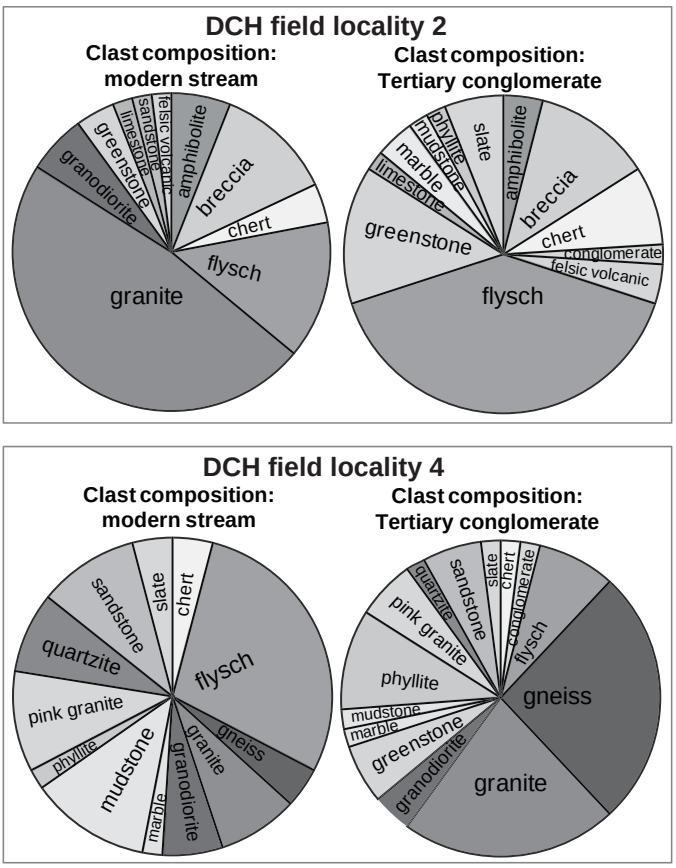

Figure 4.7. Pie charts demonstrating differences in clast composition between modern stream and local outcrop of Tertiary conglomerate from two locations with the Dulan-Chaka Highland (field sites 2 and 4). See Figure 4.3 for locations.

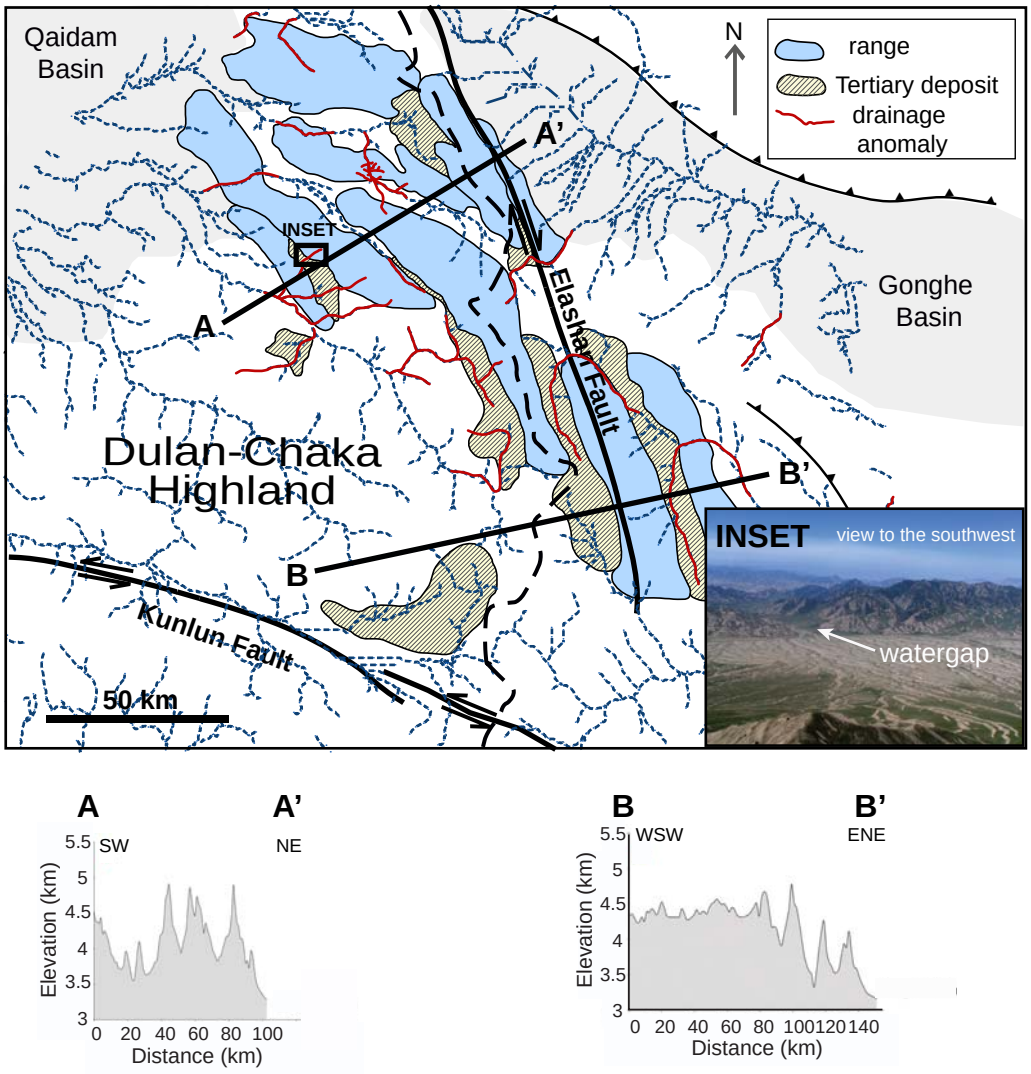

Figure 4.8. Map of the Dulan-Chaka Highland. Mountain ranges outlined in blue, Tertiary deposits in yellow-hash pattern. Fluvial network in blue dashed lines with sections of rivers considered drainage anomalies (watergaps and barbed tributaries) in red. Thick black dashed line shows drainage divide. Topographic profiles demonstrate the differences in topography across the Dulan-Chaka Highland region. Profile A shows the range-and-basin topography of the northern DCH and profile B demonstrates the more plateau-like nature of the southern DCH. Inset shows an image of a watergap taken from ~4200 m elevation along the VT2 vertical transect, view to the southwest.

Table 4.1), which makes data interpretation more difficult. Additionally, due to poor rock exposure (Figure 4.3), we do not have good structural control for this locality. Thus, it is possible that this region is more structurally complex than the others, which also may explain the more complicated age-elevation relationship. However, data from VT3 are consistent with VT1 and VT2 in that an increase in rate at ~15 Ma is permissible.

Data results from the horizontal transect show variable ages ranging from ~85 – 27 Ma. We find no obvious relationship between age and distance or modern topography; however, these data do indicate that rapid exhumation along all of the vertically-sampled ranges (VT1-3) relates to local faulting and not a broader exhumation process. Ages are older than predicted for an elevation of 4100 m (gray band, Figure 4.9d) assuming cooling histories similar to those of the vertical profiles.

Forward model results

Using the same approach as with the KFE vertical transect, we compare the observed data along the DCH vertical transects to calculated model helium ages along a depth section based on prescribed cooling histories. As before, we used a range of rapid-cooling onset times, cooling rates, and changes in rates through time to derive monotonic t-T histories. Cooling ages were calculated from t-T histories in HeFTy using the RDAMM apatite (U-Th)/He model (Flowers et al., 2009) and typical concentrations of U, Th, Sm, and grain radius dimensions for DCH apatites (21 ppm, 44 ppm, 210 ppm, 49μm respectively; Appendix Table 4.1). In all cases, geothermal gradients of 25-30°C/km and removal of 2 km of overburden provided fits most consistent with the observed data. A geotherm approximated as constant is likely appropriate in this setting because a

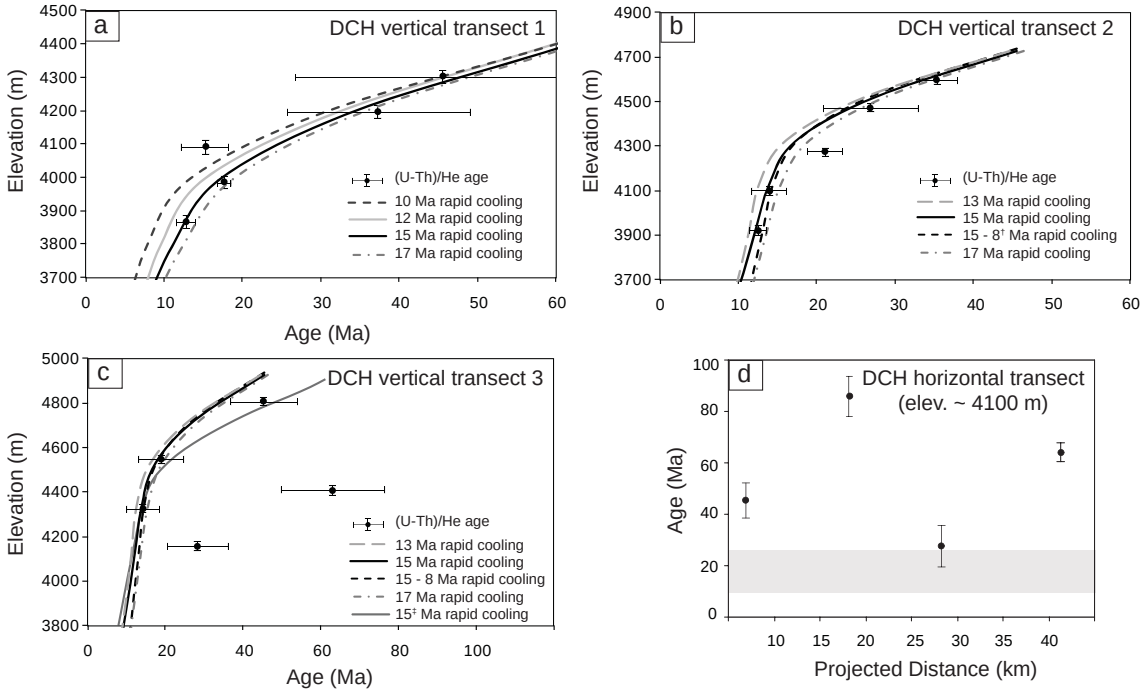

Figure 4.9. Helium age data for Dulan-Chaka Highland (see Figures 4.1-4.3 for locations). Horizontal error bars represent 2σ uncertainty of mean age based on single-grain replicate ages from each sample and vertical error bars represent uncertainty on elevation (Table 4.2; Appendix Table A4.1). For comparison with observed data, we predicted cooling ages given various montonic time-temperature histories using a range of rapid-cooling onset times, cooling rates, and changes in rates through time using HeFTy sofware (see text for details). Lines show preferred model results. Timing of change to a higher cooling rate is indicated. (a) age-elevation data, DCH vertical transect 1. (b) age-elevation data, DCH vertical transect 2. Cooling rates must slow before the present in order to fit the data. Cooling rates decrease after 10 Ma for the 13, 15, and 17 Ma curves. The black dashed curve (15-8† Ma) represents a cooling history with rapid cooling beginning at 15 Ma and abruptly terminating at 8 ma. Abrupt and graduate decreases fit the observed data equally well. (c) age-elevation data, DCH vertical transect 3. Cooling rate curves from VT1 and VT2 are superimposed onto the profile for comparison. We did not model VT3 data separately due to complexity of age/elevation relationship. First four curves are from VT2 and last curve (solid gray) is from VT1. (d) DCH horizontal transect. Age data plotted against projected distance (from location of DCH VT1, Figure 4.2f). Gray band represents the range in apatite-helium age predicted for an elevation of ~4100 m if samples along this horizontal transect experienced the same cooling history as those within the hanging wall of mapped reverse faults (a-c).

combination of maximum possible erosion rates (<1 mm/yr) and cooling duration (≤15 m.y.) yields <20% increase in thermal gradient (Ehlers, 2005).

Reported model results (solid and dashed lines, Figure 4.9a-c) correspond with simple montonic cooling histories most consistent with the observed age/elevation data. Results for VT1 (solid lines Figure 4.9a) suggest ~55°C of cooling related to erosion of hanging wall rocks starting at 15-12 Ma after a prolonged period of isothermal holding since the early Cretaceous. Earlier (17 Ma) or later (10 Ma) onsets of cooling are also possible, but do not fit the majority of the data within error (dashed lines Figure 4.9a). Our preferred models suggest increased cooling at a rate of 3.7-4.6°C/my from 15-12 Ma to the present representing erosion rates of 0.1-0.2 mm/yr. Results for VT2 (all curves Figure 4.9b) suggest ~10°C of cooling starting at 45 Ma following a period of isothermal holding from early Cretaceous followed by ~55°C of cooling starting at 17-13 Ma. Unlike VT1 models, VT2 data require either an abrupt or gradual slowdown at 10-8 Ma. Preferred models suggest a modest cooling rate (0.3-0.4°C/my) between 45 and 17-13 Ma, which represents an erosion rate of ~0.01 mm/yr, followed by more rapid cooling corresponding to an erosion rate up to 0.5 mm/yr depending on whether rates abruptly decrease to zero at 8 Ma (dashed black line Figure 4.9b) or slow down gradually starting at 10-8 Ma (solid black line, dashed gray lines Figure 4.9b). We cannot discern between these erosion scenarios.

VT3 age data do not exhibit a simple relationship with elevation (Figure 4.9c). As a result, we did not attempt to forward model this transect separately, especially without better structural context. Instead, we assess the possibility of similar cooling histories among the three profiles by importing preferred model results from VT1 and VT2 to

compare with VT3 data. VT3 is generally consistent with both VT1 and VT2 (Figure 4.9c) except two of the samples fall off of the trend within the steep part of the profile. These two older-age outliers highlight the possibility of a more complicated cooling history potentially due to greater structural complexity and non-vertical cooling pathways.

4.5 Geologic history of the Dulan-Chaka Highland

Thermochronologic histories of the three individual DCH vertical transects collectively suggest onset of rapid erosion at ca. 15 Ma, which we attribute to an increase in erosion rate following initiation of reverse faulting (Figure 4.9). Accelerated mid-Miocene cooling appears to be local to fault bounded basin and ranges as apatite helium ages of samples collected along a constant elevation transect (~4100 m) away from mapped faults are older than samples from similar elevations along the vertical transects (Figure 4.9d). Local rather than widespread cooling supports a scenario of hanging-wall relief generation from faulting and subsequent erosion rather than a regional change to a more erosive climate across a landscape with significant preexisting topography (>2.5 km). This interpretation is further supported by climatic records within the Linxia basin (Figure 4.1), which suggest a mid-to-late Miocene shift to more arid conditions (i.e. potentially less erosive) (Dettman et al., 2003; Fan et al., 2007). Such a shift would suggest that tectonics rather than a more-erosive climate is the cause of accelerated late Miocene cooling.

We relate DCH reverse faults to right-lateral Elashan faulting as previously suggested by Wang and Burchfiel (2004). En-echelon reverse faults in the northern DCH fan

westward from the Elashan fault and many curve to align parallel with Elashan fault strike, possibly rooting into this structure at depth (Figure 4.10a). On a more regional scale, similar contractional splay faults and minor extension (Chaka and Kuhai lakes) exist on opposite corners of the fault (Wang and Burchfiel, 2004) forming a classic geometry associated with strain accommodation at the terminating ends of a right-lateral fault (Figure 4.10a). Asymmetric DCH topography, with elevations decreasing westward into the Qaidam basin away from a drainage divide located far to the east, in close proximity to the Elashan fault (Figure 4.8), provides further geomorphic evidence that DCH deformation is associated with Elashan motion. Rotation and transpression may also occur in response to differences in slip rate between the Kunlun (~10 mm/yr) and Elashan (~1 mm/yr) faults (Figure 4.10a) if these rates persisted on geologic timescales.

Timing of DCH faulting found in this study (17-12 Ma) is consistent with the Elashan fault age from average Quatenary slip rates (9±3 Ma, Yuan et al., 2011). Total fault displacement can be estimated for the VT2 reverse fault. We determine the offset of the paleo-surface (at ca. 15 Ma) on either side of the fault in order to place a minimum and maximum bound on displacement (Figure 4.10b). The modern elevation of the base of the partial retention zone (determined from the timing of apparent erosion-rate change Figure 4.9b) plus the additional 2 km of initial overburden provides a measure of the modern elevation of the paleo-surface within the upthrusted-hanging wall. The approximate paleo-surface elevation within the footwall is estimated by assuming that the base of the Tertiary conglomerate represents the ca.15 Ma surface and assuming ranges in extent and dip of the basal-conglomerate (20º-30º NW) and dip of the fault plane (50º-70º NW) (Figure 4.10b). Given these parameters, we calculate ~4-7 km of total displacement,

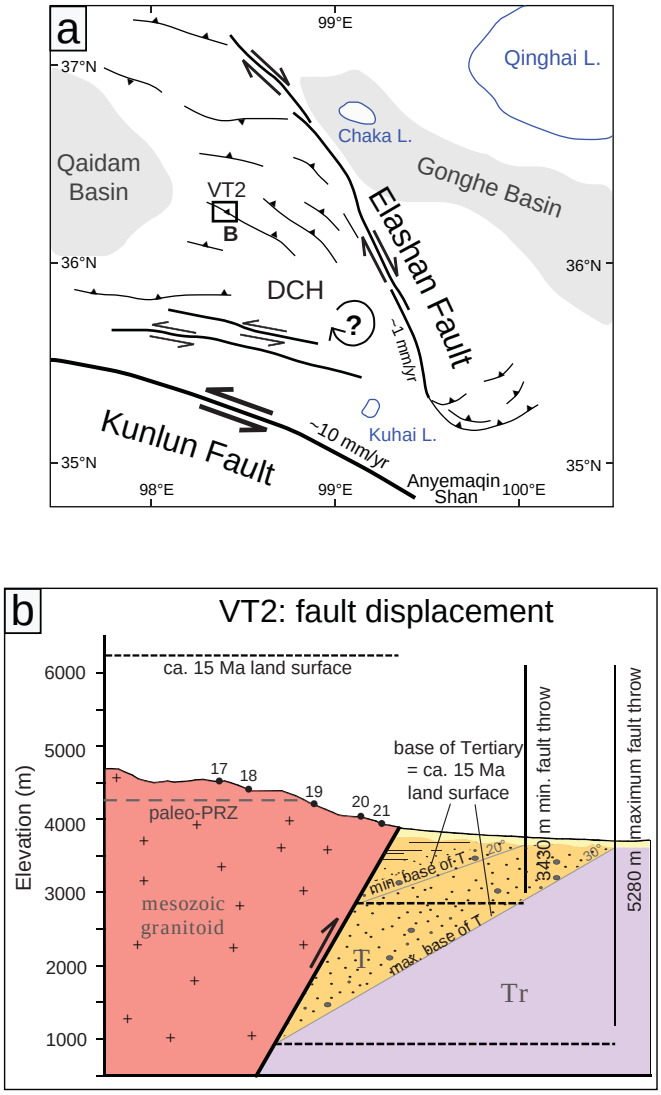

Figure 4.10. (a) Line drawing highlighting the relationship between en-echelon reverse faults of the DCH and the Elashan and Kunlun Faults. DCH faults along with a similar but smaller zone of fanning reverse faults to the southeast comprise contractional fans along the Elashan Fault. Small extensional basins (Chaka and Kuhai L.) also possibly accommodate strain related to right-lateral Elashan motion within the northeastern and southwestern fault corners (Wang and Burchfiel, 2004). Additional transpression and clockwise rotation within the DCH may result from disparate modern and Quaternary slip rates among the fast-slipping Kunlun (~10 mm/yr) and moderate-slipping Elashan fault (~1 mm/yr). Figure drafted after Wang and Burchfiel, 2004. (b) Structural offset across the VT2 reverse fault. The ca. 15 Ma land surface is reconstructed from the modern elevation of the paleo-PRZ and correlated with the base of the syntectonic Tertiary sediment in order to determine fault throw. Minimum and maximum estimates of fault throw are based on the range of possible elevations of the basal unit at the fault found by projecting the minimum and maximum surface extents and dips of Tertiary rocks to depth. Quaternary deposits cover footwall rocks at the vertical transect location. Minimum and maximum extents and dips of Tertiary deposits were extrapolated from 2-5 km east along strike where units are better exposed (Figure 4.3).

~3-5 km of vertical throw, and ~2-4 km of horizontal heave, which is of the same order of magnitude as Elashan fault displacement (9-14 km Wang and Burchfiel, 2004; Yuan et al., 2011).

A once continuous paleo-Qaidam and Gonghe basin has also been proposed previously (Zhu et al., 1994; Metivier et al., 1998; Wang and Burchfiel, 2004) and our results bear on this hypothesis. Recent work shows ~20 Ma age onset of Gonghe sedimentation (Craddock et al., in review), whereas the Qaidam basin is known to contain much older sediments of early Cenozoic and Mesozoic age (Bally et al., 1986). Barring the existence of a deeper unsampled Gonghe depocenter, deposition within a spatially continuous Qaidam-Gonghe basin must be limited to a short window of time between 20 Ma and the onset of DCH deformation at 17-12 Ma that would act to separate the two basins. We also place constraints on the thickness of such a basin to ≤2 km because the Mesozoic and early-to-mid Cenozoic (U-Th)/He cooling ages across the DCH (Table 4.2) preclude significant burial of the surface. Thus, if a connection between the Gonghe and Qaidam Basins existed it was probably short lived and the sediment was likely thin.

At present time, Tertiary sedimentary rocks are relatively scarce within the DCH. We find that ~65% of the eroded overburden is not currently contained within the VT2 fault-bounded basin based on a gross estimate of the volume of sediment removed from the mountain top versus the volume of sediment stored in the adjacent basin, assuming modern range and basin geometries. We propose several plausible scenarios to describe the evacuation of this material, though at this time we are unable to discriminate among these. In one end-member scenario, fault motion and sediment accumulation within narrow basins was concomitant among all of the DCH reverse faults at ~15 Ma and

continued until ~10-8 Ma followed by a late-stage evacuation of sediment. Regional drainage reorganization and sediment removal could potentially relate to recent fault-slip rate changes on either the Elashan or Kunlun faults, climatic variability, or base-level changes associated with Qaidam basin activity. Events such as these could explain the many obvious drainage anomalies throughout the DCH region including water gaps and barbed drainages (Figure 4.8). On the other hand, DCH range growth and basin deposition may have propagated to the west away from the Elashan fault in time such that VT3 deformation occurred earlier than VT2, which occurred earlier than VT1. In this case, piggy-back reverse faulting could induce a regional westward tilting, leading to predominate evacuation rather than deposition of sediments as they were shed from hanging walls during fault motion and possibly the formation of water gaps. Thermochronometry results permit differences in timing of rapid erosion among the locations but they are limited to at most only a few million years. It is also noteworthy that VT1 model results, unlike the other two transects, do not require a late-Miocene slow down in erosion rate. More recent fault activity along VT1, which is located closest to the Qaidam basin at the western edge of the DCH (Figure 4.3) is perhaps indicative of a later onset of faulting in this location after the apparent waning of the more eastern faults.

The Miocene phase of mountain building that we document here may have occurred amidst an antecedent drainage network that would have influenced sediment accumulation and could result in the now prevalent water gaps (Figure 4.8). Uniformly thick crust (~60 km, Meyer et al., 1998) and high elevations (~4400 m) could result from deeper crustal processes acting separately from or synchronously with Miocene upper-crustal reverse faulting. Lower-crustal flow, which was recently evoked west of the DCH

under the Kunlun Shan and southern Qaidam basin (Karplus et al., 2011) (Figure 4.1), or duplexing within the lower crust could explain most of the crustal thickening given the apparently small contribution by surface faulting.

4.6 Timing of onset of Kunlun and Haiyuan Faulting

Our results suggest that Kunlun fault motion initiated first along the central fault segment at approximately 20 Ma and then progressed to the west (12-8 Ma) and east (8-5 Ma) as the fault zone evolved (Figure 4.11). This along-strike diachronous history differs from earlier proposals of eastward fault propagation (Meyer et al., 1998; Metivier et al., 1998) or late Miocene initiation along the entire fault length (Kidd and Molnar, 1988; Fu and Awata, 2007). Faulting at 20 Ma along the Kunlun's central segment is consistent with the sedimentation record within the Gonghe basin to the northeast of the fault zone (Figure 4.1) that shows sediment accumulation from a distal source beginning at this time (Craddock et al., in review). Our results are also consistent with a previous fission-track modeling study east of the central Kunlun site (Figure 4.1) that revealed a phase of increased cooling equating to average exhumation rates of 0.1-0.15 mm/yr starting at 20 Ma (Yuan et al., 2006).

Previous thermochronometry data from steep vertical profiles in the hanging wall of the south Qaidam thrust show an interval of rapid cooling beginning at ~35 Ma (Clark et al., 2010; transect location stars in Figure 4.2a). We cannot definitively rule out an early phase of Kunlun strike-slip within a similar time frame, beginning at ~30 Ma (KFW1, Figure 4.4); yet, we have no independent evidence to support that strike-slip faulting along the main strand of the Kunlun fault occurred concurrently with compression and

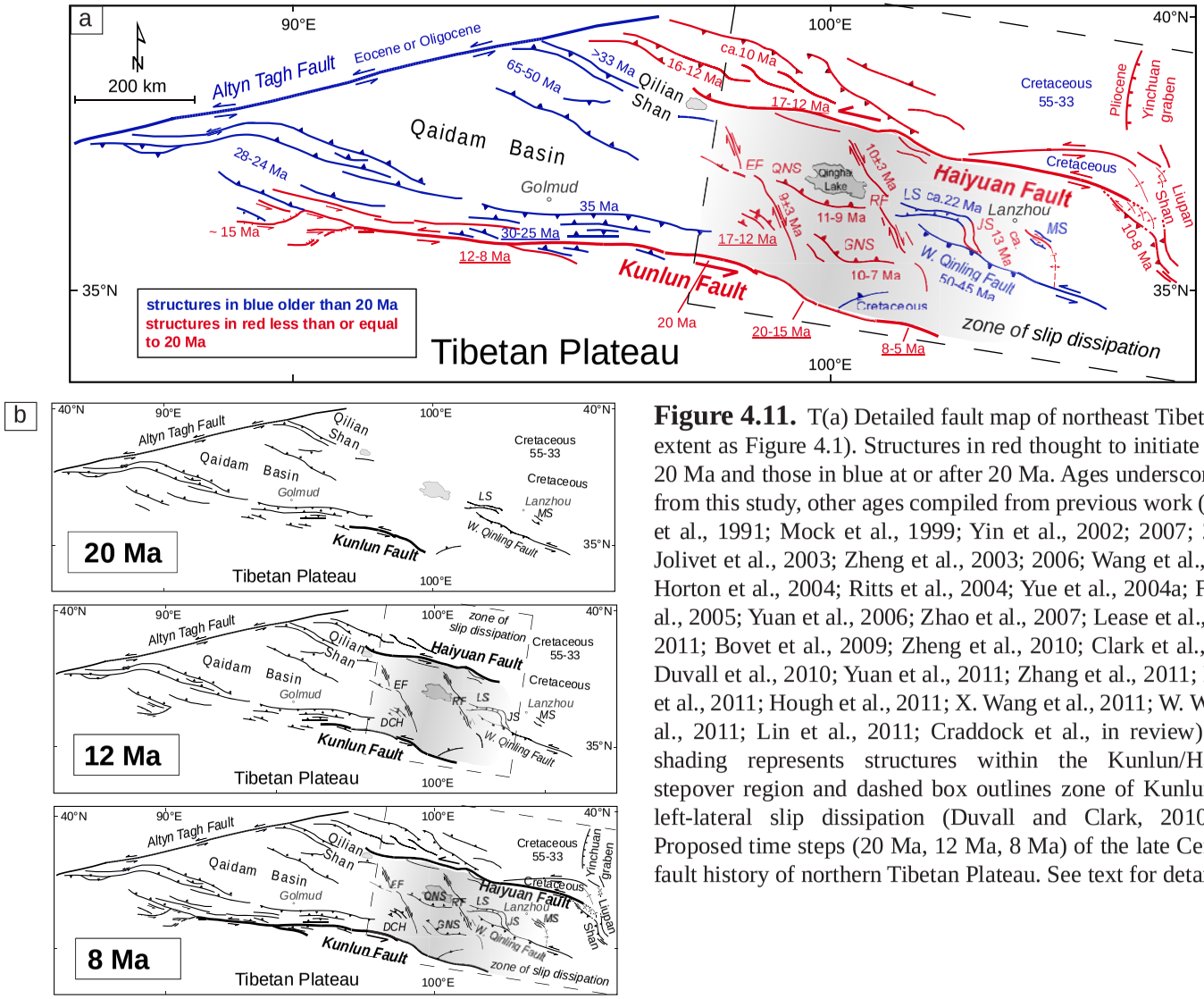

Figure 4.11. T(a) Detailed fault map of northeast Tibet (same extent as Figure 4.1). Structures in red thought to initiate before 20 Ma and those in blue at or after 20 Ma. Ages underscored are from this study, other ages compiled from previous work (Zhang et al., 1991; Mock et al., 1999; Yin et al., 2002; 2007; 2008a; Jolivet et al., 2003; Zheng et al., 2003; 2006; Wang et al., 2004; Horton et al., 2004; Ritts et al., 2004; Yue et al., 2004a; Fang et al., 2005; Yuan et al., 2006; Zhao et al., 2007; Lease et al., 2007; 2011; Bovet et al., 2009; Zheng et al., 2010; Clark et al., 2010; Duvall et al., 2010; Yuan et al., 2011; Zhang et al., 2011; Huang et al., 2011; Hough et al., 2011; X. Wang et al., 2011; W. Wang et al., 2011; Lin et al., 2011; Craddock et al., in review). Dark shading represents structures within the Kunlun/Haiyuan stepover region and dashed box outlines zone of Kunlun-fault left-lateral slip dissipation (Duvall and Clark, 2010). (b) Proposed time steps (20 Ma, 12 Ma, 8 Ma) of the late Cenozoic fault history of northern Tibetan Plateau. See text for details.

mountain building during this time. As a result, our preferred interpretation relates Eocene-Oligocene cooling recorded along the western fault segment (Mock et al., 1999; Wang et al., 2004) and along the southern Qaidam basin farther to the west (Jolivet et al., 2003; Yin et al., 2007) to reverse faulting and topographic development of the Kunlun Shan, including the 2 km escarpment between the Tibetan Plateau and the Qaidam Basin. We interpret the later pulse of cooling at 12-8 Ma (KFW2, Figure 4.4) to mark the initiation of left-lateral Kunlun faulting, which is consistent with a later estimated initiation age of 8-5 Ma along the eastern fault segment (Figure 4.11).

Thermal histories of samples from the two Haiyuan fault sites offer little information regarding timing of Cenozoic strike-slip faulting. Rather, sample HFC10 indicates an earlier, late Cretaceous cooling event between ~85 and 70 Ma. Cretaceous sediments are widely distributed across the northern margin of the Tibetan Plateau (Horton et al., 2004) and previous thermochronometry data from northeastern Tibet indicate 2-3 km of Cretaceous sediment blanketed some of the region (Clark et al., 2010). Based on detailed geologic mapping north of the Kunlun fault and south of the Gonghe and Linxia basins (Figure 4.1), Craddock et al. (2011) argue that formation of the extensive network of Cretaceous sedimentary basins within this region relates to NW-SE contractional deformation similar to that documented throughout the Qinling-Dabie orogen to the east (Ratschbacher et al., 2000; 2003; Enkelmann et al., 2006). They associate this crustal shortening with a proposed step-over between two parallel right-lateral shear zones and thus consider deformation to be relatively local. Other studies suggest that Late Jurassic-Cretaceous sediment deposition reflects regional crustal extension and post-rift thermal subsidence (Vincent and Allen, 1999; Horton et al., 2004). Although no direct structural

relationships are observed, based on location, Cretaceous cooling recorded along the Haiyuan fault likely relates to this proposed extensional deformation (Lin et al., 2011).

Liupan Shan contractional deformation beginning at 10-8 Ma (Zheng et al., 2003; W. Wang et al., 2011) at the eastern termination of the Haiyuan fault provides one of the few constraints on Cenozoic Haiyuan strike-slip timing. On the whole, sample HFE11 located ~75 km west of the Liupan Shan (Figure 4.1) shows relatively slow cooling from the Cretaceous through the present. However, a late Miocene cooling event on order of 30°C is permitted by the acceptable modeled time-temperature paths and recently published apatite fission-track modeling results from a separate study ~20 km to the east and 100 m lower elevation reveal a Miocene episode of cooling with rate increase in the late Miocene (Lin et al., 2011).

Kinematic links between Haiyuan strike-slip motion and associated contractional deformation are also useful in assessing the timing of the western segment of the Haiyuan fault. Thermochronometry results suggest that thrust deformation within the DCH region, located to the south of the Haiyuan fault (Figure 4.1), began between 17 and 12 Ma. We suggest that faults within this region relate most directly to Elashan fault motion (Figure 4.10a). However, based on the kinematic argument that the parallel right-lateral Elashan and Riyeushan faults result from concurrent Kunlun and Haiyuan fault motion (Duvall and Clark, 2010), we place bounds on the timing of western Haiyuan faulting to ca. 15 Ma by proxy (Figure 4.11). Relating the Elashan fault to Kunlun and Haiyuan motion contrasts with an earlier proposal that the Elashan fault is a conjugate to the left-lateral Altyn Tagh fault (Wang and Burchfiel, 2004) despite greater displacement along the significantly longer, older and faster-slipping Altyn Tagh fault (Sobel et al., 2001; Yin et

al., 2002; Ritts et al., 2004; Yue et al., 2004a; Meriaux et al., 2004; Meriaux et al., 2005; Cowgill et al., 2009; Zhang et al., 2007; Gold et al., 2011) and a lack of documented clockwise rotation within the Qaidam basin to account for these kinematic differences (Dupont-Nivet et al., 2002). Ca. 15 Ma initiation of western Haiyuan faulting as compared to the 10-8 Ma deformation event in the Liupan Shan at the eastern fault termination (Zheng et al., 2003; W. Wang et al., 2011) suggests eastern propagation of the fault in time. Collectively, these data indicate diachronous slip histories with left-lateral Kunlun motion initiating first along the central fault segment before expanding west and east along strike as well as to the north and east along the Haiyuan fault (Figure 4.11).

4.7 Discussion

We suggest that the Kunlun and Haiyuan strike-slip faults control deformation of northern Tibet since 20 Ma and contrasts with an earlier phase of deformation characterized by N-NNE-directed thrust faulting. Faulting, range growth, and basin deposition along many of the smaller structures (50-100 km in length) within the interior northeastern plateau margin were commensurate with or post-dated the onset timing of the bounding Kunlun and Haiyuan faults (Figure 4.11a). Prior to the Miocene Epoch, the northern margin of the Tibetan Plateau was characterized primarily by contractional structures accommodating N or NE convergence (Jolivet et al., 2001; Sobel et al., 2001; Yin et al., 2002; Horton et al., 2004; Dupont-Nivet et al., 2004; Dai et al., 2006; Yin et al., 2008a; Dayem et al., 2009; Clark et al., 2010; Duvall et al., 2011; X. Wang et al., 2011; Lin et al., 2011; Huang et al., 2011). At approximately 20 Ma, Kunlun left-lateral

faulting initiated along the central segment of the fault (Figure 4.11b, 1st panel). By 12 Ma, left-lateral faulting expanded westward (> 300 km) and possibly a little eastward along Kunlun-fault strike as well as northward to the western Haiyuan fault (Figure 4.11b, 2nd panel).

Initiation of right-lateral Elashan and Riyueshan faulting at ~13-6 Ma (Yuan et al., 2011) occurred concurrently with the onset of coeval Kunlun and Haiyuan motion. Rotation of smaller ―blocks" of crust (50 km x 50 km) accommodated by these right-lateral antithetic faults (Duvall and Clark, 2010) produces regional transpression and crustal thickening along ENE striking thrust and reverse fault-bounded mountain ranges starting at ~15 Ma in the Dulan-Chaka Highland, ~11 Ma in the Ela Shan (Zhang et al., 2011), ~10-7 Ma in the Gonghe Nan Shan (Craddock et al., in review), and ~6 Ma in the Qinghai Nan Shan (Zhang et al., 2011). East of the Riyueshan fault, formation of the N-S oriented Jishi thrust fault and associated basin sedimentation began at ~13 Ma (Zheng et al., 2003; Fang et al., 2005; Lease et al., 2011; Hough et al., 2011). By 8 Ma, Kunlun and Haiyuan faulting expanded to the eastern fault terminations (Figure 4.11b, 3rd panel) concurrent with increased deformation in the Liupan Shan region of thrusts and folds (Zheng et al., 2006; W. Wang et al., 2011; Lin et al., 2011), the adjacent Tianshui basin to the southeast (X. Wang et al., 2011), and extension in the Yinchuan graben to the north (Zhao et al., 2007).

We associate deformation within this region with a broad step-over zone resulting from Kunlun and Haiyuan strike-slip motion beginning ca. 20 Ma (Figure 4.11). This contrasts with the earlier phase of deformation characterized by N-NNE-directed thrust faulting. Perhaps notably, the timing of the development of the Kunlun-Haiyuan strike-

slip system coincides with a proposed transition at ~16 Ma from an –extrusion phase" along the Altyn Tagh fault accommodated by fast slip (>20 mm/yr) to mainly surface uplift and shortening in the Altun Shan (Ritts et al., 2008; Kent-Corson et al., 2009) and the wider Qilian Shan region (Huang et al., 2011) correlated with a period of slower slip along the Altyn Tagh fault slip (<9 mm/yr).

The interpretation that Miocene-Pliocene range growth and basin deposition within northern Tibet co-evolved with the growth of major strike-slip faults is similar to earlier proposals by Meyer et al. (1998) and Tapponnier et al. (2001) that coeval crustal deformation partitions between steep strike-slip faults and intervening thrust structures. In contrast to these previous studies, however, we suggest that the Kunlun and Haiyuan faults root into the ductile mid crust and are not lithospheric in scale nor do they extend east beyond the plateau boundary (Kirby et al., 2007; Duvall and Clark, 2010). Additionally, well-documented Eocene contractional deformation along thrust faults along the northeastern Tibetan Plateau margin (Yin et al., 2008; Clark et al., 2010; Duvall et al., 2011) challenges the view that the orogen stepped northward in successive steps in time (Tapponnier et al., 2001).

The kinematic shift to a dominantly transpressional regime within northeastern Tibet appears to occur within a protracted period and does not necessitate an abrupt change in the plateau perimeter or style of faulting (e.g., Molnar and Stock, 2009) resulting from a singular change in orogen dynamics (i.e., loss of mantle root or changes in plate rate or convergence direction). Instead, the detailed growth history of the Kunlun and Haiyuan fault system that we outline here suggests evolution over more than 15 million years, with left-lateral faulting nucleating along the central Kunlun fault segment before

growing westward and eastward along strike and northward to the Haiyuan fault. Models that involve an elastic upper crust underlain by low-viscosity lower crust result in broad zones of interacting faults whereas crust modeled as entirely elastic results in narrow zones of deformation focused on single faults (Roy and Royden, 2000). The Kunlun fault extends from a region of high crustal strength (Qaidam Basin) into a diffuse plateau margin underlain by a weak lower crust (Clark and Royden, 2000) and the DCH, which sits just north of the central Kunlun fault segment, represents the rheological boundary between these two regions (Figure 4.1). Westward expansion along the southern boundary of the Qaidam basin from the growing tip of the nascent Kunlun fault resulted in discrete deformation and fast slip rates (Molnar and Dayem, 2010) whereas eastward expansion into a region of weaker crust likely prohibited continued localized deformation, eventually resulting in the northward step to the Haiyuan fault and the much wider and complicated set of structures extant across this region (Duvall and Clark, 2010). Thus, this pattern of deformation suggests that the observed growth history of the Kunlun-Haiyuan fault system can potentially be explained by viscosity contrasts in the lower crust.

Onset ages of the Kunlun and Haiyuan faults overlap with initiation of many other major intracontinental strike-slip faults of the Tibetan Plateau (Figure 4.12). With exception to the Altyn Tagh fault and the Ailao Shan shear zone, major strike-slip fault motion appears to initiate within the span of time from ~20 to 5 Ma (see review by Searle et al., 2011 and references therein). The oldest (Kunlun and Karakorum) and youngest (Xianshuihe) faults possibly vary by as much as 15 million years, though we cannot currently discern whether this reflects true variability in onset age or is a function of poor

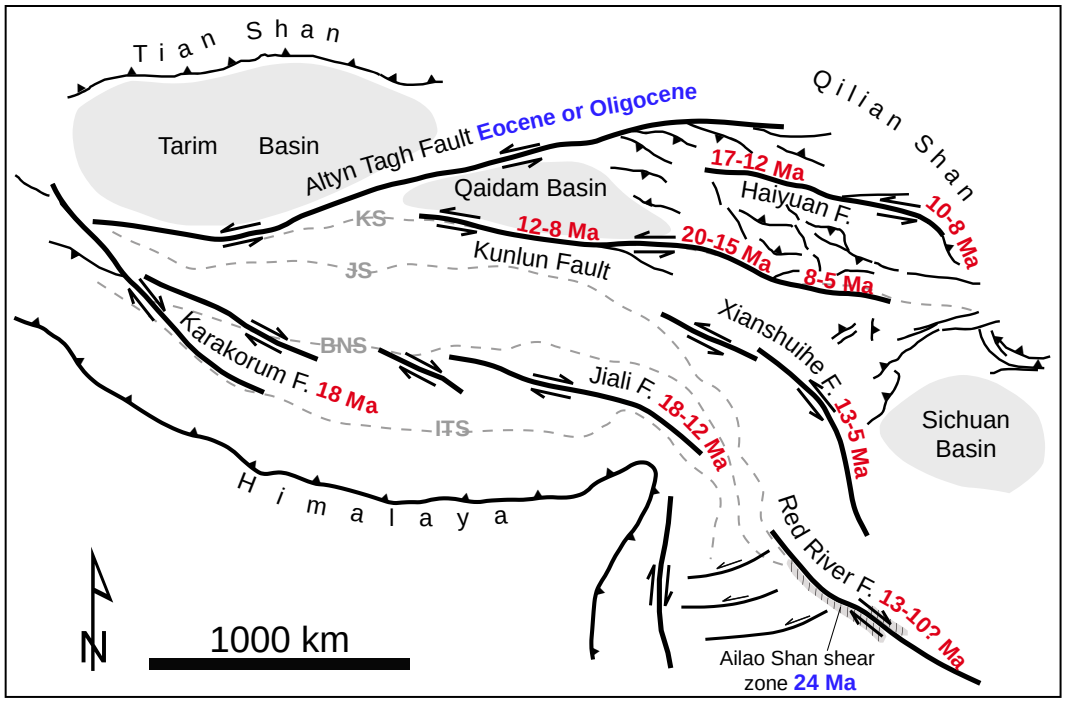

Figure 4.12. Simplified geologic map showing major strike-slip faults of the Tibetan Plateau (after Taylor and Yin, 2009 and Schoenbohm et al., 2006) as well as compressional structures of the northern Tibetan Plateau margin. Compiled estimates of initiation ages shown in blue (pre-Miocene) and red (Miocene and younger). Tibetan Plateau suture boundaries shown by dashed gray line: ITS Indus-Tsangpo suture, BNS Bangong Nujiang suture, JS Jingsha suture, KS Kunlun suture. Age brackets represent the timing of the onset of strike-slip motion; note that this occurs during the Miocene or later for the majority of major intracontinental strike-slip faults of Tibet.

data resolution. In either case, this time frame is at least 30 million years after the initial continental collision of India and Eurasia. Continued convergence and the progressive confinement of Tibetan crustal thickening against rigid crustal blocks to the north (Dayem et al., 2009; Clark, *in review*) may have eventually led to widespread lateral strain in the upper crust. The later-stage development of a strike-slip regime within the upper crust of Tibet may therefore be part of the natural evolution of the orogen in response to ongoing penetration of India northward into Eurasia.

4.8 Conclusions

Left-lateral Kunlun faulting initiated first along the central fault segment at ~20 Ma followed later by expansion to the west and east along strike and to the north along the Haiyan fault. Expansion of these fault systems to present-day extents occurred by ~8 Ma. Kunlun and Haiyuan fault activity appears to have played a fundamental role in the Miocene-Pliocene evolution of the structural landscape within interior northeastern Tibet margin. Miocene onset of Kunlun and Haiyuan left-lateral faulting is consistent with initiation ages of other major intracontinental strike-slip faults and may result in the later-stages of orogen development due simply to the long-term convergence of India rather than relate to a change in orogen dynamics.

4.9 Acknowledgements

This work was supported by the NSF (grants EAR-0507431, EAR-0908711), the National Science Foundation of China (40234040) and by the State Key Laboratory of Earthquake Dynamics (LED2008A01). We thank Lindsay Hedges for assistance with

sample analyses, and Nathan Harkins, Katherine Dayem, Karen Lease, Dao-Yang Yuan and colleagues at the Lanzhou Institute of Seismology, China Earthquake Administration and Pei-Zhen Zhang and colleagues at the State Key Laboratory of Earthquake Dynamics, Institute of Geology, China Earthquake Administration for help with sample collection and field support. We thank Eric Hetland and Nathan Niemi for thoughtful discussion regarding this work.

4.10 References

Bally, A., Ryder, T., and Euster, H., 1986, Comments on the geology of the Qaidam basin: Notes on sedimentary basins in China—Report of the American Sedimentary Basins Delegation to the People's Republic of China: US Geological Survey Open-File Report, p. 86-327.

Bilham, R., and King, G., 1989, The morphology of strike-slip faults – Examples from the San-Andreas Fault, California: Journal of Geophysical Research-Solid Earth and Planets, v. 94, p. 10204-10216.

Bovet, P. M., Ritts, B. D., Gehrels, G., Abbink, A. O., Darby, B., and Hourigan, J., 2009, Evidence of Miocene crustal shortening in the north Qilian Shan from Cenozoic stratigraphy of the western Hexi Corridor, Gansu Province, China: American Journal of Science, v. 309, p. 290-329.

Burchfiel, B., Quidong, D., Molnar, P., Royden, L., Yipeng, W., Peizhen, Z., and Weiqi, Z., 1989, Intracrustal detachment within zones of continental deformation: Geology, v. 17, p. 748-752.

Burchfiel, B. C., Zhang, P. Z., Wang, Y. P., Zhang, W. Q., Song, F. M., Deng, Q. D., Molnar, P., and Royden, L., 1991, Geology of the Haiyuan Fault Zone, Ningxia-Hui Autonomous Rregion, China, and its relation to the evolution of Northeastern margin of the Tibetan Plateau: Tectonics, v. 10, p. 1091-1110.

Cavalie, O., Lasserre, C., Doin, M. P., Peltzer, G., Sun, J., Xu, X., and Shen, Z. K., 2008, Measurement of interseismic strain across the Haiyuan fault (Gansu, China), by InSAR: Earth and Planetary Science Letters, v. 275, p. 246-257.

Clark, M.K., *in review*, Does the crust matter? A new view of post-collisional convergence rates: Nature.

Clark, M. K., and Royden, L.H., 2000, Topographic ooze: Building the eastern margin of Tibet by lower crustal flow: Geology, v. 28(8), p. 703-706.

Clark, M. K., Royden, L.H., Whipple, K.X., Burchfiel, B.C., Zhang, X., and Tang, W., 2006, Use of a regional, relict landscape to measure vertical deformation of the eastern Tibetan Plateau: J Geophys Res-Earth, v. 111, doi:10.1029/2005JF000294.

Clark, M. K., House, M.A., Royden, L.H., Whipple, K.X., Burchfiel, B.C., Zhang, X., and Tang, W., 2005, Late Cenozoic uplift of southeastern Tibet: Geology, v. 33(6), p. 525-528.

Clark, M. K., Farley, K. A., Zheng, D. W., Wang, Z. C., and Duvall, A. R., 2010, Early Cenozoic faulting of the northern Tibetan Plateau margin from apatite (U-Th)/He ages: Earth and Planetary Science Letters, v. 296, p. 78-88.

Cowgill, E., 2007, Impact of riser reconstructions on estimation of secular variation in rates of strike-slip faulting: Revisiting the Cherchen River site along the Altyn Tagh Fault, NW China: Earth and Planetary Science Letters, v. 254, p. 239-255.

Cowgill, E., Gold, R. D., Xuanhua, C., Xiao-Feng, W., Arrowsmith, J. R., and Southon, J., 2009, Low Quaternary slip rate reconciles geodetic and geologic rates along the Altyn Tagh fault, northwestern Tibet: Geology, v. 37, p. 647-650.

Craddock, W.H., Kirby, E., Zheng, D., and Liu, J., 2011, Tectonic setting of Cretaceous basins on the NE Tibetan Plateau: Insights from the Jungong basin: Basin Research, *in press*.

Craddock, W.H., Kirby, E., and Zhang, H., Late Miocene-Pliocene growth of the interior of the northeastern Tibetan Plateau: Lithosphere, *in review*.

Dai, S., Fang, X. M., Dupont-Nivet, G., Song, C. H., Gao, J. P., Krijgsman, W., Langereis, C., and Zhang, W. L., 2006, Magnetostratigraphy of Cenozoic sediments from the Xining Basin: Tectonic implications for the northeastern Tibetan Plateau: Journal of Geophysical Research-Solid Earth, v. 111, doi:10.1029/2005JB004187.

Dayem, K.E., Molnar, P., Clark, M.K., and Houseman, G.A., 2009, Far-field lithospheric deformation in Tibet during continental collision: Tectonics, v. 28, doi:10.1029/2008TC002344.

Dettman, D.L., Fang, X., Garzione, C.N., and Li, J., 2003, Uplift-driven climate change at 12 Ma: a long $\delta^{18}O$ record from the NE margin of the Tibetan plateau: Earth and Planetary Science Letters, v. 214, p. 267-277.

Donelick, R. A., O'Sullivan, P. B., and Ketcham, R. A., 2005, Apatite fission-track analysis: Reviews in mineralogy and geochemistry, v. 58, p. 49-94

Dupont-Nivet, G., Butier, R. F., Yin, A., and Chen, X. H., 2002, Paleomagnetism indicates no Neogene rotation of the Qaidam Basin in northern Tibet during Indo-Eurasian collision: Geology, v. 30, p. 263-266.

Dupont-Nivet, G., Horton, B. K., Butler, R. F., Wang, J., Zhou, J., and Waanders, G. L., 2004, Paleogene clockwise tectonic rotation of the Xining-Lanzhou region, northeastern Tibetan Plateau: Journal of Geophysical Research-Solid Earth, v. 109, doi: 10.1029/2003JB002620.

Duvall, A.R., Clark, M.K., Avdeev, B., Farley, K.A., and Chen, Z., Widespread Late Cenozoic increase in erosion rates across the interior of eastern Tibet constrained by detrital low-temperature thermochronometry: Tectonics, *in review*.

Duvall, A. R. and Clark, M. K., 2010, Dissipation of fast strike-slip faulting within and beyond northeastern Tibet: Geology, v. 38, p. 223-226.

Duvall, A. R., Clark, M. K., van der Pluijm, B. A., and Li, C., 2011, Direct dating of Eocene reverse faulting in northeastern Tibet using Ar-dating of fault clays and low-temperature thermochronometry: Earth Planet Sci Lett., v. 304(3-4), p. 520-526.

Ehlers, T. A., and Farley, K. A., 2003, Apatite (U-Th)/He thermochronometry: methods and applications to problems in tectonic and surface processes: Earth and Planetary Science Letters, v. 206, p. 1-14.

Ehlers, T.A, 2005, Crustal thermal properties and thermchronometer data interpretation in Low-Temperature Thermochonology: Techniques, Interpretations, and Applications, Rev. Mineral. Geochem., 58, edited by P.W. Reiners, and T.A. Ehlers, pp. 315-350.

England, P., and Molnar, P., 1997, Active deformation of Eurasia: From kinematics to dynamics: Science, v. 278, p. 647-650.

Enkelmann, E., L. Ratschbacher, R. Jonckheere, R. Nestler, M. Fleischer, R. Gloaguen, B. R. Hacker, Y. Q. Zhang, and Y. S. Ma, 2006, Cenozoic exhumation and deformation of northeastern Tibet and the Qinling: Is Tibetan lower crustal flow diverging around the Sichuan Basin?: Geological Society of America Bulletin, v.118(5-6), p. 651-671.

Fan, M., Dettman, D.L., Song, C., Fang, X., and Garzione, C.N., 2007, Climatic variation in the Linxia basin, NE Tibetan Plateau, from 13.1 to 4.3 Ma: The stable isotope record: Palaeogeography, Palaeoclimatology, Palaeoecology, v. 247, p. 313-328.

Fang, X., Yan, M., Van der Voo, R., Rea, D. K., Song, C., Parés, J. M., Gao, J., Nie, J., and Dai, S., 2005, Late Cenozoic deformation and uplift of the NE Tibetan Plateau: evidence from high-resolution magnetostratigraphy of the Guide Basin, Qinghai Province, China: Geological Society of America Bulletin, v. 117, p. 1208-1225.

Fang, X., Garzione, C., Van der Voo, R., Rea, D.K., Li, J., and Fan, M., 2003, Flexural subsidence by 29 Ma on the NE edge of Tibet from the magnetostratigraphy of Linxia Basin, China: Earth Planet Sci Lett., v. 210, p. 545-560.

Farley, K., 2000, Helium diffusion from apatite: General behavior as illustrated by Durango fluorapatite: Journal of Geophysical Research, v. 105, p. 2903-2914.

Farley, K. A., and Stockli, D. F., 2002, (U-Th)/He dating of phosphates: Apatite, monazite, and xenotime, *in* Kohn, M. J., Rakovan, J., and Hughes, J. M., editors, Phosphates: Geochemical, Geobiological, and Materials Importance: Reviews in Mineralogy & Geochemistry, p. 559-577.

Farley, K.A., Shuster, D.A., and Ketcham, R.A., 2011, U and Th zonation in apatite observed by laster ablation ICPMS, and implications for the (U-Th)/He system: Geochimica et Cosmochimica Acta, v. 75, p. 4515-4530.

Fitzgerald, P. G., and Gleadow, A. J. W., 1990, New Approaches in Fission-Track Geochronology as a Tectonic Tool - Examples from the Transantarctic Mountains: Nuclear Tracks and Radiation Measurements, v. 17, p. 351-357.

Flowers, R. M., Ketcham, R. A., Shuster, D. L., and Farley, K. A., 2009, Apatite (U-Th)/He thermochronometry using a radiation damage accumulation and annealing model: Geochimica Et Cosmochimica Acta, v. 73, p. 2347-2365.

Fu, B. H., and Awata, Y., 2007, Displacement and timing of left-lateral faulting in the Kunlun Fault Zone, northern Tibet, inferred from geologic and geomorphic features: Journal of Eurasian Earth Sciences, v. 29, p. 253-265.

Gansu Bureau Geological and Mineral Resources (BGMR) Gansu Province, 1989, Regional Geology of Gansu Province, Geological publishing house, Beijing (in Chinese), 690 p.

Gan, W. J., Zhang, P. Z., Shen, Z. K., Niu, Z. J., Wang, M., Wan, Y. G., Zhou, D. M., and Cheng, J., 2007, Present-day crustal motion within the Tibetan Plateau inferred from GPS measurements: Journal of Geophysical Research-Solid Earth, v. 112, doi:10.1029/2005JB004120..

Gaudemer, Y., Tapponnier, P., Meyer, B., Peltzer, G., Guo, S. M., Chen, Z. T., Dai, H. G., and Cifuentes, I., 1995, Partioning of crustal slip between linked, active faults in the eastern Qilian Shan, and evidence for a major seismic gap, the Tianzhu

Gap, on the western Haiyuan Fault, Gansu (China): Geophysical Journal International, v. 120, p. 599-645.

Gleadow, A., and Duddy, I., 1981, A natural long-term track annealing experiment for apatite: Nuclear Tracks, v. 5, p. 169-174.

Gold, R. D., Cowgill, E., Arrowsmith, J. R., Chen, X., Sharp, W. D., Cooper, K. M., and Wang, X. F., 2011, Faulted terrace risers place new constraints on the late Quaternary slip rate for the central Altyn Tagh fault, northwest Tibet: Bulletin of the Geological Society of America, v. 123, p. 958-978.

Harkins, N., Kirby, E., Heimsath, A., Robinson, R., and Reiser, U., 2007, Transient fluvial incision in the headwaters of the Yellow River, northeastern Tibet, China: Journal of Geophysical Research-Earth Surface, v. 112, doi:10.1029/2006JF000570.

Harkins, N., Kirby, E., Shi, X., Wang, E., Burbank, D., and Chun, F., 2010, Millennial slip rates along the eastern Kunlun fault: Implications for the dynamics of intracontinental deformation in Eurasia: Lithosphere, v. 2, p. 247-266.

Horton, B. K., Dupont-Nivet, G., Zhou, J., Waanders, G. L., Butler, R. F., and Wang, J., 2004, Mesozoic-Cenozoic evolution of the Xining-Minhe and Dangchang basins, northeastern Tibetan Plateau: Magnetostratigraphic and biostratigraphic results: Journal of Geophysical Research-Solid Earth, v. 109, doi:10.1029/2003JB002913.

Hough, B. G., Garzione, C. N., Wang, Z., Lease, R. O., Burbank, D. W., and Yuan, D., 2011, Stable isotope evidence for topographic growth and basin segmentation: Implications for the evolution of the NE Tibetan Plateau: Bulletin of the Geological Society of America, v. 123, p. 168-185.

Huang, G., Hourigan, J.K., Ritts, B.Z., and Kent-Corson, M.L., 2011, Cenozoic multiple-phase tectonic evolution of the northern Tibetan Plateau: Constaints from sedimentary records from Qaidam Basin, Hexi Corridor, and Subei Basin, northwest China: American Journal of Science, v. 311, p. 116-152.

Jolivet, M., Brunel, M., Seward, D., Xu, Z., Yang, J., Malavieille, J., Roger, F., Leyreloup, A., Arnaud, N., and Wu, C., 2003, Neogene extension and volcanism in the Kunlun Fault Zone, northern Tibet: New constraints on the age of the Kunlun Fault: Tectonics, v. 22, doi:10.1029/2002TC001428.

Jolivet, M., Brunel, M., Seward, D., Xu, Z., Yang, J., Roger, F., Tapponnier, P., Malavieille, J., Arnaud, N., and Wu, C., 2001, Mesozoic and Cenozoic tectonics of the northern edge of the Tibetan plateau: fission-track constraints: Tectonophysics, v. 343, p. 111-134.

Karplus, M.S., Zhao, W., Klemperer, S.L., Wu, Z., Mechie, J., Shi, D., Brown, L.D., and Chen, C., 2011, Injection of Tibetan crust beneath the south Qaidam Basin: Evidence from INDEPTH IV wide-angle seismic data: Journal of Geophysical Research, v. 116, doi:10.1029/2010JB007911.

Kent-Corson, M.L., Ritts, B.D., Zhuang, G., Bovet, P.M., Graham, S., and Chamberlain, C.P., 2009, Stable isotope constraints on the tectonic, topographic, and climatic-evolution of the northern margin of the Tibetan Plateau: Earth and Planetary Science Letters, v. 282, p. 158-166.

Ketcham, R. A., 2005, Forward and inverse modeling of low-temperature thermochronometry data: Reviews in mineralogy and geochemistry, v. 58, p. 275-314.

Ketcham, R. A., Carter, A., Donelick, R. A., Barbarand, J., and Hurford, A. J., 2007, Improved modeling of fission-track annealing in apatite: American Mineralogist, v. 92, p. 799-810.

Ketcham, R. A., Donelick, R. A., Balestrieri, M. L., and Zattin, M., 2009, Reproducibility of apatite fission-track length data and thermal history reconstruction: Earth and Planetary Science Letters, v. 284, p. 504-515.

Kidd, W. S. F., and Molnar, P., 1988, Quaternary and Active Faulting Observed on the 1985 Academia Sinica--Royal Society Geotraverse of Tibet: Philosophical Transactions of the Royal Society of London. Series A, Mathematical and Physical Sciences, v. 327vp. 337-363.

Kirby, E., Reiners, P.W., Krol, M.A., Whipple, K. X., Hodges, K. V., Farley, K.A., Tang, W.Q., and Chen, Z.L., 2002, Late Cenozoic evolution of the eastern margin of the Tibetan Plateau: Inferences from Ar-40/Ar-39 and (U-Th)/He thermochronology: Tectonics, v.21(1), 10.1029/2000TC001246.

Kirby, E., Harkins, N., Wang, E. Q., Shi, X. H., Fan, C., and Burbank, D., 2007, Slip rate gradients along the eastern Kunlun fault: Tectonics, v. 26, doi:10.1029/2006TC002033.

Lasserre, C., Gaudemer, Y., Tapponnier, P., Meriaux, A. S., Van der Woerd, J., Yuan, D. Y., Ryerson, F. J., Finkel, R. C., and Caffee, M. W., 2002, Fast late Pleistocene slip rate on the Leng Long Ling segment of the Haiyuan fault, Qinghai, China: Journal of Geophysical Research-Solid Earth, v. 107, p. 17, doi:10.1029/2000JB000060.

Lasserre, C., Morel, P. H., Gaudemer, Y., Tapponnier, P., Ryerson, F. J., King, G. C. P., Metivier, F., Kasser, M., Kashgarian, M., Baichi, L., Taiya, L., and Daoyang, Y., 1999, Postglacial left slip rate and past occurrence of M >= 8 earthquakes on the western Haiyuan fault, Gansu, China: Journal of Geophysical Research-Solid Earth, v. 104, p. 17633-17651.

Lease, R. O., Burbank, D. W., Clark, M. K., Farley, K. A., Zheng, D., and Zhang, H., 2011, Middle Miocene reorganization of deformation along the northeastern Tibetan Plateau: Geology, v. 39, p. 359-362.

Lease, R. O., Burbank, D. W., Gehrels, G. E., Wang, Z. C., and Yuan, D. Y., 2007, Signatures of mountain building: Detrital zircon U/Pb ages from northeastern Tibet: Geology, v. 35, p. 239-242.

Li, C. Y., Zhang, P. Z., Yin, J. H., and Min, W., 2009, Late Quaternary left-lateral slip rate of the Haiyuan fault, northeastern margin of the Tibetan Plateau: Tectonics, v. 28, doi:10.1029/2008TC002302.

Lin, X., Chen, H., and Wyrwoll, K.H., Batt, G.E., Liao, L., and Xiao, J., 2011, The Uplift History of the Haiyuan-Liupan Shan region northeast of the present Tibetan Plateau: Integrated constraint from stratigraphy and thermochronology: The Journal of Geology, v.119(4), p. 372-393.

Meriaux, A., Ryerson, F., Tapponnier, P., Van der Woerd, J., Finkel, R., Xu, X., Xu, Z., and Caffee, M., 2004, Rapid slip along the central Altyn Tagh Fault: morphochronologic evidence from Cherchen He and Sulamu Tagh: J. geophys. Res, v. 109, doi:10.1029/2003JB002558.

Mériaux, A. S., Tapponnier, P., Ryerson, F., Xiwei, X., King, G., Van der Woerd, J., Finkel, R., Haibing, L., Caffee, M., and Zhiqin, X., 2005, The Aksay segment of the northern Altyn Tagh fault: Tectonic geomorphology, landscape evolution, and Holocene slip rate: Journal of Geophysical Research, v. 110, p. B04404.

Metivier, F., Gaudemer, Y., Tapponnier, P., and Meyer, B., 1998, Northeastward growth of the Tibet plateau deduced from balanced reconstruction of two depositional areas: The Qaidam and Hexi Corridor basins, China: Tectonics, v. 17, p. 823-842.

Meyer, B., Tapponnier, P., Bourjot, L., Metivier, F., Gaudemer, Y., Peltzer, G., Shunmin, G., and Zhitai, C., 1998, Crustal thickening in Gansu-Qinghai, lithospheric mantle subduction, and oblique, strike-slip controlled growth of the Tibet plateau: Geophysical Journal International, v. 135, p. 1-47.

Mock, C., Arnaud, N. O., and Cantagrel, J. M., 1999, An early unroofing in northeastern Tibet? Constraints from Ar-40/Ar-39 thermochronology on granitoids from the eastern Kunlun range (Qianghai, NW China): Earth and Planetary Science Letters, v. 171, p. 107-122.

Molnar, P., and Tapponnier, P., 1975, Cenozoic tectonics of Eurasia: effects of a continental collision: Science, v. 189, p. 419-426.

Molnar, P., and Stock, J.M., 2009, Slowing of India's convergence with Eurasia since 20 Ma and its implications for Tibetan mantle dynamics: Tectonics, v. 28, doi:10.1029/2008TC002271.

Molnar, P., and Dayem, K.E., Major intracontinental strike-slip faults and contrasts in lithospheric strength: Geosphere, v. 6, p. 444-467.

Yue, Y. J., Ritts, B. D., Hanson, A. D., and Graham, S. A., 2004a, Sedimentary evidence against large strike-slip translation on the Northern Altyn Tagh fault, NW China: Earth and Planetary Science Letters, v. 228, p. 311-323.

Yue, Y. J., Ritts, B. D., Graham, S. A., Wooden, J. L., Gehrels, G. E., and Zhang, Z. C., 2004b, Slowing extrusion tectonics: lowered estimate of post-Early Miocene slip rate for the Altyn Tagh fault: Earth and Planetary Science Letters, v. 217, p. 111-122.

Zeitler, P. K., Herczeg, A. L., Mcdougall, I., and Honda, M., 1987, U-Th-He Dating of Apatite - a Potential Thermochronometer: Geochimica Et Cosmochimica Acta, v. 51, p. 2865-2868.

Zhai, Y., and Cai, T., 1984, The Tertiary system of Gansu province: Gansu Geology, v. 1984, p. 1-40.

Zhang, H.P., Craddock, W.H., Lease, R.O., Wang, W., Yuan, D.Y., Zhang, P.Z., Molnar, P., Zheng, D.W., and Zheng, W.J., 2011, Magnetostratigraphy of the Neogene Chaka basin and its implications for mountain building processes in the north-eastern Tibetan Plateau: Basin Research, doi:10.1111/j.1365-2117.2011.00512.x.

Zhang, P. Z., Burchfiel, B. C., Molnar, P., Zhang, W. Q., Jiao, D. C., Deng, Q. D., Wang, Y. P., Royden, L., and Song, F. M., 1991, Amount and style of Late Cenozoic deformation in the Liupan Shan area, Ningxia Autonomous region, China: Tectonics, v. 10, p. 1111-1129.

Zhang, P. Z., Molnar, P., and Xu, X., 2007, Late Quaternary and present-day rates of slip along the Altyn Tagh Fault, northern margin of the Tibetan Plateau: Tectonics, v. 26, doi:10.1029/2006TC002014.

Ouimet, W., K. Whipple, L. Royden, P. Reiners, K. Hodges, and M. Pringle, 2010, Regional incision of the eastern margin of the Tibetan Plateau: Lithosphere, v. 2(1), p. 50-63.

Pan, G., J. Ding, D. Yao, and L. Wang, 2004, Guidebook of 1:1,500,000 geologic map of the Qinghai-Xizang (Tibet) plateau and adjacent areas, Chengdu, China, Chengdu Cartographic Publishing House, 48 p.

Parés, J. M, Van der Voo, R., Downs, W.R., Yan, M., and Fang, X., 2003, Northeastward growth and uplift of the Tibetan Plateau: Magnetostratigraphic insights from the Guide Basin: Journal of Geophysical Research, v.108, doi:10.1029/2001JB001349.

Pullen, A., Kapp, P., Gehrels, G. E., Vervoort, J. D., and Ding, L., 2008, Triassic continental subduction in central Tibet and Mediterranean-style closure of the Paleo-Tethys Ocean: Geology, v. 36, p. 351-354.

Qinghai Bureau of Geology and Mineral Resources (QBGMR), 1991, Regional Geology of Qinghai Province, Geological Publishing House, Beijing.

Ratschbacher, L., Hacker, B.R., Calvert, A, Webb, L.E., Grimmer, J.C., McWilliams, M.O., Ireland, T., Dong, S., and Hu, J.-M., 2003, Tectonics of the Qinling (Central China): tectonostratigraphy, geochronology, and deformation history: Tectonophysics, v. 366, p. 1-53.

Ratschbacher, L., Hacker, B.R., Webb, L.E., McWilliams, M.O., Ireland, T., Dong, S., Calvert, A., Chateigner, D., and Wink, H.-R., 2000, Exhumation of the ultrahigh-pressure continental crust in east central China cretaceous and Cenozoic

Unroofing and the Tan-Lu Fault: Journal of Geophysical Research, v. 105(B6), p. 13303-13338.

Reiners, P. W., and Ehlers, T. A., 2005, Low-temperature thermochronology: techniques, interpretations, and applications: Techniques, Interpretations, and Applications, Rev. Mineral. Geochem., 58, edited by P.W. Reiners, and T.A. Ehlers, p. 1-18.

Reiners, P. W., Farley, K. A., and Hickes, H. J., 2002, He diffusion and (U-Th)/He thermochronometry of zircon: initial results from Fish Canyon Tuff and Gold Butte: Tectonophysics, v. 349, p. 297-308.

Reiners, P. W., Spell, T. L., Nicolescu, S., and Zanetti, K. A., 2004, Zircon (U-Th)/He thermochronometry: He diffusion and comparisons with 40Ar/39Ar dating: Geochimica Et Cosmochimica Acta, v. 68, p. 1857-1887.

Ritts, B. D., Yue, Y. J., and Graham, S. A., 2004, Oligocene-Miocene tectonics and sedimentation along the Altyn Tagh Fault, northern Tibetan Plateau: Analysis of the Xorkol, Subei, and Aksay basins: Journal of Geology, v. 112, p. 207-229.

Ritts, B.D., Yue, Y., Graham, S., Sobel, E.R., Abbink, O.A., and Stockli, D., 2008, From sea level to high elevation in 15 million years: Uplift history of the northern Tibetan Plateau margin in the Altun Shan: American Journal of Science, v. 308, p.657-678.

Rowley, D. B., 1996, Age of initiation of collision between India and Eurasia: A review of stratigraphic data: Earth and Planetary Science Letters, v. 145, p. 1-13.

Rowley, D.B., 1998, Minimum age of initiation of collision between India and Eurasia north of Everest based on the subsidence history of the Zhepure Mountain section: The Journal of geology, v. 106, p. 220-235.

Royden, L. H., Burchfiel, B.C., and van der Hilst, R.D., 2008, The geological evolution of the Tibetan plateau: Science, v. 321, p. 1054-1058.

Schoenbohm, L.M., Burchfiel, B.C., Liangzhong, C., and Jiyun, Y., 2006, Miocene to present activity along the Red River fault, China, in the context of continental extrusion, upper-crustal rotation, and lower-crustal flow: Geological Society of America Bulletin, v. 118, p. 672-688.

Searle, M., Elliott, J., Phillips, R., and Chung, S. L., 2011, Crustal-lithospheric structure and continental extrusion of Tibet: Journal of the Geological Society, v. 168, p. 633-672.

Sobel, E.R., Arnaud, N., Jolivet, M., Ritts, B.D., and Brunel, M., 2001, Jurassic to Cenozoic exhumation history of the Altyn Tagh range, northwest China constrained by 40Ar/39Ar and apatite fission track thermochronology, *in* Hendrix, M.S., and Davis, G.A., ed., Paleozoic and Mesozoic tectonic evolution of central and eastern Eurasia: From continental assembly to intracontinental deformation: Geological Society of America Memoir 194, p. 247-268.

Tapponnier, P., Peltzer, G., Ledain, A.Y., Armijo, R., and Cobbold, P., 1982, Propagating Extrusion Tectonics in Asia - New Insights from Simple Experiments with Plasticine: Geology, v. 10(12), p. 611-616.

Tapponnier, P., Xu, Z. Q., Roger, F., Meyer, B., Arnaud, N., Wittlinger, G., and Yang, J. S., 2001, Geology - Oblique stepwise rise and growth of the Tibet plateau: Science, v. 294, p. 1671-1677.

Taylor, M., and Yin, A., 2009, Active structures of the Himalayan-Tibetan orogen and their relationships to earthquake distribution, contemporary strain field, and Cenozoic volcanism: Geosphere, v. 5(3), p. 199-214.

Thatcher, W., 2007, Microplate model for the present-day deformation of Tibet: Journal of Geophysical Research-Solid Earth, v. 112, doi:10.1029/2005JB004244.

Van der Woerd, J., Ryerson, F. J., Tapponnier, P., Gaudemer, Y., Finkel, R., Meriaux, A. S., Caffee, M., Zhao, G. G., and He, Q. L., 1998, Holocene left-slip rate determined by cosmogenic surface dating on the Xidatan segment of the Kunlun fault (Qinghai, China): Geology, v. 26, p. 695-698.

Van der Woerd, J., Ryerson, F. J., Tapponnier, P., Meriaux, A. S., Gaudemer, Y., Meyer, B., Finkel, R. C., Caffee, M. W., Zhao, G. G., and Xu, Z. Q., 2000, Uniform Slip-Rate along the Kunlun Fault: Implications for seismic behaviour and large-scale tectonics: Geophysical Research Letters, v. 27, p. 2353-2356.

Van Der Woerd, J., Tapponnier, P., Ryerson, F. J., Meriaux, A. S., Meyer, B., Gaudemer, Y., Finkel, R. C., Caffee, M. W., Zhao, G. G., and Xu, Z. Q., 2002, Uniform postglacial slip-rate along the central 600 km of the Kunlun Fault (Tibet), from Al-26, Be-10, and C-14 dating of riser offsets, and climatic origin of the regional morphology: Geophysical Journal International, v. 148, p. 356-388.

Vincent, S.J., and Allen, M.B., 1999, Evolution of the Minle and Chaoshui Basins, China: Implications for Mesozoic strike-slip basin formation in central Asia: Geological Society of America Bulletin, v. 111, p. 725-742.

Wagner, G. A., and Reimer, G. M., 1972, Fission track tectonics – Tectonic Interpretation of fission track apatite ages: Earth and Planetary Science Letters, v. 14, p. 263-268.

Wang, E. C., and Burchfiel, B. C., 2004, Late cenozoic right-lateral movement along the Wenquan fault and associated deformation: Implications for the kinematic history of the Qaidam Basin Northeastern Tibetan Plateau: International Geology Review, v. 46, p. 861-879.

Wang, F., Lo, C.H., Li, Q., Yeh, M.H., Wan, J., Zheng, D., and Wang, E., 2004, Onset timing of significant unroofing around Qaidam basin, northern Tibet, China: constraints from $^{40}Ar/^{39}Ar$ and FT thermochronology on granitoids: Journal of Eurasian Earth Sciences, v.24(1), p. 59-69.

Wang, W., Zhang, P. Z., Kirby, E., Wang, L. H., Zhang, G. L., Zheng, D. W., and Chai, C. Z., 2011, A revised chronology for Tertiary sedimentation in the Sikouzi basin: Implications for the tectonic evolution of the northeastern corner of the Tibetan Plateau: Tectonophysics, v. 505, p. 100-114.

Wang, X., Zattin, M., Li, J., Song, C., Peng, T., Liu, S., and Liu, B., 2011, Eocene to Pliocene exhumation history of the Tianshui-Huicheng region determined by Apatite fission track thermochronology of the northeastern Tibetan Plateau margin: Journal of Eurasian Earth Sciences, v. 42(1-2), p. 97-110.

Wilson, C.J.L., and Fowler, A.P., 2011, Denudational response to surface uplift in east Tibet: Evidence from apatite fission-track thermochronology: Bulletin of the Geological Society of America, doi:10.1130/B30331.1.

Wolf, R. A., Farley, K. A., and Kass, D. M., 1998, Modeling of the temperature sensitivity of the apatite (U-Th)/He thermochronometer: Chemical Geology, v. 148, p. 105-114.

Wolf, R. A., Farley, K. A., and Silver, L. T., 1996, Helium diffusion and low-temperature thermochronometry of apatite: Geochimica Et Cosmochimica Acta, v. 60, p. 4231-4240.

Wu, Z., Ye, P., Patrick, B.J., Hu, D., Zhao, W., and Wu, Z., 2009, Late Oligocene-Early Miocene thrusting in southern East Kunlun Mountains, northern Tibetan plateau: Journal of Earth Science, v. 20(2), p. 381-390.

Yan, M., VanderVoo, R., Fang, X., Parés, J. M., and Rea, D. K., 2006, Paleomagnetic evidence for a mid-Miocene clockwise rotation of about 25 of the Guide Basin area in NE Tibet: Earth and Planetary Science Letters, v. 241, p. 234-247.

Yao, H. Beghein, C., and van der Hilst, R.D., 2008, Surface wave array tomography in SE Tibet from ambient seismic noise and two-station analysis: II. Crustal and upper-mantle structure: Geophys. J. Int., v.163, p.205-219.

Yao, H., van der Hilst, R.D., and Montagner, J.-P., 2010, Heterogeneity and anisotropy of the lithosphere of SE Tibet from surface wave array tomography: Journal of Geophysical Research, v. 115, doi:10.1029/2009JB007142.

Yin, A., Dang, Y., Zhang, M., McRivette, M. W., Burgess, W. P., and Chen, X., 2007, Cenozoic tectonic evolution of Qaidam basin and its surrounding regions (part 2): Wedge tectonics in southern Qaidam basin and the Eastern Kunlun Range: Geological Society of America Special Papers, v. 433, p. 369-390.

Yin, A., Dang, Y. Q., Wang, L. C., Jiang, W. M., Zhou, S. P., Chen, X. H., Gehrels, G. E., and McRivette, M. W., 2008a, Cenozoic tectonic evolution of Qaidam basin and its surrounding regions (Part 1): The southern Qilian Shan-Nan Shan thrust belt and northern Qaidam basin: Geological Society of America Bulletin, v. 120, p. 813-846.

Yin, A., Dang, Y. Q., Zhang, M., Chen, X. H., and McRivette, M. W., 2008b, Cenozoic tectonic evolution of the Qaidam basin and its surrounding regions (Part 3): Structural geology, sedimentation, and regional tectonic reconstruction: Geological Society of America Bulletin, v. 120, p. 847-876.

Yin, A., Rumelhart, P. E., Butler, R., Cowgill, E., Harrison, T. M., Foster, D. A., Ingersoll, R. V., Zhang, Q., Zhou, X. Q., Wang, X. F., Hanson, A., and Raza, A., 2002, Tectonic history of the Altyn Tagh fault system in northern Tibet inferred from Cenozoic sedimentation: Geological Society of America Bulletin, v. 114, p. 1257-1295.

Yuan, D.Y., Champagnac, J.D., Ge, W.P., Molnar, P., Zhang, P.Z., Zheng, W.J., Zhang, H.P., and Liu, X.W., 2011, Late Quaternary right-lateral slip rates of faults adjacent to the lake Qinghai, northeastern margin of the Tibetan Plateau: Geological Society of America Bulletin, doi:10.1130/B30315.1.

Yuan, W., Dong, J., Shicheng, W., and Carter, A., 2006, Apatite fission track evidence for Neogene uplift in the eastern Kunlun Mountains, north Qinghai-Tibet Plateau, China: Journal of Asian Earth Sciences, v. 27, p. 847-856.

Zhang, P. Z., Shen, Z., Wang, M., Gan, W. J., Burgmann, R., and Molnar, P., 2004, Continuous deformation of the Tibetan Plateau from global positioning system data: Geology, v. 32, p. 809-812.

Zheng, D. W., Zhang, P. Z., Wan, J. L., Li, C. Y., and Cao, J. X., 2003, Late Cenozoic deformation subsequence in northeastern margin of Tibet - Detrital AFT records from Linxia Basin: Science in China Series D-Earth Sciences, v. 46, p. 266-275.

Zheng, D. W., Zhang, P.Z., Wan, J.L., Yuan, D.Y., Li, C.Y., Yin, G.M., Zhang, G.L., Wang, Z.C., Min, M., and Chen, J., 2006, Rapid exhumation at similar to 8 Ma on the Liupan Shan thrust fault from apatite fission-track thermochronology: Implications for growth of the northeastern Tibetan Plateau margin: Earth and Planetary Science Letters, v. 248(1-2), p. 198-208.

Zheng, D., Clark, M.K., Zhang, P., Zheng, W., and Farley, K.A., 2010, Erosion, fault initiation and topographic growth of the North Qilian Shan (northern Tibetan Plateau): Geosphere, v. 6(6), p. 937-941.

Zhao, H.G., Liu, C.Y., Wang, F., Wang, J.Q., Li, Q., and Yao, Y.M., 2007, Uplift and evolution of Helan Mountain: Science in China Series D: Earth Sciences, v.50, p.217-226.

Zhou, J. X., Xu, F. Y., Wang, T. C., Cao, A. F., and Yin, C. M., 2006, Cenozoic deformation history of the Qaidam Basin, NW China: Results from cross-section restoration and implications for Qinghai-Tibet Plateau tectonics: Earth and Planetary Science Letters, v. 243, p. 195-210.

Zhu, L., Owens, T. J., and Randall, G. E., 1995, Lateral variation in crustal structure of the northern Tibetan Plateau inferred from teleseismic receiver functions: Bulletin of the Seismological Society of America, v. 85, p. 1531-1540.

Zhu, Y., Zhong, J., and Li, W., 1994, The neotectonic movement and the evolution of saline lakes of Qaidam Basin in northwestern China (Shen, W.B., ed.): Beijing, China, Geologic Publishing House, p. 1-132 (in Chinese with English abstract).

Appendix: Chapter IV

This appendix contains a detailed table (Table A4.1) of low-temperature thermochronometry analysis results.

Appendix Table A4.1. Thermochronometry analyses

Kunlun Fault

Kunlun Fault West (KFW)

Apatite (U-Th)/He

Sample #	U (ppm)	Th (ppm)	He (nmol/g)	Mass (µg)	Radius (µm)	Length (µm)	F_T
$KFW1_A$	6.59	15.66	0.73	1.86	42.86	188.56	0.68
$KFW1_B$	12.43	21.58	1.13	2.03	42.86	205.70	0.69
$KFW1_C$	14.32	13.56	0.95	1.08	34.28	171.42	0.63
$KFW2_A$	22.75	5.42	0.77	2.31	45.71	205.70	0.71
$KFW2_B$	17.52	6.29	0.52	2.61	48.57	205.70	0.72
$KFW2_C$	35.82	12.07	1.03	1.33	40.00	154.28	0.67

Sm (ppm)	Raw Age (Ma)	Corrected Age (Ma)	Elevation (m)
-	13.13	19.25	4755
-	11.86	17.22	
-	9.95	15.86	
-	5.86	8.23	4935
-	5.05	6.97	
-	4.91	7.37	

Zircon (U-Th)/He

Sample #	U (ppm)	Th (ppm)	He (nmol/g)	Mass (µg)	Radius (µm)	Length (µm)	F_T
$KFW1_A$	1008.22	327.23	137.45	14.83	50.55	312.16	0.81
$KFW1_B$	546.02	173.96	75.90	21.61	56.48	364.24	0.83

$KFW2_A$	1085.65	71.08	41.99	8.77	47.46	209.36	0.79
$KFW2_B$	260.12	53.47	7.87	9.26	51.18	189.99	0.80

Sm (ppm)	Raw Age (Ma)	Corrected Age (Ma)	Elevation (m)
-	23.26	28.74	4755
-	23.75	28.62	
-	7.01	8.89	4935
-	5.31	6.67	

Kunlun Fault Central (KFC)

Apatite (U-Th)/He

Sample #	U (ppm)	Th (ppm)	He (nmol/g)	Mass (µg)	Radius (µm)	Length (µm)	F_T
$KFC4_A$	13.67	10.24	1.39	4.87	57.00	186.00	0.75
$KFC4_B$	2.01	2.75	0.21	5.14	62.00	166.00	0.75
$KFC4_C$[†*]	0.08	0.97	0.85	4.59	64.50	137.00	0.73
$KFC4_D$	9.84	5.18	0.86	3.26	63.00	102.00	0.73

Sm (ppm)	Raw Age (Ma)	Corrected Age (Ma)	Elevation (m)
106.05	15.72	20.93	3944
8.11	14.78	19.54	
4.41	486.40	653.53	
22.69	14.21	19.51	

Zircon (U-Th)/He

Sample #	U (ppm)	Th (ppm)	He (nmol/g)	Mass (µg)	Radius (µm)	Length (µm)	F_T
$KFC3_A$	363.85	173.53	108.54	4.18	38.16	154.43	0.73

$KFC3_B$	81.56	27.46	22.11	4.18	39.58	143.56	0.74
$KFC3_C$	289.04	72.05	60.70	3.38	40.15	112.62	0.73
$KFC4_A$	183.59	205.90	121.43	3.78	33.26	183.55	0.71
$KFC4_B$	103.59	43.08	57.03	2.71	34.66	121.51	0.70
$KFC4_C$†	534.08	534.73	244.45	7.21	44.37	196.95	0.77

Sm (ppm)	Raw Age (Ma)	Corrected Age (Ma)	Elevation (m)
-	49.14	66.84	
-	46.02	62.18	
-	36.38	49.94	
-	95.52	134.20	
-	91.47	129.80	
-	67.78	87.89	

Apatite Fission Track (age data)

Sample#	Grain #	N_s	Area (cm x cm)	$^{238}U/^{43}Ca$ (dmnls)	1σ (dmnls)	^{43}Ca	^{238}U
KFC3	2	0	7.77E-06	1.63E-02	1.63E-03	4.83E-01	9.08E-01
	3	5	1.94E-05	1.11E-01	1.11E-02	2.67E-02	4.32E-04
	4	5	1.46E-05	2.07E-01	2.07E-02	2.67E-02	4.81E-04
	5	0	1.75E-05	3.33E-02	3.33E-03	2.90E-02	7.98E-03
	6	1	3.88E-05	2.16E-02	2.16E-03	2.91E-02	7.19E-03
	7	3	1.21E-05	1.58E-01	1.58E-02	4.48E-02	4.42E-04
	8	0	1.94E-05	3.08E-03	3.08E-04	3.62E-02	3.51E-02
	9	2	1.75E-05	3.28E-02	3.28E-03	2.94E-02	4.40E-03
	10	0	1.21E-05	1.86E-03	1.86E-04	2.41E-02	9.15E-02
	11	1	1.02E-05	6.85E-02	6.85E-03	3.09E-02	8.02E-04

12	3	3.11E-05	7.46E-02	7.46E-03	2.81E-02	3.83E-03
13	2	1.46E-05	9.69E-02	9.69E-03	3.05E-02	1.91E-03
14	0	2.43E-05	1.81E-04	1.81E-05	2.65E-02	1.12E
15	1	3.88E-05	1.21E-02	1.21E-03	3.18E-02	5.40E-03
16	2	3.40E-05	6.22E-02	6.22E-03	2.93E-02	2.08E-03
17	4	1.36E-05	1.88E-01	1.88E-02	3.01E-02	4.57E-04
18	0	9.71E-06	8.93E-03	8.93E-04	3.30E-02	4.61E-02
19	2	1.46E-05	1.77E-01	1.77E-02	3.48E-02	1.13E-03
20	0	1.21E-05	2.96E-02	2.96E-03	3.07E-02	1.06E-02
21	2	1.46E-05	2.95E-02	2.95E-03	2.98E-02	1.01E-02
22	0	2.33E-05	1.04E-02	1.04E-03	3.46E-02	9.32E-03
23	2	9.71E-06	6.14E-02	6.14E-03	4.02E-02	8.90E-04
24	7	1.21E-05	6.73E-01	6.73E-02	3.96E-02	2.64E-04
25	2	1.21E-05	3.32E-02	3.32E-03	4.68E-02	2.74E-02
26	5	1.75E-05	2.45E-01	2.45E-02	4.71E-02	6.01E-04
27	1	9.71E-06	3.46E-02	3.46E-03	3.97E-02	2.40E-03
28	2	1.46E-05	2.98E-02	2.98E-03	3.48E-02	0.00E
29	2	1.55E-05	1.87E-02	1.87E-03	4.32E-02	5.52E-03
30	0	3.88E-05	1.06E-02	1.06E-03	3.81E-02	1.74E-02
31	1	1.75E-05	1.41E-02	1.41E-03	3.43E-02	9.44E-03
32	8	9.71E-06	7.28E-01	7.28E-02	3.66E-02	7.70E-05
33	0	3.11E-05	3.94E-02	3.94E-03	3.64E-02	5.90E-03
34	7	1.21E-05	5.01E-01	5.01E-02	3.55E-02	4.58E-04
35	5	1.75E-05	8.47E-02	8.47E-03	3.20E-02	8.97E-03
36	16	1.70E-05	3.47E-01	3.47E-02	3.74E-02	6.34E-04
37	6	7.77E-06	1.32E-01	1.32E-02	3.65E-02	2.81E-03
38	0	1.75E-05	2.21E-02	2.21E-03	4.93E-02	1.32E-02
39	0	1.94E-05	1.27E-04	1.27E-05	5.09E-02	7.37E-01
40	1	1.16E-05	9.04E-02	9.04E-03	5.86E-02	1.41E-03

^{232}Th	^{147}Sm	FT Age (Ma)	2σ (Ma)	Etch	Dpar (µm)	Dper (µm)	U (ppm)
1.02E 9.	1.40E+00	0	191.18	1	1.47	0.53	5.64
7.05E-03	1.11E-02	18.98	17.42	2	1.51	0.21	38.42
1.53E-03	4.20E-03	13.58	12.46	4	1.49	0.15	71.63
8.45E-03	4.54E-03	0	42.04	1	1.39	0.38	11.54
2.18E-02	8.02E-03	9.72	19.54	2	1.44	0.13	7.5
1.68E-02	5.28E-03	12.76	14.96	2	1.13	0.2	54.87
3.69E-01	4.33E-02	0	397.72	1	1.7	0.21	1.07
7.58E-03	2.11E-02	28.5	40.72	1	1.39	0.14	11.36
9.54E-01	1.52E-01	0	1003.52	0	-0.22	-0.09	0.65
7.10E-02	1.08E-02	11.7	23.52	1	1.38	0.05	23.75
6.88E-02	9.20E-01	10.57	12.4	2	1.26	0.24	25.88
1.23E	5.64E-03	11.58	16.56	1	1.6	0.16	33.59
4.74E	3.10E	0	4016.42	1	1.38	0.1	0.06
1.39E	3.90E-02	17.36	34.9	1	1.15	0.19	4.2
4.69E-01	5.59E-03	7.74	11.06	2	1.64	0.12	21.56
3.44E-03	1.67E-02	12.81	13.08	4	1.48	0.2	65.06
4.61E	6.97E-02	0	276.88	1	0.97	0.11	3.1
9.76E-03	2.61E-02	6.35	9.08	2	1.42	0.07	61.28
1.57E-02	1.62E-01	0	67.9	1	1.47	0.19	10.27
2.24E-02	1.63E-02	37.9	54.16	2	1.49	0.16	10.24
7.70E-02	4.78E-02	0	100.88	1	1.78	0.21	3.59
6.64E-03	5.65E-03	27.37	39.12	1	1.44	0.24	21.29
1.53E-03	1.35E-02	7.01	5.48	3	1.56	0.09	233.3
3.23E-02	7.58E-02	40.52	57.9	2	1.15	0.14	11.5
2.23E-03	7.13E-03	9.53	8.74	4	1.39	0.15	85.03
1.13E-02	1.93E-02	24.29	48.82	1	1.59	0.07	12
2.25E	1.17E-01	37.63	53.78	2	1.28	0.26	10.32
3.33E-02	1.87E-02	55.98	79.98	2	1.47	0.08	6.49

2.19E	1.00E-01	0	59.26	1	1.78	0.19	3.68
3.03E-02	3.94E-03	33.18	66.7	1	1.44	0.09	4.88
2.06E-02	3.24E-03	9.25	6.8	2	1.41	0.11	252.36
1.13E-02	9.14E-03	0	20.02	1	1.34	0.1	13.66
1.83E-02	3.97E-02	9.4	7.36	2	1.41	0.26	173.87
4.43E-02	2.25E-02	27.58	25.3	2	1.21	0.31	29.36
2.70E-03	6.86E-03	22.13	11.96	4	1.25	0.12	120.47
1.89E-02	7.74E-03	47.57	40.04	2	1.66	0.09	45.87
1.80E-02	1.67E-02	0	63.12	1	1.19	0.18	7.67
1.24E	2.72E-01	0	6029.82	0	-0.22	-0.09	0.04
1.14E-01	9.96E-02	7.76	15.6	1	1.47	0.24	31.33

Th (ppm)	**Sm (ppm)**	**Pit Depth (µm)**
50.73	197.08	8.62
71.51	201.75	13.76
214.09	313.95	12.72
74.58	565.82	12.24
28.88	357.46	12.74
23.28	592.04	8.24
0.76	91.41	9.61
47.31	97.71	12.61
0.25	18.01	14.31
5.82	285.02	12.92
5.24	0.39	13.5
0.14	234.4	12.34
0.23	0	14.14
0.07	59.49	12.49
0.21	343.2	14.5
120.49	172.81	12.79
0.07	44.02	12.28

53.05	108.67	11.88
15.09	12.45	12.81
18.68	124.95	15.14
7.43	47.78	12.45
90.24	476.57	11.1
148.61	289.79	10.07
24.45	46.53	8.86
242.6	558.21	8.93
40.97	192.19	10.12
0.13	17.28	11.94
12.95	110.2	10.37
0.15	13.96	11
12.08	561.27	11.94
33.69	656.38	12.14
55.53	200.82	11.26
29.79	81.48	11.76
11.22	115.15	13.56
234.72	441.49	11.64
27.97	308.78	11.22
38.53	262.19	8.47
0.37	14.89	9.32
5.38	30.96	9.84
Mean Dpar	1.34	
Mean Dper	0.16	
Modified Zeta	16.352	0.335
Mean ^{29}Si b:s	0.047	
Mean ^{43}Ca b:s	0.047	
Mean ^{238}U b:s	0.337	

# of grains	39	
Chi-squared	38.5	
Chi-squared prob.	0.4458	
Pooled Age (Ma)	**12.90**	**2.8**

Sample#	Grain #	N_s	Area (cm x cm)	$^{238}U/^{43}Ca$ (dmnls)	1σ (dmnls)	^{43}Ca	^{238}U
KFC4	1	15	1.75E-05	4.45E-01	4.45E-02	3.72E-02	1.81E-04
	2	2	1.46E-05	1.17E-01	1.17E-02	3.07E-02	1.75E-03
	3	0	3.88E-05	1.37E-02	1.37E-03	3.59E-02	6.38E-03
	4	0	1.75E-05	4.05E-03	4.05E-04	4.10E-02	6.19E-02
	5	5	3.88E-05	1.09E-01	1.09E-02	3.31E-02	3.03E-04
	6	11	3.88E-05	2.23E-01	2.23E-02	3.89E-02	1.63E-03
	7	0	1.94E-05	4.91E-03	4.91E-04	3.88E-02	6.27E-02
	8	4	1.70E-05	1.02E-01	1.02E-02	2.94E-02	1.23E-03
	9	24	1.21E-05	8.25E-01	8.25E-02	3.31E-02	1.42E-04
	10	27	2.33E-05	5.32E-01	5.32E-02	4.42E-02	2.24E-03
	11	2	3.40E-05	4.86E-02	4.86E-03	3.76E-02	4.82E-03
	12	2	3.88E-05	5.48E-02	5.48E-03	3.59E-02	1.80E-03
	13	3	4.85E-05	2.20E-02	2.20E-03	3.99E-02	1.84E-02
	14	2	1.75E-05	1.66E-03	1.66E-04	3.05E-02	6.66E-02
	15	2	4.85E-05	6.19E-03	6.19E-04	3.78E-02	3.87E-03
	16	14	2.91E-05	1.06E-01	1.06E-02	3.87E-02	1.37E-03
	17	14	1.94E-05	2.59E-01	2.59E-02	3.60E-02	1.19E-03
	18	1	1.46E-05	3.55E-02	3.55E-03	3.35E-02	3.52E-03
	19	3	3.11E-05	2.09E-02	2.09E-03	3.10E-02	3.14E-03
	21	43	1.46E-05	1.01E 1.0	1.00E-01	3.55E-02	1.75E-04
	22	19	3.88E-05	3.64E-01	3.64E-02	4.02E-02	1.01E-03
	23	31	1.16E-05	7.77E-01	7.77E-02	3.64E-02	1.38E-04
	24	2	1.70E-05	2.27E-02	2.27E-03	3.97E-02	2.77E-02

	25	2	3.88E-05	7.76E-04	7.76E-05	4.56E-02	1.82E-01
	26	3	4.37E-05	2.06E-02	2.06E-03	3.26E-02	7.77E-03
	27	0	2.43E-05	1.59E-03	1.59E-04	3.46E-02	1.89E-01
	28	1	2.43E-05	1.37E-02	1.37E-03	3.43E-02	4.13E-03
	29	2	3.88E-05	3.19E-02	3.19E-03	3.93E-02	1.69E-03
	30	4	1.75E-05	8.01E-02	8.01E-03	4.40E-02	6.84E-04
	31	36	2.91E-05	5.06E-01	5.06E-02	3.91E-02	3.50E-04
	32	9	1.94E-05	1.52E-01	1.52E-02	3.92E-02	1.11E-03
	33	22	1.16E-05	8.91E-01	8.91E-02	3.37E-02	2.37E-04
	34	43	1.75E-05	1.12E	1.12E-01	3.48E-02	2.75E-04
	35	2	2.33E-05	5.28E-03	5.28E-04	3.24E-02	1.35E-01
	36	5	4.85E-05	4.67E-02	4.67E-03	3.28E-02	2.03E-03
	37	5	4.85E-05	3.57E-02	3.57E-03	3.19E-02	4.29E-03
	38	7	2.33E-05	7.87E-02	7.87E-03	3.36E-02	8.37E-04
	39	2	4.85E-05	2.11E-02	2.11E-03	4.32E-02	1.24E-02
	40	6	4.85E-05	6.79E-02	6.79E-03	3.81E-02	1.28E-03

^{232}Th	^{147}Sm	FT Age (Ma)	2σ (Ma)	Etch	Dpar (µm)	Dper (µm)	U (ppm)
7.20E-03	7.45E-03	15.94	8.86	4	1.62	0.49	152.51
1.40E-02	2.06E-02	9.69	13.86	3	1.66	0.25	40.14
1.31E-02	1.36E-02	0	46.52	1	1.43	0	4.69
4.38E-01	8.56E-03	0	342.06	1	0.94	0.12	1.39
1.92E-01	1.00E	9.77	8.96	4	1.52	0.27	37.34
9.49E-03	5.79E-02	10.49	6.68	4	1.54	0.17	76.52
1.27E 1.	5.80E-01	0	255.14	0	-0.22	-0.09	1.68
4.41E-02	1.01E-02	19.08	19.48	4	1.35	0.18	34.94
2.21E-03	6.68E-03	19.81	9.04	4	1.6	0.18	282.64
3.12E-03	1.15E-02	18.01	7.84	4	1.67	0.51	182.18
1.61E-02	4.87E-03	10.01	14.3	3	1.35	0.2	16.66
3.20E-02	5.74E-02	7.77	11.1	2	1.82	0.17	18.78

4.98E-02	4.86E-02	23.19	27.2	4	1.73	0.35	7.54
6.31E-01	1.09E-01	547.12	781.78	2	1.53	0.4	0.57
5.97E-02	3.11E-01	54.9	78.44	2	1.52	0.23	2.12
3.58E-03	6.87E-03	37.28	21.34	4	2.03	0.56	36.45
1.67E-01	1.87E-02	22.99	13.16	4	1.8	0.5	88.77
4.25E-03	1.58E-02	16.01	32.18	1	1.18	0.16	12.15
2.56E-01	1.97E-02	38.19	44.78	3	1.42	0.02	7.15
2.22E-03	2.47E-01	24.09	8.84	4	1.69	0.51	346.91
6.81E-02	7.77E-03	11.13	5.6	4	1.71	0.19	124.52
9.38E-03	3.72E-03	28.28	11.68	4	1.51	0.18	266.24
1.26E-01	2.78E-02	42.7	61.02	2	0.97	0.2	7.79
2.54E	8.13E-02	527.17	753.26	3	1.19	0.04	0.27
1.49E-01	8.27E-02	27.57	32.32	2	1.74	0.23	7.05
5.38E-01	1.42E-01	0	613.32	0	-0.22	-0.09	0.54
1.82E 2.	3.70E-01	24.85	49.96	1	1.34	0.14	4.69
2.07E-02	3.42E-02	13.35	19.08	2	1.34	0.42	10.92
5.30E-03	7.13E-02	23.62	24.1	4	1.58	0.25	27.43
6.63E-03	1.93E-02	20.19	7.9	4	1.58	0.13	173.31
1.83E-02	5.68E-02	25.22	17.58	4	1.51	0.29	52.02
2.01E-02	6.33E-03	17.53	8.28	4	1.58	0.34	305.09
2.28E-03	1.06E+01	18.12	6.66	4	1.94	0.28	384.56
4.20E	1.43E	133.18	190.3	3	1.48	0.21	1.81
3.46E-01	1.72E-02	18.22	16.72	3	1.67	0.23	16.01
1.06E-02	1.78E-02	23.84	21.88	3	1.43	0.15	12.23
4.36E-03	8.23E-03	31.52	24.68	4	1.64	0.18	26.96
3.68E-02	3.53E-02	16.13	23.06	3	1.57	0.09	7.23
6.98E-03	1.71E-02	15.06	12.68	4	1.65	0.43	23.24

Th (ppm)	**Sm (ppm)**	**Pit Depth (µm)**
55.7	406.83	10.15

20.24	127.26	12.06
37.22	214.42	11.17
0.93	424.73	9.9
1.88	0.6	11.87
46.08	63.25	10.5
0.17	155.73	10.86
15.79	289.74	13.66
200.68	190.29	11.97
352.5	244.83	9.63
51.12	620.33	10.94
17.71	40.88	11.98
7.68	46.6	11.63
0.49	25.41	13.05
5.36	8.96	11.6
120.02	336.86	10.85
3.26	173.18	12.46
90.07	129.78	12.88
1.63	155.61	12.41
226.24	178.52	10.81
9.43	344.27	10.13
42.01	674.3	10.8
3.99	96.63	9.95
0.12	46.91	8.83
1.95	23.55	12.77
0.45	19.19	11.56
0.12	108.4	11.87
28	86.45	10.24
160.76	43.14	9.64
55.59	176.83	10.47

32.09	50.48	10.48
19.86	445.56	11.93
236.17	152.86	12.02
0.09	0.02	13.08
0.63	174.05	12.42
28.93	144.6	12.99
97.6	199.8	12.51
14.75	90.39	10.14
56.89	185.18	11.98
Mean Dpar	1.45	
Mean Dper	0.23	
Modified Zeta	16.56	0.344
Mean ^{29}Si b:s	0.037	
Mean ^{43}Ca b:s	0.037	
Mean ^{238}U b:s	0.021	
# of grains	39	
Chi-squared	86.6	
Chi-squared prob.	0	
Pooled Age (Ma)	**19.1**	**2.4**

(length data)

Sample#	Track #	Length (µm)	Etch	Dpar (µm)	Dper (µm)	Angle to c-axis (°)
KFC3	1	13.97	4	1.54	0.25	61.24
	2	13.65	3	1.44	0.12	24.19
	3	12.53	3	1.33	0.37	68.8
	4	14.05	4	1.26	0.23	36.21
	5	15.17	4	1.26	0.23	32.26
	6	12.45	4	1.26	0.23	50.79

7	8.87	4	1.26	0.23	66.26
8	14.51	4	1.33	0.18	54.64
9	15.09	4	1.34	0.26	34.94
10	11.01	4	1.34	0.26	71.92
11	11.42	2	1.27	0.14	52.93
12	11.36	2	1.27	0.14	55.58
13	15.25	4	1.34	0.29	65.69
14	14.56	4	1.34	0.29	45.81
15	10.1	4	1.34	0.29	65.99
16	12.16	4	1.34	0.29	39.22
17	11.37	3	1.71	0.1	48.22
18	13.89	4	1.57	0.14	69.4
19	9.92	4	1.57	0.14	69.99
20	12.25	4	1.21	0.21	63.22
21	14.79	4	1.21	0.21	48.86
22	13.84	1	0.19	1.55	55.33
23	13.52	1	0.19	1.55	42.02
24	16.49	4	1.44	0.07	23.84
25	16.51	4	1.44	0.07	39.46
26	8.87	4	1.57	0.28	57.79
27	14.04	4	1.43	0.24	67.01
28	14.77	4	1.43	0.24	28.36
29	15.21	4	1.53	0.12	60.01
30	13.58	4	1.41	0.15	70.7
31	16.27	3	1.19	0.16	41.27
32	14.27	3	1.19	0.16	53.32
33	13.53	4	1.38	0.18	33.19
34	14.57	4	1.72	0.21	31.54
35	13.21	4	1.72	0.21	48.8

	36	13.13	4	1.72	0.21	43.3
	37	15.01	4	1.28	0.2	53.31
	38	15.65	4	1.28	0.2	23.5
	39	13.54	4	1.2	0.04	70.19
	40	15.14	4	1.2	0.04	40.67
	41	15.63	4	1.2	0.04	41.36
	42	14.11	4	1.2	0.04	75.69
	43	12.36	4	1.2	0.04	59.41
	44	16.22	4	1.47	0.16	65.04
	45	14.03	4	1.47	0.16	50.07
	46	14.09	4	1.47	0.16	57.51
	47	10.04	4	1.47	0.16	57.73
	48	11.48	4	1.47	0.16	50.44
	49	12.96	4	1.47	0.16	89.97
	50	11.04	4	1.47	0.16	52.32
	51	9.07	4	1.47	0.16	69.8
	52	14.04	4	1.41	0.16	43.08
	53	15.47	4	1.46	0.26	45.37
	54	14.71	4	1.46	0.26	39.58
	55	14.16	4	1.46	0.26	58.74
	56	13.19	4	1.46	0.26	66.98
	57	13.16	4	1.76	0.2	81.42
Mean Dpar	1.36					
Mean Dper	0.23					
Mean Length (µm)	13.43	0.26				
Std. Dev. (µm)	1.93					
Skewness	-0.680					
Kurtosis	-0.240					

Sample#	Track #	Length (µm)	Etch	Dpar (µm)	Dper (µm)	Angle to c-axis (°)
KFC4	1	11.98	4	1.4	0.39	75.3
	2	14.53	4	1.61	0.29	82.65
	3	10.46	4	1.61	0.29	44.45
	4	12.58	4	1.61	0.29	45.91
	5	13.68	4	1.61	0.29	78.71
	6	10.98	4	1.43	0.3	60.9
	7	9.48	4	1.43	0.3	76.47
	8	13.61	4	1.43	0.3	42.19
	9	10.99	4	1.73	0.42	70.28
	10	13.77	4	1.73	0.42	47.88
	11	14.84	4	1.57	0.18	26.1
	12	14.42	4	1.57	0.18	76.78
	13	16.76	4	1.78	0.16	68.31
	14	14.13	4	1.78	0.16	62.27
	15	14.4	4	1.78	0.16	33.51
	16	14.54	4	1.92	0.2	33.94
	17	11.69	4	1.92	0.2	66.5
	18	13.8	4	1.92	0.2	33.1
	19	11.59	4	1.92	0.2	57.95
	20	14.65	4	1.92	0.2	22.29
	21	15.18	4	1.92	0.2	25.93
	22	12.1	4	1.92	0.2	59.9
	23	13.72	4	1.85	0.4	57.25
	24	13.28	4	1.85	0.4	82.35
	25	14.44	4	1.85	0.4	61.82
	26	15.24	4	1.85	0.4	49.97
	27	14.35	4	1.41	0.05	50.37
	28	13.22	4	1.78	0.18	67.71

29	15.61	2	1.77	0.25	53.58
30	15.23	2	1.77	0.25	53.26
31	13.77	2	1.77	0.25	67.19
32	15.15	4	1.66	0.14	34.16
33	10.81	4	1.66	0.14	67.74
34	15.82	4	1.48	0.07	51.75
35	12.2	4	1.84	0.07	27.04
36	15.21	4	1.59	0.11	38.8
37	12.44	4	1.48	0.15	61.76
38	15.16	4	1.48	0.15	44.9
39	12.96	4	1.48	0.15	55.09
40	13.85	4	1.48	0.15	71.52
41	9.47	4	1.48	0.15	52.54
42	15.14	4	1.48	0.15	44.46
43	13.25	4	1.48	0.15	50.79
44	15.23	4	1.48	0.15	70.72
45	13.73	4	1.48	0.15	58.34
46	13.95	4	1.65	0.2	45.87
47	12.67	4	1.65	0.2	75.74
48	11.01	4	1.66	0.12	74.19
49	10.27	4	1.66	0.12	70.07
50	14.87	4	1.58	0.14	80.18
51	11.87	4	1.58	0.14	62.54
52	11.44	4	1.61	0.14	62.86
53	13.37	4	1.61	0.14	27.12
54	11.54	4	1.61	0.14	77.97
55	14.69	4	1.48	0.1	78.98
56	14.21	4	1.23	0.19	85.94
57	11.28	4	1.23	0.19	73.98

58	15.36	4	1.58	0.23	50.55
59	11.12	3	1.73	0.29	42.88
60	14.31	4	1.57	0.18	74.07
61	8.64	4	1.57	0.18	67.25
62	10.69	4	1.57	0.18	52.39
63	11.97	4	1.71	0.37	80.56
64	14.09	4	1.71	0.37	36.37
65	14.02	4	1.71	0.37	64.77
66	13.38	4	1.67	0.34	46.25
67	13.08	4	1.67	0.34	75.84
68	13.91	4	1.97	0.24	51.73
69	8.84	4	1.97	0.24	63.41
70	13.14	4	1.72	0.2	49.38
71	9.71	4	1.72	0.2	86.77
72	14.79	4	1.57	0.21	62.56
73	14.35	4	1.57	0.21	61.11
74	14.68	4	1.57	0.21	61.91
75	15.55	4	1.57	0.21	43.75
76	14.44	4	1.57	0.21	28.08
77	13.69	4	1.57	0.21	38.64
78	16.37	4	1.57	0.21	32
79	14.76	4	1.57	0.21	39.84
80	16.08	4	1.57	0.21	13.16
81	13.04	4	1.57	0.21	53.74
82	10.6	4	1.57	0.21	58.64
83	8.84	4	1.57	0.21	78.8
84	12.85	4	1.57	0.21	46.41
85	14.57	4	1.6	0.21	63.33
86	16.41	4	1.6	0.21	1.26

87	13.9	4	1.6	0.21	47.75
88	14.14	4	1.53	0.4	63.32
89	12.18	4	1.6	0.53	55.45
90	12.43	4	1.6	0.53	71.4
91	15.26	4	1.24	0.16	69.98
92	14.55	4	1.9	0.19	54.99
93	16.6	4	1.9	0.19	40.51
94	13.71	4	1.9	0.19	42.59
95	12.75	4	1.9	0.19	58.51
96	13.55	4	1.41	0.09	60.39
97	13.83	4	1.98	0.57	51.24
98	13.24	4	1.98	0.57	44.62
99	14.2	4	1.98	0.57	63.23
100	13.05	4	1.98	0.57	55.35
101	10.06	4	1.98	0.57	76.17
102	11.44	4	1.98	0.57	68.59
103	14.2	4	1.57	0.33	59.08
104	9.76	4	1.57	0.33	58.61
105	9.69	4	1.57	0.33	70.45
106	14.63	4	1.57	0.33	33.53
107	14.88	4	1.67	0.16	55.54
108	15.31	4	1.67	0.16	60.79
109	11.86	4	1.67	0.16	45.46
110	16.12	4	1.67	0.16	50.4
111	8.75	4	1.67	0.16	52.43
112	11.86	4	1.58	0.33	44.38
113	13.51	4	1.58	0.33	60.13
114	13.85	4	1.58	0.33	62.17
115	12.63	4	1.58	0.33	41.89

116	13.52	4	1.58	0.33	72.03
117	15.42	4	1.19	0.28	74.39
118	10.1	4	1.86	0.28	58.88
119	9.41	4	1.86	0.28	80.06
120	13.56	4	1.9	0.11	63.2
121	13.58	4	1.9	0.11	56.75
122	12.97	4	1.65	0.14	56.13
123	12.9	4	1.65	0.14	69.27
124	11.48	4	1.65	0.14	45.07
125	15.02	3	1.57	0.31	62.84
126	16.49	4	1.5	0.31	73.81
127	12.97	4	1.5	0.31	39.07
128	14.68	4	1.5	0.31	34.67
129	13.36	4	1.5	0.31	63.55
130	14.31	4	1.41	0.12	89.09
131	15.51	4	1.41	0.12	46.14
132	15.06	4	1.78	0.23	41.46
133	13.38	4	1.78	0.23	51.33
134	12.81	4	1.43	0.3	71.55
135	13.47	4	1.84	0.3	32.31
136	13.35	4	1.54	0.19	32.7
137	13.11	4	1.54	0.19	57.18
138	15.75	2	1.23	0.18	82.35
139	16.28	2	1.23	0.18	43.3
140	15.65	4	1.57	0.1	43.99
141	12.27	4	1.57	0.1	80.62
142	13.49	4	1.57	0.1	63.77
143	14.62	4	1.77	0.21	23.77
144	9.73	4	1.77	0.21	88.18

145	16.11	4	1.77	0.21	37.19
146	6.42	4	1.77	0.21	72.73
147	16.24	4	1.77	0.21	19.69
148	15.44	4	1.77	0.21	39.41
149	14.53	4	1.77	0.21	24.48
150	11.3	4	1.55	0.2	52.35
151	12.6	4	1.55	0.2	45.76
152	13.54	4	1.55	0.2	74.61
153	14.26	4	1.66	0.31	48.69
154	11.08	4	1.45	0.11	87.71
155	12.88	4	1.45	0.11	64.63
156	12.89	4	1.45	0.11	77.21
157	12.57	4	1.44	0.28	64.94
158	14.58	4	1.73	0.23	46.14
159	8.97	4	1.73	0.23	83.47
160	13.27	4	1.73	0.23	85.68
161	12.93	4	1.48	0.24	86.03
162	6.54	4	1.48	0.24	66.74
163	16.34	4	1.67	0.25	26.41
164	15.66	4	1.76	0.2	25.8
165	9.76	4	1.65	0.21	71.16
166	14.23	4	1.61	0.2	88.02
167	14.82	4	1.61	0.2	19.78
168	12.27	4	1.61	0.2	35.68
169	11.24	4	1.45	0.09	63.31
170	12.41	4	1.45	0.09	68.1
171	16.33	4	1.41	0.3	56.06
172	13.3	4	1.41	0.3	64.66
173	14.33	4	1.41	0.3	73.17

	174	14.71	4	1.58	0.29	73.86
	175	14.23	4	1.58	0.29	57.18
	176	14.89	4	1.58	0.29	25.2
	177	12.66	4	1.58	0.29	31.4
	178	13.15	4	1.58	0.29	82.22
	179	11.12	4	1.58	0.29	52.02
	180	12.6	4	1.58	0.29	55.54
	181	12.02	4	1.58	0.29	60.31
	182	11.53	4	1.58	0.29	59.52
	183	15.58	4	1.72	0.23	65.76
	184	16.77	4	1.72	0.23	16.56
	185	12.94	4	1.72	0.23	77.44
	186	15.68	4	1.72	0.23	56.85
	187	13.07	4	1.72	0.23	81.1
	188	14.97	4	1.72	0.23	49.57
	189	15.43	4	1.73	0.2	33.78
	190	15	4	2.08	0.26	44.15
	191	15.37	4	1.57	0.16	35.66
	192	16.45	4	1.57	0.16	23.94
	193	13.11	4	1.6	0.35	73.93
	194	13.77	4	1.6	0.35	64.25
	195	15.06	4	1.6	0.35	37.18
	196	14.96	4	1.6	0.35	47.2
	197	15.84	4	1.6	0.35	33.55
	198	14.85	1	1.39	0.43	34.09
	199	12.41	1	1.39	0.43	65.89
	200	15.3	1	1.39	0.43	16.51

Mean Dpar 1.63

Mean Dper	0.24	
Mean Length (µm)	13.4	0.14
Std. Dev. (µm)	1.980	
Skewness	-0.820	
Kurtosis	0.600	

Kunlun Fault East (KFE)

Apatite (U-Th)/He: vertical transect

Sample #	U (ppm)	Th (ppm)	He (nmol/g)	Mass (µg)	Radius (µm)	Length (µm)	F_T
$KFE5_A$	84.51	91.08	3.62	1.68	48.50	124.50	0.69
$KFE5_B$	34.35	52.81	4.38	2.45	51.00	178.50	0.72
$KFE5_C$	19.37	99.37	2.58	2.65	44.00	132.00	0.66
$KFE5_D$	27.43	74.34	7.16	2.86	51.00	294.00	0.74
$KFE6_A$	82.90	67.17	4.36	5.78	58.00	358.50	0.78
$KFE6_B$	87.62	96.22	4.82	1.65	42.00	172.50	0.68
$KFE6_C$	92.75	93.35	4.92	1.74	50.50	163.50	0.72
$KFE6_D$	96.18	103.09	5.94	2.03	45.50	189.00	0.70
$KFE7_A$†	7.91	21.28	2.94	2.41	44.00	228.00	0.69
$KFE7_B$	52.75	106.75	4.57	1.97	40.50	256.50	0.68
$KFE7_C$	55.47	103.72	3.94	1.73	47.50	147.00	0.69
$KFE7_D$	78.72	45.02	6.19	1.69	45.50	142.50	0.69
$KFE8_A$	29.55	41.07	2.55	2.36	54.50	187.50	0.74
$KFE8_B$	32.58	45.95	3.69	1.78	44.00	174.00	0.69
$KFE8_C$	47.72	75.35	3.59	1.33	42.50	145.50	0.67
$KFE8_D$	89.45	88.37	1.26	1.76	40.00	184.50	0.67
$KFE9_A$	50.29	101.35	3.97	1.67	44.50	162.00	0.68
$KFE9_B$	49.08	88.36	2.94	1.33	41.50	159.00	0.67

$KFE9_C$	53.76	99.41	4.56	1.87	43.50	193.50	0.69
$KFE9_D$†	22.65	35.03	5.94	2.07	53.00	130.50	0.71

Sm (ppm)	Raw Age (Ma)	Corrected Age (Ma)	Elevation (m)
362.58	6.26	9.03	4428
321.63	17.05	23.57	
556.18	10.92	16.40	
730.41	28.73	38.70	
310.26	8.10	10.44	4259
355.99	8.01	11.78	
339.00	7.86	10.95	
347.52	9.04	12.86	
195.97	41.05	58.56	4091
452.16	10.71	15.66	
434.35	9.02	12.95	
336.11	12.69	18.36	
272.74	11.85	16.02	3841
313.74	15.50	22.43	
360.36	10.02	14.91	
345.27	2.09	3.11	
434.88	9.79	14.26	3659
466.60	7.68	11.46	
435.61	10.80	15.63	
273.26	34.90	48.90	

Apatite Fisson Track: vertical transect (age data)

Sample#	Grain #	N_s	Area (cm x cm)	$^{238}U/^{43}Ca$ (dmnls)	1σ (dmnls)	^{43}Ca	^{238}U

KFE5	1	106	3.40E-05	2.12E-01	6.37E-03	1.00E-01	2.04E-01
	2	4	1.94E-05	1.59E-01	4.82E-03	1.04E-01	4.40E-01
	3	5	2.91E-05	7.44E-02	2.35E-03	7.39E-02	9.94E-02
	4	19	4.85E-05	1.12E-01	3.27E-03	5.74E-02	1.46E-01
	5	7	2.33E-05	4.03E-01	1.16E-02	3.60E-02	3.52E-02
	6	20	4.85E-05	1.43E-01	3.91E-03	3.67E-02	3.73E-02
	7	13	3.88E-05	2.80E-01	7.82E-03	4.97E-02	8.76E-02
	8	2	3.88E-05	1.19E-01	3.46E-03	2.92E-02	2.59E-02
	9	15	1.94E-05	3.20E-02	1.03E-03	5.36E-02	1.94E-02
	10	14	3.40E-05	3.63E-01	1.19E-02	3.19E-02	3.11E-02
	11	8	2.91E-05	2.30E-01	7.28E-03	3.85E-02	1.11E-01
	12	3	3.88E-05	5.08E-02	1.54E-03	2.17E-02	1.26E-02
	13	14	3.11E-05	1.58E-01	4.80E-03	3.26E-02	8.51E-02
	14	16	3.40E-05	3.12E-01	9.70E-03	6.90E-02	2.29E-01
	15	20	2.91E-05	4.36E-01	1.26E-02	7.18E-02	2.73E-01
	16	5	2.43E-05	1.54E-01	4.91E-03	4.50E-02	6.80E-02
	17	9	4.85E-05	9.61E-02	2.79E-03	1.20E-01	1.51E-01
	18	11	2.91E-05	2.31E-01	6.73E-03	6.36E-02	1.22E-01
	19	14	3.40E-05	2.77E-01	7.66E-03	1.18E-01	3.23E-01
	21	8	3.40E-05	1.54E-02	5.02E-04	5.68E-02	2.29E
	22	0	2.91E-05	3.74E-02	1.22E-03	1.31E-01	7.38E-01
	23	31	4.85E-05	2.70E-01	7.92E-03	6.18E-02	9.41E-02
	24	6	3.88E-05	2.07E-01	6.15E-03	9.01E-02	1.85E-01
	25	10	4.37E-05	2.09E-01	4.48E-03	8.61E-01	9.73E-01

^{232}Th	^{147}Sm	FT Age (Ma)	2σ (Ma)	Etch	Dpar (µm)	Dper (µm)	U (ppm)
1.49E-01	1.28E-01	100.49	20.86	4	1.23	0.3	89.54
1.50E-01	1.27E-01	8.88	8.9	4	1.62	0.38	67.39
4.51E-02	2.93E-02	15.84	14.22	4	0.1	1.22	31.47
3.93E-02	3.50E-02	24.07	11.18	4	1.78	0.38	47.17

3.13E-02	2.36E-02	5.13	3.9	3	1.45	0.14	170.3
3.12E-02	2.60E-02	19.84	8.98	4	1.25	0.16	60.26
1.82E-02	1.80E-02	8.22	4.6	3	1.45	0.27	118.3
2.84E-02	2.04E-02	2.96	4.2	3	1.54	0.37	50.51
2.11E-02	6.49E-02	163.63	85.42	2	2.86	1.6	13.55
1.92E-02	2.19E-02	7.79	4.2	3	1.52	0.38	153.62
5.67E-02	3.43E-02	8.2	5.84	2	1.88	0.3	97.29
2.22E-02	1.21E-02	10.45	12.08	2	1.22	0.28	21.48
2.03E-02	1.53E-02	19.61	10.58	4	1.8	0.31	66.7
6.09E-02	5.00E-02	10.38	5.24	4	1.61	0.18	131.75
1.05E-01	9.05E-02	10.83	4.9	4	1.32	0.18	184.17
5.88E-02	4.11E-02	9.18	8.24	3	1.53	0.26	65.19
1.10E-01	7.69E-02	13.25	8.88	4	1.41	0.26	40.65
1.02E-01	7.10E-02	11.23	6.82	3	1.14	0.1	97.67
1.15E-01	1.01E-01	10.23	5.52	3	1.59	0.25	116.93
7.44E-02	5.27E-02	104.1	74.04	3	1.44	0.06	6.52
1.01E-01	9.69E-02	0	18.9	1	1.55	0.47	15.82
5.11E-02	4.42E-02	16.23	5.94	4	1.52	0.26	114.22
8.95E-02	7.67E-02	5.14	4.22	2	1.5	0.35	87.34
9.83E-01	1.05E	7.52	4.78	2	1.3	0.28	88.41

Th (ppm)	Sm (ppm)	Pit Depth (µm)
173.29	113.82	18.06
152.8	574.67	16.44
57.59	388.16	16.81
86.52	437.75	13.62
132.58	532.95	12.7
104.28	450.83	12.26
156.14	557.58	12.15
29.92	324.01	14.64

31.98	22.03	13.24
155.96	529.54	16.65
198.89	671.88	16.9
36.21	259.63	16.16
120.31	507.2	16.06
183.48	627.69	16.78
159.11	691.07	15.61
119.54	504.22	16.3
33.13	327.75	15.12
174.07	618.44	15.1
62.27	479.79	14.2
36.06	304.91	14.38
41.6	290.21	14.7
56.86	404.14	15.69
93.87	450.47	14.81
178.01	565.13	8.26
Mean Dpar	1.48	
Mean Dper	0.36	
Modified Zeta	13.75	0.285
Mean ^{29}Si b:s	0.098	
Mean ^{43}Ca b:s	0.070	
Mean ^{238}U b:s	0.282	
# of grains	24	
Chi-squared	503.6	
Chi-squared prob.	0	
Pooled Age (Ma)	**15.90**	**1.8**

Sample#	**Grain #**	**N_s**	**Area (cm x cm)**	**^{238}U/^{43}Ca (dmnls)**	**1σ (dmnls)**	**^{43}Ca**	**^{238}U**

KFE6	1	4	1.75E-05	3.35E-01	1.00E-02	3.56E-02	1.15E-01
	2	20	3.40E-05	2.93E-01	9.24E-03	3.29E-02	2.22E-01
	3	84	3.88E-05	2.75E-01	8.40E-03	3.84E-02	1.02E-01
	4	17	3.88E-05	2.89E-01	9.73E-03	3.16E-02	3.25E-02
	5	20	3.11E-05	4.81E-01	1.45E-02	2.90E-02	8.13E-02
	6	14	4.85E-05	1.27E-01	3.98E-03	1.14E-01	4.19E-01
	7	16	4.85E-05	8.68E-02	2.58E-03	5.64E-02	3.15E-01
	8	23	3.11E-05	3.03E-01	9.43E-03	5.26E-02	3.01E-01
	9	13	2.91E-05	5.23E-01	1.52E-02	4.71E-02	7.40E-02
	10	23	4.85E-05	2.32E-01	7.40E-03	4.57E-02	6.93E-02
	11	32	1.46E-05	3.10E-01	9.66E-03	7.01E-02	8.21E-02
	12	44	1.75E-05	4.68E-01	1.36E-02	3.52E-02	1.35E-01
	13	48	1.36E-05	3.77E-01	1.22E-02	5.19E-02	1.22E-01
	14	7	1.46E-05	3.46E-01	1.11E-02	5.20E-02	1.06E-01
	15	43	2.91E-05	1.90E-01	5.96E-03	3.46E-02	3.74E-02
	16	13	2.91E-05	3.98E-01	1.10E-02	5.41E-02	1.12E-01
	17	9	2.91E-05	2.07E-01	6.43E-03	4.36E-02	1.83E-01
	18	7	3.88E-05	3.06E-01	9.61E-03	6.97E-02	8.57E-02
	19	10	3.11E-05	4.04E-01	1.31E-02	5.15E-02	9.17E-02
	20	70	3.11E-05	1.99E-01	5.73E-03	5.02E-02	1.16E-01
	21	38	2.91E-05	1.11E-01	3.48E-03	8.54E-02	3.03E-01
	22	76	2.43E-05	2.51E-01	7.41E-03	8.19E-02	1.09E-01
	23	17	3.88E-05	2.98E-01	9.21E-03	4.04E-02	4.56E-02
	24	24	3.88E-05	3.39E-01	9.98E-03	6.38E-02	5.93E-02
	25	3	2.91E-05	8.92E-02	2.66E-03	1.12E-01	2.12E-01

^{232}Th	^{147}Sm	FT Age (Ma)	2σ (Ma)	Etch	Dpar (µm)	Dper (µm)	U (ppm)
2.56E-02	1.68E-02	4.7	4.72	3	1.51	0.29	141.48
2.17E-02	1.63E-02	13.82	6.26	4	1.56	0.3	123.69
1.09E-01	7.28E-02	53.96	12.42	4	1.6	0.47	116.03

2.61E-02	2.24E-02	10.43	5.12	4	1.55	0.14	121.9
3.16E-02	1.95E-02	9.21	4.18	3	1.12	0.29	203.01
9.86E-02	6.80E-02	15.63	8.44	3	1.47	0.15	53.57
1.27E-01	7.54E-02	26.08	13.18	3	1.28	0.07	36.66
5.07E-02	4.72E-02	16.78	7.1	3	1.65	0.35	128.07
5.67E-02	5.23E-02	5.87	3.28	3	1.64	0.26	220.98
5.94E-02	4.23E-02	14.04	5.96	3	1.45	0.32	97.97
6.14E-02	5.56E-02	48.64	17.58	4	1.35	0.22	130.82
4.22E-02	4.47E-02	36.92	11.44	4	1.61	0.33	197.69
4.77E-02	3.81E-02	64.18	19.16	3	1.54	0.11	159.15
5.18E-02	6.01E-02	9.55	7.26	2	1.51	0.12	146.13
3.42E-02	4.18E-02	53.25	16.72	1	1.77	0.3	80.27
6.91E-02	5.29E-02	7.73	4.32	2	1.65	0.45	167.83
5.41E-02	5.04E-02	10.25	6.88	2	1.6	0.29	87.56
6.02E-02	7.24E-02	4.05	3.08	2	1.65	0.21	129.24
5.62E-02	4.03E-02	5.48	3.5	3	1.58	0.19	170.57
5.55E-02	7.14E-02	77.46	19.32	4	1.59	0.25	84.05
3.97E-02	3.79E-02	80.16	26.68	4	1.61	0.4	47.02
5.40E-02	4.88E-02	85.3	20.5	4	1.52	0.3	106.01
2.75E-02	2.55E-02	10.1	4.96	3	1.5	0.14	125.94
6.23E-02	9.40E-02	12.54	5.2	2	1.51	0.23	143.1
7.94E-02	6.43E-02	7.95	9.2	2	1.64	0.34	37.65

Th (ppm)	Sm (ppm)	Pit Depth (µm)
136.57	479.62	15.57
222.14	538.11	16.21
64.03	77.92	16.03
169.75	571.39	15.71
264.87	642.14	15.47
34.69	267.65	14.56

30.04	217.81	14.78
137.71	468.34	15.93
220.38	568.44	14.86
83.67	361.11	15.81
249.02	138.04	15.31
277.17	159.67	16.49
212.44	125.89	16.53
199.43	478.25	17.04
201.34	107.54	14.93
279.19	667.75	15.28
99.54	356.54	15.51
118.2	442.33	15.15
286.48	720.53	15.73
115.38	88.71	14.8
162.58	128.56	14.51
220.85	161.2	14.39
192.68	496.76	15.17
111.83	443.44	14.06
76.31	392.48	13.14
Mean Dpar	1.54	
Mean Dper	0.26	
Modified Zeta	13.768	0.284
Mean ^{29}Si b:s	0.055	
Mean ^{43}Ca b:s	0.055	
Mean ^{238}U b:s	0.141	
# of grains	25	
Chi-squared	634.6	
Chi-squared prob.	0.0000	

Pooled Age (Ma)	21.90	2.0					
Sample#	**Grain #**	**N_s**	**Area (cm x cm)**	**$^{238}U/^{43}Ca$ (dmnls)**	**1σ (dmnls)**	**^{43}Ca**	**^{238}U**
KFE7	2	0	1.75E-05	2.27E-02	7.27E-04	1.04E-01	2.97E-01
	3	5	4.85E-05	1.16E-01	3.35E-03	8.76E-02	1.97E-01
	4	2	1.75E-05	1.93E-01	6.32E-03	1.11E-01	1.95E-01
	5	1	4.85E-05	3.07E-02	8.59E-04	8.08E-02	4.28E-01
	6	2	2.43E-05	2.53E-01	6.73E-03	4.32E-02	7.46E-02
	7	3	2.91E-05	1.49E-01	4.47E-03	5.32E-02	7.67E-02
	8	1	3.11E-05	2.55E-05	1.72E-06	5.37E-02	4.26E
	9	2	1.75E-05	2.73E-01	8.52E-03	3.78E-02	5.01E-02
	10	1	1.75E-05	4.56E-02	1.46E-03	8.71E-02	1.92E-01
	11	1	4.85E-05	2.50E-02	7.06E-04	4.85E-02	1.83E-01
	12	3	3.11E-05	4.55E-02	1.22E-03	7.60E-02	5.51E-01
	13	5	1.75E-05	3.09E-01	8.90E-03	4.14E-02	5.82E-02
	14	0	2.62E-05	2.30E-01	7.36E-03	4.42E-02	1.27E-01
	15	2	2.91E-05	6.93E-02	2.17E-03	4.39E-02	8.91E-02
	16	7	2.91E-05	3.10E-01	8.28E-03	3.72E-02	2.60E-02
	17	2	2.18E-05	5.00E-02	1.48E-03	4.33E-02	7.07E-02
	18	1	2.91E-05	5.75E-02	1.78E-03	6.27E-02	1.74E-01
	19	12	3.88E-05	2.06E-01	6.14E-03	3.49E-02	5.13E-03
	20	0	1.75E-05	4.86E-02	1.39E-03	3.13E-02	1.71E-01
	21	1	2.91E-05	7.06E-02	2.14E-03	3.60E-02	2.78E-01
	22	2	1.21E-05	6.80E-02	2.05E-03	3.15E-02	1.01E-01
	23	10	3.88E-05	2.34E-01	7.55E-03	6.32E-02	9.67E-02
	24	5	2.91E-05	2.57E-01	7.22E-03	9.53E-02	5.14E-02
	25	55	4.85E-05	3.38E-01	9.61E-03	5.95E-02	8.43E-02
^{232}Th	**^{147}Sm**	**FT Age (Ma)**	**2σ (Ma)**	**Etch**	**Dpar (µm)**	**Dper (µm)**	**U (ppm)**

1.38E-01	1.68E-01	0	51.86	1	1.35	0.25	9.59
1.03E-01	9.16E-02	6.11	5.48	2	1.73	0.19	49
9.79E-02	8.63E-02	4.09	5.78	2	1.27	0.16	81.4
8.61E-02	7.86E-02	4.62	9.24	3	1.59	0.08	12.96
5.16E-02	3.59E-02	2.24	3.18	2	1.42	0.13	106.74
7.75E-02	5.97E-02	4.75	5.5	2	1.58	0.17	62.98
2.74E-01	1.97E-01	5506.58	11040.42	1	1.4	0.01	0.01
3.96E-02	2.58E-02	2.9	4.1	2	1.44	0.25	114.91
1.49E-01	7.96E-02	8.65	17.32	1	1.4	0.33	19.21
7.78E-02	6.29E-02	5.69	11.38	1	1.2	0.1	10.52
7.37E-02	7.22E-02	14.6	16.9	3	1.37	0.16	19.2
6.16E-02	4.36E-02	6.38	5.72	3	1.53	0.21	130.29
1.09E-02	1.41E-02	0	3.44	2	1.29	0.23	96.91
7.29E-02	5.03E-02	6.83	9.68	2	1.39	0.24	29.2
2.69E-02	1.37E-02	5.34	4.06	3	1.3	0.12	130.66
8.97E-02	4.24E-02	12.6	17.84	2	1.65	0.12	21.09
7.75E-02	7.08E-02	4.11	8.24	2	1.33	0.33	24.24
9.15E-03	8.16E-03	10.31	6	4	1.74	0.14	87.04
3.03E-02	1.53E-02	0	24.3	1	1.44	0.25	20.5
4.09E-02	4.19E-02	3.35	6.7	1	1.55	0.29	29.77
3.06E-02	2.09E-02	16.69	23.64	1	1.2	0.37	28.66
6.42E-02	6.49E-02	7.58	4.82	3	1.41	0.16	98.7
2.81E-02	2.36E-02	4.6	4.12	2	1.41	0.12	108.36
6.97E-02	5.02E-02	23.04	6.42	4	1.46	0.52	142.69

Th (ppm)	**Sm (ppm)**	**Pit Depth (µm)**
12.19	73.36	16.53
89.34	509.95	16.24
193.44	819.11	16.83
22.71	280.59	12.62

197.19	713.54	12.32
111.37	653.5	16.89
2.11	19.2	16
259.49	891.11	15.38
26.4	291.72	14.94
6.06	30.54	14.85
48.6	355.48	11.42
159.29	754.23	14.98
123.82	598.25	15.77
13.6	50.87	13.6
283.51	848.69	11.21
29.17	331.07	13.57
42.69	398.78	15.46
186.35	682.6	12.09
31.84	368.61	11.73
45.34	385.17	13.65
35.99	413.09	14.94
177.12	646.57	15.89
236.03	812.12	12.58
62.44	185.61	14.32
Mean Dpar	1.44	
Mean Dper	0.21	
Modified Zeta	13.79	0.283
Mean ^{29}Si b:s	0.059	
Mean ^{43}Ca b:s	0.059	
Mean ^{238}U b:s	0.327	
# of grains	24	
Chi-squared	117.2	

Chi-squared prob.	0	
Pooled Age (Ma)	**8.50**	**1.6**

Sample#	**Grain #**	**N_s**	**Area (cm x cm)**	**$^{238}U/^{43}Ca$ (dmnls)**	**1σ (dmnls)**	**^{43}Ca**	**^{238}U**
KFE8	1	2	2.33E-05	2.17E-01	7.57E-03	3.21E-02	1.44E-01
	2	2	3.88E-05	6.13E-02	1.91E-03	5.28E-02	6.16E-02
	3	1	1.21E-05	6.98E-02	1.93E-03	6.91E-02	7.05E-01
	6	3	3.88E-05	9.39E-02	2.50E-03	8.79E-02	9.92E-02
	7	5	3.88E-05	2.76E-02	9.37E-04	8.43E-02	9.42E-01
	8	4	4.37E-05	9.29E-02	2.86E-03	2.45E-01	5.45E-01
	9	3	3.88E-05	9.30E-02	3.04E-03	4.53E-02	1.14E-01
	10	1	2.91E-05	4.57E-02	1.44E-03	2.83E-02	1.47E-01
	11	3	3.40E-05	1.04E-01	3.07E-03	8.48E-02	1.39E-01
	12	7	3.88E-05	1.89E-01	5.58E-03	5.06E-02	8.96E-02
	13	6	3.40E-05	1.33E-01	3.69E-03	4.76E-02	5.35E-02
	14	0	3.40E-05	7.94E-02	2.39E-03	6.54E-02	2.26E-01
	15	3	2.91E-05	1.03E-01	3.60E-03	3.53E-02	1.00E-01
	16	9	3.88E-05	2.24E-01	7.03E-03	7.99E-02	1.21E-01
	17	6	3.88E-05	8.89E-02	2.69E-03	4.24E-02	5.06E-02
	18	5	3.40E-05	1.39E-01	4.35E-03	4.61E-02	1.99E-02
	19	0	1.75E-05	1.41E-01	4.16E-03	8.85E-02	1.05E-01
	20	4	4.37E-05	1.33E-01	4.27E-03	3.53E-02	4.33E-02
	21	2	3.11E-05	9.28E-02	2.78E-03	3.48E-02	6.31E-02
	22	2	1.75E-05	4.88E-02	1.35E-03	3.26E-02	4.77E-02
	23	0	2.43E-05	1.98E-01	5.63E-03	3.82E-02	8.13E-02
	24	7	3.88E-05	8.52E-02	2.34E-03	1.15E-01	3.48E-01
	25	1	2.91E-05	7.26E-02	2.28E-03	4.15E-02	1.72E-01

^{232}Th	**^{147}Sm**	**FT Age (Ma)**	**2σ (Ma)**	**Etch**	**Dpar (µm)**	**Dper (µm)**	**U (ppm)**

3.16E-02	3.41E-02	2.73	3.86	2	1.53	0.35	91.44
3.28E-02	6.21E-02	5.8	8.22	3	1.56	0.4	25.8
2.34E-01	1.06E-01	8.15	16.3	1	1.67	0.19	29.37
4.68E-02	4.86E-02	5.68	6.56	2	1.39	0.25	39.53
1.09E-01	7.59E-02	32.1	28.82	2	1.39	0.21	11.63
3.66E-01	3.67E-01	6.8	6.82	3	1.54	0.37	39.1
3.05E-02	2.93E-02	5.73	6.64	2	1.51	0.19	39.13
2.02E-02	1.59E-02	5.18	10.38	2	1.59	0.35	19.25
8.34E-02	9.38E-02	5.84	6.76	2	1.4	0.25	43.96
4.93E-02	2.81E-02	6.59	5	2	1.43	0.24	79.4
4.94E-02	2.66E-02	9.14	7.5	3	1.46	0.22	56.09
7.78E-02	4.36E-02	0	7.68	2	1.2	0.22	33.41
4.70E-02	3.86E-02	6.91	8	2	1.35	0.31	43.28
9.61E-02	8.34E-02	7.13	4.78	4	1.5	0.17	94.45
4.87E-02	4.04E-02	11.99	9.82	2	1.38	0.35	37.42
2.29E-02	1.82E-02	7.33	6.58	2	1.67	0.23	58.34
4.84E-02	5.62E-02	0	8.42	1	1.47	0.23	59.28
3.92E-02	2.41E-02	4.74	4.74	2	1.35	0.12	56.18
2.24E-02	1.52E-02	4.79	6.78	2	1.46	0.35	39.06
2.23E-02	1.29E-02	16.17	22.9	2	1.61	0.16	20.55
2.95E-02	2.15E-02	0	4.3	1	1.81	0.29	83.54
1.21E-01	9.69E-02	14.58	11.06	2	1.36	0.04	35.89
5.81E-02	3.39E-02	3.26	6.52	1	1.41	0.31	30.58

Th (ppm)	**Sm (ppm)**	**Pit Depth (µm)**
108.72	494.52	16.4
45.04	331.94	16.41
83.73	515.76	11.82
75.59	454.29	11.54
31.94	311.86	15.55

82.89	428.69	13.46
70.81	451.74	15.61
33.66	358.72	15.07
79.13	445.74	13.9
166.44	591.28	15.49
118.08	617.45	11.21
33.21	292.28	16.49
65.89	475.27	17.59
223.79	682.48	15.82
68.2	485.97	16.82
97.51	487.62	16.24
110.89	707.1	14.87
111.88	655.13	14.82
30.47	313.14	14.94
36.38	363.88	11.9
143.14	635.88	11.82
66.54	422.53	11.78
47.13	382.93	15.94
Mean Dpar	1.48	
Mean Dper	0.25	
Modified Zeta	13.808	0.282
Mean ^{29}Si b:s	0.064	
Mean ^{43}Ca b:s	0.064	
Mean ^{238}U b:s	0.192	
# of grains	23	
Chi-squared	25.6	
Chi-squared prob.	0.2714	
Pooled Age (Ma)	**6.40**	**1.4**

Sample#	Grain #	N_s	Area (cm x cm)	$^{238}U/^{43}Ca$ (dmnls)	1σ (dmnls)	^{43}Ca	^{238}U
KFE9	1	5	4.85E-05	2.02E-01	6.85E-03	5.25E-02	5.47E-02
	2	1	1.94E-05	5.57E-02	1.78E-03	9.22E-02	1.28E-01
	3	6	3.40E-05	2.16E-01	6.35E-03	5.68E-02	1.43E-01
	4	2	3.88E-05	1.38E-01	4.70E-03	6.22E-02	1.22E-01
	5	0	1.94E-05	2.49E-02	7.60E-04	1.99E	1.51E
	6	0	1.75E-05	4.97E-02	1.30E-03	1.66E-01	6.07E-01
	7	2	1.36E-05	8.23E-02	2.29E-03	6.21E-02	1.91E-01
	8	10	4.37E-05	1.45E-01	3.89E-03	9.62E-02	9.84E-02
	9	0	1.75E-05	1.04E-01	2.99E-03	7.46E-02	9.01E-02
	10	1	1.16E-05	1.04E-01	2.93E-03	1.31E-01	4.14E-01
	11	1	3.11E-05	3.11E-02	9.33E-04	5.66E-02	1.15E-01
	12	6	2.33E-05	1.21E-01	3.36E-03	4.59E-02	5.90E-02
	13	2	4.37E-05	5.28E-02	1.50E-03	4.18E-02	4.16E-02
	14	14	2.91E-05	8.87E-02	2.44E-03	9.43E-02	2.71E-01
	15	2	3.40E-05	5.63E-02	1.60E-03	9.49E-02	8.77E-02
	16	1	3.40E-05	1.34E-01	3.72E-03	1.26E-01	1.80E-01
	17	1	1.46E-05	1.70E-01	5.00E-03	9.35E-02	3.63E-01
	18	0	1.21E-05	2.02E-02	6.24E-04	1.59E-01	1.16E
	19	0	1.36E-05	5.25E-02	1.43E-03	4.64E-02	6.37E-02
	20	1	2.04E-05	5.33E-02	1.61E-03	8.68E-02	5.46E-01
	21	5	2.91E-05	1.89E-01	5.30E-03	1.48E-01	2.01E-01
	22	0	1.94E-05	2.67E-02	7.45E-04	9.49E-02	1.05E-01
	23	0	2.43E-05	5.64E-02	1.52E-03	5.89E-02	3.63E-02
	24	1	2.91E-05	3.42E-01	1.04E-02	6.90E-02	8.08E-02
	25	0	3.11E-05	1.02E-02	3.01E-04	4.45E-02	1.39E-01
^{232}Th	**^{147}Sm**	**FT Age (Ma)**	**2σ (Ma)**	**Etch**	**Dpar (µm)**	**Dper (µm)**	**U (ppm)**

4.70E-02	3.36E-02	3.52	3.16	3	1.35	0.25	84.99
1.49E-01	9.57E-02	6.39	12.78	2	1.41	0.22	23.42
5.10E-02	5.03E-02	5.65	4.64	2	1.25	0.13	90.79
4.75E-02	4.15E-02	2.58	3.66	3	1.38	0.15	58
3.16E	3.41E	0	42.78	1	1.18	0.06	10.46
2.14E-01	1.93E-01	0	23.84	1	1.34	0.54	20.9
5.61E-02	5.26E-02	12.34	17.48	1	1.03	0	34.61
8.14E-02	6.29E-02	10.9	6.94	3	1.48	0.07	60.98
8.49E-02	6.39E-02	0	11.36	1	1.32	0.06	43.86
1.02E-01	8.30E-02	5.73	11.46	1	1.24	0.39	43.53
3.81E-02	4.12E-02	7.15	14.32	2	1.27	0.32	13.07
1.24E-01	3.82E-02	14.74	12.08	2	1.44	0.09	50.72
4.58E-02	4.00E-02	6	8.5	1	1.91	0.18	22.18
6.61E-02	5.72E-02	37.36	20.14	2	1.61	0.12	37.29
8.12E-02	9.17E-02	7.22	10.22	1	1.06	0.19	23.68
2.60E-01	1.42E-01	1.52	3.04	1	1.4	0.19	56.21
9.05E-02	7.85E-02	2.79	5.58	2	1.11	0.1	71.61
0.00E	1.40E-01	0	84.04	1	1.19	0.43	8.49
4.53E-02	2.68E-02	0	29	1	1.27	0.28	22.08
1.50E-01	1.20E-01	6.36	12.74	2	1.49	0.29	22.4
1.70E-01	1.25E-01	6.28	5.64	3	1.46	0.19	79.36
0.00E	1.54E-01	0	39.92	1	1.27	0.35	11.22
4.60E-02	3.10E-02	0	15.14	1	1.64	0.37	23.7
6.55E-02	5.58E-02	0.69	1.38	2	1.23	0.13	143.96
7.37E-02	3.09E-02	0	64.96	2	1.66	0.34	4.3

Th (ppm)	**Sm (ppm)**	**Pit Depth (µm)**
140.81	729.48	16.09
43.47	378.99	15.96
212.87	744.67	13.2

83.71	452.88	15.4
0.04	12.96	4.64
33.02	75.09	11.66
57.82	379.77	12.22
97.17	480.75	11.48
87.69	459.26	13.01
39.32	412.47	12.76
29.95	351.86	12.89
3.47	155.13	11.1
10.92	56.05	12.27
97.04	509.44	11.36
35.16	344.23	12.52
14.7	212.92	12.87
178.54	682.19	14.29
0	287.7	13.38
35.23	332.72	11.15
31.64	228.64	13.59
162.17	700.29	12.25
0	33.87	12.78
32.15	310.98	11.23
304.79	929.3	13.98
4.26	226.49	12.96
Mean Dpar	1.36	
Mean Dper	0.22	
Modified Zeta	13.828	0.280
Mean ^{29}Si b:s	0.162	
Mean ^{43}Ca b:s	0.162	
Mean ^{238}U b:s	0.272	

# of grains	25	
Chi-squared	68.1	
Chi-squared prob.	0.0000	
Pooled Age (Ma)	**5.80**	**1.6**

(length data)

Sample#	Track #	Length (µm)	Etch	Dpar (µm)	Dper (µm)	Angle to c-axis (°)
KFE5	1	13.18	2	1.68	0.2	78.43
	2	14.8	2	1.68	0.2	49.07
	3	13.6	2	1.68	0.2	28.42
	4	14.02	2	1.68	0.2	55.31
	5	12.44	4	1.66	0.23	72.14
	6	14.62	3	1.5	0.2	39.71
	7	15.81	3	1.5	0.2	60.21
	8	16.6	3	1.5	0.2	73.15
	9	16.56	4	1.64	0.3	16.15
	10	13.57	4	1.64	0.3	61.49
	11	8.19	3	1.88	0.31	50.82
	12	13.05	3	1.88	0.31	60.97
	13	9.89	3	1.88	0.31	67.97
	14	17.63	4	1.73	0.3	32.01
	15	14.61	4	1.73	0.3	43.81
	16	15.48	4	1.58	0.39	53.52
	17	15.44	4	1.58	0.39	55.71
	18	15.58	4	1.79	0.28	59.02
	19	11.91	4	1.79	0.28	60.1
	20	11.59	4	1.79	0.28	72.19
	21	15.2	4	1.79	0.28	32.57
	22	13.86	4	1.33	0.2	84.9

23	14.98	4	1.33	0.2	61.37
24	16.57	4	1.33	0.2	25.11
25	13.23	2	1.58	0.25	80.47
26	16.76	2	1.58	0.25	31.31
27	14.51	4	1.63	0.2	54.65
28	14.62	4	1.63	0.2	40.41
29	14.77	4	1.63	0.2	73.65
30	16.63	4	1.63	0.2	45.06
31	11.82	4	1.63	0.2	60.26
32	13.87	3	1.64	0.3	67.87
33	12.76	3	1.64	0.3	70.72
34	12.33	3	1.64	0.3	68.18
35	12.46	3	1.64	0.3	64.35
36	13.72	3	1.5	0.16	62.62
37	15.39	3	1.45	0.26	58.84
38	11.76	3	1.45	0.26	63.56
39	13.44	3	1.45	0.26	67.57
40	17.63	2	1.77	0.29	32.28
41	11.88	3	1.52	0.24	46.61
42	14.95	4	1.65	0.14	39.56
43	13.82	4	1.65	0.14	41.42
44	14.81	4	1.65	0.14	67.7
45	15.42	4	1.65	0.14	44.01
46	14.17	3	1.48	0.12	39.96
47	15.58	3	1.48	0.12	65.85
48	12.25	3	1.48	0.12	68
49	12.74	3	1.48	0.12	74.89
50	13.9	3	1.48	0.12	65.68
51	16.13	3	1.48	0.12	19.6

52	13.09	3	1.48	0.12	39
53	14.71	3	1.48	0.12	43.92
54	9.7	3	1.48	0.12	74.03
55	14.06	2	1.83	0.31	74.11
56	15.55	2	1.83	0.31	37.87
57	15.97	2	1.83	0.31	22.29
58	10.37	2	1.83	0.31	76.88
59	14.3	2	1.83	0.31	54.64
60	15.59	4	1.64	0.21	61.07
61	15.52	2	1.58	0.2	47.97
62	15.11	2	1.58	0.2	51.56
63	10.92	2	1.58	0.2	68.02
64	14.58	3	1.43	0.29	50.57
65	15.89	3	1.43	0.29	25.83
66	13.23	3	1.7	0.18	71.8
67	15.85	3	1.7	0.18	32.24
68	15.01	4	1.61	0.23	51.91
69	15.59	4	1.61	0.23	68.07
70	15.62	4	1.61	0.23	82.76
71	14	2	1.5	0.12	74.67
72	13.88	1	1.63	0.12	52.11
73	15.34	3	1.51	0.19	69.46
74	15.47	3	1.51	0.19	38.76
75	12.04	3	1.51	0.19	88.25
76	15.38	3	1.51	0.19	75.24
77	15.39	3	1.51	0.19	34.9
78	11.07	2	1.39	0.19	67.89
79	14.57	4	1.37	0.15	45.11
80	16.6	4	1.37	0.15	27.49

81	12.87	4	1.37	0.15	67.74
82	14.37	4	1.37	0.15	46.17
83	14.71	4	1.48	0.14	40.54
84	15.93	3	1.66	0.18	32.37
85	13.16	3	1.66	0.18	40.96
86	11.55	4	1.4	0.23	69.48
87	14.68	4	1.4	0.23	57.72
88	14.02	4	1.4	0.23	59.47
89	15.55	4	1.33	0.2	51.53
90	14.43	4	1.33	0.2	70.98
91	14.49	3	1.31	-0.04	53.32
92	14.66	2	1.96	0.29	62.3
93	16.47	2	1.96	0.29	34.19
94	10.86	2	1.96	0.29	51.46
95	13.36	2	1.96	0.29	70.61
96	15	2	1.96	0.29	49.31
97	15.62	2	1.96	0.29	29.69
98	14.84	3	1.63	0.19	64.29
99	12.84	3	1.63	0.19	74.29
100	13.08	3	1.57	0.33	43.83
101	11.44	3	1.57	0.33	45.69
102	14.99	3	1.57	0.33	59.4
103	13.9	3	1.57	0.33	89.47
104	13.16	3	1.57	0.33	87.51
105	13.92	2	1.17	0.2	44.96
106	10.35	2	1.17	0.2	72.82
107	14.42	2	1.17	0.2	69.23
108	12.65	2	1.17	0.2	58.64
109	13.48	2	1.17	0.2	56.89

	110	12	4	1.53	0.33	89.3
	111	11.41	3	1.7	0.14	63.32
	112	11.2	3	1.46	0.16	87.6
	113	14.67	3	1.46	0.16	29.4
	114	14.89	4	1.55	0.3	71.86
	115	16.44	4	1.55	0.3	4.38
	116	14.63	4	1.55	0.3	45.61
	117	16.53	4	1.55	0.3	64.76
	118	13.87	4	1.55	0.3	85.06
	119	14.99	4	1.55	0.3	20.71
	120	16.01	4	1.55	0.3	39.1
	121	16.2	4	1.55	0.3	31.15
	122	14.39	4	1.26	0.28	70.47
	123	14.45	4	1.26	0.28	37.93
	124	14.79	2	1.5	0.25	75.44
	125	14.21	3	1.35	0.1	58.86
Mean Dpar	1.57					
Mean Dper	0.23					
Mean Length (µm)	14.1	0.16				
Std. Dev. (µm)	1.750					
Skewness	-0.690					
Kurtosis	0.340					

Sample#	Track #	Length (µm)	Etch	Dpar (µm)	Dper (µm)	Angle to c-axis (°)
KFE6	1	14.44	3	1.86	0.26	30.07
	2	14.52	3	1.86	0.26	39.36
	3	14.46	3	1.86	0.26	72.27
	4	16.52	3	1.86	0.26	54.13
	5	14.42	3	1.86	0.26	59.3

6	13.95	4	1.65	0.18	56.44
7	14.81	4	1.65	0.18	35.74
8	14.33	4	1.65	0.18	26.39
9	15.39	2	1.68	0.18	36.82
10	12.1	2	1.68	0.18	44.62
11	13.36	2	1.68	0.18	44.15
12	12.12	3	1.73	0.26	39.27
13	13.88	3	1.73	0.26	63.12
14	14.09	3	1.73	0.26	51.35
15	15.4	3	1.65	0.19	64.6
16	15.56	3	1.65	0.19	47.33
17	14.27	3	1.65	0.19	50.01
18	16.89	3	1.65	0.19	34.85
19	15.84	3	1.51	0.25	24.12
20	12.96	3	1.51	0.25	55.35
21	14.93	4	1.5	0.16	53.86
22	15.56	4	1.5	0.16	35.76
23	10.3	4	1.5	0.16	80.49
24	14.54	4	1.5	0.16	29.18
25	13.32	4	1.57	0.2	77.57
26	15.12	4	1.57	0.2	46.06
27	13.5	4	1.57	0.2	49.21
28	13.66	2	1.76	0.43	62.38
29	14.5	2	1.78	0.35	54.08
30	14	2	1.78	0.35	40.57
31	13.05	3	1.6	0.2	75.49
32	13.5	3	1.6	0.2	54.93
33	14.37	3	1.6	0.2	81.82
34	9.97	3	1.6	0.2	73.05

35	13.63	3	1.6	0.2	83.9
36	15.19	3	1.6	0.2	34.73
37	13.08	3	1.6	0.2	45.18
38	14.47	3	1.6	0.2	53.3
39	12.92	3	1.6	0.2	82.67
40	12.91	3	1.6	0.2	58.93
41	13.96	3	1.6	0.2	39.09
42	14.5	3	1.6	0.2	66.88
43	15.27	4	1.43	0.25	71.53
44	16.22	4	1.43	0.25	49.22
45	15.41	4	1.43	0.25	74.01
46	13.2	4	1.43	0.25	57.4
47	13.22	4	1.43	0.25	49.78
48	13.53	4	1.43	0.25	58.09
49	13.23	4	1.43	0.25	44.51
50	15.63	4	1.43	0.25	59.78
51	13.79	3	1.61	0.25	57.61
52	14.51	3	1.57	0.33	38.89
53	15.1	3	1.57	0.33	53.96
54	15.26	3	1.57	0.33	41.62
55	11.06	3	1.43	0.23	69.67
56	10.66	3	1.43	0.23	73.69
57	15.22	3	1.43	0.23	52.36
58	15.66	3	1.43	0.23	57.34
59	10.73	3	1.43	0.23	56.46
60	12.33	3	1.43	0.23	44.24
61	10.8	3	1.64	0.21	82.34
62	9.55	3	1.64	0.21	86.14
63	16.96	3	1.64	0.21	41.83

64	12.54	3	1.64	0.21	81.69
65	12.39	3	1.64	0.21	78.05
66	14.3	3	1.64	0.21	50.25
67	13.43	3	1.64	0.21	89.6
68	14.16	3	1.64	0.21	51.68
69	15	3	1.64	0.21	58.04
70	13.01	3	1.64	0.21	67.87
71	15.93	3	1.64	0.21	59.44
72	14.56	3	1.66	0.39	44.7
73	14.66	3	1.66	0.39	65.38
74	16.06	3	1.66	0.39	62.75
75	15.27	3	1.66	0.39	54.11
76	14.81	2	1.63	0.1	36.38
77	16.31	2	1.63	0.1	22.94
78	12.88	2	1.63	0.1	76.37
79	13.85	2	1.57	0.15	73.39
80	12.23	2	1.57	0.15	86.15
81	14.85	2	1.57	0.15	63.65
82	14.86	2	1.57	0.15	80.74
83	14.55	2	1.57	0.15	81.37
84	15.12	3	1.55	0.28	66.93
85	15.61	3	1.55	0.28	49.91
86	15.58	3	1.55	0.28	18.19
87	13.16	3	1.55	0.28	74.76
88	15.53	3	1.47	0.25	79.32
89	16.21	3	1.47	0.25	22.96
90	15.13	3	1.47	0.25	38.64
91	13.51	3	1.59	0.16	53.41
92	12.93	3	1.59	0.16	69.29

93	13.39	3	1.59	0.16	76.44
94	15.39	3	1.59	0.16	63.54
95	11.9	3	1.59	0.16	65.48
96	15.42	3	1.59	0.16	21.13
97	12.36	3	1.59	0.16	73.49
98	14.89	3	1.65	0.21	84.29
99	12.34	3	1.65	0.21	54.34
100	14.46	3	1.79	0.34	35.47
101	15.06	3	1.79	0.34	57.06
102	15.43	3	1.79	0.34	36.48
103	14.52	3	1.79	0.34	68.71
104	15.41	4	1.77	0.18	68.61
105	15.06	4	1.77	0.18	27.96
106	11.01	4	1.77	0.18	68.17
107	14.41	4	1.77	0.18	81.4
108	16.04	4	1.77	0.18	49.53
109	12.53	4	1.77	0.18	70.34
110	12.78	4	1.77	0.18	87.55
111	13.43	4	1.77	0.18	69.11
112	14.93	4	1.77	0.18	29.58
113	13.24	4	1.77	0.18	88.49
114	14.89	3	1.9	0.37	70.82
115	14.61	3	1.9	0.37	73.2
116	12.73	3	1.9	0.37	72.61
117	13.55	3	1.9	0.37	52.26
118	14.43	3	1.9	0.37	47.92
119	12.79	3	1.9	0.37	68.88
120	13.8	3	1.9	0.37	38.95
121	14.44	3	1.9	0.37	71.71

	122	13.87	4	2.01	0.29	58.35
	123	13.71	4	2.01	0.29	43.62
	124	15.48	4	2.01	0.29	78
	125	14.47	4	2.01	0.29	79.98
Mean Dpar	1.65					
Mean Dper	0.24					
Mean Length (µm)	14.07	0.13				
Std. Dev. (µm)	1.46					
Skewness	-0.720					
Kurtosis	0.460					

Sample#	Track #	Length (µm)	Etch	Dpar (µm)	Dper (µm)	Angle to c-axis (°)
KFE7	1	14.96	2	1.37	0.15	60.75
	2	13.74	4	1.28	0.1	46
	3	14.48	4	1.28	0.1	31.14
	4	11.66	4	1.35	0.29	52.68
	5	13.47	4	1.35	0.29	36.96
	6	12.67	3	1.38	0.18	72.75
	7	13.66	3	1.38	0.18	29.92
	8	14.46	3	1.38	0.18	86.49
	9	14.81	2	1.35	0.07	31.61
	10	13.24	2	1.35	0.07	40.15
	11	14.71	3	1.31	0.2	34.74
	12	13.2	3	1.31	0.2	57.57
	13	14.4	3	1.31	0.2	45.71
	14	16.1	4	1.77	0.18	57.66
	15	15.21	4	1.77	0.18	57.57
	16	13.25	4	1.3	0.23	47.67
	17	15.58	2	1.63	0.18	39.59

18	13.16	2	1.63	0.18	54.62
19	13.5	4	1.53	0.26	74.24
20	14.05	4	1.53	0.26	50.59
21	14.26	4	1.53	0.26	54.67
22	13.05	3	1.54	0.2	58.97
23	14.34	3	1.54	0.2	75.96
24	14.33	3	1.54	0.2	28.41
25	12.62	2	1.54	0.4	40.15
26	13.03	2	1.54	0.4	46.74
27	13.19	4	1.32	0.11	19.26
28	15.8	4	1.32	0.11	70.02
29	14.94	3	1.84	0.24	71.63
30	14.25	3	1.84	0.24	30.55
31	14.33	4	1.47	0.2	49.09
32	12.89	4	1.47	0.2	48.1
33	13.81	4	1.47	0.2	63.33
34	16.81	4	1.47	0.2	59.11
35	15.7	2	1.41	0.11	49.23
36	11.55	3	1.25	0.12	75.07
37	15.2	3	1.25	0.12	15.42
38	15.45	3	1.25	0.12	61.73
39	14.77	4	1.58	0.16	13.16
40	14.31	4	1.58	0.16	46.06
41	14.55	4	1.58	0.16	46.47
42	15.43	2	1.31	0.42	14.37
43	14.31	3	1.25	0.21	26.75
44	13.91	3	1.25	0.21	80.35
45	15.5	2	1.37	0.11	29.09
46	13.12	2	1.25	0.18	79.74

	47	8.64	2	1.25	0.18	51.45
	48	14.16	2	1.25	0.18	76.17
	49	14.75	2	1.25	0.18	59.84
	50	15.79	2	1.25	0.18	28.15
	51	14.48	3	1.35	0.26	59.45
	52	14.39	3	1.35	0.26	48.05
	53	13.24	3	1.35	0.26	66.76
	54	13.06	3	1.27	0.14	82
	55	13.74	3	1.18	0.11	28.13
	56	13.96	3	1.54	0.14	29.72
	57	15.31	3	1.54	0.14	45.09
	58	13.81	4	1.53	0.23	45.27
	59	13.35	3	1.26	0.05	76.6
Mean Dpar	1.42					
Mean Dper	0.19					
Mean Length (µm)	14.08	0.17				
Std. Dev. (µm)	1.28					
Skewness	-1.18					
Kurtosis	3.94					

Sample#	Track #	Length (µm)	Etch	Dpar (µm)	Dper (µm)	Angle to c-axis (°)
KFE8	1	14.33	2	1.37	0.21	37.74
	2	14.5	2	1.27	0.19	17.61
	3	14.07	3	1.35	0.2	67.18
	4	14.75	3	1.35	0.2	68.48
	5	14.49	3	1.35	0.2	31.77
	6	14.14	3	1.35	0.2	89.3
	7	13.49	2	1.71	0.34	28.25
	8	13.71	4	1.47	0.11	44.22

9	12.33	4	1.47	0.11	59.72
10	14.83	4	1.47	0.11	44.56
11	15.65	4	1.47	0.11	48.59
12	14.23	2	1.53	0.06	35.81
13	15.36	3	1.25	0.25	80.31
14	13.76	2	1.24	0.23	59.24
15	14.89	2	1.24	0.23	51.46
16	15.41	3	1.4	0.11	32.06
17	13.53	3	1.4	0.11	61.57
18	14.73	3	1.4	0.11	69.95
19	13.87	4	1.79	0.2	66.76
20	16.13	4	1.31	0.07	28.9
21	16.86	3	1.53	0.25	30.5
22	13.94	4	1.34	0.19	21.11
23	13.84	4	1.34	0.19	62.6
24	17.26	3	1.3	0.18	43.78
25	14.46	4	1.01	0.31	56.57
26	16.02	4	1.01	0.31	15.26
27	14.48	4	1.01	0.31	70.54
28	15.65	4	1.55	0.09	21.91
29	15.43	4	1.55	0.09	60.28
30	15.52	4	1.61	0.18	30.79
31	12.66	3	1.52	0.18	48.42
32	15.49	4	1.4	0.34	29.72
33	14.49	3	1.38	0.23	32.76
34	14.28	4	1.52	0.24	37.12
35	15.42	4	1.52	0.24	34.26
36	14.26	4	1.31	0.06	47.97
37	13.58	4	1.31	0.06	67.18

	38	14.02	4	1.31	0.06	33.16
	39	15.41	4	1.51	0.12	19.8
	40	15.37	3	1.44	0.21	35.37
	41	15.15	3	1.44	0.21	35
	42	14.96	4	1.41	0.1	50.98
	43	15.04	4	1.55	0.06	65.67
	44	14.47	4	1.55	0.06	62.58
	45	11.4	4	1.55	0.06	62.65
	46	15.75	4	1.55	0.06	19.68
	47	15.56	4	1.65	0.15	70.63
	48	15.43	4	1.65	0.15	31.78
Mean Dpar	1.42					
Mean Dper	0.17					
Mean Length (µm)	14.67	0.16				
Std. Dev. (µm)	1.08					
Skewness	-0.390					
Kurtosis	0.890					

Sample#	**Track #**	**Length (µm)**	**Etch**	**Dpar (µm)**	**Dper (µm)**	**Angle to c-axis (°)**
KFE9	1	15.01	4	1.34	0.09	24.95
	2	14.25	2	1.14	0.35	15.8
	3	15.85	2	1.53	0.14	80.04
	4	15.5	2	1.53	0.14	33.06
	5	15.67	3	1.13	0.43	38.02
	6	15.64	3	1.13	0.43	32.42
	7	13.82	3	1.3	0.18	69.07
	8	15.14	3	1.5	0.24	21.51
	9	13.76	2	1.37	0.09	26.29
	10	14.46	2	1.2	0.1	48.94

	11	14.39	2	1.52	0.25	41.22
	12	15.62	4	1.2	0.1	28.67
	13	15.39	4	1.2	0.1	48.25
	14	13.58	4	1.2	0.1	36.52
	15	16.03	4	1.2	0.1	26.6
	16	15.7	4	1.4	0.21	52.55
	17	13.96	4	1.4	0.21	46.79
	18	13.93	4	1.4	0.21	65.35
Mean Dpar	1.32					
Mean Dper	0.19					
Mean Length (µm)	14.87	0.20				
Std. Dev. (µm)	0.84					
Skewness	-0.17					
Kurtosis	-1.7					

Haiyuan Fault

Haiyuan Fault Central (HFC)

Apatite (U-Th)/He

Sample #	U (ppm)	Th (ppm)	He (nmol/g)	Mass (µg)	Radius (µm)	Length (µm)	F_T
$HFC10_A$	34.90	58.36	14.40	3.50	50	174	0.72
$HFC10_B$	34.68	84.09	14.21	2.88	49.5	146	0.70
$HFC10_C$	31.66	65.40	13.17	2.46	50	122	0.69
$HFC10_D$	25.83	56.75	11.03	2.92	45.5	175	0.69

Sm (ppm)	Raw Age (Ma)	Corrected Age (Ma)	Elevation (m)
142.00	54.09	75.38	2766

137.01	47.71	67.96
149.57	51.12	73.73
133.98	51.43	74.00

Apatite Fission Track (age data)

Sample#	Grain #	N_s	Area (cm x cm)	$^{238}U/^{43}Ca$ (dmnls)	1σ (dmnls)	^{43}Ca	^{238}U
HFC10	1	75	2.91E-05	2.32E-01	2.32E-02	2.12E-02	1.19E-04
	2	40	3.88E-05	9.71E-02	9.71E-03	2.76E-02	6.28E-03
	3	35	1.94E-05	1.14E-01	1.14E-02	3.70E-02	8.86E-03
	4	31	1.75E-05	2.19E-01	2.19E-02	3.28E-02	3.44E-03
	5	64	3.88E-05	1.53E-01	1.53E-02	3.23E-02	3.25E-03
	6	13	1.55E-05	7.58E-02	7.58E-03	4.16E-02	1.66E-02
	7	29	3.11E-05	9.28E-02	9.28E-03	3.02E-02	2.11E-03
	8	23	2.91E-05	9.19E-02	9.19E-03	3.52E-02	4.97E-03
	9	21	1.75E-05	8.26E-02	8.26E-03	3.08E-02	3.55E-03
	10	28	1.94E-05	1.12E-01	1.12E-02	3.56E-02	4.69E-03
	11	34	3.88E-05	1.20E-01	1.20E-02	3.05E-02	4.13E-03
	12	13	2.91E-05	2.30E-02	2.30E-03	3.39E-02	2.81E-02
	13	40	3.40E-05	9.18E-02	9.18E-03	3.14E-02	2.25E-03
	14	27	1.75E-05	1.22E-01	1.22E-02	3.63E-02	2.76E-03
	15	25	2.91E-05	9.47E-02	9.47E-03	3.50E-02	2.18E-03
	16	42	3.88E-05	1.13E-01	1.13E-02	3.95E-02	1.82E-03
	17	38	2.91E-05	1.23E-01	1.23E-02	3.27E-02	2.91E-03
	18	23	2.43E-05	1.25E-01	1.25E-02	3.43E-02	9.73E-04
	19	28	3.88E-05	8.94E-02	8.94E-03	3.86E-02	2.40E-03
	21	11	1.46E-05	9.66E-02	9.66E-03	3.31E-02	1.46E-03

	22	14	3.11E-05	8.96E-02	8.96E-03	3.57E-02	1.28E-03
	23	38	2.91E-05	1.17E-01	1.17E-02	3.22E-02	1.63E-03
	24	35	3.88E-05	7.43E-02	7.43E-03	3.57E-02	2.19E-03
	25	68	3.88E-05	1.22E-01	1.22E-02	3.49E-02	1.51E-03
	26	16	1.94E-05	1.05E-01	1.05E-02	3.37E-02	2.09E-03
	27	11	1.16E-05	9.73E-02	9.73E-03	3.85E-02	4.18E-03
	28	29	2.91E-05	1.06E-01	1.06E-02	5.01E-02	1.40E-03
	29	28	3.11E-05	8.06E-02	8.06E-03	4.85E-02	6.99E-03
	30	45	3.11E-05	1.24E-01	1.24E-02	4.98E-02	1.27E-03
	31	58	3.88E-05	9.48E-02	9.48E-03	4.82E-02	5.01E-03
	32	17	1.75E-05	7.90E-02	7.90E-03	4.66E-02	8.75E-04
	33	34	3.88E-05	9.82E-02	9.82E-03	4.95E-02	1.84E-03
	34	13	1.75E-05	9.59E-02	9.59E-03	5.19E-02	1.89E-03
	35	60	3.40E-05	1.54E-01	1.54E-02	4.03E-02	1.21E-03
	36	39	3.40E-05	1.27E-01	1.27E-02	4.15E-02	5.57E-03
	37	24	1.94E-05	9.84E-02	9.84E-03	4.71E-02	6.91E-03
	38	37	3.88E-05	8.31E-02	8.31E-03	3.47E-02	3.45E-03
	39	27	2.91E-05	9.01E-02	9.01E-03	3.66E-02	5.18E-03
	40	16	1.55E-05	9.75E-02	9.75E-03	3.46E-02	2.64E-03

^{232}Th	^{147}Sm	FT Age (Ma)	2σ (Ma)	Etch	Dpar (µm)	Dper (µm)	U (ppm)
2.17E-03	4.01E-03	87.98	27.1	4	1.77	0.32	82.35
7.87E-03	9.48E-03	84.03	31.62	4	2.02	0.21	34.5
1.20E-02	1.01E-02	124.86	49.3	4	1.77	0.42	40.5
2.39E-02	2.10E-02	64.19	26.52	4	1.81	0.47	77.9
2.37E-03	7.99E-03	85.38	27.54	4	1.96	0.44	54.32
1.38E-02	1.99E-02	87.43	51.68	4	1.93	0.71	26.93
6.40E-03	1.13E-02	79.68	33.76	4	1.61	0.25	32.98
1.19E-02	1.06E-02	68.14	31.64	4	1.68	0.23	32.66
6.84E-03	7.72E-03	114.99	55.4	4	1.87	0.37	29.34

5.84E-03	1.45E-02	101.75	43.7	4	1.91	0.45	39.83
2.81E-03	1.08E-02	57.81	23.06	4	1.62	0.27	42.71
3.86E-02	2.41E-02	152.65	90.22	4	1.62	0.42	8.19
2.97E-03	1.16E-02	101.49	38.18	4	2.05	0.21	32.6
4.62E-03	1.34E-02	99.85	43.5	4	1.89	0.49	43.5
5.99E-03	7.29E-03	71.87	32.26	4	1.73	0.39	33.65
5.96E-03	1.52E-02	75.72	28	4	1.74	0.44	40.22
4.30E-03	9.91E-03	83.84	32.14	4	1.79	0.35	43.8
2.00E-03	8.11E-03	60	27.86	4	2.26	0.4	44.53
7.67E-03	9.32E-03	63.99	27.48	4	1.96	0.49	31.76
2.96E-03	1.11E-02	62.06	39.5	4	1.87	0.29	34.31
4.73E-03	1.21E-02	39.99	22.88	2	1.99	0.52	31.83
4.11E-03	1.10E-02	87.95	33.7	4	1.81	0.48	41.74
8.40E-03	1.57E-02	96.04	37.92	4	1.98	0.43	26.39
3.44E-03	1.15E-02	113.84	36.08	4	2	0.58	43.19
3.79E-03	9.12E-03	62.49	33.74	4	1.78	0.49	37.18
6.19E-03	9.80E-03	76.92	48.96	4	1.69	0.45	34.57
4.13E-03	1.38E-02	74.4	31.52	4	1.81	0.6	37.69
9.68E-03	1.61E-02	88.5	38	4	1.83	0.23	28.65
4.55E-03	1.04E-02	92.52	33.42	4	1.96	0.39	44.03
7.25E-03	9.38E-03	124.39	41.36	4	1.96	0.39	33.69
9.17E-03	1.59E-02	97.48	51.3	4	1.66	0.51	28.06
6.42E-03	1.87E-02	70.73	28.22	4	1.81	0.45	34.88
7.62E-03	2.28E-02	61.58	36.4	4	1.78	0.4	34.06
3.34E-03	8.12E-03	90.84	29.88	4	2.09	0.69	54.68
7.98E-03	1.85E-02	71.84	27.28	4	1.75	0.57	45.01
6.08E-03	1.22E-02	99.4	45.36	4	1.9	0.38	34.96
6.09E-03	1.26E-02	90.73	35.1	4	2.05	0.24	29.54
3.85E-03	1.48E-02	81.54	35.52	4	1.89	0.64	32

8.26E-03	1.15E-02	83.69	45.18	4	1.54	0.51	34.64

Th (ppm)	Sm (ppm)	Pit Depth (µm)
155.96	327.74	16.02
117.67	243.7	14.3
131.14	307.01	12.74
55.86	200.51	13.4
166.37	303.22	13.24
103.71	221.59	11.85
85.02	223.56	13.4
69.91	212.47	12.47
108.98	241.73	12.96
120.26	245.71	11.99
153.16	217.38	13.31
22.07	109.45	13.08
107.95	243.58	13.29
143.79	299.34	11.9
130.43	312.92	11.48
144.44	245.53	10.7
153.95	252.34	13.71
172.06	297.74	11.4
102.08	239.96	10.97
104.41	218.66	12.32
100.96	251.46	11.76
118.99	275.3	13.11
96.5	220.68	12.02
83.79	191.82	11.73
130.47	285.05	11.59
111.42	233.87	11.5
155.65	283.14	8.18

100.13	245.63	8.93
177.66	296.2	8.4
106.62	227.57	8.35
103.49	236.97	8.28
125.43	274.28	8.19
108.64	226.44	8.49
198.23	350.39	10.56
118	236.29	10.33
134.01	271.9	9.19
91.28	225.5	11.65
114.02	246.82	12.7
80.27	225.74	11.56

Mean Dpar	1.85	
Mean Dper	0.43	
Modified Zeta	15.94	0.318
Mean ^{29}Si b:s	0.037	
Mean ^{43}Ca b:s	0.037	
Mean ^{238}U b:s	0.004	
# of grains	39	
Chi-squared	47.2	
Chi-squared prob.	0.1459	
Pooled Age (Ma)	**83.90**	**6.6**

(length data)

Sample#	Track #	Length (µm)	Etch	Dpar (µm)	Dper (µm)	Angle to c-axis (°)
HFC10	1	14.98	4	1.65	0.19	56.48
	2	13.6	4	1.65	0.19	42.99

3	14.07	4	1.65	0.19	73.56
4	13.19	4	1.65	0.19	51.95
5	9.51	4	1.65	0.19	70.34
6	15.03	4	1.65	0.19	51.02
7	14.85	4	1.93	0.58	61.52
8	14.55	4	1.93	0.58	47.59
9	13.78	4	1.93	0.58	72.26
10	13.64	4	1.93	0.58	46.75
11	8.56	4	1.93	0.58	62.32
12	14.53	4	1.93	0.58	44.02
13	14.06	4	1.93	0.58	35.88
14	15.5	4	1.93	0.58	39.15
15	9.14	4	1.93	0.58	52.64
16	14.26	4	1.93	0.58	48.69
17	13.37	4	1.93	0.58	70.17
18	8.63	4	1.93	0.58	66.42
19	13.39	4	1.93	0.58	84.3
20	13.06	4	2.16	0.37	37.7
21	13.71	4	2.16	0.37	34.25
22	13.07	4	2.16	0.37	37.06
23	14.29	4	2.16	0.37	37.03
24	12.64	4	2	0.26	62.7
25	15.46	4	2	0.26	19.22
26	13.61	4	2	0.26	73.13
27	14.52	4	2	0.26	33.09
28	13.62	4	2	0.26	71.98
29	16.25	4	1.76	0.16	40.47
30	16.11	4	1.76	0.16	24.78
31	12.82	4	1.76	0.16	64.97

32	15.22	4	1.76	0.16	61.48
33	15.2	4	1.76	0.16	60.47
34	14.08	4	1.76	0.16	71.09
35	12.81	4	2.03	0.37	71.86
36	11.38	4	2.03	0.37	46.02
37	14.51	4	2.03	0.37	36.64
38	15.47	4	2.03	0.37	77.51
39	16.16	4	2.07	0.54	81.88
40	14.76	4	2.07	0.54	53.69
41	14.75	4	2.07	0.54	49.51
42	12.77	4	2.07	0.54	67.36
43	14.73	4	2.01	0.44	31.52
44	11.56	4	2.01	0.44	52.54
45	13.84	4	2.01	0.44	69.11
46	10.81	4	2.01	0.44	54.54
47	15.9	4	2.01	0.44	22.75
48	14.85	4	2.01	0.44	42.18
49	14.8	4	2.01	0.44	38.66
50	13.14	4	2.01	0.44	60.45
51	12.96	4	2.01	0.44	85.99
52	15.89	4	2.01	0.44	30.83
53	15.27	4	2.01	0.44	48.77
54	15.02	4	2.01	0.44	47.38
55	14.71	4	2.01	0.44	40.16
56	15.89	4	2.01	0.44	13.36
57	15.31	4	2.11	0.48	57.96
58	13.71	4	2.11	0.48	60.94
59	14.33	4	2.11	0.48	89.86
60	12.98	4	2.11	0.48	69.69

61	14.69	4	2.11	0.48	33.73
62	12.41	4	1.79	0.54	73.72
63	12.13	4	1.79	0.54	77.62
64	15.4	4	1.79	0.54	33.68
65	15.74	4	1.79	0.54	11.38
66	10.13	4	1.79	0.54	65.16
67	14.28	4	1.79	0.54	25.43
68	15.72	4	1.79	0.54	14.83
69	13.58	4	1.8	0.2	61.46
70	14.42	4	1.8	0.2	29.16
71	14.83	4	1.8	0.2	23.73
72	13.78	4	1.8	0.2	78.83
73	14.07	4	2.32	0.54	51.59
74	12.58	4	2.32	0.54	25.29
75	12.39	4	2.32	0.54	67.29
76	14.2	4	2.32	0.54	84.57
77	14.12	4	2.32	0.54	74.33
78	13.96	4	2.32	0.54	69.87
79	13.81	4	2.32	0.54	62.89
80	14.82	4	2.32	0.54	45.55
81	14.27	4	2.32	0.54	36.04
82	13.86	4	2.32	0.54	74.85
83	13.93	4	2.32	0.54	82.95
84	14.56	4	2.32	0.54	81.01
85	15.22	4	2.32	0.54	18.82
86	14.93	4	2.5	0.57	16.74
87	14.15	4	2.5	0.57	68.24
88	10.56	4	2.5	0.57	77.51
89	10.89	4	2.5	0.57	71.04

90	14.7	4	2.5	0.57	73.74
91	12.93	4	2.5	0.57	55.02
92	15.83	4	2.5	0.57	36.88
93	14.54	4	1.85	0.29	61.89
94	13.53	4	1.85	0.29	41.49
95	15.27	4	1.85	0.29	63.64
96	13.67	4	1.85	0.29	77.72
97	9.89	4	1.85	0.29	68.85
98	15.77	4	1.85	0.29	84.62
99	14.11	4	1.85	0.29	67.2
100	15.48	4	1.85	0.29	59.34
101	15.28	4	1.85	0.29	73.38
102	15.02	4	1.85	0.29	45.02
103	18.15	4	1.85	0.29	39.42
104	15.23	4	2.57	0.62	68.95
105	15.92	4	2.57	0.62	32.54
106	11.45	4	2.57	0.62	59.42
107	14.35	4	2.57	0.62	67.41
108	15.43	4	2.57	0.62	46.9
109	17.62	4	2.57	0.62	39.42
110	14.11	4	2.57	0.62	66.88
111	14.57	4	2.57	0.62	56.21
112	14.19	4	2.19	0.68	57.06
113	13.49	4	2.19	0.68	73.84
114	14.21	4	2.19	0.68	49.87
115	14.48	4	2.19	0.68	63.75
116	13.86	4	2.19	0.68	38.1
117	14.7	4	2.19	0.68	44.79
118	14.55	4	2.19	0.68	66.36

119	15.72	4	2.19	0.68	45.72
120	14.67	4	2.19	0.68	35.5
121	14.5	4	1.9	0.38	24.44
122	15.09	4	1.9	0.38	49.35
123	15.39	4	1.9	0.38	23.23
124	12.52	4	1.9	0.38	79.36
125	15	4	2.07	0.59	33.66
126	16.48	4	2.07	0.59	78.77
127	11.07	4	2.07	0.59	66.04
128	13.93	4	2.07	0.59	83.36
129	14.63	4	2.07	0.59	25.67
130	15.59	4	2.07	0.59	64.26
131	15.37	4	2.07	0.59	58.5
132	12.59	4	2.07	0.59	72.7
133	12.69	4	2.13	0.66	71.63
134	15.14	4	2.13	0.66	35.23
135	14.86	4	2.13	0.66	89.4
136	13.87	4	2.13	0.66	64.73
137	11.9	4	2.13	0.66	57.44
138	12.97	4	2.13	0.66	55.1
139	10.42	4	2.13	0.66	52.88
140	11.31	4	2.13	0.66	53.16
141	7.62	4	2.13	0.66	41.67
142	13.84	4	1.96	0.85	62.97
143	13.97	4	1.96	0.85	27.72
144	15.13	4	1.96	0.85	56.39
145	15	4	1.96	0.85	81.61
146	13.59	4	1.96	0.85	60.49
147	15.93	4	1.98	0.18	35.43

148	15.3	4	1.98	0.18	62.49
149	15.03	4	1.98	0.18	45.3
150	14.56	4	1.98	0.18	76.2
151	16.19	4	1.98	0.18	58.33
152	14.54	4	1.98	0.18	52.3
153	11.7	4	1.98	0.18	30.89
154	13.99	4	1.98	0.18	60.53
155	15.02	4	1.98	0.18	77.82
156	14.14	4	1.98	0.18	59.95
157	14.85	4	1.98	0.18	69.32
158	10.97	4	1.98	0.18	83.41
159	14.31	4	1.98	0.18	76.62
160	15.5	4	1.98	0.18	18.81
161	15.59	4	1.98	0.18	65.1
162	14.3	4	1.98	0.18	84.12
163	15.48	4	1.98	0.18	15.26
164	14.11	4	1.98	0.18	70.56
165	15.41	4	1.98	0.18	60.97
166	16.07	4	1.98	0.18	71.07
167	13.87	4	1.86	0.58	81.27
168	15.93	4	1.86	0.58	51.58
169	15.35	4	1.86	0.58	18.4
170	14.96	4	1.86	0.58	69.28
171	14.49	4	1.86	0.58	81.36
172	16.06	4	1.86	0.58	40.45
173	17.13	4	1.86	0.58	28.15
174	14.06	4	1.86	0.58	54.08
175	13.87	4	1.86	0.58	74.54
176	14.53	4	1.9	0.51	60.86

	177	13.73	4	1.9	0.51	73.67
	178	13.99	4	1.9	0.51	35.13
	179	12.74	4	1.9	0.51	71.95
	180	15.07	4	1.9	0.51	78.78
	181	13.21	4	2.1	0.67	54.54
	182	13.99	4	2.1	0.67	66.8
	183	14.41	4	2.1	0.67	70.53
	184	14.11	4	2.1	0.67	39.62
	185	17.02	4	2.1	0.67	12.35
	186	12.37	4	1.83	0.58	61.87
	187	13.79	4	1.83	0.58	59.8
	188	14.76	4	1.83	0.58	30.89
	189	13.61	4	1.83	0.58	64.98
	190	15.61	4	1.83	0.58	29.35
	191	15.48	4	2.06	0.61	22.64
	192	16.75	4	2.06	0.61	45.46
	193	15.02	4	2.06	0.61	71.16
	194	14.63	4	2.06	0.61	76.85
	195	14.57	4	2.06	0.61	36.22
	196	13.8	4	1.84	0.47	59.05
	197	14.48	4	1.84	0.47	74.77
	198	12.53	4	1.84	0.47	36.71
	199	13.78	4	1.84	0.47	35.42
	200	13.63	4	1.84	0.47	73.88
Mean Dpar	2.03					
Mean Dper	0.47					
Mean Length (µm)	14.12	0.11				
Std. Dev. (µm)	1.62					
Skewness	-1.18					

Kurtosis 2.38

Haiyuan Fault East (HFE)

Apatite (U-Th)/He

Sample #	U (ppm)	Th (ppm)	He (nmol/g)	Mass (µg)	Radius (µm)	Length (µm)	F_T
$HFE11_A$	6.67	8.43	0.56	1.51	47.5	83	0.65
$HFE11_B$	7.14	11.29	1.23	1.57	48.5	83	0.65
$HFE11_C$	8.67	11.39	1.07	2.83	51	135	0.71
$HFE11_D$	11.36	14.50	2.16	2.06	48	111	0.68

Sm (ppm)	Raw Age (Ma)	Corrected Age (Ma)	Elevation (m)
63.18	11.75	17.96	2308
47.96	22.97	35.00	
67.94	17.13	24.18	
68.41	26.66	39.11	

Apatite Fission Track (age data)

Sample#	Grain #	N_s	Area (cm x cm)	$^{238}U/^{43}Ca$ (dmnls)	1σ (dmnls)	^{43}Ca	^{238}U
HFE11	1	22	2.91E-05	3.84E-02	3.84E-03	3.23E-02	3.43E-03
	2	7	1.21E-05	2.28E-02	2.28E-03	3.06E-02	6.85E-03
	3	15	2.91E-05	3.63E-02	3.63E-03	3.07E-02	2.64E-03
	4	12	1.75E-05	4.30E-02	4.30E-03	3.02E-02	1.08E-03
	5	16	2.33E-05	3.73E-02	3.73E-03	2.87E-02	3.66E-03
	6	13	1.94E-05	2.77E-02	2.77E-03	3.07E-02	2.77E-03
	7	9	1.16E-05	3.20E-02	3.20E-03	3.80E-02	1.13E-03

8	11	1.94E-05	2.98E-02	2.98E-03	4.58E-02	2.46E-03
9	12	1.75E-05	3.57E-02	3.57E-03	3.67E-02	2.21E-03
10	7	1.75E-05	2.84E-02	2.84E-03	3.51E-02	9.34E-03
11	8	1.94E-05	4.87E-02	4.87E-03	4.05E-02	7.88E-03
12	13	1.75E-05	3.41E-02	3.41E-03	3.51E-02	5.01E-03
13	11	1.94E-05	2.93E-02	2.93E-03	3.80E-02	3.88E-03
14	18	3.11E-05	4.23E-02	4.23E-03	3.38E-02	1.51E-03
15	8	1.46E-05	4.10E-02	4.10E-03	4.55E-02	1.07E-02
16	18	1.94E-05	4.27E-02	4.27E-03	3.45E-02	7.56E-03
17	9	1.94E-05	4.38E-02	4.38E-03	3.06E-02	1.01E-03
19	9	1.94E-05	3.86E-02	3.86E-03	4.25E-02	7.08E-04
20	17	3.11E-05	3.78E-02	3.78E-03	3.95E-02	3.10E-03
21	11	1.75E-05	3.47E-02	3.47E-03	3.37E-02	4.64E-03
22	9	1.21E-05	3.95E-02	3.95E-03	4.29E-02	3.19E-03
23	14	1.75E-05	4.58E-02	4.58E-03	4.00E-02	5.33E-03
25	21	2.91E-05	3.52E-02	3.52E-03	4.75E-02	7.18E-03
26	11	1.46E-05	3.99E-02	3.99E-03	5.74E-02	5.57E-03
27	13	2.91E-05	3.85E-02	3.85E-03	5.90E-02	5.64E-03
28	13	1.75E-05	4.07E-02	4.07E-03	6.16E-02	1.06E-02
29	14	2.43E-05	3.27E-02	3.27E-03	4.44E-02	4.86E-03
30	2	3.11E-05	1.67E-03	1.67E-04	3.91E-02	1.17E-01
31	7	1.16E-05	3.55E-02	3.55E-03	3.99E-02	1.19E-03
32	14	1.94E-05	3.29E-02	3.29E-03	4.24E-02	2.26E-03
33	12	3.88E-05	3.32E-02	3.32E-03	4.43E-02	6.42E-03
34	12	2.91E-05	3.39E-02	3.39E-03	4.05E-02	5.19E-03
36	7	1.16E-05	3.84E-02	3.84E-03	4.97E-02	3.44E-03
37	11	1.36E-05	3.14E-02	3.14E-03	6.06E-02	1.17E-02
38	7	1.21E-05	4.03E-02	4.03E-03	4.54E-02	9.60E-03
39	20	2.91E-05	4.12E-02	4.12E-03	4.22E-02	3.39E-03

	40	15	1.75E-05	3.51E-02	3.51E-03	3.90E-02	3.13E-03
^{232}Th	**^{147}Sm**	**FT Age (Ma)**	**2σ (Ma)**	**Etch**	**Dpar (µm)**	**Dper (µm)**	**U (ppm)**
4.73E-02	3.05E-02	157.08	74.26	4	1.45	0.17	13.47
3.09E-02	1.91E-02	200.97	157.36	4	1.45	0.2	8.01
3.44E-02	3.68E-02	113.46	63	4	1.74	0.17	12.75
2.34E-02	2.58E-02	127.56	78.12	4	1.27	0.12	15.11
4.66E-02	1.61E-02	147.16	79.48	4	1.43	0.17	13.08
4.70E-02	2.43E-02	192.37	113.7	4	1.48	0.15	9.72
3.04E-02	3.88E-02	191.82	133.74	4	1.48	0.21	11.25
2.78E-02	2.31E-02	151.88	96.68	4	1.4	0.16	10.45
4.75E-02	3.66E-02	153.32	93.88	4	1.36	0.17	12.55
3.11E-02	3.46E-02	113.05	88.52	3	1.66	0.18	9.96
2.07E-02	1.59E-02	67.91	49.98	4	1.5	0.21	17.11
3.02E-02	3.93E-02	173.57	102.58	4	1.33	0.19	11.99
5.33E-02	2.57E-02	154.4	98.3	4	1.66	0.34	10.28
3.89E-02	2.00E-02	109.78	56.38	4	1.54	0.25	14.83
2.16E-02	2.63E-02	107.2	78.9	4	1.54	0.29	14.41
6.24E-02	2.54E-02	172.91	88.82	4	1.53	0.33	15
1.59E-02	1.73E-02	84.91	59.2	4	1.75	0.13	15.37
6.32E-02	2.56E-02	96.31	67.14	4	1.55	0.18	13.54
3.23E-02	2.95E-02	115.9	61	3	1.69	0.15	13.26
5.11E-02	3.75E-02	144.76	92.16	4	1.72	0.37	12.19
5.01E-02	2.91E-02	150.04	104.6	4	1.74	0.16	13.85
4.20E-02	2.14E-02	139.86	80.02	3	1.68	0.37	16.06
5.00E-02	3.44E-02	163.15	78.6	4	1.77	0.22	12.37
7.94E-02	5.91E-02	150.99	96.12	4	1.65	0.24	14.02
2.19E-01	6.98E-02	92.95	54.94	3	1.51	0.21	13.51
2.21E-02	5.09E-02	146.08	86.34	4	2.01	0.28	14.27
3.87E-02	3.81E-02	140.98	80.66	4	1.43	0.26	11.47

6.85E	1.14E-01	33.48	433.64	2	1.55	0.24	0.59
3.15E-02	2.63E-02	135.43	106.04	4	1.35	0.16	12.44
3.27E-02	3.90E-02	174.38	99.76	4	1.43	0.05	11.56
5.41E-02	3.10E-02	74.72	45.76	2	1.75	0.37	11.65
1.72E-02	1.25E-02	97.49	59.7	4	2.11	0.18	11.89
5.61E-02	3.57E-02	125.28	98.1	3	1.52	0.18	13.46
2.47E-02	2.85E-02	204.59	130.24	4	1.51	0.29	11.04
5.46E-02	4.62E-02	114.49	89.64	4	1.65	0.03	14.16
2.98E-02	3.11E-02	133.24	65.5	4	1.55	0.14	14.46
5.46E-02	2.98E-02	194.54	108.02	3	1.59	0.18	12.32

Th (ppm)	**Sm (ppm)**	**Pit Depth (µm)**
11.18	88.37	12.76
11.26	124.3	12.71
12.5	80.44	13.05
12.35	78.2	13.59
11.93	72.94	14.07
10.08	94.67	13.42
9.06	54	11.19
16.04	133.33	9.99
13.02	76.35	10.8
12.32	85.05	12.35
19.6	105.21	11.73
11.85	84.21	12.07
11.52	80.34	12.13
15.35	100.17	13.07
11.84	96.39	12.74
12.19	79.02	12.74
14.08	90.92	14.03
11.59	107.29	10.38

11.65	70.09	11.31
7.36	64.9	12.73
12	74.95	10.56
11.34	141.68	11.3
14.46	74.04	9.89
11.67	80.1	8.44
2.77	54.13	8.07
15.08	84.02	7.77
10.01	80.85	9.85
0.05	27.41	10.66
15.48	90.84	10.96
14.12	83.31	10.35
10.36	87.19	9.28
25.22	167.4	11.06
11.62	95.14	8.08
17.82	126.97	7.16
9.85	75.89	10.95
12.24	83.99	10.54
9.81	65.1	10.95
Mean Dpar	1.58	
Mean Dper	0.21	
Modified Zeta	16.147	0.327
Mean ^{29}Si b:s	0.041	
Mean ^{43}Ca b:s	0.041	
Mean ^{238}U b:s	0.008	
# of grains	37	
Chi-squared	28.6	
Chi-squared prob.	0.8059	

Pooled Age (Ma)	**132.70**	**14.4**

(length data)

Sample#	Track #	Length (µm)	Etch	Dpar (µm)	Dper (µm)	Angle to c-axis (°)
HFE11	1	8.79	4	1.74	0.1	55.22
	2	12.35	4	1.74	0.1	68.41
	3	10.39	4	1.74	0.1	68.71
	4	13.27	4	1.74	0.1	84.69
	5	9.98	4	1.74	0.1	63.1
	6	12.73	4	1.74	0.1	79.35
	7	12.57	4	1.74	0.1	44.92
	8	11.19	4	1.74	0.1	39.67
	9	11.73	4	1.74	0.1	58.53
	10	10.44	4	1.74	0.1	45.15
	11	10.68	4	1.74	0.1	42.59
	12	10.06	4	1.74	0.1	88.8
	13	13.59	4	1.74	0.1	23.69
	14	10.64	4	1.74	0.1	40.85
	15	12.18	4	1.7	0.12	48.12
	16	10.82	4	1.7	0.12	71.17
	17	11.25	4	1.33	0.11	55.23
	18	14.46	4	1.33	0.11	26.7
	19	10.31	4	1.55	0.25	41.55
	20	9.93	4	1.55	0.25	45.85
	21	12.47	4	1.55	0.25	89.64
	22	10.06	4	1.55	0.25	40.2
	23	13.1	4	1.52	0.25	31.3
	24	10.14	4	1.76	0.14	48.04
	25	10.95	4	1.76	0.14	43.97

26	8.1	4	1.76	0.14	62.83
27	10.32	4	1.58	0.06	62.15
28	12.07	4	1.58	0.06	64.8
29	9.62	4	1.52	0.18	58.19
30	10.52	4	1.52	0.18	74.36
31	12.55	4	1.52	0.18	66.52
32	15.11	4	1.52	0.18	35.78
33	10.15	4	1.39	0.2	79.11
34	14.68	4	1.39	0.2	34.89
35	14.91	4	1.39	0.2	37.35
36	11.83	4	1.39	0.2	53.84
37	8.51	4	1.54	0.16	58.99
38	9.34	4	1.54	0.16	72.11
39	16.65	4	1.52	0.11	24.85
40	13.32	4	1.52	0.11	76.04
41	15.56	4	1.52	0.11	38.9
42	8.51	4	1.28	0.07	70.53
43	13.5	4	1.28	0.07	74.45
44	11.82	4	1.76	0.19	62.18
45	15.37	4	1.76	0.19	35.07
46	12.88	4	1.76	0.19	55.75
47	13.02	4	1.26	0.23	69.61
48	12.89	4	1.26	0.23	44.08
49	9	4	1.26	0.23	49.89
50	10.15	4	1.67	0.2	63.03
51	14.56	4	1.67	0.2	81.27
52	9.29	4	1.67	0.2	74.91
53	12.44	4	1.67	0.2	53.16
54	11.3	4	1.67	0.2	35.96

55	13.86	4	1.67	0.2	41.87
56	10.41	4	1.67	0.2	37.62
57	10.79	4	1.45	0.11	53.01
58	12.38	4	1.3	0.11	72.85
59	14.59	4	1.3	0.11	48.53
60	12.93	4	1.3	0.11	51.86
61	14.62	4	1.3	0.11	29.33
62	12.9	4	1.63	0.28	85.49
63	12.13	4	1.54	0.15	85.98
64	11.86	4	1.54	0.15	78.94
65	14.18	4	1.54	0.15	69.55
66	13.23	4	1.61	0.25	56.96
67	10.32	4	1.61	0.25	55.77
68	8.87	4	1.61	0.25	88.43
69	11.38	4	1.38	0.16	16.01
70	12.02	4	1.38	0.16	24.53
71	12.93	4	1.38	0.2	74.68
72	14.02	4	1.38	0.2	42.68
73	10.59	4	1.38	0.2	73.53
74	13.83	4	1.03	0.26	51.16
75	13.95	4	1.03	0.26	54.54
76	9.76	4	1.03	0.26	81.3
77	12.68	4	1.51	0.19	84.92
78	13.53	4	1.33	0.2	71.04
79	14.57	4	1.17	0.14	56.43
80	15.01	4	1.17	0.14	48.52
81	15.04	4	1.43	0.19	43.11
82	9.88	4	1.43	0.19	58.68
83	16.35	4	1.43	0.19	24.49

84	9.38	4	1.52	0.21	54.26
85	14.16	4	1.52	0.21	69.26
86	10.89	4	1.44	0.23	41.63
87	10.27	4	1.44	0.23	49.63
88	13.57	4	1.44	0.23	46.61
89	8.46	4	1.44	0.23	86.55
90	12.05	4	1.21	0.11	75.38
91	7.64	4	1.21	0.11	71.73
92	15.6	4	1.3	0.18	76.96
93	12.44	4	1.3	0.21	41.01
94	12.84	4	1.25	0.02	28.76
95	14.09	4	1.25	0.02	40.6
96	12.2	4	1.33	0.14	65.49
97	16.14	4	1.33	0.14	82.68
98	13.15	4	1.67	0.29	75.2
99	13.84	4	1.66	0.1	47.1
100	12.12	4	1.66	0.1	87.32
101	8.21	4	1.66	0.1	62.07
102	12.12	4	1.66	0.1	70.41
103	10.84	4	1.27	0.23	54.76
104	14.98	4	1.27	0.23	8.94
105	12.9	4	1.27	0.23	54.79
106	15.45	4	1.27	0.23	54.08
107	12.87	4	1.99	0.2	44.12
108	14.9	4	1.99	0.2	19.15
109	10.39	4	1.53	0.15	53.15
110	9.49	4	1.53	0.15	48.83
111	11.7	4	1.53	0.15	70.21
112	10.74	4	1.63	0.18	57.89

113	6.87	4	1.37	0.04	68.83
114	9.31	4	1.59	0.15	79.46
115	7.75	4	1.59	0.15	62.53
116	14.84	4	1.59	0.15	34.78
117	13.12	4	1.45	0.07	36.36
118	11.55	4	1.45	0.07	74.41
119	12.01	4	1.45	0.07	65.84
120	12.11	4	1.32	0.16	79.56
121	12.74	4	1.37	0.2	85.68
122	14.04	4	1.64	0.09	49.39
123	17.17	4	1.64	0.09	34.76
124	10.76	4	1.64	0.09	55.09
125	11.06	4	1.26	0.21	60.91
126	9.92	4	1.32	0.1	74.48
127	12.22	4	1.32	0.1	34.85
128	12.95	4	1.48	0.26	81.09
129	13.42	3	1.11	0.09	72.71
130	14.18	4	1.76	0.33	52.1
131	12.05	4	1.76	0.33	48.43
132	10.6	4	1.76	0.33	58.1
133	12.35	4	1.33	0.25	77.17
134	12.99	4	1.33	0.25	27.28
135	14.35	4	1.25	0.25	66.3
136	10.26	4	1.25	0.25	75.89
137	12.58	4	1.44	0.19	67.63
138	13.43	4	1.34	0.25	24.02
139	13.29	4	1.34	0.25	56.26
140	14.01	4	1.32	0.37	31.43
141	13.86	4	1.54	0.24	67.15

142	13.39	4	1.54	0.24	38.53
143	14.85	4	1.54	0.24	35.97
144	15.68	4	1.53	0.25	46.48
145	14.67	4	1.53	0.25	44.06
146	12.31	4	1.53	0.25	80.94
147	16.26	4	1.53	0.25	43.28
148	11.91	4	1.78	0.25	56.28
149	12.81	4	1.78	0.25	89.12
150	11.12	4	1.78	0.25	79.18
151	12.06	4	1.78	0.25	56.51
152	14.32	4	1.57	0.12	33.86
153	13.61	4	1.18	0.16	80.81
154	9.81	4	1.18	0.16	68.55
155	8.49	4	1.71	0.05	56.35
156	10.58	4	1.71	0.05	45.51
157	9.57	4	1.71	0.05	52.9
158	13.28	4	1.51	0.21	53.23
159	15.17	4	1.51	0.21	42.11
160	9	4	1.51	0.21	80.08
161	9.06	4	1.44	0.24	42.14
162	13.47	4	1.44	0.24	81.1
163	11.77	4	1.6	0.18	21.02
164	13.52	4	1.58	0.37	40.34
165	15.02	4	1.54	0.34	36.77
166	11.82	4	1.54	0.34	68.92
167	14.53	4	1.54	0.34	70.45
168	14.61	4	1.54	0.34	42.92
169	14.17	4	1.51	0.26	37.27
170	13.34	4	1.51	0.26	46.24

171	13.91	3	1.43	0.26	36.69
172	10.4	4	1.47	0.25	59.9
173	12.78	4	1.47	0.25	65.45
174	14.48	4	1.38	0.1	32.79
175	12.98	4	1.38	0.1	41.57
176	14.03	4	1.38	0.1	45.08
177	14.45	4	1.38	0.1	56.77
178	10.62	4	1.38	0.1	62.29
179	11.81	4	1.25	0.23	47.78
180	13.29	4	1.25	0.23	86.17
181	13.05	3	1.64	0.3	65.7
182	12.68	4	1.27	0.14	59.08
183	10.56	4	1.27	0.14	64.45
184	14.99	4	1.27	0.14	33.55
185	13.15	4	1.31	0.19	44.94
186	11.71	4	1.39	0.11	85.43
187	14.33	4	1.39	0.11	14.4
188	8.65	4	1.39	0.11	55.41
189	8.97	4	1.39	0.11	85.44
190	12.75	4	1.57	0.25	84.13
191	12.82	4	1.57	0.25	83.91
192	17.01	4	1.57	0.25	29.04
193	13.13	4	1.57	0.25	47.3
194	11.95	4	1.4	0.2	51.98
195	15.76	4	1.4	0.2	29.19
196	6.71	4	1.4	0.2	64.55
197	11.09	4	1.47	0.11	76.53
198	13.97	4	1.51	0.18	47.6
199	13.02	4	1.47	0.25	80.55

	200	13.09	4	1.47	0.25	33.45
	201	10.05	4	1.47	0.25	50.17
Mean Dpar	1.49					
Mean Dper	0.18					
Mean Length (µm)	12.28	0.2				
Std. Dev. (µm)	2.11					
Skewness	-0.21					
Kurtosis	-0.47					

Dulan-Chaka Highland

Apatite (U-Th)/He: DCH vertical transect 1

Sample #	U (ppm)	Th (ppm)	He (nmol/g)	Mass (µg)	Radius (µm)	Length (µm)	F_T
$DCH12_A$	7.70	35.33	2.79	2.01	49.5	121	0.68
$DCH12_B$	4.82	13.29	2.12	1.40	51	87	0.66
$DCH12_C$	5.66	23.85	1.00	2.65	49.5	138	0.69
$DCH12_D$	9.42	39.55	3.13	2.04	47.5	139	0.68
$DCH13_A$	10.56	42.78	3.58	1.90	40	134	0.64
$DCH13_B$	8.12	21.23	1.18	3.04	48.5	167	0.70
$DCH13_C$	6.30	19.12	1.34	2.51	48.5	122	0.68
$DCH13_D$	6.36	20.76	1.84	1.72	43.5	105	0.64
$DCH14_A$	24.88	42.83	2.00	2.47	40	142	0.65
$DCH14_B$	27.87	43.25	2.73	2.38	47.5	131	0.69
$DCH14_C$	26.36	47.24	1.68	2.02	43.5	148	0.67
$DCH14_D$	20.81	43.41	1.67	2.63	54.5	120	0.71
$DCH15_A$†	34.84	61.81	4.13	2.39	51	133	0.70
$DCH15_B$	35.36	62.70	3.06	2.85	56.5	137	0.72

$DCH15_C$	30.53	60.01	2.94	3.35	54	156	0.72
$DCH15_D$	24.35	55.52	2.35	2.38	48.5	137	0.69
$DCH16_A$[†]	38.26	71.21	4.58	3.49	47.5	184	0.71
$DCH16_B$	37.46	63.78	2.67	2.93	53.5	144	0.72
$DCH16_C$	41.01	66.29	2.92	2.80	51.5	128	0.70
$DCH16_D$	14.29	45.55	1.08	3.17	46	138	0.68

Sm (ppm)	Raw Age (Ma)	Corrected Age (Ma)	Elevation (m)
249.27	31.41	45.67	4302
264.76	47.16	69.64	
188.24	16.02	22.95	
302.86	30.14	43.70	
277.02	31.37	48.51	4198
168.83	16.27	23.00	
211.51	22.23	32.27	
242.97	29.34	44.83	
251.06	10.43	15.92	4093
212.55	13.10	18.97	
240.82	8.19	12.09	
248.45	9.81	13.81	
202.91	15.30	21.73	3986
187.43	11.17	15.40	
166.80	12.04	16.61	
192.80	11.47	16.53	
158.81	15.24	21.55	3867
139.95	9.34	13.00	
139.73	9.47	13.45	
146.74	7.91	11.64	

Apatite (U-Th)/He: DCH vertical transect 2

Sample #	U (ppm)	Th (ppm)	He (nmol/g)	Mass (µg)	Radius (µm)	Length (µm)	F_T	Sm (ppm)	Raw Age (Ma)	Corrected Age (Ma)	Elevation (m)
$DCH17_A$†	26.64	46.37	18.68	3.13	60	162	0.75		90.90	121.53	4598
$DCH17_B$	16.16	40.04	3.49	2.25	45.5	202.5	0.70		25.10	35.91	
$DCH17_C$									25.85	36.96	
$DCH17_D$									22.38	32.93	
$DCH18_A$†	0.98	3.66	1.12	2.93	57.5	165	0.73		110.53	150.33	4473
$DCH18_B$	12.75	38.81	2.81	2.67	53	177	0.72		23.60	32.62	
$DCH18_C$	13.64	42.34	2.25	2.59	45	238.5	0.70		17.54	25.01	
$DCH18_D$	20.34	38.76	2.59	2.12	50.5	154.5	0.71				
$DCH19_A$	73.48	87.16	7.42	2.66	44.5	250.5	0.71				
$DCH19_B$	52.51	84.38	6.41	2.01	48.5	159	0.70				
$DCH19_C$	54.98	49.47	4.83	1.58	45	145.5	0.69				
$DCH20_A$	17.46	56.21	1.66	1.23	41	136.5	0.65				
$DCH20_B$	29.54	41.64	1.78	2.47	46.5	213	0.71				
$DCH20_C$	17.16	35.01	1.44	2.15	53	142.5	0.71				
$DCH21_A$	33.98	28.15	1.61	1.12	41	124.5	0.66				
$DCH21_B$	88.99	149.90	6.71	1.72	44	165	0.68				
$DCH21_C$	21.27	30.12	1.11	1.78	42.5	183	0.68				
$DCH21_D$	47.81	52.85	3.27	2.07	51.5	145.5	0.71				

	16.18	22.80	
	14.52	20.52	4276
	16.28	23.12	
	13.34	19.43	
	9.93	15.28	4100
	8.35	11.75	
	10.44	14.62	
	7.31	11.16	3924
	9.93	14.51	
	7.20	10.55	
	9.98	13.97	

Apatite (U-Th)/He: DCH vertical transect 3

Sample #	U (ppm)	Th (ppm)	He (nmol/g)	Mass (µg)	Radius (µm)	Length (µm)	F_T
$DCH22_A$	9.47	19.53	2.57	4.23	47.00	192.60	0.71
$DCH22_B$	24.45	47.24	5.16	3.98	47.45	159.10	0.70
$DCH22_C$†	19.61	29.45	2.12	4.31	56.75	150.70	0.73
$DCH22_D$	13.61	60.10	5.62	2.90	50.00	124.70	0.69
$DCH23_A$	21.38	44.73	2.96	4.05	48.10	140.80	0.69
$DCH23_B$	15.08	50.03	1.43	2.83	51.65	107.90	0.68
$DCH23_C$	41.31	32.32	3.19	2.41	45.60	92.10	0.66
$DCH24_A$	129.91	141.11	48.43	7.03	66.05	190.70	0.77
$DCH24_B$†	65.26	93.29	37.97	2.40	50.70	113.50	0.69
$DCH24_C$	122.98	128.16	30.67	2.13	42.80	95.80	0.64
$DCH25_A$	19.32	64.02	1.64	4.28	49.75	182.30	0.71
$DCH25_B$	8.23	17.86	0.77	2.69	46.50	120.90	0.67
$DCH25_C$‡	96.07	127.58	22.68	5.33	62.80	145.10	0.75
$DCH25_D$‡	16.10	32.47	4.51	8.03	64.20	184.20	0.76

$DCH26_A$	12.50	47.54	3.29	3.18	44.65	160.00	0.68
$DCH26_B$	20.92	65.30	4.19	2.94	45.10	108.80	0.66
$DCH26_C$	8.78	37.86	1.25	3.00	47.00	149.80	0.68
$DCH26_D$	7.32	24.55	1.35	3.69	54.35	135.00	0.71

Sm (ppm)	Raw Age (Ma)	Corrected Age (Ma)	Elevation (m)
351.11	32.63	45.66	4808
504.55	26.20	37.26	
411.05	14.43	19.56	
434.81	36.53	52.75	
405.27	16.79	24.05	4548
398.29	9.65	13.98	
375.12	11.90	18.05	
1015.41	54.00	69.55	4407
707.54	78.85	113.19	
902.21	36.49	56.39	
406.86	8.65	12.10	4328
285.99	11.09	16.21	
735.10	32.78	43.63	
308.05	34.31	44.67	
367.60	25.08	36.64	4160
422.18	20.94	31.64	
318.69	12.74	18.42	
290.62	18.42	25.64	

Apatite (U-Th)/He: DCH horizontal transect

Sample #	U (ppm)	Th (ppm)	He (nmol/g)	Mass (µg)	Radius (µm)	Length (µm)	F_T
$DCH27_A$	9.81	22.30	3.48	3.67	43.5	194	0.69
$DCH27_B$†	13.47	26.36	2.69	1.62	40	128	0.64

$DCH27_C$	10.26	23.98	3.99	2.05	50	111	0.68
$DCH27_D$	11.81	23.66	4.25	2.34	41.5	150	0.66
$DCH28_A$	39.45	39.51	3.97	3.06	49.5	150	0.71
$DCH28_B$	33.66	57.12	5.74	1.38	40.5	95	0.63
$DCH28_C$	19.00	54.78	3.74	1.51	42	97	0.63
$DCH28_D$	20.62	20.25	1.84	1.16	42	94	0.64
$DCH29_A$	22.49	35.56	10.75	6.62	54.5	189	0.74
$DCH29_B$	26.13	40.57	11.28	3.27	53	185	0.73
$DCH29_C$	27.05	37.38	11.78	3.08	54	178	0.73
$DHC29_D$	27.41	47.76	12.78	3.70	54	149	0.72
$DCH29_E$	31.94	42.84	17.87	6.18	63.5	189	0.77
$DCH30_A$	18.15	52.21	4.62	2.59	47.5	155	0.69
$DCH30_B$	14.22	47.81	4.51	3.63	44.5	225	0.70
$DCH30_C$	17.69	62.54	6.63	2.27	47	139	0.68
$DCH30_D$	12.40	46.57	3.30	1.46	42	91	0.62

Sm (ppm)	Raw Age (Ma)	Corrected Age (Ma)	Elevation (m)
159.03	41.93	60.61	4143
225.01	24.75	38.08	
210.92	45.30	65.73	
186.14	44.29	66.25	
158.22	14.90	20.99	4083
253.93	22.24	35.35	
208.92	21.41	33.74	
223.73	13.20	20.56	
97.68	63.59	86.04	4123
136.51	57.64	78.64	
141.21	59.92	81.43	
149.84	60.32	83.31	

104.58	77.53	100.97	
163.60	27.70	39.82	4106
140.30	32.30	46.29	
178.06	37.32	54.51	
227.46	25.68	40.94	

†anamolous age: a replicate with age greater than 30% different from the others sample replicates.

‡"rextract": grains that yielded helium upon a second reheating step following the initial laster heating and degassing.

*likely not an apatite

Chapter V

Widespread late Cenozoic increase in erosion rates across the interior of eastern Tibet constrained by detrital low-temperature thermochronometry[1]

Abstract

New detrital low-temperature thermochronometry provides estimates of long-term erosion rates and the timing of initiation of river incision from across the interior of the Tibetan Plateau. The erosion history of this region provides an important means to evaluate proposed models of orogenic development as well as a potential record of regional climatic events. Here we study the externally drained portion of the east-central Tibetan Plateau by sampling from sandbars along major rivers across a transect that spans > 750 km and covers a region with few thermochronometric ages. Apatite grains from eight catchments were analyzed for (U-Th)/He and fission-track thermochronometry. A wide distribution in ages that in most cases spans the entire Cenozoic and late Mesozoic eras requires a long period of slow or no erosion with a relative increase in erosion rate

[1] Citation: Duvall, A.R., Clark, M.K., Avdeev, B., Farley, K.A., and Chen, Z., *in review*, Widespread Late Cenozoic increase in erosion rates across the interior of eastern Tibet constrained by detrital low-temperature thermochronometry: Tectonics.

toward the present. We apply a recently developed methodology for inversion of detrital thermochronometric data for three specified erosion scenarios: constant erosion rate, two-stage erosion history, and three-stage erosion history. Modeling results suggest that rates increase by at least an order of magnitude between 11-4 Ma following a period of slow erosion across the studied catchments. Synchroneity in accelerated erosion across the expanse of the Tibetan Plateau rather than a spatial or temporal progression challenges the widely held notion that the plateau evolved as a steep, northward-propagating topographic front. Instead, we suggest that accelerated river incision late in the orogen's history relates to regional-scale uplift that occurred in concert with eastern expansion of the plateau.

5.1 Introduction

Ongoing India-Eurasia continental convergence since ~55-45 Ma (Rowley, 1996; 1998 and references therein; Zhu et al., 2005; Henderson et al., 2010) is the widely accepted cause of deformation within Tibet and the surrounding region. The manner in which this convergence is accommodated, however, is controversial. A number of competing mechanisms to explain crustal thickening and uplift of this region have been proposed: underthrusting of the Indian lithospheric mantle (Argand, 1924; Powell, 1986) or injection of Indian crust into Tibetan lower crust (Zhao and Morgan, 1987), block extrusion and intracontinental subduction (Tapponnier et al., 1982; 2001), distributed thickening and shortening of Asian lithosphere (England and Houseman, 1986; 1989; Dewey et al., 1988), which may result in the removal of mantle lithosphere from beneath Tibet (Molnar et al., 1993), and preferential thickening of the lower crust through channel flow (Bird, 1991; Royden et al., 1997; Clark and Royden, 2000; Royden et al., 2008).

Temporal records of elevation relate to our mechanical understanding of plateau development because the isostatic response of the continental lithosphere to thickening or reduction in average lithospheric density results in an increase in mean topography. Several attempts to quantify Cenozoic paleoaltimetry from geochemical proxies at various locations within the central Tibetan Plateau suggest that paleoelevations are comparable with modern elevations by at least Miocene time (Garzione et al., 2000; Rowley et al., 2001; Spicer et al., 2003; Currie et al., 2005; Cyr et al., 2005; Rowley and Currie, 2006; DeCelles et al., 2007; Polissar et al., 2009). However, applicability of these results is hindered, at least in part, by limited spatial coverage and large uncertainties (>1000 m) associated with paleoaltimetry techniques. Alternatively, plateau-wide erosion histories from the externally drained part of Tibet may be used as a proxy for timing of elevation change (e.g., Clark et al., 2005; Ouimet et al., 2010) because the erosive response predicted from surface uplift and resulting base-level change should also vary among proposed mechanical scenarios. River steepening, channel narrowing, or some combination of both that likely occurs in response to accelerated surface uplift leads to increased fluvial erosion (Whipple and Tucker, 1999). Increased precipitation and storminess (Reiners et al., 2003) or incision into weaker rocks, however, may also lead to accelerated incision irrespective of surface uplift if topographic relief preexisted.

The influence of climate-enhanced erosion rates is not entirely dissociated from topography. Once even moderately high topography (~3000 m) is achieved, the Himalaya and Tibetan plateau are thought to profoundly influence Asian monsoon processes (e.g., Prell and Kutzbach, 1992; Molnar et al., 1993; An et al., 2001; Molnar, 2005). It is commonly thought that the South Asian monsoon results from increased contrast in air

temperatures between the high-elevation land surface of Tibet and the surrounding lowlands (Flohn, 1968; Li and Yanai, 1996; Yanai and Wu, 2006) and that tectonic uplift of the Tibetan plateau drives increased monsoon intensity (An et al., 2001; Molnar et al., 1993). Recent atmospheric records challenge this view because upper-tropospheric (250 hPa) temperatures are highest, not over the Tibetan plateau, but southward over India and Pakistan (Yanai and Wu, 2006). Rather than acting as a heat source, Global Circulation Model (GCM) results demonstrate that high topography in and surrounding Tibet may be most influential as a barrier to circulation of cool, dry air from the north in the case of the South Asian monsoon (Boos and Kuang, 2010) and as a deflector of the jet stream in the case of the "East-Asian monsoon" (Molnar et al., 2010 and refs. therein), which is actually the head of a mid-latitude storm track (Chao and Chen, 2005). Changes in strength and/or duration of these systems may be reflected in the regional erosion record due to the correlation of spatial patterns of erosion with climatic variability across a landscape (e.g., Montgomery et al., 2001; Reiners et al., 2003; Theide et al., 2004).

Despite the significance of the erosion record, most studies document rates from the perimeter of Tibet while relatively little is known about the erosion history of the plateau interior. In this study, we determine erosion patterns across the Tibetan Plateau using (U-Th)/He and fission tracks in single-grain detrital apatites (nominal closure temperatures ~55 – 75°C and ~100-120°C respectively) (Flowers et al., 2009; Ketcham et al., 2007) collected from modern river sands (Figure 5.1). Detrital studies are best-suited for work of this scope because a single sample contains rock materials integrated from a large spatial area. Applying a recently developed inversion approach that derives erosion histories from thermochronometric ages within each catchment (Avdeev et al., 2011), we

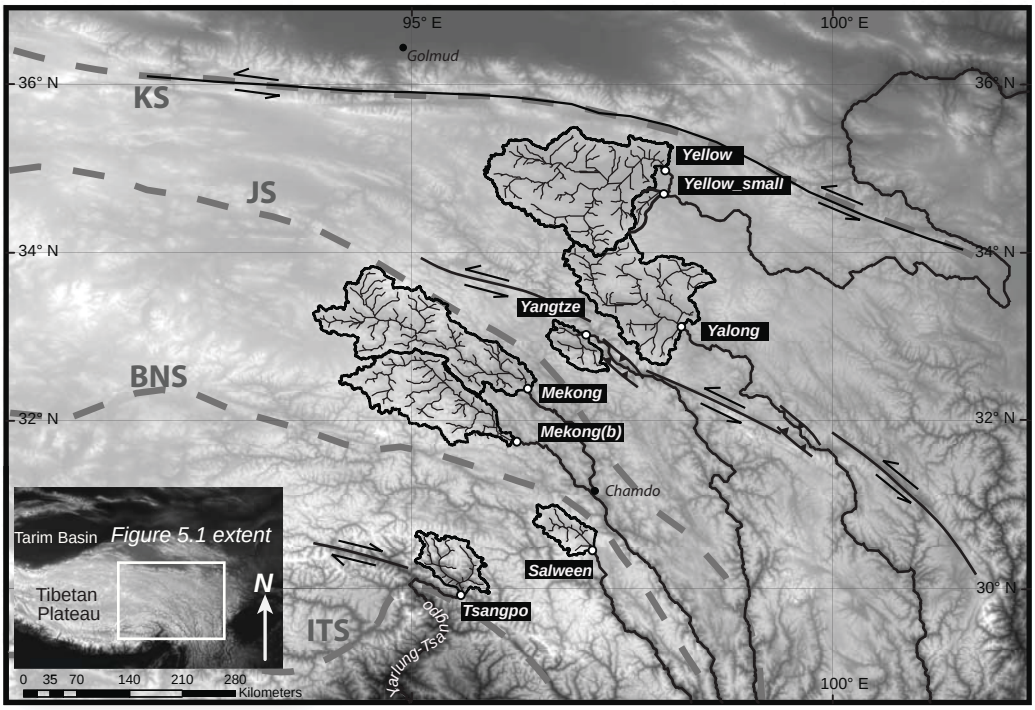

Figure 5.1. Shaded relief map of study area. Sampled catchments outlined in black, circle represents collection sites of modern river sands. Regional faults shown in black (simplified from active fault map of Taylor and Yin, 2009) and suture boundaries shown in thicker gray line: ITS Indus-Tsangpo suture, BNS Bangong Nujiang suture, JS Jingsha suture, KS Kunlun suture. Inset shows broader Tibetan Plateau region.

quantify rates of erosion as well as timing of erosion-rate changes along a NE-SW transect that extends across the entire width of the externally drained portion of the Tibetan Plateau (Figure 5.1).

5.2 Erosion rates across Tibet from previous studies

Short-term erosion rates calculated by measurements of in-situ cosmogenic ^{10}Be in quartz from exposed rock surfaces from the internally-drained Tibetan plateau interior are low during the late Pleistocene – Holocene (< 0.03 mm/yr) with exception of the northern perimeter of the plateau where rates are higher (0.06 – 2 mm/yr) (Figure 5.2a) (Lal et al., 2004). A suite of ^{10}Be detrital data from modern river sands of the Three Rivers Region, SE Tibet (middle reaches of the Salween, Mekong, and Yangtze rivers; Figure 5.2a) yields estimates of millennial basin-wide average erosion rates that vary from 0.01 to 8 mm/yr across catchments that range from small tributaries (drainage area ~2 km^2) to the main trunk rivers (drainage area >300,000 km^2) (Henck et al., 2011). Average erosion rates within the upper river reaches (0.1 – 0.2 mm/yr) are low compared to average rates downstream (0.2 - >1 mm/yr) (Henck et al., 2011). A similar ^{10}Be detrital study from catchments along the eastern margin of the Tibetan Plateau (Figure 5.2a) yields basin-averaged erosion rates that range from 0.03 mm/yr to 3 mm/yr (over timescales of 27,000 to 200 yrs respectively) and are on average ~0.3 – 0.5 mm/yr within the trunk rivers (Ouimet et al., 2009). In addition, small basins draining the frontal part of the Longmen Shan yield mean erosion rates of 0.2 – 0.4 mm/yr (Figure 5.2a) (Godard et al., 2009a).

Longer term erosion rates (10^6 – 10^7 yr timescale) relevant to Cenozoic history of tectonic and climate forcing are derived from low-temperature thermochronometry,

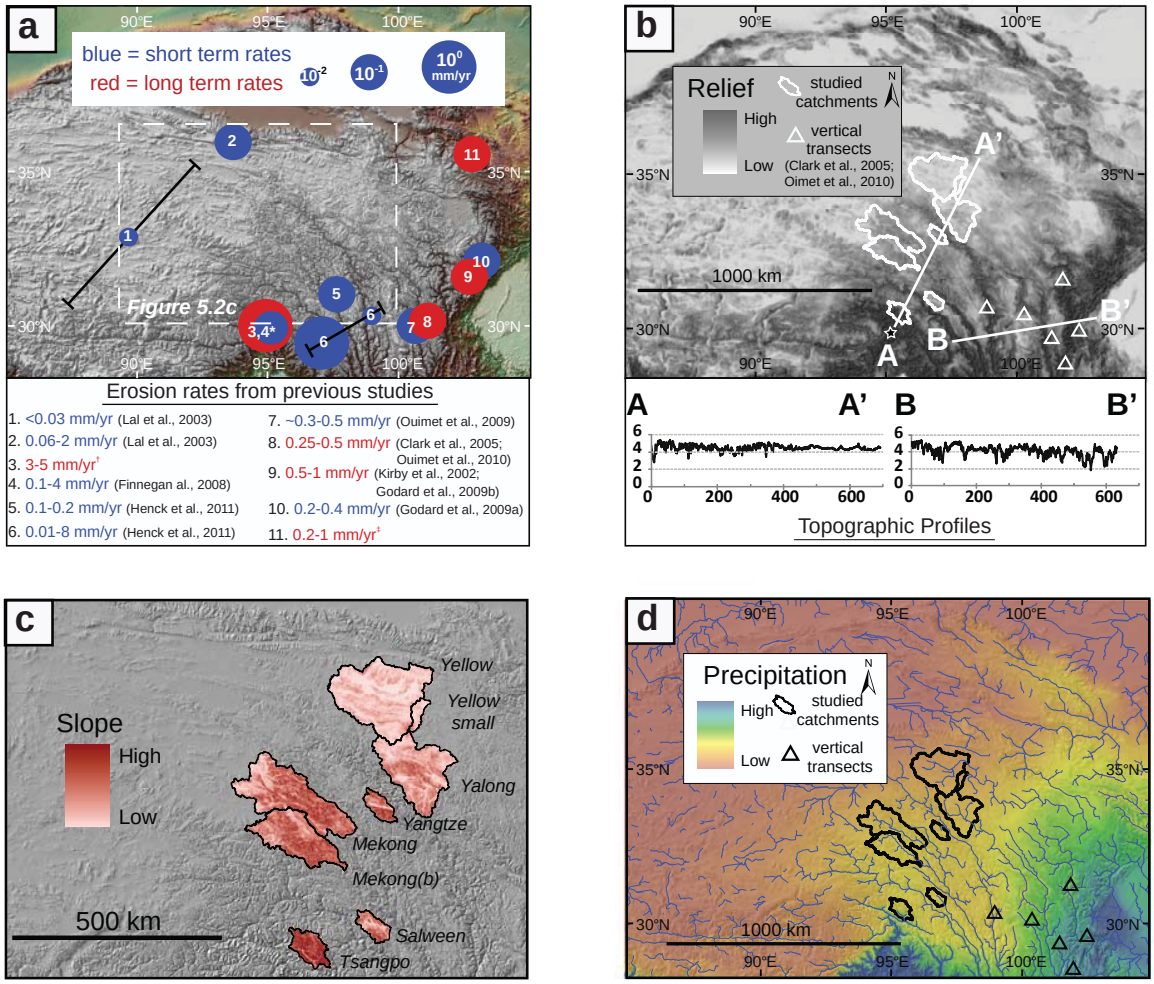

Figure 5.2. Maps of surficial parameters of central and eastern Tibetan Plateau and perimeter. a) Reported erosion rates from previous studies. Circles located at the center of the studied area and weighted based on reported erosion rates, which are shown with corresponding number in the table below. Short-term rates (~10^4-10^5 yrs timescale from cosmogenic radionuclide dating) in blue and long-term rates (~10^6 yrs timescale from low-temperature thermochronometry) in red. Asterisk indicates rates range widely for this location. † Burg et al., 1997; 1998; Ding et al., 2001; Malloy, 2004; Booth et al., 2004; 2009; Zeitler et al., 2006; Seward and Burg, 2008; Stewart et al., 2008. ‡ Jolivet et al., 2001; Zheng et al., 2003; 2006; 2010; Lease et al., 2007; 2011; Clark et al., 2010; Zheng et al., 2010. See section 2 in text for details. b) Relief map generated using a 5km moving average window over 250 m resolution digital elevation map (downsampled 90 m SRTM data). Topographic profiles demonstrate differences in relief between less incised plateau headwaters (A-A') and more incised eastern plateau perimeter (B-B'). Catchments analyzed for detrital thermochronometry in this study outlined in white, previously published bedrock thermochronometry vertical transect locations shown as white triangles (Clark et al., 2005; Ouimet et al., 2010). Black star shows start location for the projected distance line, which is the x-axis of Figure 5.13c). Slope map of study catchments from 90 m SRTM digital elevation data. Map extent shown in panel 2a. Highest slopes shown in red, lowest slopes in white. Note the gradient of shallower slopes across the study transect from south to north. d) Map of annual average precipitation compiled from University of Delaware, Center for Climate Research global climate database (Matsuura and Wilmott, 2007). Warm colors show low precipitation, cool colors represent high precipitation.

which records cooling and exhumation from shallow crustal levels (roughly 2 – 4 km depth). Across the northern plateau region, apatite fission track (AFT) and apatite helium (AHe) bedrock cooling histories suggest increases in erosion to rates of ~0.2-1 mm/yr likely associated with deformation events during Eocene (Jolivet et al., 2001; Clark et al., 2010), Late Oligocene (Jolivet et al., 2001), and mid-to-late Miocene time (Lease et al., 2007; 2011; Zheng et al., 2003; 2006; 2010). Apatite fission-track and helium thermochronology from eastern Tibet suggests that a change from slow to rapid cooling occurred during the mid-to-late Miocene along the southeastern and eastern plateau margins (Arne et al., 1997; Xu and Kamp, 2000; Kirby et al., 2002; Clark et al., 2005; Enkelmann et al., 2006; Godard et al., 2009b; Ouimet et al., 2010; Wilson and Fowler, 2011) (Figure 5.2). This pattern is consistent with an erosional response to crustal thickening and broad regional uplift around this time (Clark et al., 2005; Clark et al., 2006; Wilson and Fowler, 2011). Age/depth data collected along river gorges incised into a low-relief erosion surface yield estimates of late Cenozoic erosion rates on the order of 0.25 – 0.5 mm/yr for the Dadu, Yangtze, and Yalong River gorges (Clark et al., 2005; Ouimet et al., 2010) and 0.5 – 1 mm/yr for the Longmen Shan (Kirby et al., 2002; Godard et al., 2009b) (Figure 5.2a).

Some of the highest erosion rates in the Himalaya-Tibetan orogenic system lie just south of our sampling transect in the Namche Barwa region at the eastern end of the Himalayan syntaxis (Figure 5.2a). Comparisons of high- and low-temperature mineral cooling data ($^{40}Ar/^{39}Ar$ hornblende/biotite, U-Pb zircon, (U-Th)/He zircon/apatite, zircon/apatite fission track) from this area show a "bull's-eye" pattern of very rapid focused exhumation (3 – 5 mm/yr) since 5 Ma or earlier (Burg et al., 1997; 1998; Ding et

al., 2001; Malloy, 2004; Booth et al., 2004; 2009; Zeitler et al., 2006; Seward and Burg, 2008; Stewart et al., 2008). Expansion of the high-exhumation region into the lower Parlung River watershed to the north appears to have occurred since 4 Ma, likely related to growth of a north-plunging antiform (Seward and Burg, 2008). Additionally, short-term basin-wide erosion rates calculated from ^{10}Be analysis range from 0.1 – 4 mm/yr, with the highest rates corresponding to basins with the greatest relief centered on Namche Barwa (Finnegan et al., 2008). Studies of Brahmaputra River sediment flux using detrital zircon fission-track and U-Pb dating for provenance demonstrate that ~50% of the sediment accumulation in the Brahmaputra system comes from only ~2% of its drainage, which further supports the notion of extreme localization of rapid erosion within this region (Stewart et al., 2008).

5.3 Approach and assumptions

We constrain erosion patterns across Tibet by first determining detrital apatite helium and fission-track ages from modern rivers and then combining these data with basin hypsometries to estimate catchment-wide erosion histories. The ^{4}He concentration in apatite is a function of both production rate and temperature-dependent diffusive loss and the rate of fission-track annealing is likewise a function of temperature. Due to relatively low effective closure and annealing temperatures (~55 – 75°C and ~100-120°C, respectively) (Gleadow and Duddy, 1981; Wolf et al., 1996; Farley, 2000; Ketcham et al., 2007; Flowers et al., 2009), both alpha particles and fission tracks are appropriate for assessing thermal histories in the shallow crust (Zeitler et al., 1987; Wolf et al., 1996;1998; Ehlers and Farley, 2003). Closure temperatures vary depending on grain size

and cooling rate (Dodson, 1973) as well as correlate with effective uranium concentration (eU) due to trapping of helium within radiation-damage sites in the apatite crystal (Shuster et al., 2006; Flowers et al., 2009). The effect of radiation damage on T_c and thus apatite age is greatest in cases of high eU and is particularly sensitive to the time a sample spends at temperatures below ~90º C (Shuster et al., 2006; Flowers et al., 2007, Flowers et al., 2009).

In many cases, thermochronometry ages record the sequential cooling of rocks as they are exhumed toward Earth's surface either by erosive processes or normal faulting. Bedrock elevation transects, which are collections of rocks sampled from incremental elevations over short horizontal distances, are used commonly to calculate apparent exhumation rates from the age-elevation gradients (e.g., Fitzgerald and Gleadow, 1990). The overall shape of the age-elevation profile reflects the thermal history of the samples. An obvious increase in gradient (i.e. a "break in slope") indicates an approximate time of increased exhumation rate. However, in the case of prolonged thermal stability followed by cooling related to exhumation, apparent rates deduced from age gradients are only valid where the total amount of exhumation exceeds the depth to the base of the apatite He or FT partial retention zone (e.g., Fiztgerald and Gleadow, 1990). Thus, this sampling approach is useful in assessing long-term geologic exhumation histories (10^6 Ma) rather than recent events unless those recent events are of large magnitude (>2 km). In cases where enough denudation has occurred to reveal the preserved partial-retention/annealing zone (~2-5 km), then age data along the profile provide the onset timing of the denudation event and give information on denudation rate. Alternatively, ages along a vertical transect within a region that experienced millions of years of slow or no cooling

followed by recent and rapid exhumation <~2 km magnitude will largely represent time spent in the partial retention zone and not be useful in determining apparent denudation rates. In this landscape, we interpret age-elevation relationships to relate to the long-term erosion history of the region.

Poor access and sparse bedrock outcrops preclude sampling bedrock for age/elevation profiles in this study. Instead, we utilize modern river sands collected from single sample sites to measure a suite of ages for each catchment. Catchment-wide erosion histories are evaluated using a recently developed methodology for interpreting detrital thermochronometry data (Avdeev et al., 2011). Several assumptions are inherent to this approach. We relate thermochronometry ages to the cooling history of rocks as they move toward the surface by erosion rather than due to cooling of volcanics or shallowly-emplaced plutons or exhumation by normal faulting. Our model results are estimated assuming piece-wise linear age-elevation relationships, just as in a bedrock sampling approach. We derive apparent erosion history assuming vertical advection, a flat closure isotherm, and constant geothermal gradient and surface temperature through time. We also assume that sediment is not stored for significant periods of time ($\leq 10^5$ yrs) within catchments and that erosion rates as well as apatite concentrations in bedrock are spatially uniform.

Catchments without major mapped Cenozoic fault systems (Figure 5.1) were targeted for sampling because we are interested in erosion related to regional processes rather than to local deformation. However, it is possible that unmapped structures and minor splays may be present within our catchments. Topography has been shown to influence the interpretation of erosion rates from the age/elevation relationship, both by warping of

isotherms in the shallow crust and by the effect of cooling rate on the effective closure temperature (e.g., Stüwe et al., 1994; Mancktelow et al., 1997; Braun, 2002; Ehlers and Farley, 2003; Reiners and Brandon, 2006). Therefore, we consider the estimated erosion rates in this study to be apparent and recognize these values may overestimate real long-term rates if significant advection of the isotherms has occurred. However, we note that relief within catchments on the high plateau (generally 1000-2000 m) is focused in trunk rivers, effectively creating short-wavelength topography and therefore the closure isotherms should be relatively flat (Braun, 2002). Regional geologic mapping (Pan et al., 2004) shows widespread occurrence of rock types that likely contain apatite, which diminishes the potential for point sources. Moreover, recent cosmogenic radionuclide (CRN) studies show that sampling larger catchments (>100 km^2 drainage area) for longer-term erosion rates (10^6 years), as we do here, likely averages out temporal and spatial point sources related to sediment flux from isolated landsliding events (Niemi et al., 2005; Yanites et al., 2009).

In previous detrital-thermochronometry studies, time-averaged catchment-wide erosion rates were calculated either by differencing the oldest and youngest ages and the lowest and highest elevations within the catchment (Ruhl and Hodges, 2005) or by using the mean age and elevation within the catchment along with an estimated elevation of the closure isotherm determined from a thermal model (Brewer et al., 2003) (Figure 5.3). The principal limitation in these approaches is the assumption of steady-state erosion histories. In contrast, our approach allows estimation of time-varying thermal histories by using the distribution of elevation and age data from each catchment (Avdeev et al., 2011) (Figure 5.3). We aim to find the simplest geologically reasonable erosion histories

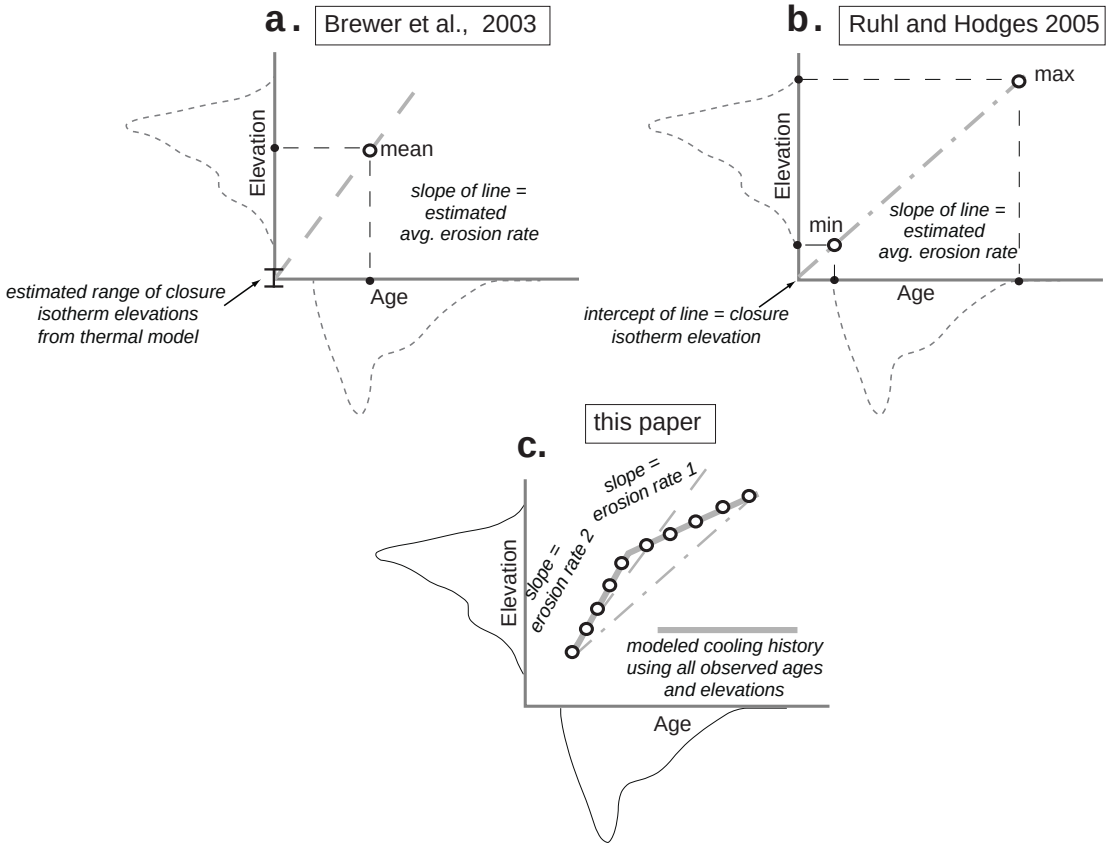

Figure 5.3. Cartoon plots demonstrating different approaches to estimating basin-wide long-term erosion rates a) Method of Brewer et al. (2003): average erosion rate (slope of gray dashed line) determined using the catchment mean cooling age and mean elevation and a range of closure isotherm elevations estimated from a thermal model. b) Method of Ruhl and Hodges (2005): average erosion rate (slope of gray dash/dot line) determined using the catchment minimum and maximum ages and elevations. The intercept of the line is the estimated isotherm elevation. c) Method of this paper: catchment wide cooling histories are modeled using an MCMC algorithm to estimate erosion rate (slope of solid gray line), allowing for more complicated histories (i.e. breaks in slope) (Avdeev et al., 2011). Linear segments from A (dashed line) and B (dash/dot line) are shown for comparison.

that adequately explain the data for each catchment beginning with assessment of constant erosion rate through time. Scenarios with zero or more changes in rate through time were considered until additional erosion-rate changes did not result in a noticeably better fit with the data. We recognize that more complicated alternative histories with spatially varying erosion and non-vertical pathways not considered here may also be permissible.

5.4 Sampled Catchments

We collected detrital samples from modern headwater rivers along a NE-SW transect that spans > 750 km within the externally-drained east-central plateau (Figure 5.1). Catchments along this transect include seven larger basins (drainage area 2000 to 20000 km^2): the Yellow, Yalong, Yangtze, Mekong and Mekong(b) (both part of the Mekong River watershed), Salween, and the Parlung tributary to the Yarlong-Tsangpo, referred to here after simply as Tsangpo, and one smaller basin (1000 km^2), Yellow_small, which is a tributary of the Yellow River (Table 5.1; Figure 5.1). The hypsometry (relation between area and elevation) and landscape characteristics (mean/min/max elevation, slope, and relief) for each catchment were estimated using 90 m resolution SRTM digital elevation data and are shown in Figure 5.2 and Table 5.1. Mean elevation (~4600 m) and mean relief (~1500 m) are similar within the studied river basins, with exception to the high-relief, glaciated Tsangpo catchment (mean relief of f3500 m) (Figure 5.2b; Table 5.1). Mean slope angle decreases from south to north, with lowest average slopes (<10º) in the Yellow and Yalong catchments, middle average slopes (~15º) in the Yangtze, Mekong, Mekong(b) and Salween catchments, and highest average slopes (~25º) in the Tsangpo

Table 5.1 Catchment geomorphology

Catchment Name	Drainage Area (km^2)	Min. Elev. (m)	Max. Elev. (m)	Elev. Range (m)	Mean Elev. (m)	Mean Slope (°)
Tsangpo	3520	2750	6184	3434	4535	24.9
Salween	2401	4318	5646	1328	4799	13.6
Mekong	15869	3748	5796	2048	4681	14.6
Mekong(b)	11150	3663	5682	2019	4751	16.3
Yangtze	2210	3684	5461	1777	4475	16.9
Yalong	14011	3980	5208	1228	4536	8.6
Yellow	19170	4219	5219	1000	4507	3.8
Yellow_small	998	4217	5174	957	4502	4.9

catchment (Figure 5.2c, Table 5.1). The high plateau in the vicinity of our sampled catchments is generally arid with a north to south increase in average annual precipitation that is inversely correlated with slope (~300 mm/yr within the northern catchments and ~600 mm/yr within the southern catchments) (New et al., 2002; Matsuura and Willmott, 2007). In contrast, the surrounding regions to our study area to the south and east are wetter with average annual precipitation as much as 1100 – 1500 mm/yr (New et al., 2002) (Figure 5.2d).

Study-area catchments include mapped geologic units of variable age and rock type (Pan et al., 2004) (Figure 5.4a-h). Paleozoic rocks are predominantly sedimentary, including shale, limestone, sandstone, and conglomerate, with minor amounts of slate, schist, marble, and volcanics. Mesozoic rocks are mainly marine facies mudstone, siltstone, limestone, and sandstone as well as granitoids (granite, granodiorite, quartz diorite), with minor amounts of continental clastic deposits. Cenozoic rocks are less abundant within the study area as we purposefully avoided sampling catchments with large volumes of mapped sedimentary or igneous rocks from this time period to assure minimal sediment storage and that cooling relates to erosion. U-Pb ages measured from detrital zircons from two of the sampled catchments are older than Cenozoic age (Appendix Table A5.3), which supports our assumption that minerals from Cenozoic volcanic rocks or shallowly-emplaced plutons were avoided. Quaternary deposits, mostly fluvial, are present mainly in small volume within all studied catchments.

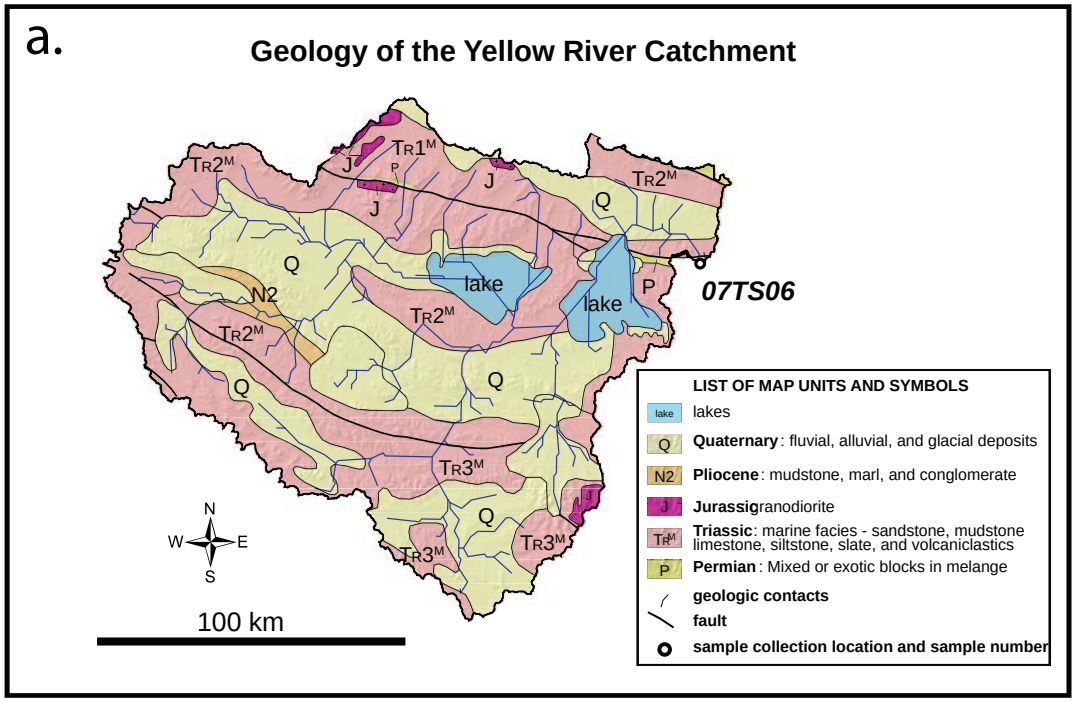

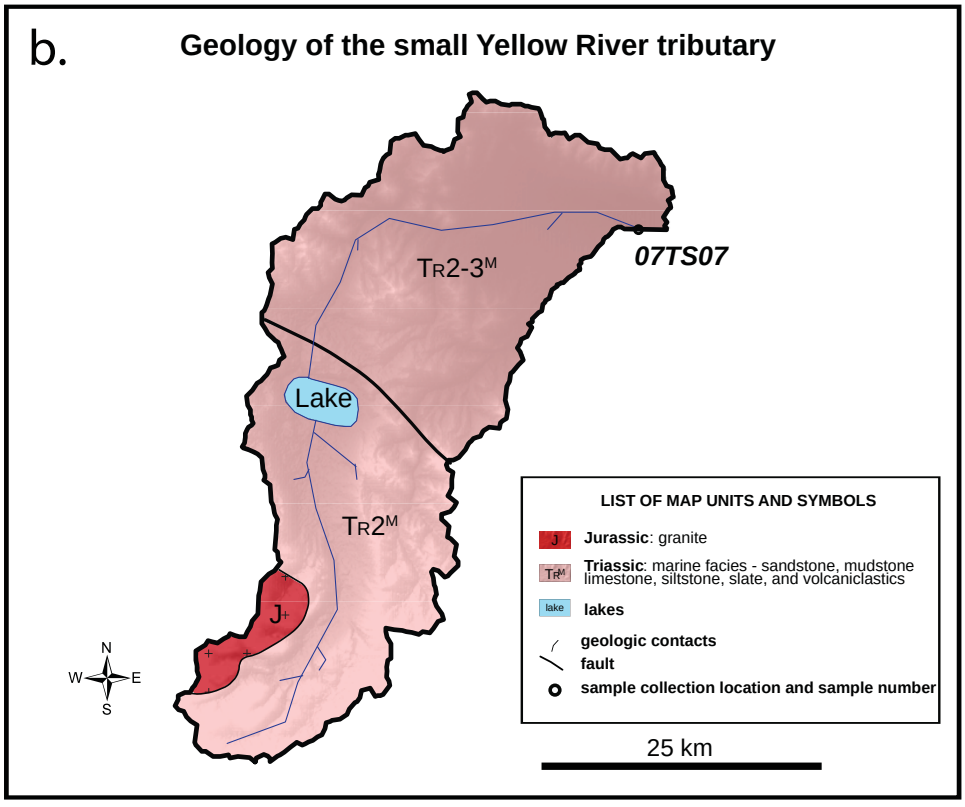

Figure 5.4a-b. Generalized geologic maps of studied catchment a) Yellow River and b) small Yellow River tributary. Geology simplified from 1:1,500,000 geologic map of Pan et al., 2004.

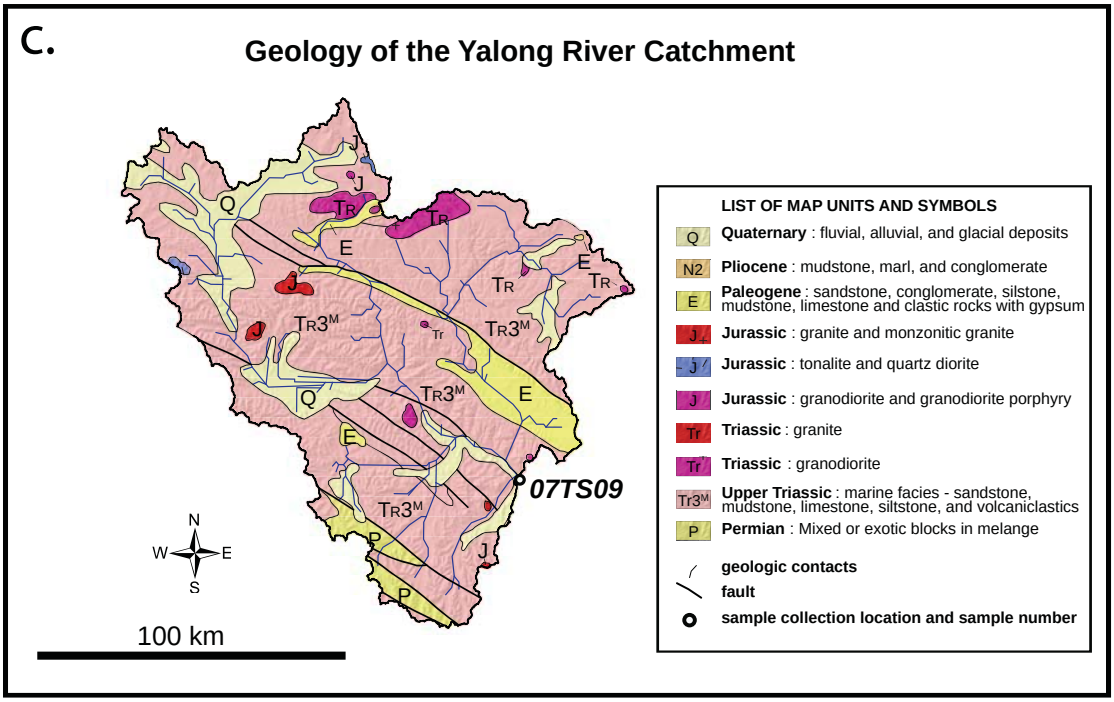

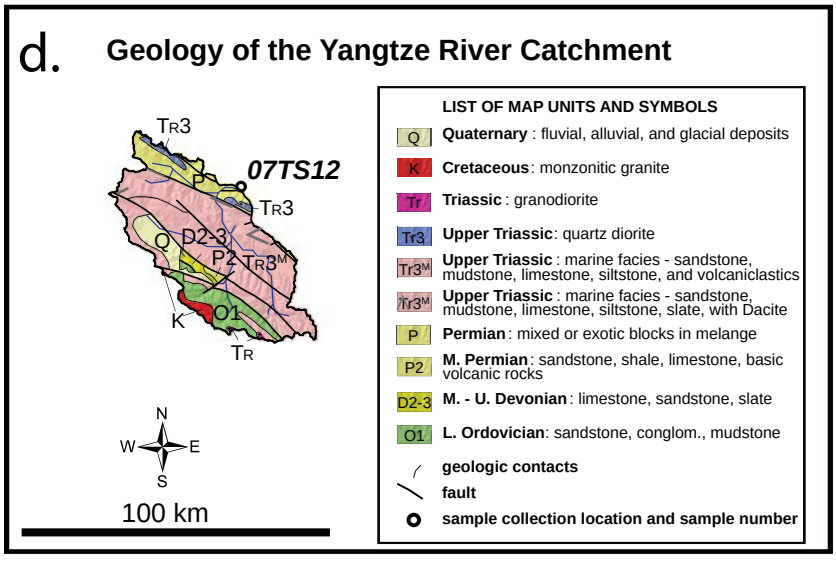

Figure 5.4c-d. Generalized geologic maps of studied catchment c) Yalong River and b) Yangtze River. Geology simplified from 1:1,500,000 geologic map of Pan et al., 2004.

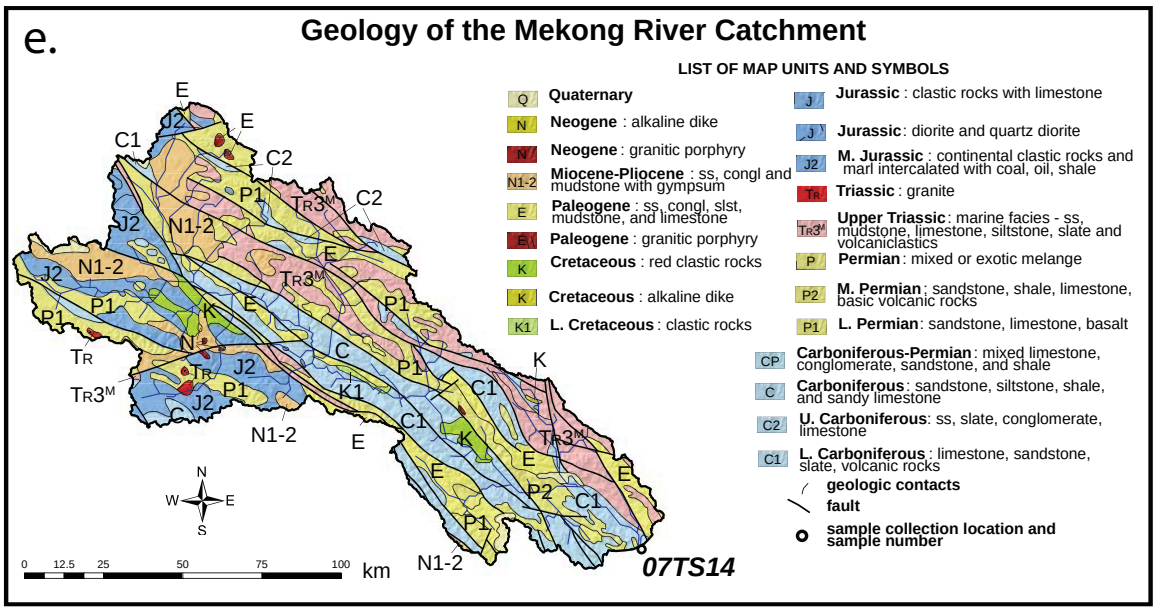

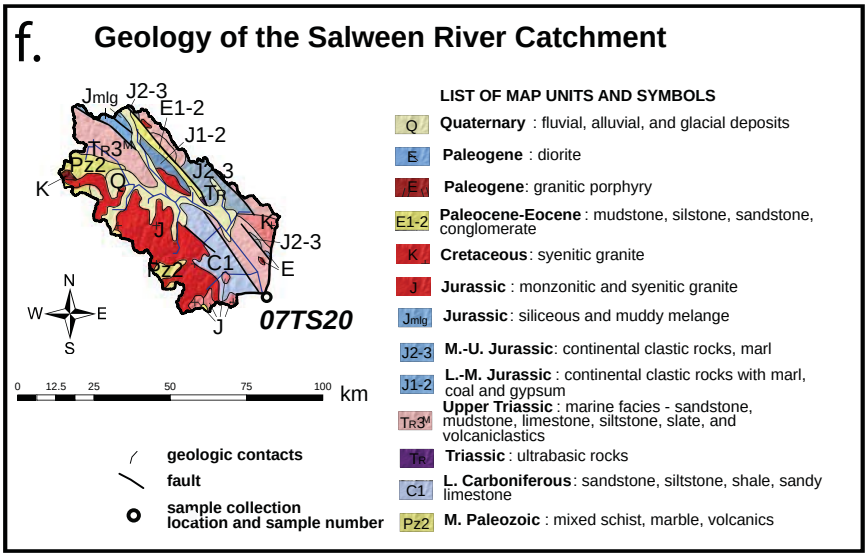

Figure 5.4e-f. Generalized geologic maps of studied catchment e) Mekong River and f) Salween River. Geology simplified from 1:1,500,000 geologic map of Pan et al., 2004.

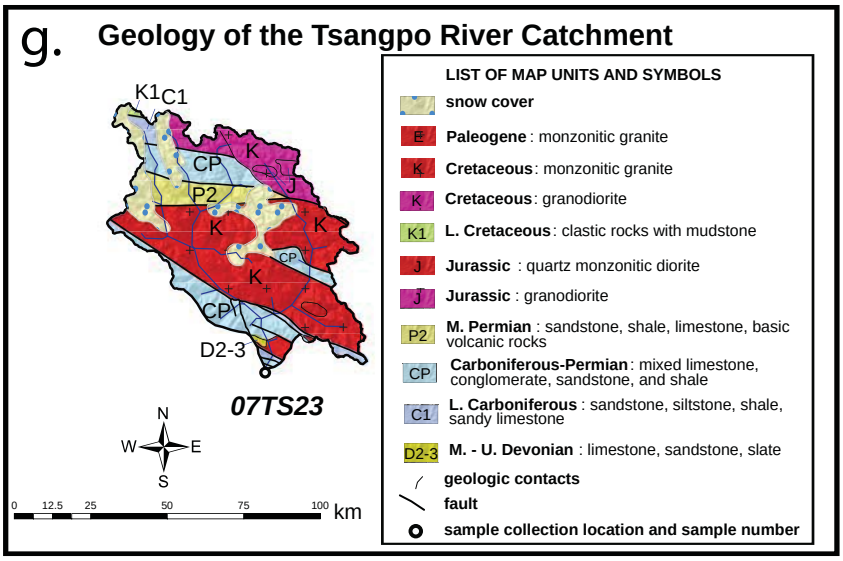

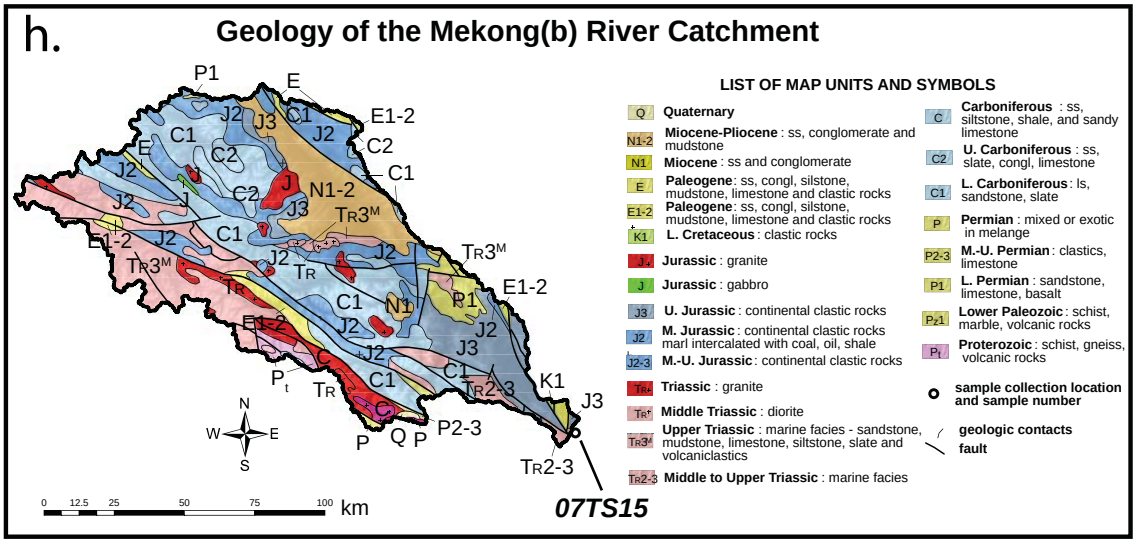

Figure 5.4g-h. Generalized geologic maps of studied catchment g) Tsangpo River and h) Mekong(b) River. Geology simplified from 1:1,500,000 geologic map of Pan et al., 2004.

5.5 Methods

River sands were collected from sandbars within the active channel during the early winter months when river levels were low. To ensure a well-mixed population of material from each catchment, each ~5 kg sample was compiled from multiple smaller aliquots spaced a few meters apart (DeGraaff-Surpless et al., 2003; Lease et al., 2007). Samples were sieved (Standard #18 1,000 μm mesh sieve), washed in de-ionized water and dried in an oven at low temperatures (40°C) then further separated by grain size using a U.S. Standard #60 250 μm mesh sieve. Apatite and zircon separates were derived from these < 250 μm aliquots by exploiting density and magnetic susceptibility differences.

5.5.1 Apatite (U-Th)/He dating (AHe)

Individual apatite grains were handpicked at the University of Michigan and analyzed for (U-Th)/He ages at the Noble Gas Laboratory at Caltech with ~20 single-grain analyses for each sample (135 total grains analyzed, Appendix Table A5.1). To avoid additional bias, we selected grains of varying morphology rather than preferentially picking only euhedral, unbroken grains as is common in bedrock studies. In many catchments, this resulted in morphologies that range from pristine to rounded (Figure 5.5) but all grains were selected to have minimal visible inclusions using a Leica MZ16 stereozoom microscope under cross polarization at 160x magnification. Single grains were loaded into a platinum packet and laser heated in a vacuum to 1025ºC for five minutes to release all helium. Helium was measured in a quadrupole mass spectrometer using ^{3}He isotope dilution. After initial degassing, samples were reheated to ensure complete release of helium. Analyses that yield helium upon a second reheating step ("re-

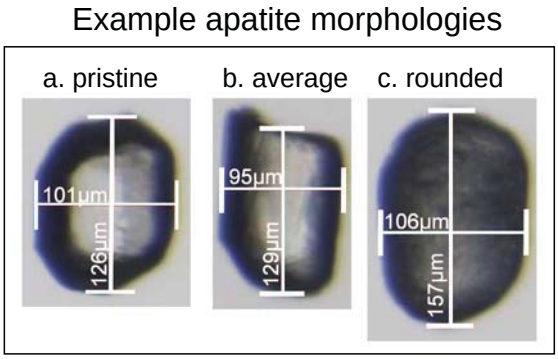

Figure 5.5. Digital images of typical apatite grains selected for helium analysis in this study. Grains categorized into three classes: a. Example of "pristine" apatite grains, which are generally clear, euhedral, and in many cases, has well-preserved terminations at either ends of the crystal. b. Example of "average" apatite grain, which are relatively glassy, have decent crystal form but that lack one or both well-preserved terminations and possibly have broken edges. These are similar to typical apatites dated in bedrock helium studies. c. Example of "rounded " grains, which are those that are significantly weathered such that edges are abraded, grains are clouded, and the grain is somewhat spherical rather than euhedral cylindrical.

extract") likely contain inclusion(s) of a different radiogenic mineral phase, such as zircon. In this study, no samples yielded significant re-extraction of gas during this step. After gas extraction, each grain was placed in HNO_3, spiked with ^{235}U and ^{230}Th and heated to 95ºC for one hour to facilitate complete dissolution. The solution was analyzed on an inductively coupled plasma mass spectrometer (ICP-MS) for uranium and thorium content. Raw and "corrected" ages were calculated for each replicate. The alpha-ejection correction (F_T) is based on the measured size of the grain and is applied to correct for ^4He ejected from the grain due to the long distance (~20 μms) that alpha particles travel during production (Farley et al., 1996). Apatite grains in this study ranged from 40 μms to 75 μms in prism half-width and F_T values ranged from 0.61 to 0.8 (Table 5.2). Grain abrasion during transport has been shown to complicate alpha-ejection correction in detrital apatite helium studies (Rahl et al., 2003), which we considered when calculating corrected ages (see section 5.6.1).

5.5.2 Apatite fission track (AFT)

Apatite fission-track ages were determined for six of the larger catchments and the one small catchment by Apatite to Zircon, Inc. (Donelick et al., 2005), with ~40 single grains analyzed per sample (275 total grains analyzed, Appendix Table A5.2). Natural fission tracks were revealed by immersing polished apatite grain mounts in 5.5N HNO_3 for 20 s (±0.5 s) at 21ºC (±1 ºC). Grain mounts were then irradiated with ~10^7 tracks/cm^2 from a ^{252}Cf source in a vacuum chamber in order to measure horizontal, confined tracks, and track lengths. Fission-track ages were determined using a modified decay equation that includes calibration for the LA-ICP-MS using the Durango fluorapatite standard (fission-

Table 5.2 Detrital thermochronometry age summary

Catchment	N^{a}_{AHe}	AHe age range (Ma)	N^{b}_{AFT}	AFT age range (Ma)	Elev. Range (m)	Mean Elev. (m)
Tsangpo	19	1.17-14.29	40	1.33-44.46	2750-6184	4535
Salween	20	28.2-145.12	40	13.21-145.99	4318-5646	4799
Mekong	10	9.98-57.12	0	-	3663-5682	4681
Mekong(b)	20	9-76.4	40	9.32-224.27	3748-5796	4751
Yangtze	20	3.93-72.69	40	3.01-264.66	3684-5461	4475
Yalong	19	12.57-143.92	40	5.42-163.29	3980-5208	4536
Yellow	20	4.32-160.22	40	16.24-238.30	4219-5219	4507
Yellow_small	17	32.11-203.73	35	21.66-277.91	4217-5174	4502

[a]Number of apatite grains analyzed for (U-Th)/He.
[b]Number of apatite grains analyzed for fission track.

track age of 30.6 Ma) (Donelick et al., 2005). The discrete nature of tracks formed by spontaneous fission biases the age estimate for grains with zero to few counts. This is less of an issue in bedrock studies that typically report an average of 20-40 single grain ages or a pooled age, which is calculated from the sum of spontaneous counts divided by the sum of induced counts for all grains analyzed per sample. However, in our detrital approach, we rely on every individual age and therefore apply a 1/2 track correction in calculating ages, which has negligible effect for grains with large counts (Galbraith, 2005). The average difference between the ages calculated with and without the track correction is less than 10% among the 275 grains analyzed (Appendix Table A5.2).

5.5.3 Inverse detrital erosion models

We jointly model AHe and AFT data for each catchment using a Bayesian estimation technique (Avdeev et al., 2011) to estimate specified erosion models that, in some cases, allow for changes in spatially uniform erosion rate through time. Estimates of free model parameters, which are erosion rates (e_i in km/My), age of change in erosion rate (α_{br} in My), and modern elevation of the closure isotherm (h_c in km), were obtained (see supplementary materials and Avdeev et al., 2011 for further method details). All inversion models in this study are based on the following likelihood function that defines the probability of the observed detrital data given values of model parameters and hypsometry

$$p_d(\alpha) = \iint_W p_b(h(w), \alpha)\, dw \qquad (1)$$

where p_d is the probability density of observing a detrital grain with age α and is an integral of the probability of observing this age in bedrock p_b over a watershed W where elevations h(w) are defined by a digital elevation model. The probability of observing a bedrock age a at the catchment surface is defined by $\bar{b}$ and its measurement error (s) where $\bar{b}$ is a function of the exhumation history of the catchment. We assume that measurement error has a normal distribution with a mean equal to the true age and a standard deviation σ, thus

$$p_b(h,a) = 1/\sqrt{2\pi\sigma}\exp\left(-\frac{1}{2}\left(\frac{a-\bar{b}(h)}{\sigma}\right)^2\right) \quad (2)$$

Because we assume a vertical exhumation pathway and a flat closure isotherm, bedrock cooling ages are invariant in the horizontal direction and thus a function only of elevation. We rely on approximately twenty individual age analyses per each catchment and estimate average standard deviation from AHe bedrock age replicates reported previously from bedrock data in northeastern Tibet (Clark et al., 2010), eastern Tibet (Kirby et al., 2002) and southeastern Tibet (Clark et al., 2005; Ouimet et al., 2010) and use it as the uncertainty on detrital ages (22% of age). Error estimation for single fission-track ages is problematic, especially for grains with low track counts (Galbraith, 2005). We estimate error along with other model parameters assuming that it is proportional to the true fission-track age ($\sigma = s\bar{b}$) (Avdeev et al., 2011).

Each model specifies priors, which are probability distributions of model parameters that express prior knowledge. Soft data inputs of this type eliminate unrealistic model results (e.g., closure isotherm elevations at or above the Earth's surface, or unreasonably high erosion rates). In this study, priors for erosion rate in all cases were set uniform

between 0 mm/yr to 1 mm/yr, which encompasses a wide range of reasonable erosion rates for high-elevation plateaus such as Tibet. Priors for the age(s) of erosion-rate change(s) (i.e. "break in slope") were set uniform between 0 Ma to 65 Ma, allowing for rate change(s) at any time during the Cenozoic Era. Finally, the priors for the closure isotherm elevation were assigned as a truncated normal distribution about a mean value, which was calculated on a per-catchment basis by subtracting 2.2 km and 3.7 km from the average elevation within the sampled catchment for AHe and AFT respectively. These closure isotherm depths are based on geothermal gradients across the sampling transect of 20-35ºC/km determined from heat-flow measurements (Hu et al., 2000) in combination with appropriate ranges in effective closure temperatures of helium in apatite of 55-75ºC, predicted by the RDAMM model (Flowers et al., 2009) assuming cooling rates, eU, and grain sizes reasonable for this study, and fission-track annealing temperatures of 100-120ºC (Ketcham et al., 2007).

5.6 Results

5.6.1 Detrital cooling ages

The catchments have widely- distributed apatite helium and fission-track ages that span the entire Cenozoic and into the Mesozoic eras and mean basin-wide elevations of ~4600 m (Table 5.2; Figure 5.6). Cooling-age distributions from the Tsangpo catchment are more limited, with no AHe ages older than mid-Miocene or AFT ages older than Eocene (Table 5.2; Figure 5.6). Although the Salween and Yellow_small catchments have broadly ranging age populations that include Mesozoic ages, they have no AHe or AFT ages younger than Miocene (Table 5.2; Figure 5.6).

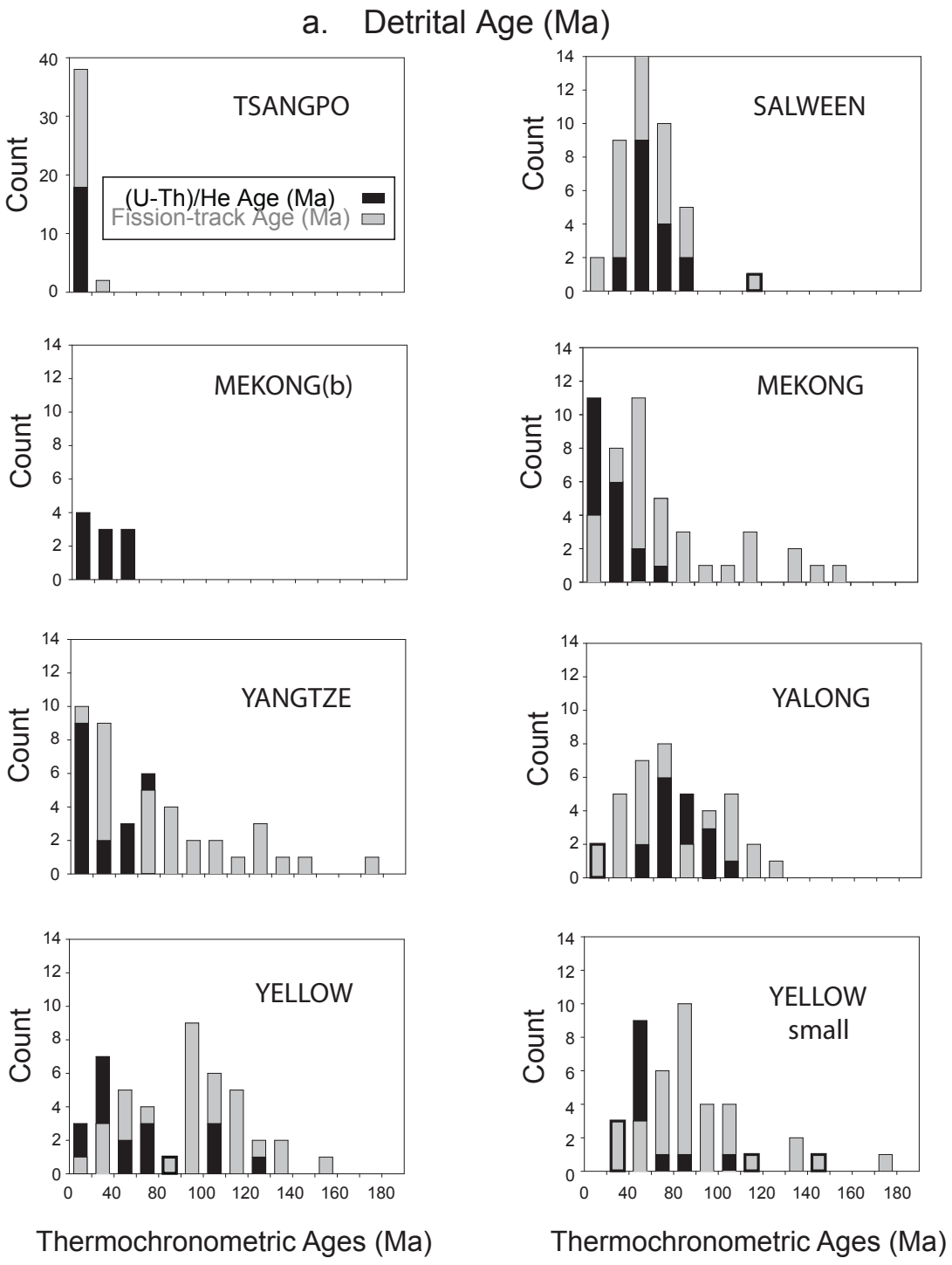

Figure 5.6a. Sampled catchment thermochronometric ages. PDF plots of apatite (U-Th)/He ages shown in black and apatite fission-track ages shown in gray for studied catchments, south to north. Probability density functions constructed using kernel density estimation.

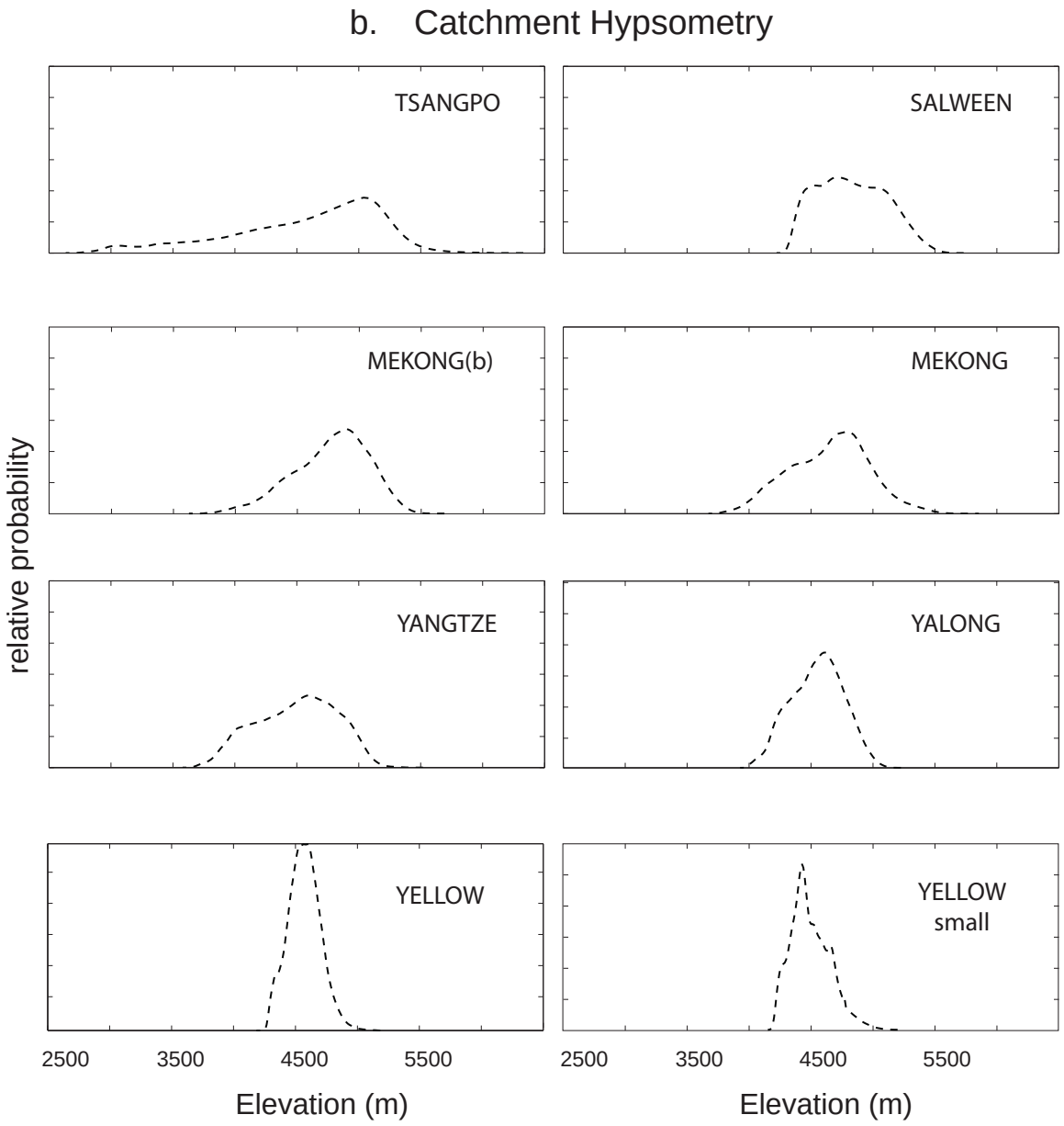

Figure 5.6b. Sampled catchment hypsometries. PDF plots of elevation within each catchment. Probability density functions constructed using kernel density estimation.

Apatite grain quality varies across the sampled catchments from pristine to rounded (Figure 5.5), yet there is no strong correlation between grain morphology and corrected helium age and all morphology types yield ages that span the Cenozoic era (Figure 5.7). Detrital helium results are potentially complicated by the partial or entire loss of the He depleted rim of apatite due to abrasion during transport. Abrasion may alter crystal shape such that the analyzed and original grain shapes are significantly different, thereby complicating the Ft correction (Rahl et al., 2003). The majority of uncorrected AHe ages (Table 5.2) are younger than the depositional age of most sedimentary units (Paleozoic and early Mesozoic) mapped throughout the study area (Pan et al., 2004) (Figure 5.4), which suggests that rocks were buried and heated after sedimentary deposition to temperatures greater than 70°C. Additionally, a strong positive correlation between grain quality and bedrock geology (Table 5.2) suggests that the majority of the rounding/clouding in highly weathered grains probably occurred before deposition in pre-Cenozoic sedimentary basins rather than from more recent weathering and river transport. Because grains are likely reset with respect to the AHe system, we apply the full alpha-ejection correction to all analyses.

5.6.2 Modeled erosion histories

We jointly inverted AHe and AFT data for each individual catchment assuming three erosion scenarios: (1) constant erosion rate through time (2) two distinct erosion rates in time and (3) three distinct erosion rates in time. We found that including more than three distinct periods of erosion did not provide additional information (i.e. additional periods produced similar erosion rates). The fit of models to data is evaluated by comparing

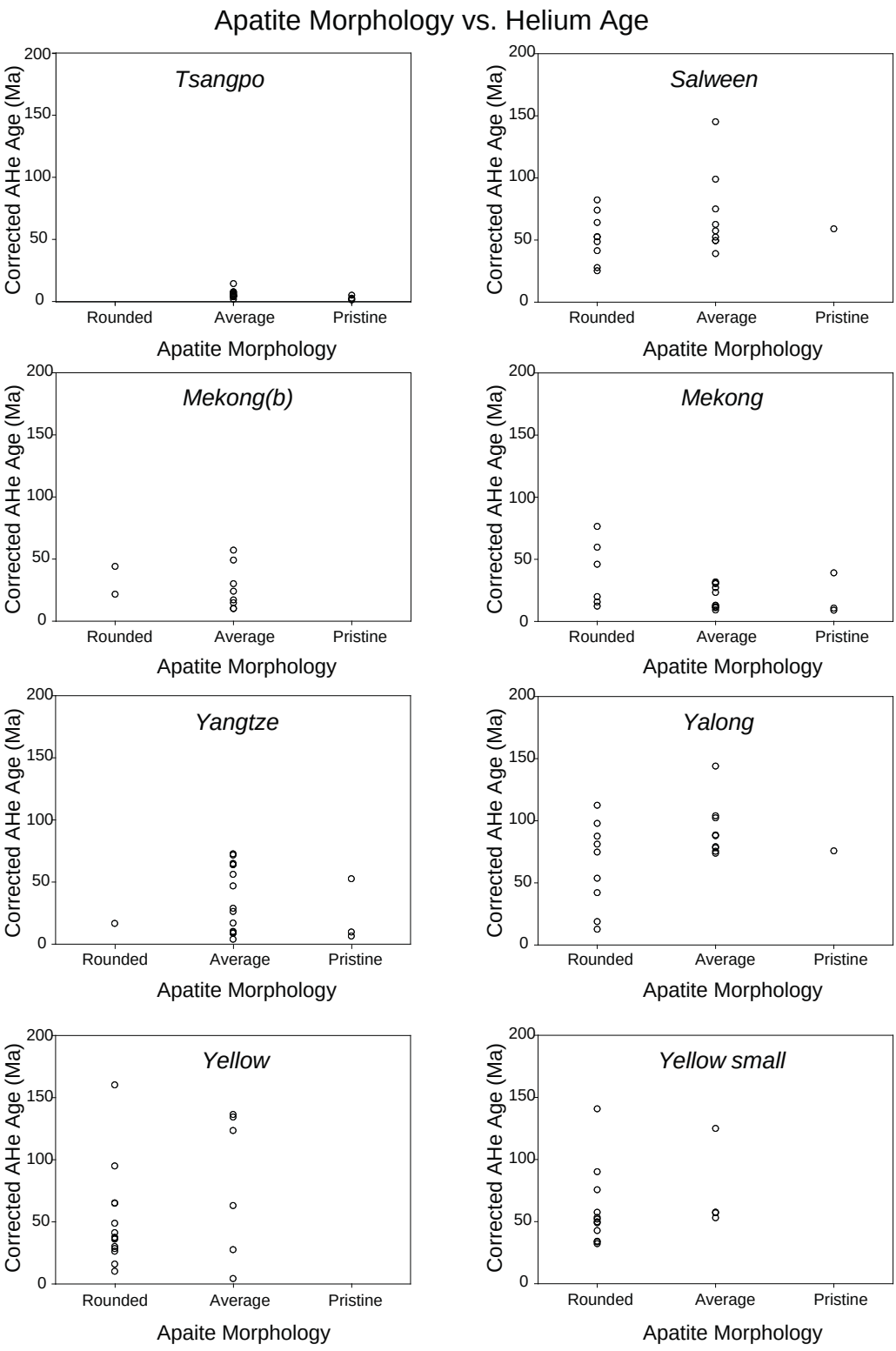

Figure 5.7. Plots of corrected helium age versus grain morphology for each catchment showing no pattern of correlation.

cumulative probability distribution from the actual samples to those of synthetic samples generated from model parameters using a goodness-of-fit plot (Avdeev et al., 2011). All reasonable models should produce synthetic data that are similar to observed data; therefore, overlap of the two sample suites indicates an acceptable model fit. Inability to find reasonable fits for proposed models likely invalidates the tested erosion history or model assumptions. Model estimates of erosion rates over various intervals and timing of rate changes for all catchments individually are reported as 95% confidence intervals (Table 5.3).

5.6.2.1 Constant erosion rate through time

Initially, we constrain a constant exhumation model assuming that erosion rate does not change through time within the catchments. In this scenario, bedrock ages ($b(w)$ in Eq. 2) are described by a piecewise linear function of elevation with one segment:

$$\bar{b}\,(h_c) = h_c/e \qquad (3)$$

where e is the slope. Model results are displayed as a series of plots (Figure 5.8). Panel a. shows cooling pathways predicted for AHe (blue lines) and AFT (green lines) plotted on a graph of age versus elevation. Panel b. is a cumulative probability density plot displaying the observed AHe (blue dots) and AFT (green dots) detrital ages and synthetic data (gray band) generated using results of predicted model parameters. Model fidelity is judged by visual comparison of the observed data and simulated data, with high degree of overlap between the dots and the swath indicating an acceptable model fit. Panels c. and d. show the relative probability of predicted erosion rate and closure isotherm elevation for AHe (blue) and AFT (green). Model runs that include changes in erosion rate will

Table 5.3 Model results summary

2-stage erosion history	Joint inversion			AHe only			AFT only		
Catchment	**a_{br} (Ma)**	**e_1 (mm/yr)**	**e_2 (mm/yr)**	**a_{br} (Ma)**	**e_1 (mm/yr)**	**e_2 (mm/yr)**	**a_{br} (Ma)**	**e_1 (mm/yr)**	**e_2 (mm/yr)**
Tsangpo	4-9	0.01-0.14	0.38-0.67	0.5-55[a]	0.004-0.91	0.258-0.691	4-12	0.003-0.141	0.315-0.86
Salween	3-61[b]	0.003-0.03	0.05-0.73	1-58[c]	0.003-0.024	0.03-0.75	3-60	0.01-0.93	0.0002-0.324
Mekong	-	-	-	1-20	0.006-0.038	0.06-0.67	-	-	-
Mekong(b)	10-14	0.006-0.01	0.18-0.29	10-15	0.005-0.17	0.12-0.27	5-51	0.002-0.009	0.054-0.41
Yangtze	3-24[d]	0.003-0.005	0.06-0.72	0-30	0.003-0.029	0.001-0.825	43-60	0.001-0.002	0.053-0.104
Yalong	3-8	0.003-0.005	0.35-0.97	2-10	0.002-0.005	0.138-0.918	0-56	0.008-0.063	0.0002-0.712
Yellow	4-58[e]	0.003-0.009	0.05-0.49	8-60[f]	0.001-0.008	0.03-0.23	0-57	0.006-0.08	0.0001-0.782
3-stage erosion history	**Joint inversion**			**AHe only**			**AFT only**		
Catchment	**a_{br1} a_{br2}**	**e_1 e_2**	**e_3**	**a_{br1} a_{br2}**	**e_1 e_2**	**e_3**	**a_{br1} a_{br2}**	**e_1 e_2**	**e_3**
Yangtze[a]	54-60 6-12	0.001-0.002 0.08-0.18	0.21-0.44	25-60 7-13	0.005-0.95 0.0001-0.015	0.122-0.35	16-55 0-21	0.001-0.002 0.0003-0.81	0.0001-0.690

[a]Two breaks in slope model preferred. Joint inversion single break model results shown in Figure 5.12.

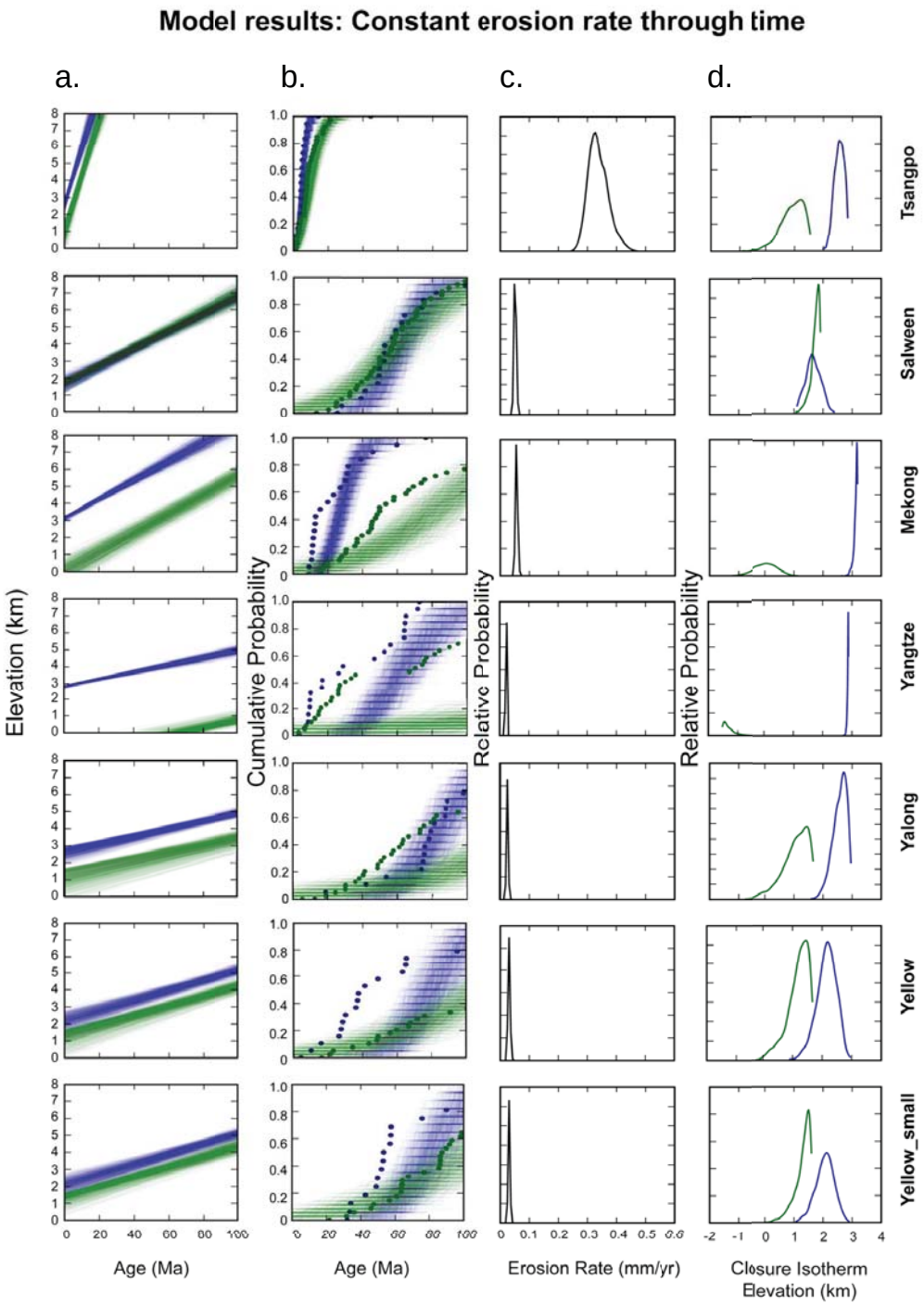

Figure 5.8. Model results of joint AHe and AFT inversion assuming a constant erosion rate through time. Panel a) plots of age (Ma) against elevation (km), blue lines represent AHe cooling pathways and green lines represent AFT cooling pathways. Panel b) "Goodness of Fit" plots: cumulative probability density plots showing actual AHe (blue dots) and AFT (green dots) ages and swaths of synthetic AHe (blue) and AFT (green) data. Because reasonable models should produce synthetic data that are similar to observed data, overlap of the two sample suites indicates an acceptable model fit. Panel c) Relative probability of erosion rate (mm/yr). Panel d) Relative probability of closure isotherm elevation (km) for AHe (blue) and AFT (green).

have an additional panel showing the relative probability of the timing of the rate change(s) (Figures 5.9-5.13).

Strong mismatch between predicted synthetic data and observed data suggests that the constant erosion model is unsuitable for all of the catchments with two exceptions in the southern part of our study area (Figure 5.8b). The Tsangpo catchment is reasonably well described by a constant erosion rate of 0.28-0.41 mm/yr (Figure 5.8, Table 5.3). The goodness-of-fit plot for the Salween catchment also shows that these data are reasonably fit by a constant erosion rate model with an erosion rate of 0.04-0.06 mm/yr (Figure 5.8, Table 5.3).

5.6.2.2 Two-stage erosion history

Next we assume a two-stage exhumation model assuming bedrock ages are described by a piecewise linear function of elevation with two segments:

$$\bar{b}\,(h_c) = (h_c - h_{c1})/e_1,\ \bar{b} > a_{br}$$
$$(h_c - h_{c2})/e_2,\ \bar{b} < a_{br} \qquad (4)$$

where e_i is the slope and h_{ci} is the intercept of each segment and α_{br} is the age of the break in slope. Goodness-of-fit plots show that an erosion history with an increase in erosion rate is reasonable for all of the catchments (Figure 5.9b). Although the constant erosion rate model provided a reasonable fit to the Tsangpo and Salween data, adding a break in slope results in a better fit to the oldest ages in these samples, thus we prefer a two-stage model for these catchments. Assuming a single break in slope occurred, four of the catchments (Tsangpo, Mekong, Yangtze, and Yellow) have relatively narrow probability peaks for the timing of erosion-rate change suggesting that the erosion rate, which was

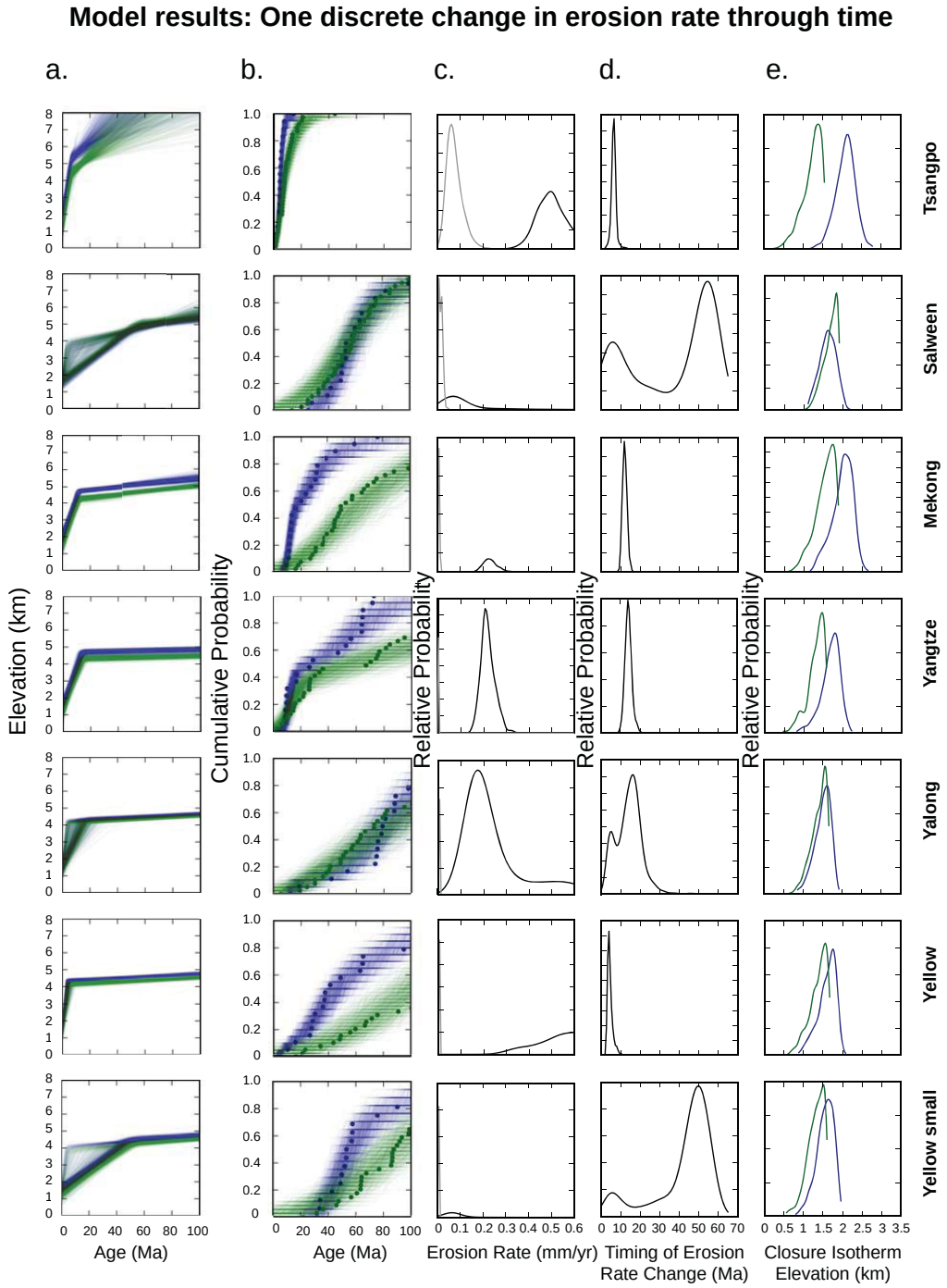

Figure 5.9. Model results of joint AHe and AFT inversion assuming one discrete change in erosion rate through time. Panel a) plots of age (Ma) against elevation (km), blue lines represent AHe cooling pathways and green lines represent AFT cooling pathways. Panel b) "Goodness of Fit" plots: cumulative probability density plots showing actual AHe (blue dots) and AFT (green dots) ages and swaths of synthetic AHe (blue) and AFT (green) data. Because reasonable models should produce synthetic data that are similar to observed data, overlap of the two sample suites indicates an acceptable model fit. Panel c) Relative probability of erosion rate (mm/yr). Initial erosion rate is shown as light gray line and post-change erosion rate is shown in black. Panel d) Relative probability of timing of erosion rate change (Ma). Panel E) Relative probability of closure isotherm elevation (km) for AHe (blue) and AFT (green).

slow (0.003-0.01 mm/yr), increased at least an order of magnitude (0.1-1 mm/yr) sometime between 17 and 4 Ma (Figure 5.9, Table 5.3). The Yalong River shows an increase in erosion rate from 0.003-0.005 mm/yr to 0.06-0.72 mm/yr between 24 and 3 Ma (Figure 5.6). The change in erosion rates from 0.003-0.03 mm/yr to 0.05-0.73 mm/yr and 0.003-0.009 mm/yr to 0.05-0.49 mm/yr for the Salween and Yellow_small catchments are less precisely constrained between 61-3 and 58-4 Ma respectively (Figure 5.6; Table 5.3).

5.6.2.3 Three-stage erosion history

Bedrock ages described by a piecewise linear function of elevation with three segments (i.e. two breaks in slope) can be expressed as:

$$\begin{aligned} \bar{b}\,(\underline{h_c}) &= (\underline{h_c} - h_{c1})/e_1,\ \bar{b} > a_{br1} \\ &(\underline{h_c} - h_{c2})/e_2,\ \bar{b} < a_{br1} > a_{br2} \\ &(\underline{h_c} - h_{c3})/e_3,\ \bar{b} < a_{br2} \end{aligned} \qquad (5)$$

With one exception (Yangtze), results from this model do not show significant improvement in goodness of fit from two-stage models and relative probabilities of timing of the first and second breaks in slope overlap (Figure 5.10b). In the Yalong case, precision on the timing of rate changes is reduced as the window of ages within the 95% confidence interval spans almost the entire Cenozoic (Figure 5.10d; Table 5.3). For these reasons, we prefer the two-stage erosion rate models for all catchments except for the Yangtze. The Yangtze catchment data is well fit by a three-stage erosion history with an initial increase in erosion rate from 0.001-0.002 mm/yr to 0.08-0.18 mm/yr at 60-54 Ma

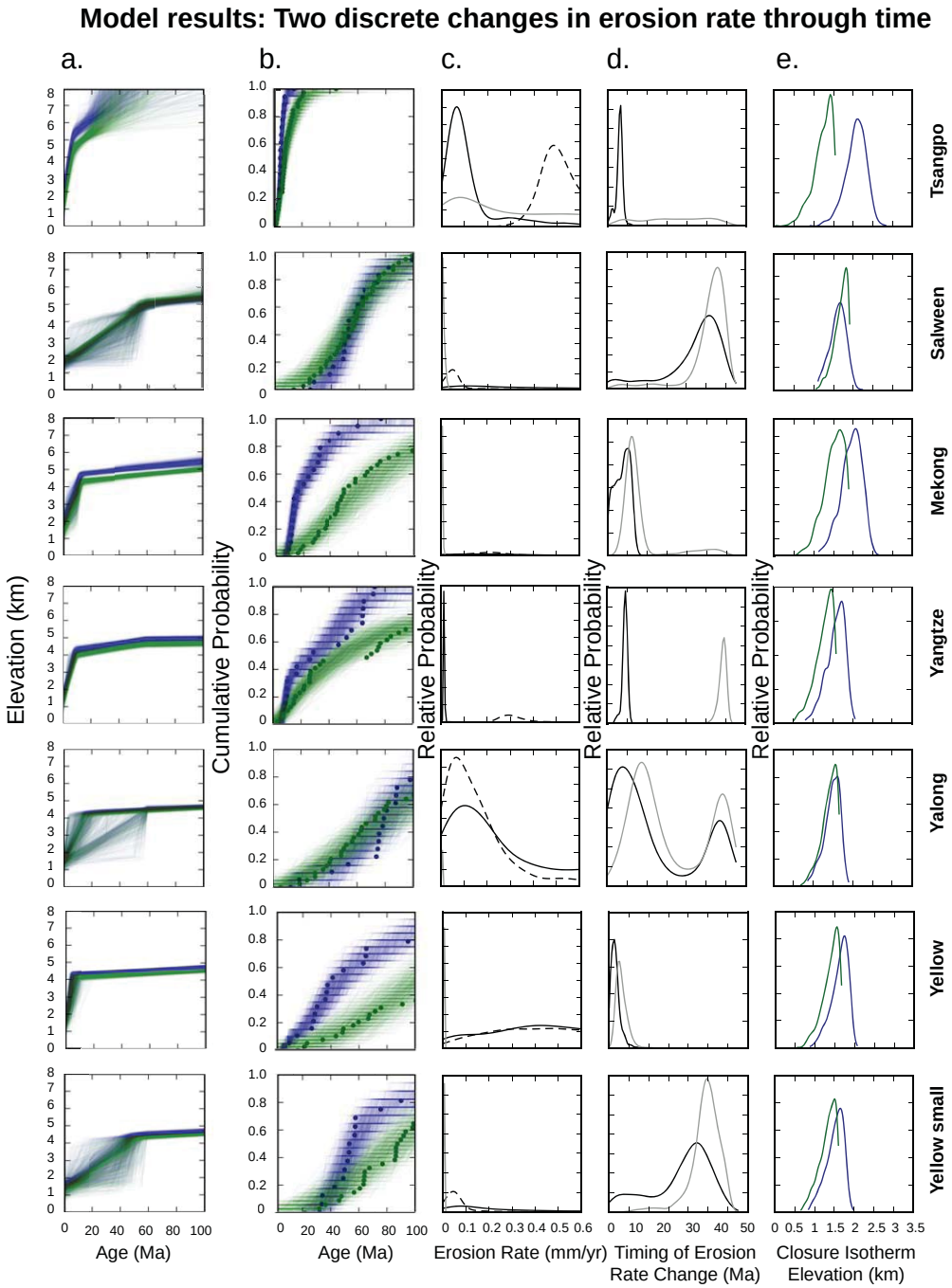

Figure 5.10. Model results of joint AHe and AFT inversion assuming two discrete changes in erosion rate through time. Panel a) plots of age (Ma) against elevation (km), blue lines represent AHe cooling pathways and green lines represent AFT cooling pathways. Panel b) "Goodness of Fit" plots: cumulative probability density plots showing actual AHe (blue dots) and AFT (green dots) ages and swaths of synthetic AHe (blue) and AFT (green) data. Because reasonable models should produce synthetic data that are similar to observed data, overlap of the two sample suites indicates an acceptable model fit. Panel c) Relative probability of erosion rate (mm/yr). Initial erosion rate is shown as light gray line, rate post first erosion-rate change is shown in black, and rate post second erosion-rate change is shown as black dashed line. Panel d) Relative probability of timing of erosion rate change (Ma). Timing of first change in erosion rate shown in light gray and timing of second change in erosion rate is shown in black. Panel E) Relative probability of closure isotherm elevation (km) for AHe (blue) and AFT (green).

followed by a second and larger increase to erosion rates of 0.21-0.44 mm/yr at 12-6 Ma (Figure 5.10; Table 5.3).

5.6.2.4 Common erosion history among catchments

The overlap in timing (late Miocene to early Pliocene) of an increase in erosion rates shown by individual catchment models suggests a synchronous erosion history across the sampling transect. In order to test this hypothesis, we considered all of the data together in a single model. Essentially, a larger dataset may allow us to more precisely constrain the timing of rate change. The common erosion model assumes that all catchments experienced an increase in erosion rate at the same time and allows for three linear segments, the most flexible model that was found prior. Model results show reasonable fits to data with an increase in erosion rate across all catchments at 11-4 Ma (95% confidence; Figure 5.11, Table 5.4). Results also show an earlier change in erosion rate at 60-54 Ma (95% confidence; Figure 5.11, Table 5.4). The goodness-of-fit plots demonstrate that this erosion history is permissible for all of the catchments. However, because only the Yangtze catchment showed two distinct peaks in timing of erosion rate increase in individual modeling (at 60-54 Ma and 12-6 Ma, see section 5.6.2.3), the timing of the initial break in slope for the common erosion model may be weighted by this catchment.

5.6.3 Comparison of joint versus independent AHe and AFT inversions

In theory, analysis of minerals from the same sample with multiple thermochronometers should resolve consistent erosion histories when modeled

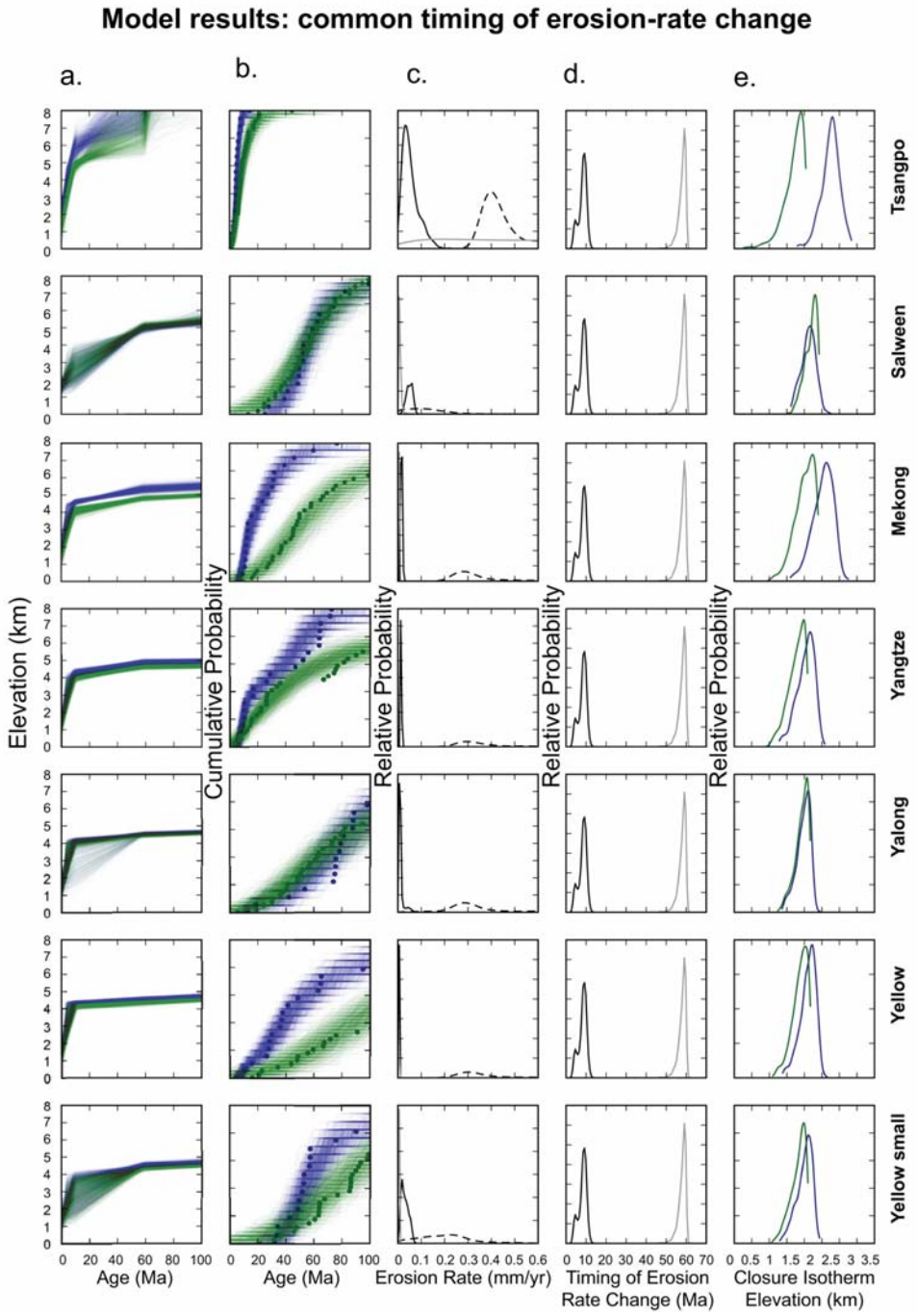

Figure 5.11. Model results of inversion using all of the data assuming that catchments share a common erosion history. Panel a) plots of age (Ma) against elevation (km), blue lines represent AHe cooling pathways. Panel b) "Goodness of Fit" plots: cumulative probability density plots showing actual AHe (blue dots) ages and swaths of synthetic data. Because reasonable models should produce synthetic data that are similar to observed data, overlap of the two sample suites indicates an acceptable model fit. Panel c) Relative probability of erosion rate (mm/yr). Initial erosion rate is shown as light gray line and post-change erosion rate is shown in black. Panel d) Relative probability of timing of erosion rate change (Ma). Note that the earlier break in slope at 60-54 Ma is an artifact of the model (see text for details). Panel e) Relative probability of closure isotherm elevation (km) for AHe (blue).

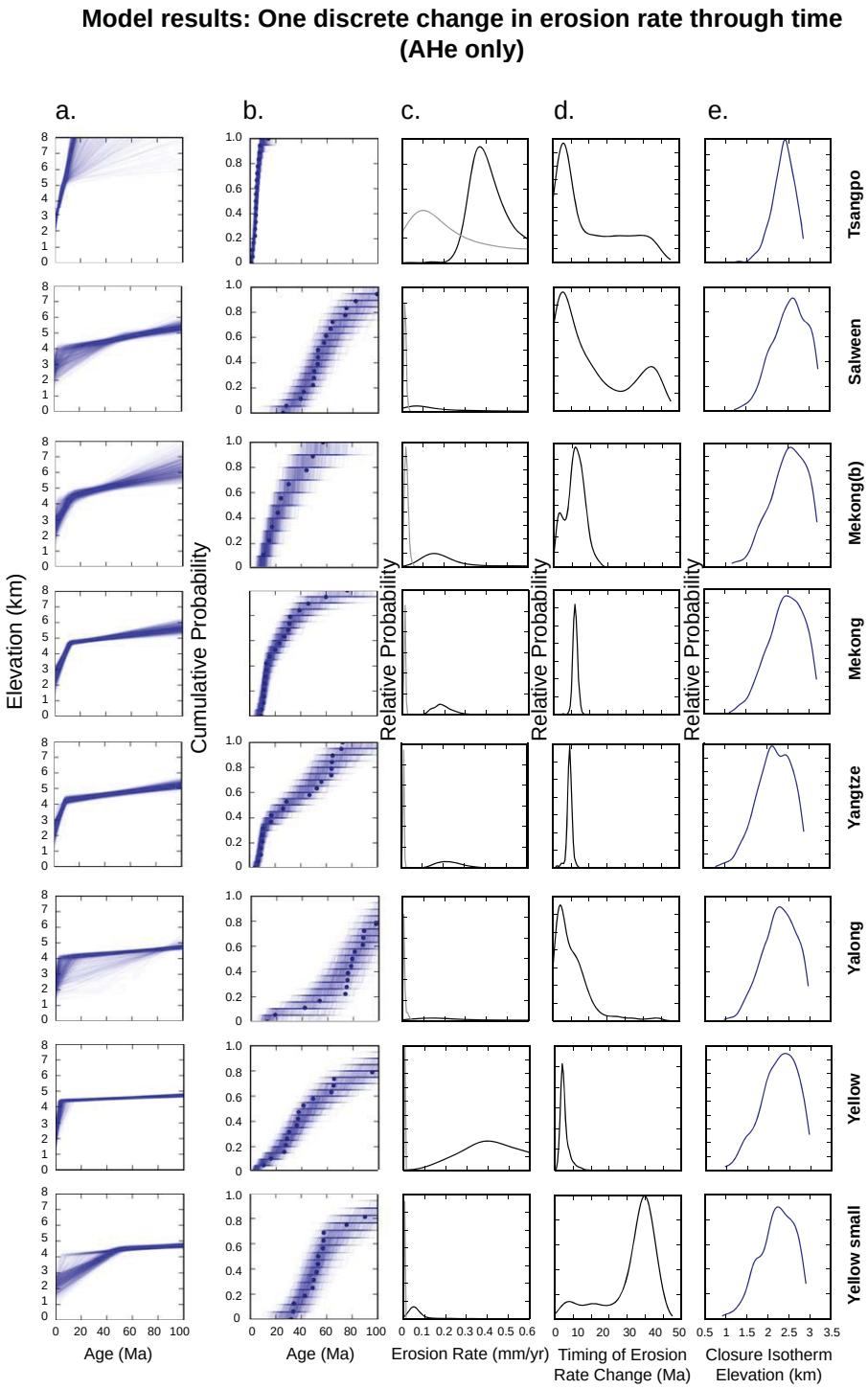

Figure 5.12. Model results of AHe only inversion assuming one discrete change in erosion rate through time. Panel a) plots of age (Ma) against elevation (km), blue lines represent AHe cooling pathways. Panel b) "Goodness of Fit" plots: cumulative probability density plots showing actual AHe (blue dots) ages and swaths of synthetic data. Because reasonable models should produce synthetic data that are similar to observed data, overlap of the two sample suites indicates an acceptable model fit. Panel c) Relative probability of erosion rate (mm/yr). Initial erosion rate is shown as light gray line and post-change erosion rate is shown in black. Panel d) Relative probability of timing of erosion rate change (Ma). Panel e) Relative probability of closure isotherm elevation (km) for AHe (blue).

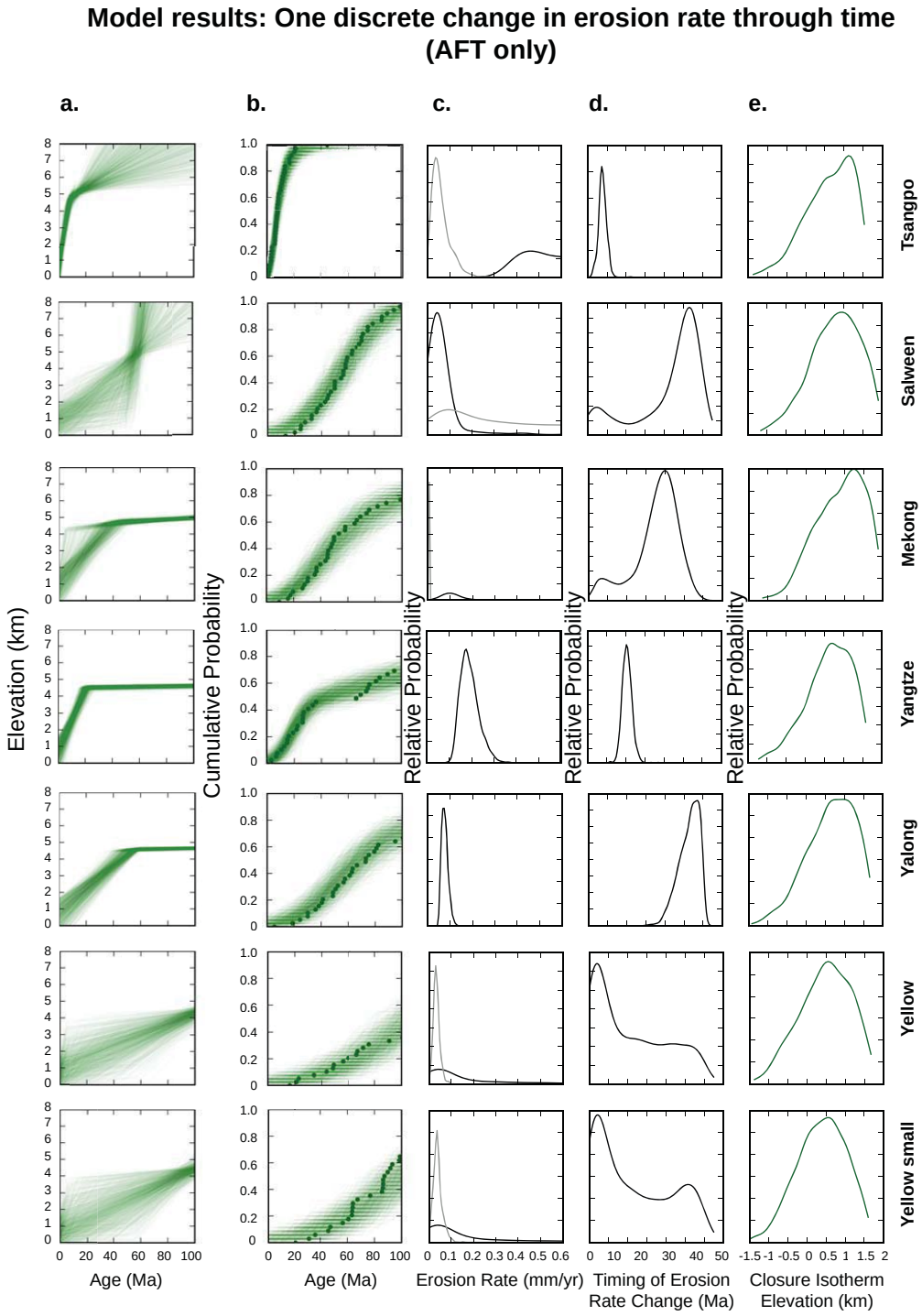

Figure 5.13. Figure 5.13. Model results of AFT only inversion assuming one discrete change in erosion rate through time. Panel a) plots of age (Ma) against elevation (km), green lines represent AFT cooling pathways. Panel b) "Goodness of Fit" plots: cumulative probability density plots showing actual AFT (green dots) ages and swaths of synthetic data. Because reasonable models should produce synthetic data that are similar to observed data, overlap of the two sample suites indicates an acceptable model fit. Panel c) Relative probability of erosion rate (mm/yr). Initial erosion rate is shown as light gray line and post-change erosion rate is shown in black. Panel d) Relative probability of timing of erosion rate change (Ma). Panel e) Relative probability of closure isotherm elevation (km) for AFT (green).

independently, though AFT and AHe data will be sensitive to older and younger erosion events respectively due to differences in closure temperature. For comparison, we present results of independent AHe and AFT inversion models assuming one discrete change in erosion rate in time (Figure 5.12-5.13; Table 5.3). In general, the independent AHe and AFT models are compatible with one another and with a late Cenozoic increase in erosion rate interpreted from joint inversions using both thermochronometers (Figure 5.9). Joint inversions increase the precision of estimated parameters compared to models using AHe or AFT data independently.

Comparison of independent AHe and AFT modeling results also sheds light on potential point-source biases in the Yellow_small catchment. Results show a different AHe age distribution and model result between this catchment and the adjacent larger Yellow River (Figure 5.6, 5.12, Table 5.2), yet fission-track age distributions and model results are very similar between the two (Figure 5.6, 5.13, Table 5.2). One possible explanation for this discrepancy relates to point-source biasing of apatite of the correct size and quality required in helium analysis. Only two mapped geologic units comprise the smaller Yellow drainage basin: Jurassic granite of Mt. Lunag Dungze (between 4600 m and 5200 m elevation) and Triassic marine facies (below 4600 m elevation; Figure 5.4h). Given this geologic pattern and the smaller size of this catchment, it is possible that apatite suitable for helium dating is not well distributed within this catchment. Rather, the sample may be dominated by grains from granitoid rocks present at higher elevations, causing a disproportionate influx of older ages. Bedrock data would allow for further assessment of the validity or degree of such biasing.

Table 5.4 Common erosion history model results summary

Joint inversion

Catchment Name	abr^1	abr^2	e^1	e^2	e^3
Tsangpo	54-60	4-11	0.05-1	0.002-0.12	0.33-0.67
Salween	54-60	4-11	0.0005-0.27	0.02-0.07	0.002-0.02
Mekong	54-60	4-11	0.002-0.007	0.009-0.02	0.2-0.58
Yangtze	54-60	4-11	0.0006-0.001	0.01-0.02	0.23-0.63
Yalong	54-60	4-11	0.002-0.004	0.004-0.04	0.08-0.63
Yellow	54-60	4-11	0.002-0.005	0.002-0.007	0.22-0.67
Yellow_small	54-60	4-11	0.002-0.006	0.008-0.06	0.002-0.4

abr^1 age of first erosion rate change.

abr^2 age of second erosion rate change.

e_1 earliest erosion rate.

e_2 erosion rate after first change.

e_3 erosion rate after second change.

5.6.4 Model assumptions

Fast exhumation can result in heat advection that significantly alters the thermal field thereby invalidating the assumption of constant geothermal gradient in time and complicating interpretation of erosion rates from age/elevation relationships. However, a geotherm approximated as constant is appropriate in this study because a combination of maximum possible erosion rates (<1 mm/yr) and cooling duration (<15 Myr) yields <20% increase in thermal gradient (Ehlers, 2005).

Quantitative predictions of variable erosion rates are not possible using previous approaches to detrital thermochronometry because these methods necessitate the assumption of exhumational steady state (Ruhl and Hodges, 2005; Brewer et al., 2003). Statistical tests outlined in Ruhl and Hodges (2005) provide a means to assess the steady-state assumption but not to directly estimate rates during the different erosive stages. As we have shown in section 6.2.1. and 6.2.2., the Tibet detrital data are in general poorly fit by a constant erosion rate therefore violating a steady-state condition. If constant erosion rates were assumed despite this obvious misfit, calculated erosion rates using methods outlined in this paper and these previous methodologies would be similar and would underestimate true late Cenozoic erosion rates by an order of magnitude (10^{-2} vs. 10^{-1} mm/yr).

A wide range in AHe and AFT ages and weak correlation between apatite morphology and AHe age supports our assumption that analyzed grains are broadly sourced from within the catchment and that the numbers of grains analyzed are sufficient to characterize catchment age distributions. Goodness-of-fit plots of model results show that

sample sizes of ~20 grains per catchment are large enough to reject a constant erosion rate model and to estimate reasonable exhumation parameters for the two-and three-stage erosion histories for most catchments (Figures 5.8-5.13). Models with more than three stages of erosion do not produce significantly different erosion histories. Thus, the model results shown here provide reasonable first order interpretations of the data. Comparison of the Mekong and neighboring Mekong(b) catchment, which share similar erosion histories, further supports the reliability of our sample size. Due to low apatite yields, Mekong(b) has no fission-track ages and 50% fewer AHe ages. Both Mekong(b) (AHe N=10) and Mekong (AHe N=20) are well fit by a two-stage erosion history with a late Cenozoic increase in erosion rate (Figure 5.11), though the larger sample size for the Mekong does result in a higher precision estimate of the timing of erosion-rate increase (15-10 Ma as opposed to 20-1 Ma for Mekong(b)).

5.7 Discussion

Erosion histories from the externally drained portion of the Tibetan Plateau potentially provide a record of surface uplift and climate conditions during orogen evolution, though erosion histories alone do not uniquely indicate a given tectonic or climatic scenario. Specifically, our samples should be sensitive to expansion of high topography related to plateau growth following continental collision. In addition, because the catchments we study are at or near the headwaters of major rivers that drain off the plateau, erosion histories are also potentially sensitive to upstream propagation of erosion signals that originate on the plateau perimeter. By comparing our results to studies on the same rivers at the plateau margins, we can evaluate whether or not the subdued

topography of the interior of Tibet is isolated from erosion rates affecting its margins. Isolation from base-level changes by either slow or stalled knick-point propagation (Ouimet, 2007; Whipple, 2010) has been suggested as a means by which the interior of Tibet has been or will continue to be protected from erosion allowing the plateau to remain high and relatively flat.

Despite differences in precipitation, mean drainage-basin slope and relief, catchments spanning over 6º latitude share similar erosion histories (Figures 5.2 and 5.14). To first order, regional slow erosion for much of the Cenozoic must be followed by a recent and widespread increase in erosion rate in order to preserve both old and young ages observed in each individual catchment. Inverse modeling results confirm that data are poorly fit by a constant erosion rate model (Figure 5.8) and instead require increases in erosion rate since at least the mid-to-late Miocene in order to adequately describe the data (Figure 5.14). Posterior probabilities of the timing of increased erosion are centered during the mid-to-late Miocene for four of the studied catchments (Tsangpo, Mekong, Yangtze, Yellow) indicating a regional pattern of increased erosion rate beginning over a 7 Myr period (Figure 5.14). Such an erosion history is also permissible by the other large catchments studied (Salween, Yalong), although the lack of ages younger than 13 Ma in these catchments do not allow precise constraints on the timing of rate change.

Sample sites within the center of the study transect along eastward draining rivers appear to have an earlier onset of increased erosion rate (mid-to-late Miocene) as compared to sample sites on the northern and southern edges of the plateau (Miocene to early Pliocene) (Figure 5.14a). The 11-4 Ma age range found from a common-erosion history model for all of the catchments may encompass real variability in the timing of

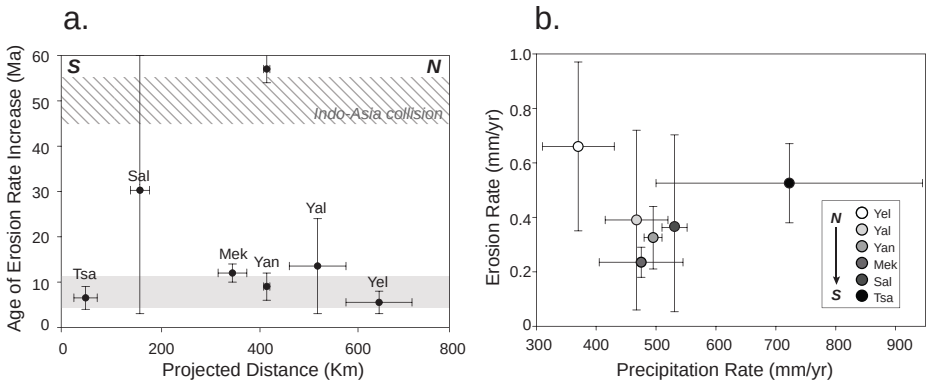

Figure 5.14. a) Summary plot of the timing of late Cenozoic erosion rate increase within large catchments studied. The x-axis plots the catchments in order from south to north with distance away from the eastern syntaxis (black star in Figure 5.2b shows the start location of the projected distance line). Error bars reflect catchment width. The y-axis shows the age range (within 95% confidence) in Ma for each catchment determined from preferred model results (Table 5.3). b) Plot of mean annual precipitation rate (mm/yr) across each catchment (Matsuura and Willmott, 2007) against late Cenozoic erosion rate (mm/yr) within 95% confidence (Table 5.3). Ranges in precipitation rate reflect the minimum and maximum cell values within each catchment (Figure 5.2d). Note the lack of obvious positive correlation between precipitation and erosion rates as is expected (see text for details).

erosion rate change within 7 Myr or may be due to imperfect sampling of catchment surfaces. If the age variability is real, we imagine either a time-transgressive response of individual fluvial systems to common base-level change or uplift event, or true spatial variability in tectonic or climatic forcing across the plateau interior. Future work, including additional analyses from these samples and other smaller catchments along the study transect, may potentially highlight important nuances in the erosional response to forcing, geomorphic processes, and details in the spatial variability of the tectonic record.

An earlier erosion event at 60-54 Ma is observed in the Yangtze catchment, though of lesser magnitude than the late Miocene event. Models that allow for two breaks in slope do not produce significantly better data fits for the other individual catchments. Yet, the simultaneous inversion of all data assuming a common erosion history shows that a widespread change in erosion rate at ~55 Ma is permissible, albeit the erosion rates still remain fairly low (<0.1 mm/yr).

5.7.1 Implications with respect to previous Tibetan erosion studies

Extensive preservation of low-relief relict-landscape remnants (Clark et. al., 2006), knickpoints in river profiles, and variability in short-term erosion rates have been cited as evidence that late-Miocene incision of the eastern margin of the Tibetan Plateau has yet to equilibrate throughout the landscape (Clark et al., 2006; Ouimet et al., 2010). Ouimet et al. (2010) also proposed that the erosion increase on the eastern plateau margin has not yet propagated into the headwaters of the major rivers. Similarity in timing between our results and accelerated erosion downstream suggests an incision signal has in fact reached the headwaters of eastern Tibet rivers. Elevation transects of apatite and zircon helium

and apatite fission track collected over short horizontal distances in the Dadu, Yalong, and Yangtze River gorges (Clark et al., 2005; Ouimet et al., 2010), in the Longmen Shan (Kirby et al., 2002; Godard et al., 2009b), and from a regional study of the eastern plateau margin (Wilson and Fowler, 2011) (Figure 5.2a) record an onset of rapid fluvial incision into a regional low-relief surface across the eastern margin of the Tibetan Plateau between 15 and 5 Ma compared to between 11 and 4 Ma from the detrital data presented here. Bedrock data from elevation transects show a change in erosion rate from 0.01-0.06 to 0.25-5 mm/yr compared to catchment-wide increases in erosion rate from a slowly-eroding landscape (~0.005 mm/yr) to ~0.2-0.6 mm/yr from this study. The similarity in timing between our results and accelerated erosion downstream suggests that the relatively low-relief interior of east-central Tibet is not protected from dissection by slow or stalled knickpoint migration along trunk rivers (Ouimet et al., 2007; Korup and Montgomery, 2008). Similar to reaches on the plateau perimeter, isolated relict surface remnants and early Cenozoic to Mesozoic helium ages in the headwater region suggest that the landscape is adjusting to new conditions (Clark et al., 2005; Ouimet et al., 2010). Mesozoic (U-Th)/He cooling ages and fission-track ages across eastern Tibet also preclude significant burial of the high-plateau surface as suggested by Liu-Zeng et al., (2009).

Estimates of long-term erosion rates since late Miocene time from low-temperature thermochronology are consistent with short-term (10^2-10^5 yr) erosion rates measured with cosmogenic ^{10}Be within the Dadu, Yalong, and Yangtze gorges (~0.3-0.5 mm/yr) (Ouimet et al., 2009) as well as the headwaters of the Salween, Mekong, and Yalong rivers (~0.1-0.2 mm/yr; Figure 5.4 in Henck et al., 2011). However, millennial erosion

rates vary locally from 0.01-8 mm/yr within the Three Rivers Region, an area of focused high rock-uplift rates (Henck et al., 2011).

The Tsangpo River has a much more limited range of AHe and AFT ages (22 – 2 Ma) and significantly higher catchment relief (Figure 5.2, 5.6), despite broadly similar timing and rates of increased erosion as compared to the other catchments. Higher erosion rates from the early Miocene to the late Miocene (~0.1 mm/yr compared to ~0.005 mm/yr; Figure 5.9) likely contribute to the difference in relief between this catchment and the others. Erosion events that account for 1-2 km of exhumation since 2 Ma (i.e. more recent than the youngest thermochronometric ages measured) cannot be resolved with our approach. Thus, it is possible that modern and/or Quaternary erosion rates are also higher within this catchment due to glaciation and/or the northward expansion of the eastern Himalayan syntaxis (Seward and Burg, 2008). It is also noteworthy that we find erosion rates of ~0.4 mm/yr within the Tsangpo catchment (Figure 5.9). Thus, despite its proximity to the eastern Himalaya indenter corner, very rapid exhumation rates (3-5 mm/yr) (Burg et al., 1997; 1998) are locally confined to within ~60 km of Namche Barwa (Seward and Burg, 2008), and do not extend (yet) throughout the catchment, at least on geologic timescales.

Rates of clastic sediment accumulation offshore of Southeast Asia have been used as proxies for rates of continental erosion (Clift et al., 2002; Clift, 2006, Clift et al., 2006). Recent sediment budgets derived from compilations of seismic data from Asian marginal seas show that sediment flux first peaked in the early-middle Miocene, which is thought to relate to increases in precipitation and possibly rock-uplift rate (Clift, 2006). Our results indicate slow erosion within east-central Tibet before the late Miocene. Thus, the

pulse of sedimentation offshore is not correlative with an erosion event in the headwaters of the Tibetan Plateau at this time.

5.7. 2 Impact of climate on Tibetan Plateau erosion rates

Our results show no obvious correlation between erosion and precipitation rates across the study site or when comparing the high plateau to the wetter eastern plateau margin. Modern mean annual precipitation amounts increase across the study transect from south to north (~600 mm/yr in the south to ~300 mm/yr in the north (New et al., 2002)). Isotopic evidence supports that the northern plateau was arid by Neogene time (Kent-Corson et al., 2009), which suggests that modern trends in precipitation existed in the geologic past. A correlated pattern of northward-decreasing erosion rates is not borne out in our results (Figure 5.14b). Instead, the catchments with the highest erosion rates (Tsangpo and Yellow) are in the wettest and driest regions, respectively (Figure 5.2, Table 5.3). These catchments are also characterized by extremes in mean catchment relief and slope (Figure 5.2). Moreover, erosion rates from our sites on the Tibetan Plateau highland are very similar to rates from the high-precipitation eastern plateau margin (>1000 mm/yr mean annual precipitation (New et al., 2002)).

The shift to increased erosion rates between 11-4 Ma overlaps broadly with the timing of various purported climate changes in Asia at about 10 Ma, many of which have been linked with strengthening monsoon intensity (see review by Molnar et al., 2010 and references therein). However, correlating climatic events with changes in erosion rates is difficult in the east-central Tibetan Plateau. Although in some cases increased precipitation has been shown to drive enhanced erosion (e.g., Brozovic et al., 1997;

Montgomery et al., 2001; Reiners et al., 2003; Theide et al., 2004), our results are consistent with other studies that suggest that there is not always a direct influence of precipitation on erosion rates (e.g., Riebe et al., 2001; Burbank et al., 2003; Finnegan et al., 2008; Binnie et al., 2010; Henck et al., 2011). Relating erosion rate changes to climatic events is further complicated by complex moisture source interactions in this region (e.g., Hren et al., 2009), particularly with respect to the monsoonal systems. The Asian monsoon systems surely influence study catchments but not necessarily to the same degree across the sampling transect. Furthermore, a lack of understanding as to how the monsoonal systems along the eastern plateau have evolved through time yields even greater uncertainty in speculating the role of climate change on erosion history in this region.

Although erosion histories alone cannot be used to definitively discern the relative roles of climatic and tectonic processes, it is unlikely that monsoon strengthening is the sole driver of the observed increase in erosion rates at 11-4 Ma. Attributing erosion-rate increases exclusively to climatic changes requires that high topography existed in the east-central plateau prior to at least the middle Miocene. Our results show constant low erosion rates throughout the early and middle Cenozoic. Thus, creation of this high topography prior to 11-4 Ma would have occurred without discernable widespread increases in erosion rate, which seems improbable. If the rivers of this region were internally drained in the past, surface uplift could occur without discernable increases in erosion rate. However, there is no evidence in the large-scale drainage patterns to suggest major reorganization from isolated paleo-basins to the current externally-drained system (Clark et al., 2004). Perhaps a more likely scenario is that the creation of high

topography, changes in climate, and increased erosion rates are linked such that both surface uplift and an associated stronger monsoon system acted in concert to drive higher erosion rates across east-central Tibet.

5.7.3 Tectonic interpretation of Tibetan Plateau erosion patterns

A common prediction of many tectonic scenarios for Tibet is the northward propagation of topography since collision time. If the onset of increased erosion rates across the east-central Tibetan Plateau interior is interpreted as a proxy for the timing of significant elevation increase, the spatial patterns in erosion documented here challenge competing descriptions of plateau development. Mechanical and geodynamic models of Tibetan Plateau formation as disparate as localized shear and stepwise growth (e.g., Tapponnier et al., 2001), distributed shortening and thickening of Asian lithosphere (e.g., England and Houseman, 1986), and underthrusting of Indian crust and/or lithosphere (e.g., Powell, 1986) share the common prediction of topographic growth progressing northward away from the collision boundary with time. If Tibet grew by appending material to a northward-expanding deformation front starting with initial collision circa 50 Ma, then we expect a similarly migrating front of high erosion rates either continuously or in stages. Results from this study, which document relatively uniform rather than spatial or temporal progressions in timing or rates of erosion, are inconsistent with this prediction across the east-central high plateau.

Nor do our results support the proposition of widespread surface uplift of the eastern plateau at 40 Ma (Chung et al., 1998) or that an early Cenozoic central nucleus of high topography grew outward to the south and north as collision progressed (Wang et al.,

2008). An Eocene increase in erosion rate within the Yangtze and possibly the other catchments, is roughly coincident with the timing of Indo-Asian collision (Rowley, 1996; 1998). Fault studies in the Yushu-Nangqian region in close proximity to the Yangtze catchment, suggest contractional deformation from prior to 50 Ma to 37 Ma (Spurlin et al., 2005). Eocene faulting thought to be related to collision has also been identified across the northern margin of Tibet (Yin et al., 2008; Clark et al., 2010; Duvall et al., 2011) and in the Fenghuo Shan-Nangqian thrust belt in central Tibet (Horton et al., 2002; Liu et al., 2003; Wang et al., 2008). A subtle Eocene increase in erosion rate could signify widespread faulting close to collision time, but we suggest that it was not accompanied by regional surface uplift that affected the eastern plateau.

We find that the timing of increased erosion rate is similar across the length of our sampling transect. Thus, our results are generally consistent with processes thought to result in wide-spread, uniform surface uplift such as loss of a mantle root (Molnar et al., 1993), injection of Indian crust into Tibetan lower crust (Zhao and Morgan, 1987), or channel flow (Bird, 1991; Royden, 1996; Clark and Royden, 2000; Royden et al., 2008). Late Miocene initiation of major river incision within the easternmost margin of Tibet (Figure 5.2) (Clark et al., 2005; Ouimet et al., 2010; Wilson and Fowler; 2011) has been proposed to relate to broad uplift due to crustal thickening by lower crustal flow (Clark and Royden, 2000; Kirby et al., 2002; Clark et al., 2006; Royden et al., 2008; Ouimet et al., 2010). A late-Miocene shift to increased erosion rate is also observed along our study transect (Figure 5.14a) and the magnitude of erosion rates after this shift is similar in each region, suggesting surface uplift related to lower crustal flow may also have influenced the east-central Tibetan Plateau. Due to the relatively broad range in estimated timing of

onset of increased erosion rates in both locations (15-5 Ma in the eastern margin of the Tibetan Plateau and 11-4 Ma from this study), we cannot conclude if increased erosion rates occurred truly simultaneously or if rates increased first in the east and then later in the west as knickpoints moved upstream or if a rate increase propagated from west to east relating to a migrating front of lower-crustal material. Testing specific predictions of west-to-east (or vice versa) propagation within a 10 million year window requires more precise estimates in timing.

5.8 Conclusions

This study determines patterns in erosion rates and timing of erosion-rate change across the east-central Tibetan Plateau interior by measurements of low-temperature thermochronometry in detrital apatites collected from modern river sands. The following points summarize the main conclusions from this work, which have implications regarding Tibetan Plateau tectonic and geomorphic evolution.

1. AHe and AFT ages range widely within all but one of the large catchments studied, which suggests that erosion histories are relatively uniform among catchments that span the entire width of the east-central Tibetan Plateau. Generalized modeling results show slow erosion until the late Cenozoic (11-4 Ma) when an abrupt increase to faster erosion rates (~0.2-0.6 mm/yr) occurred. The timing and rates of increased erosion found in this study also overlap results from the eastern plateau margin.
2. Uniform, slow erosion across much of Tibet until the late Cenozoic does not support a steep propagating plateau migrating to the north from collision time,

as is predicted for many geodynamic and mechanical descriptions of plateau evolution.

3. Although we cannot definitively distinguish between tectonic and climatic influences on the erosion record from this dataset alone, our results are consistent with broad surface uplift as the main driver of late Cenozoic erosion rate increase. We suggest that regional uplift potentially relates to flux of lower crustal material into this region, driving widespread and abrupt increases in erosion rate across the east-central Tibetan Plateau. We also relate a smaller-magnitude Eocene erosional event to local surface faulting associated with Indo-Asian plate collision.
4. We find no obvious correlation between erosion rate and precipitation either across the study site or when comparing to erosion rates within much wetter parts of the plateau (i.e. the eastern plateau perimeter). Erosion rates and timing of rate increases are commensurate along upstream and downstream sections of the major rivers draining Tibet. Thus, fluvial reaches within the Tibetan highlands are not isolated from base-level changes by a migrating knickpoint that has yet to drive into the headwaters regions, as has been thought previously.

5.9 Acknowledgements

This work was supported by the NSF grants EAR-0507431, EAR-0908711, EAR-0507788 and EAR-0810067, the National Science Foundation of China (40234040) and by the State Key Laboratory of Earthquake Dynamics (LED2008A01). We thank Lindsay

Hedges for assistance with sample analyses and John Bershaw and Pei-zhen Zhang for field support. Nathan Niemi provided helpful feedback that greatly improved this manuscript.

5.10 References

An, Z., Kutzbach, J.E., Prell, W.L., and Porter, S.C., 2001, Evolution of Asian monsoons and phased uplift of the Himalaya–Tibetan plateau since Late Miocene times: Nature, v. 411(6833), p. 62-66.

Argand, E., 1924, La tectonique de l'Asie, Proc. 13th Int. Geological Congr., 7, p. 170-372.

Arne, D., Worley, B., Wilson, C., Chen, S.F., Foster, D., Luo, Z.L., Liu, S.G., and Dirks, P., 1997, Differential exhumation in response to episodic thrusting along the eastern margin of the Tibetan Plateau: Tectonophysics, v. 280(3-4), p. 239-256.

Avdeev, B., Niemi, N.A., and Clark, M.K., 2011, Doing more with less: Bayesian estimation of erosion models with detrital thermochronometric data: Earth Planet Sci Lett., v. 305(3-4), p. 385-395.

Binnie, S. A., Phillips, W.M., Summerfield, M.A., Fifield, L,K., and Spotila, J.A., 2010, Tectonic and climatic controls of denudation rates in active orogens: The San Bernardino Mountains, California: Geomorphology, v. 118(3-4), p. 249-261.

Bird, P., 1991, Lateral Extrusion of Lower Crust from under High Topography, in the Isostatic Limit: J Geophys Res-Solid, v. 96(B6), p. 10275-10286.

Boos, W. R., and Kuang, Z.M., 2010, Dominant control of the South Asian monsoon by orographic insulation versus plateau heating: Nature, v. 463(7278), p. 218-222.

Booth, A. L., Chamberlain, C.P., Kidd, W.S.F., and Zeitler, P.K., 2009, Constraints on the metamorphic evolution of the eastern Himalayan syntaxis from geochronologic and petrologic studies of Namche Barwa: Geol Soc Am Bull, v. 121(3-4), p. 385-407.

Booth, A. L., Zeitler, P.K., Kidd, W.S.F., Wooden, J., Liu, Y., Idleman, B., Hren, M., and Chamberlain, C.P., 2004, U-Pb zircon constraints on the tectonic evolution of southeastern Tibet, Namche Barwa Area: Am J Sci, v. 304(10), p. 889-929.

Braun, J., 2002, Quantifying the effect of recent relief changes on age-elevation relationships: Earth Planet Sci. Lett, v. 200(3-4), p. 331-343.

Brewer, I. D., Burbank, D.W., and Hodges, K.V., 2003, Modelling detrital cooling-age populations: insights from two Himalayan catchments: Basin Res, v. 15(3), p. 305-320.

Brozovic, N., Burbank, D.W., and Meigs, A.J., 1997, Climatic limits on landscape development in the northwestern Himalaya: Science, v. 276(5312), p. 571-574.

Burbank, D. W., Blythe, A.E., Putkonen, J., Pratt-Sitaula, B., Gabet, E., Oskin, M., Barros, A., and Ojha, T.P., 2003, Decoupling of erosion and precipitation in the Himalayas: Nature, v. 426(6967), p. 652-655.

Burg, J. P., Davy, P., Nievergelt, P., Oberli, F., Seward, D., Diao, Z.Z., and Meier, M., 1997, Exhumation during crustal folding in the Namche-Barwa syntaxis: Terra Nova, v. 9(2), p. 53-56.

Burg, J. P., Nievergelt, P., Oberli, F., Seward, D., Davy, P., Maurin, J.C., Diao, Z.Z., and Meier, M., 1998, The Namche Barwa syntaxis: evidence for exhumation related to compressional crustal folding: J Asian Earth Sci, v. 16(2-3), p. 239-252.

Chung, S. L., Lo, C.H., Lee, T.Y., Zhang, Y.Q., Xie, Li, X.H., Wang, K.L., and Wang, P.L., 1998, Diachronous uplift of the Tibetan plateau starting 40 Myr ago: Nature, v. 394(6695), p. 769-773.

Clark, M. K., and Royden, L.H., 2000, Topographic ooze: Building the eastern margin of Tibet by lower crustal flow: Geology, v. 28(8), p. 703-706.

Clark, M. K., Farley, K.A., Zheng, D.W., Wang, Z.C., and Duvall, A.R., 2010, Early Cenozoic faulting of the northern Tibetan Plateau margin from apatite (U-Th)/He ages: Earth Planet Sci Lett, v. 296(1-2), p. 78-88.

Clark, M. K., Royden, L.H., Whipple, K.X., Burchfiel, B.C., Zhang, X., and Tang, W., 2006, Use of a regional, relict landscape to measure vertical deformation of the eastern Tibetan Plateau: J Geophys Res-Earth, v. 111(F3), doi:10.1029/2005JF000294.

Clark, M. K., House, M.A., Royden, L.H., Whipple, K.X., Burchfiel, B.C., Zhang, X., and Tang, W., 2005, Late Cenozoic uplift of southeastern Tibet: Geology, v. 33(6), p. 525-528.

Clift, P. D., 2006, Controls on the erosion of Cenozoic Asia and the flux of clastic sediment to the ocean: Earth Planet Sci Lett, v. 241(3-4), p. 571-580.

Clift, P. D., and Sun, Z., 2006, The sedimentary and tectonic evolution of the Yinggehai-Song Hong basin and the southern Hainan margin, South China Sea: Implications for Tibetan uplift and monsoon intensification: J Geophys Res-Sol Ea, v. 111(B6), doi:10.1029/2005JB004048.

Clift, P., Lee, J., Clark, M.K., and Blusztajn, J., 2002, Erosional response of South China to arc rifting and monsoonal strengthening; a record from the South China Sea: Mar Geol, v. 184(3-4), p. 207-226.

Currie, B. S., Rowley, D.B., and Tabor, N.J., 2005, Middle Miocene paleoaltimetry of southern Tibet: Implications for the role of mantle thickening and delamination in the Himalayan orogen: Geology, v. 33(3), p. 181-184.

Cyr, A. J., Currie, B.S., and Rowley, D.B., 2005, Geochemical evaluation of Fenghuoshan Group lacustrine carbonates, North-Central Tibet: Implications for the paleoaltimetry of the Eocene Tibetan Plateau: J Geol, v. 113(5), p. 517-533.

DeCelles, P. G., Quade, J., Kapp, P., Fan, M.J., Dettman, D.L., and Ding, L., 2007, High and dry in central Tibet during the late Oligocene: Earth Planet Sci Lett, v. 253(3-4), p. 389-401.

DeGraaff-Surpless, K., Mahoney, J. B., Wooden, J.L., and McWilliams, M.O., 2003, Lithofacies control in detrital zircon provenance studies: Insights from the Cretaceous Methow basin, southern Canadian Cordillera: Geol Soc Am Bull, v. 115(8), p. 899-915.

Dewey, J. F., Shackleton, R.M., Chengfa, C., and Yiyin, S., 1988, The tectonic evolution of the Tibetan Plateau: Philosophical Transactions of the Royal Society of London. Series A, Mathematical and Physical Sciences, 327(1594), 379 pp.

Ding, L., Zhong, D., Yin, A., Kapp, P., and Harrison, T.M., 2001, Cenozoic structural and metamorphic evolution of the eastern Himalayan syntaxis (Namche Barwa): Earth Planet Sci Lett, v. 192(3), p. 423-438.

Dodson, M., 1973, Closure temperature in cooling geochronological and petrological systems: Contributions to Mineralogy and Petrology, v. 40(3), p. 259-274.

Donelick, R. A., O'Sullivan, P.B., and Ketcham, R.A., 2005, Apatite fission-track analysis: Reviews in mineralogy and geochemistry, v. 58(1), p. 49-94.

Duvall, A. R., Clark, M.K., van der Pluijm, B.A., and Li, C., 2011, Direct dating of Eocene reverse faulting in northeastern Tibet using Ar-dating of fault clays and low-temperature thermochronometry: Earth Planet Sci Lett., v. 304(3-4), p. 520-526.

Ehlers, T. A., and Farley, K.A., 2003, Apatite (U-Th)/He thermochronometry: methods and applications to problems in tectonic and surface processes: Earth Planet Sci Lett, v. 206(1-2), p. 1-14.

Ehlers, T.A., 2005, Crustal thermal properties and thermchronometer data interpretation in Low-Temperature Thermochonology: Techniques, Interpretations, and Applications: Rev. Mineral. Geochem., 58, edited by P.W. Reiners, and T.A. Ehlers, p. 315-350.

England, P., and Houseman, G., 1986, Finite Strain Calculations of Continental Deformation .2. Comparison with the India-Asia Collision Zone: J Geophys Res-Solid, v. 91(B3), p. 3664-3676.

England, P., and Houseman, G., 1989, Extension during continental convergence, with application to the Tibetan Plateau: Journal of Geophysical Research, v. 94(B12), p. 17561-17579.

Enkelmann, E., Ratschbacher, L., Jonckheere, R., Nestler, R., Fleischer, M., Gloaguen, R., Hacker, B.R., Zhang, Y.Q., and Ma, Y.S., 2006, Cenozoic exhumation and

deformation of northeastern Tibet and the Qinling: Is Tibetan lower crustal flow diverging around the Sichuan Basin?: Geol Soc Am Bull, v. 118(5-6), p. 651-671.

Farley, K., 2000, Helium diffusion from apatite: General behavior as illustrated by Durango fluorapatite: Journal of Geophysical Research, v. 105(B2), p. 2903-2914.

Farley, K. A., Wolf, R.A., and Silver, L.T., 1996, The effects of long alpha-stopping distances on (U-Th)/He ages: Geochim Cosmochim Ac, v. 60(21), p. 4223-4229.

Finnegan, N. J., Hallet, B., Montgomery, D.R., Zeitler, P.K., Stone, J.O., Anders, A.M., and Yuping, L., 2008, Coupling of rock uplift and river incision in the Namche Barwa-Gyala Peri massif, Tibet: Geol Soc Am Bull, v. 120(1-2), p. 142-155.

Fitzgerald, P. G., and Gleadow, A.J.W., 1990, New Approaches in Fission-Track Geochronology as a Tectonic Tool - Examples from the Transantarctic Mountains: Nucl Tracks Rad Meas, v. 17(3), p. 351-357.

Flohn, H., Hantel, M., and Ruprecht, E., 1968, Air-Mass Dynamics or Subsidence Processes in Arabian Sea Summer Monsoon: J Atmos Sci, v. 25(3), p. 527-528.

Flowers, R.M., Shuster, D.L., Wernicke, B.P., and Farley, K.A., 2007, Radiation damage control on apatite (U-Th)/He dates from the Grand Canyon region, Colorado Plateau: Geology, 35(5), p. 447-450.

Galbraith, R., 2005, Statistics for fission track analysis: Interdisciplinary Statistics, Chapman & Hall/CRC, 219 pp.

Garzione, C. N., Quade, J., DeCelles, P.G., and English, N.B., 2000, Predicting paleoelevation of Tibet and the Himalaya from delta O-18 vs. altitude gradients in meteoric water across the Nepal Himalaya: Earth Planet Sci Lett, v. 183(1-2), p. 215-229.

Gleadow, A., and Duddy, I., 1981, A natural long-term track annealing experiment for apatite: Nuclear Tracks, v. 5(1-2), p. 169-174.

Godard, V., Cattin, R., and Lave, J., 2009, Erosional control on the dynamics of low-convergence rate continental plateau margins: Geophys J Int, v. 179(2), p. 763-777.

Godard, V., Pik, R., Lave, J., Cattin, R., Tibari, B., de Sigoyer, J., Pubellier, M., and Zhu, J., 2009, Late Cenozoic evolution of the central Longmen Shan, eastern Tibet: Insight from (U-Th)/He thermochronometry: Tectonics, v. 28, p. doi:10.1029/2008TC002407.

Henck, A. C., Huntington, K.W., Stone, J.O., Montgomery, D.R., and Hallet, B., 2011, Spatial controls on erosion in the Three Rivers Region, southeastern Tibet and southwestern China: Earth Planet Sci Lett: v. 303, p.71-83.

Henderson, A. L., Foster, G.L., and Najman, Y., 2010, Testing the application of in situ Sm-Nd isotopic analysis on detrital apatites: A provenance tool for constraining the timing of India-Eurasia collision: Earth Planet Sci Lett, v. 297(1-2), p. 42-49.

Horton, B. K., Yin, A., Spurlin, M.S., Zhou, J., and Wang, J., 2002, Paleocene–Eocene syncontractional sedimentation in narrow, lacustrine-dominated basins of east-central Tibet: Geol Soc Am Bull, v. 114(7), p. 771-786.

Hren, M. T., Bookhagen, B., Blisniuk, P.M., Booth, A.L., and Chamberlain, C.P., 2009, (delta) 18O and (delta) D of streamwaters across the Himalaya and Tibetan Plateau: Implications for moisture sources and paleoelevation reconstructions: Earth Planet Sci Lett, v. 288(1-2), p. 20-32.

Hu, S., He, L., and Wang, J., 2000, Heat flow in the continental area of China: a new data set: Earth Planet Sci Lett, v. 179(2), p. 407-419.

Jolivet, M., Brunel, M., Seward, D., Xu, Z., Yang, J., Roger, F., Tapponnier, P., Malavieille, J., Arnaud, N., and Wu, C., 2001, Mesozoic and Cenozoic tectonics of the northern edge of the Tibetan plateau: fission-track constraints: Tectonophysics, v. 343(1-2), p. 111-134.

Kent-Corson, M.L., Ritts, B.D., Zhuang, G., Bovet, P.M., Graham, S.A., and Chamberlain, C.P., 2009, Stable isotope constraints on the tectonic, topographic, and climate evolution of the northern margin of the Tibetan Plateau: Earth Planet Sci Lett, v. 282(1-4), p. 158-166.

Ketcham, R. A., Carter, A., Donelick, R.A., Barbarand, J., and Hurford, A.J., 2007, Improved modeling of fission-track annealing in apatite: American Mineralogist, v. 92(5-6), p. 799-810.

Kirby, E., Reiners, P.W., Krol, M.A., Whipple, K.X., Hodges, K.V., Farley, K.A., Tang, W.Q., and Chen, Z.L., 2002, Late Cenozoic evolution of the eastern margin of the Tibetan Plateau: Inferences from Ar-40/Ar-39 and (U-Th)/He thermochronology: Tectonics, v. 21(1), doi:10.1029/2000TC001246.

Korup, O., and Montgomery, D., 2008, Tibetan plateau river incision inhibited by glacial stabilization of the Tsangpo gorge: Nature, v. 455, p. 786-789.

Lal, D., Harris, N.B.W., Sharma, K.K., Gu, Z., Ding, L., Liu, T., Dong, W., Caffee, M.W., and Jull, A., 2004, Erosion history of the Tibetan Plateau since the last interglacial: constraints from the first studies of cosmogenic 10Be from Tibetan bedrock: Earth Planet Sci Lett, v. 217(1-2), p. 33-42.

Lease, R. O., Burbank, D.W., Gehrels, G.E., Wang, Z.C., and Yuan, D.Y., 2007, Signatures of mountain building: Detrital zircon U/Pb ages from northeastern Tibet: Geology, v. 35(3), p. 239-242.

Lease, R. O., Burbank, D.W., Clark, M.K., Farley, K.A., Zheng, D., and Zhang, H., 2011, Middle Miocene reorganization of deformation along the northeastern Tibetan Plateau: Geology, v. 39(4), p. 359-362.

Li, C. F., and Yanai, M., 1996, The onset and interannual variability of the Asian summer monsoon in relation to land sea thermal contrast: J Climate, v. 9(2), p. 358-375.

Liu, Z., Zhao, X., Wang, C., Liu, S., and Yi, H., 2003, Magnetostratigraphy of Tertiary sediments from the Hoh Xil Basin: implications for the Cenozoic tectonic history of the Tibetan Plateau: Geophys J Int, v. 154(2), p. 233-252.

Liu-Zeng, J., Tapponnier, P., Gaudemer, Y., and Ding, L., 2008, Quantifying landscape differences across the Tibetan plateau: Implications for topographic relief evolution: Journal of Geophysical Research, v. 113(F4), doi:10.1029/2007JF000897.

Malloy, M., 2004, Rapid erosion at the Tsangpo knickpoint and exhumation of southeastern Tibet (MS thesis): Bethlehem, Pennsylvania, Lehigh University, 84.

Mancktelow, N. S., and Grasemann, B., 1997, Time-dependent effects of heat advection and topography on cooling histories during erosion: Tectonophysics, v. 270(3-4), p. 167-195.

Matsuura, K., and Willmott, C., 2007, Terrestrial Air Temperature and Precipitation: 1900-2006 Gridded Monthly Time Series, Version 1.01, University of Delaware, http://climate. geog. udel. edu/~ climate.

Molnar, P., 2005, Mio-pliocene growth of the Tibetan Plateau and evolution of East Asian climate: Palaeontol Electron, v. 8(1), 2A:23p.

Molnar, P., England, P., and Martinod, J., 1993, Mantle Dynamics, Uplift of the Tibetan Plateau, and the Indian Monsoon: Rev Geophys, v. 31(4), p. 357-396.

Molnar, P., Boos, W.R., and Battisti, D.S., 2010, Orographic Controls on Climate and Paleoclimate of Asia: Thermal and Mechanical Roles for the Tibetan Plateau: Annu Rev Earth Pl Sc, v. 38, p. 77-102.

Montgomery, D. R., Balco, G., and Willett, S.D., 2001, Climate, tectonics, and the morphology of the Andes: Geology, v. 29(7), p. 579-582.

New, M., Lister, D., Hulme, M., and Makin, I., 2002, A high-resolution data set of surface climate over global land areas: Climate Res, v. 21(1), p. 1-25.

Niemi, N. A., Oskin, M., Burbank, D.W., Heimsath, A.M., and Gabet, E.J., 2005, Effects of bedrock landslides on cosmogenically determined erosion rates: Earth Planet Sci Lett, v. 237(3-4), p. 480-498.

Ouimet, W., 2007, Dissecting the Eastern Margin of the Tibetan Plateau: A Study of Landslides, Erosion and River Incision in a Transient Landscape (Ph.D. thesis): Cambridge, Massachusetts Institute of Technology, 197 p.

Ouimet, W., Whipple, K., Royden, L., Sun, Z., and Chen, Z., 2007, The influence of large landslides on river incision in a transient landscape: Eastern margin of the Tibetan Plateau (Sichuan, China): Geological Society of America Bulletin, v. 119(11), p. 1462– 1476.

Ouimet, W. B., Whipple, K.X., and Granger, D.E., 2009, Beyond threshold hillslopes: Channel adjustment to base-level fall in tectonically active mountain ranges, Geology, 37(7), 579.

Ouimet, W., Whipple, K., Royden, L., Reiners, P., Hodges, K., and Pringle, M., 2010, Regional incision of the eastern margin of the Tibetan Plateau: Lithosphere, v. 2(1), p. 50-63.

Pan, G., Ding, J., Yao, D., and Wang, L., 2004, Guidebook of 1:1,500,000 geologic map of the Qinghai-Xizang (Tibet) plateau and adjacent areas, Chengdu, China, Chengdu Cartographic Publishing House, 48 pp.

Polissar, P. J., Freeman, K.H., Rowley, D.B., McInerney, F.A., and Currie, B.S., 2009, Paleoaltimetry of the Tibetan Plateau from D/H ratios of lipid biomarkers: Earth Planet Sci Lett, v. 287(1-2), p. 64-76.

Powell, C. M. A., 1986, Continental underplating model for the rise of the Tibetan Plateau: Earth Planet Sc Lett, v. 81(1), p. 79-94.

Prell, W. L., and Kutzbach, J.E., 1992, Sensitivity of the Indian monsoon to forcing parameters and implications for its evolution: Nature, v. 360(6405), p. 647-652.

Rahl, R. M., Reiners, P.W., Campbell, I.H., Nicolescu, S., and Allen, C.M., 2003, Combined single-grain (U-Th)/He and U/Pb dating of detrital zircons from the Navajo Sandstone, Utah: Geology, v. 31(9), p. 761-764.

Reiners, P. W., and Brandon, M.T., 2006, Using thermochronology to understand orogenic erosion: Annu. Rev. Earth Planet. Sci., v. 34, p. 419-466.

Reiners, P. W., Ehlers, T.A., Mitchell, S.G., and Montgomery, D.R., 2003, Coupled spatial variations in precipitation and long-term erosion rates across the Washington Cascades: Nature, v. 426(6967), p. 645-647.

Riebe, C. S., Kirchner, J.W., Granger, D.E., and Finkel, R.C., 2001, Minimal climatic control on erosion rates in the Sierra Nevada, California: Geology, v. 29(5), p. 447-450.

Rowley, D. B., 1996, Age of initiation of collision between India and Asia: A review of stratigraphic data: Earth Planet Sci Lett, v. 145(1-4), p. 1-13.

Rowley, D. B., 1998, Minimum age of initiation of collision between India and Asia north of Everest based on the subsidence history of the Zhepure Mountain section: The Journal of geology, v. 106(2), p. 220-235.

Rowley, D. B., and Currie, B.S., 2006, Palaeo-altimetry of the late Eocene to Miocene Lunpola basin, central Tibet: Nature, v. 439(7077), p. 677-681.

Rowley, D. B., Pierrehumbert, R.T., and Currie, B.S., 2001, A new approach to stable isotope-based paleoaltimetry: implications for paleoaltimetry and paleohypsometry of the High Himalaya since the Late Miocene: Earth Planet Sci Lett, v. 188(1-2), p. 253-268.

Royden, L.H., Burchfiel, B.C., King, R.W., Wang, E., Chen, Z., Shen, F., and Liu, Y., 1997, Surface deformation and lower crustal flow in Eastern Tibet: Science, v. 276(5313), p. 788-790.

Royden, L. H., Burchfiel, B.C., and van der Hilst, R.D., 2008, The geological evolution of the Tibetan plateau: Science, v. 321(5892), p. 1054-1058.

Ruhl, K. W., and Hodges, K.V., 2005, The use of detrital mineral cooling ages to evaluate steady state assumptions in active orogens: An example from the central Nepalese Himalaya: Tectonics, v. 24(4), doi:10.1029/2004TC001712.

Shuster, D.L., Flowers, R.M., and Farley, K.A., 2006, The influence of natural radiation damage on helium diffusion kinetics in apatite: Earth Planet Sci Lett, v. 249, p. 148-161.

Shuster, D.L., and Farley, K.A., 2009, The influence of artificial radiation damage and thermal annealing on helium diffusion kinetics in apatite: Geochim. Cosmochim. Acta, v. 73, p. 183-196.

Seward, D., and Burg, J.P., 2008, Growth of the Namche Barwa Syntaxis and associated evolution of the Tsangpo Gorge: Constraints from structural and thermochronological data: Tectonophysics, v. 451(1-4), p. 282-289.

Spicer, R. A., Harris, N.B.W., Widdowson, M., Herman, A.B., Guo, S.X., Valdes, P.J., Wolfe, J.A., and Kelley, S.P., 2003, Constant elevation of southern Tibet over the past 15 million years: Nature, v. 421(6923), p. 622-624.

Spurlin, M. S., Yin, A., Horton, B.K., Zhou, J., and Wang, J., 2005, Structural evolution of the Yushu-Nangqian region and its relationship to syncollisional igneous activity, east-central Tibet: Bulletin of the Geological Society of America, v. 117(9-10), p. 1293-1317.

Stewart, R. J., Hallet, B., Zeitler, P.K., Malloy, M.A., Allen, C.M., and Trippett, D., 2008, Brahmaputra sediment flux dominated by highly localized rapid erosion from the easternmost Himalaya: Geology, v. 36(9), p. 711-714.

Stuwe, K., White, L., and Brown, R., 1994, The influence of eroding topography on steady-state isotherms. Application to fission track analysis: Earth Planet Sci Lett, v. 124(1-4), p. 63-74.

Tapponnier, P., Peltzer, G., Ledain, A.Y., Armijo, R., and Cobbold, P., 1982, Propagating Extrusion Tectonics in Asia - New Insights from Simple Experiments with Plasticine: Geology, v. 10(12), p. 611-616.

Tapponnier, P., Xu, Z.Q., Roger, F., Meyer, B., Arnaud, N., Wittlinger, G., and Yang, J.S., 2001, Oblique stepwise rise and growth of the Tibet plateau: Science, v. 294(5547), p. 1671-1677.

Taylor, M., and Yin, A., 2009, Active structures of the Himalayan-Tibetan orogen and their relationships to earthquake distribution, contemporary strain field, and Cenozoic volcanism: Geosphere, v. 5(3), p.199-214.

Thiede, R. C., Bookhagen, B., Arrowsmith, J.R., Sobel, E.R., and Strecker, M.R., 2004, Climatic control on rapid exhumation along the Southern Himalayan Front: Earth Planet Sci Lett, v. 222(3-4), p. 791-806.

Vermeesch, P., 2004, How many grains are needed for a provenance study?, Earth Planet Sci Lett, v. 224(3-4), p. 441-451.

Wang, C., Zhao, X., Liu, Z., Lippert, P.C., Graham, S.A., Coe, R.S., Yi, H., Zhu, L., Liu, S., and Li, Y., 2008, Constraints on the early uplift history of the Tibetan Plateau, Proceedings of the National Academy of Sciences: v. 105(13), p. 4987-4992.

Whipple, K.X., 2010, Transient landscapes: Recorders of history and engines of discovery, Abstract EP51G-02, presented at 2010 Fall Meeting, AGU, San Francisco, Calif., 13-17 Dec.

Whipple, K. X., and Tucker, G.E., 1999, Dynamics of the stream-power river incision model: Implications for height limits of mountain ranges, landscape response timescales, and research needs: J Geophys Res-Sol Ea, v. 104(B8), p. 17661-17674.

Wilson, C.J.L., and Fowler, A.P., 2011, Denudational response to surface uplift in east Tibet: Evidence from apatite fission-track thermochronology: Bulletin of the Geological Society of America, doi:10.1130/B30331.1.

Wolf, R. A., Farley, K.A., and Silver, L.T., 1996, Helium diffusion and low-temperature thermochronometry of apatite: Geochim Cosmochim Ac, v. 60(21), p. 4231-4240.

Wolf, R. A., Farley, K.A., and Kass, D.M., 1998, Modeling of the temperature sensitivity of the apatite (U-Th)/He thermochronometer: Chem Geol, v. 148(1-2), p. 105-114.

Xu, G. Q., and Kamp, P.J.J., 2000, Tectonics and denudation adjacent to the Xianshuihe Fault, eastern Tibetan Plateau: Constraints from fission track thermochronology: J Geophys Res-Sol Ea, v. 105(B8), p. 19231-19251.

Yanai, M., and Wu, G.X., 2006, Effects of the Tibetan Plateau: The Asian Monsoon: Part 3, p. 513-549.

Yanites, B. J., Tucker, G.E., and Anderson, R.S., 2009, Numerical and analytical models of cosmogenic radionuclide dynamics in landslide-dominated drainage basins: J Geophys Res-Earth, v. 114, doi:10.1029/2008JF001088.

Yin, A., and Harrison, T.M., 2000, Geologic evolution of the Himalayan-Tibetan orogen: Annual Review of Earth and Planetary Sciences, v. 28, p. 211-280.

Yin, A., Dang, Y.Q., Wang, L.C., Jiang, W.M., Zhou, S.P., Chen, X.H., Gehrels, G.E., and McRivette, M.W., 2008, Cenozoic tectonic evolution of Qaidam basin and its

surrounding regions (Part 1): The southern Qilian Shan-Nan Shan thrust belt and northern Qaidam basin: Geol Soc Am Bull, v. 120(7-8), p. 813-846.

Zeitler, P. K., Herczeg, A.L., Mcdougall, I., and Honda, M., 1987, U-Th-He Dating of Apatite - a Potential Thermochronometer: Geochim Cosmochim Ac, v. 51(10), p. 2865-2868.

Zeitler, P., Malloy, M., Kutney, M., Idleman, B., Liu, Y., Kidd, W., and Booth, A., 2006, Geochronological evidence for the tectonic and topographic evolution of SE Tibet: Eos Trans. AGU, 87(52), Fall Meet. Suppl., Abstract T32B-02.

Zhao, W. L., and Morgan, W.J., 1987, Injection of Indian Crust into Tibetan Lower Crust - a Two-Dimensional Finite-Element Model Study: Tectonics, v. 6(4), p. 489-504.

Zheng, D. W., Zhang, P.Z., Wan, J.L., Li, C.Y., and Cao, J.X., 2003, Late Cenozoic deformation subsequence in northeastern margin of Tibet - Detrital AFT records from Linxia Basin: Sci China Ser D, v. 46, p. 266-275.

Zheng, D., Clark, M.K., Zhang, P., Zheng, W., and Farley, K.A., 2010, Erosion, fault initiation and topographic growth of the North Qilian Shan (northern Tibetan Plateau): Geosphere, v. 6(6), p. 937-941.

Zheng, D. W., Zhang, P.Z., Wan, J.L., Yuan, D.Y., Li, C.Y., Yin, G.M., Zhang, G.L., Wang, Z.C., Min, W., and Chen, J., 2006, Rapid exhumation at similar to 8 Ma on the Liupan Shan thrust fault from apatite fission-track thermochronology: Implications for growth of the northeastern Tibetan Plateau margin: Earth Planet Sci Lett, v. 248(1-2), p. 198-208.

Zhu, B., Kidd, W.S.F., Rowley, D.B., Currie, B.S., and Shafique, N., 2005, Age of initiation of the India-Asia collision in the east-central Himalaya: J Geol, v. 113(3), p. 265-285.

Appendix: Chapter V

This appendix contains three tables. Table A5.1 contains the detailed results of apatite (U-Th)/He analyses for all catchments studied. All samples were analyzed at the Noble Gas Laboratory, California Institute of Technology. Table A5.2 contains the detailed results of apatite fission-track analyses for all catchments with exception to the Mekong(b) due to low apatite yields. All analyses were completed by A to Z, Inc. Table A5.3 contains the detailed results from zircon U-Pb dating for two catchments: 07TS06 (Yellow River) and 07TS12 (Yangtze River). All analyses were completed at the University of Arizona LaserChron Center.

Appendix Table A 5.1. (U-Th)/He analyses

Sample ID: 07TS06
Catchment Name: Yellow

Grain #	U (ppm)	Th (ppm)	He (nmol/g)	mass (µg)	radius (µm)	length (µm)	F_T	Sm (ppm)	Grain Quality	Raw Age (Ma)	Corrected Age (Ma)
1	0.5682	7.2731	0.0344	1.2385	45	101	0.64	10.8694	average	2.76	4.33
2	65.1636	66.3498	3.2118	2.2656	54	131	0.72	111.5369	round	7.30	10.18
3	7.1737	26.3314	0.7869	1.4430	44.5	132	0.67	139.8997	round	10.69	15.95
4	11.8241	71.5893	2.5319	0.7766	40	91	0.61	269.6239	round	16.06	26.32
5	1.3232	0.3215	0.1657	4.1134	75	136	0.78	12.4518	average	21.53	27.57
6	141.4949	77.5360	16.0960	1.2571	41	110	0.65	364.6495	round	18.47	28.42
7	43.2489	547.1283	17.5152	0.8840	41	105	0.62	734.7415	round	18.63	30.08
8	10.8649	170.4991	6.7017	1.1475	46.5	132	0.66	289.0506	round	24.00	36.04
9	15.2565	47.9028	3.9583	2.0417	60.5	128	0.73	266.6664	round	27.09	37.01
10	29.2982	123.7718	7.7721	1.1690	44.5	105	0.65	165.2700	round	24.37	37.53
11	30.0693	615.2657	24.5641	1.1675	41	117	0.62	509.9883	round	25.73	41.24
12	4.3171	1.4277	1.0067	6.7616	74	192	0.79	64.1010	round	39.03	48.84
13	11.2695	32.5788	4.6892	2.2613	58	113	0.71	137.3905	average	45.05	63.06
14	30.6448	79.6085	11.3081	1.2996	40	120	0.64	370.0944	round	41.65	64.89
15	15.1334	15.6466	4.6584	2.1647	47.5	128	0.69	92.0223	round	45.13	65.23
16	9.4123	29.3993	5.9202	1.4016	47.5	139	0.69	167.1902	round	65.62	94.95
17	2.0433	13.5788	2.3915	1.3689	45.5	136	0.67	39.0118	average	82.90	123.44
18	2.0969	7.1870	2.0121	1.1442	40	120	0.63	274.6730	average	89.42	134.31
19	4.8914	38.0207	7.0472	2.4816	40	231	0.66	240.1309	average	91.37	136.35
20	6.0389	29.4378	8.3964	2.8740	57.5	164	0.73	60.7066	round	117.67	160.22

Sample ID: 07TS07

Catchment Name: Yellow_small

Grain #	U (ppm)	Th (ppm)	He (nmol/g)	mass (µg)	radius (µm)	length (µm)	F_T	Sm (ppm)	Grain Quality	Raw Age (Ma)	Corrected Age (Ma)
1	9.7024	52.6342	2.6279	1.3829	47.5	114	0.67	266.6014	round	21.56	32.11
2	6.6583	85.4565	3.4653	2.0891	54.5	129	0.70	215.1702	round	23.57	33.63
3	42.0176	788.6660	28.1581	1.6891	48.5	118	0.66	505.8811	round	22.68	34.14
4	11.3910	13.5671	2.5295	2.6940	52.5	144	0.72	344.7026	round	30.97	42.70
5	17.9748	161.1187	10.5005	1.7376	53	134	0.70	363.3221	round	34.25	48.92
6	9.7160	101.3119	6.2748	1.9885	48	149	0.68	225.3955	round	34.08	49.77
7	23.7852	17.8350	5.7760	2.7105	54.5	144	0.73	27.8609	round	37.82	51.99
8	15.0756	65.3514	5.9847	2.7245	44	152	0.67	248.4425	average	35.74	53.01
9	16.2846	94.4107	7.9080	1.7830	52	137	0.70	301.7372	round	37.37	53.26
10	35.9440	47.4060	10.4943	3.3759	47.5	193	0.71	221.3858	average	40.65	56.98
11	1.6281	2.2785	0.5145	2.6186	56.5	137	0.73	58.5635	round	42.24	57.43
12	1.8080	1.3281	0.4852	2.4134	52	132	0.71	29.4517	average	41.28	57.58
13	30.9600	111.2264	15.1604	1.1362	43	105	0.64	86.1166	round	48.60	75.58
14	3.2203	3.4413	1.5789	4.1098	65	171	0.77	97.2021	round	69.67	90.07
15	47.8478	30.1847	27.1934	2.7018	51	152	0.72	159.8583	average	90.00	124.95
16	2.0381	2.6458	1.6007	2.5469	54	128	0.71	142.2234	round	103.19	140.72
17	0.3223	0.8646	0.4322	2.7003	54	152	0.72	5.5495	round	147.82	203.73

Sample ID: 07TS09

Catchment Name: Yalong

					radius	length			Grain	Raw	Corrected

Grain #	U (ppm)	Th (ppm)	He (nmol/g)	mass (µg)	(µm)	(µm)	F_T	Sm (ppm)	Quality	Age (Ma)	Age (Ma)
1	7.5377	38.8916	0.7481	1.6805	42	103	0.63	352.4895	round	8.04	12.57
2	18.7376	64.5104	2.1588	0.7551	40	97	0.62	185.8961	round	11.63	18.74
3	32.2204	15.2213	6.4126	5.9360	65.5	194	0.78	175.4176	round	32.68	42.01
4	17.5033	101.3750	8.2416	1.4099	49	120	0.68	199.6356	round	36.39	53.63
5	46.9028	69.9552	16.1972	0.7582	41.5	88	0.63	417.9409	average	46.51	73.75
6	13.5112	80.0182	8.6480	1.6469	42.5	119	0.64	346.7802	round	48.46	74.72
7	18.6100	38.2835	7.8264	2.6657	45	144	0.68	204.0002	average	51.50	75.36
8	58.2622	84.6305	21.7982	1.3745	45.5	113	0.67	342.1092	pristine	50.85	75.69
9	30.6823	54.3019	12.8740	2.8473	45	159	0.69	216.4889	average	53.97	78.20
10	46.9567	75.9527	21.4139	3.8071	60.5	202	0.76	263.4065	average	60.21	79.07
11	43.2994	85.7092	20.3837	2.4430	52	163	0.72	339.1656	round	58.48	81.09
12	42.2972	70.4664	20.5499	3.6421	52	178	0.72	266.0665	round	63.57	87.49
13	15.1033	30.6203	6.9009	1.0123	42	101	0.64	109.0181	average	56.36	87.83
14	34.2057	25.4286	12.3610	1.3349	39	98	0.63	305.5899	average	55.82	88.51
15	30.5342	45.3332	16.7678	3.9806	58	178	0.75	474.9376	round	73.45	97.79
16	88.9123	72.2961	44.3184	3.6931	56.5	182	0.75	83.5800	average	76.41	102.23
17	44.8167	83.7470	22.7884	0.7638	40	87	0.61	363.3162	average	64.25	103.90
18	31.2034	66.2913	20.1137	1.4328	51.5	110	0.69	325.8570	round	77.98	112.39
19	22.5634	48.9997	19.7419	3.4644	55	150	0.72	246.7064	average	104.82	143.92

Sample ID: 07TS12

Catchment Name: Yangtze

Grain #	U (ppm)	Th (ppm)	He (nmol/g)	mass (µg)	radius (µm)	length (µm)	F_T	Sm (ppm)	Grain Quality	Raw Age (Ma)	Corrected Age (Ma)
1	21.5792	0.3246	0.3861	3.5363	57.00	148.00	0.74	42.0561	average		3.93
2	14.4981	0.3691	0.4706	3.7847	49.00	213.00	0.72	90.6723	pristine		6.46
3	56.9753	1.4231	2.6462	2.2562	51.00	108.00	0.69	81.6991	average		8.77
4	36.1053	1.6540	2.3041	2.6671	50.00	154.00	0.70	161.5433	average		8.88

5	47.0040	1.2645	2.8584	3.9299	55.50	215.00	0.74	84.7471	pristine		9.74
6	44.9780	1.4425	2.7764	3.4412	49.50	146.00	0.70	103.4576	average		9.84
7	30.5403	1.2697	1.9815	2.6048	45.50	159.00	0.68	103.3520	average		10.21
8	23.7303	1.3928	2.8717	2.2390	48.00	121.00	0.68	150.0686	round		16.66
9	16.1424	0.3300	1.0308	1.8600	42.50	136.00	0.68	31.8425	average		16.96
10	60.6591	0.6067	7.2183	3.6009	52.50	171.00	0.73	75.0166	average		26.26
11	59.3538	0.8133	7.0581	1.6959	51.50	75.00	0.66	95.0413	average		28.83
12	58.0705	0.8305	13.9314	4.4711	55.50	202.00	0.75	167.5963	average		46.85
13	71.7449	0.6787	17.9689	4.4126	56.50	221.00	0.76	108.7270	pristine		52.57
14	62.7380	0.5146	13.8411	1.9084	46.00	110.00	0.68	81.1809	average		56.15
15	68.4758	0.5004	17.3911	2.1565	45.50	124.00	0.68	125.1859	average		63.94
16	3.3819	0.6219	1.6134	1.4870	40.00	84.00	0.60	92.7366	average		64.05
17	60.0751	0.4842	15.9562	2.5609	46.00	154.00	0.70	102.5350	average		64.40
18	35.0824	0.6466	9.7100	2.6406	41.00	96.00	0.63	136.5434	average		64.94
19	172.7170	0.6895	51.4926	3.8564	49.00	162.00	0.72	118.4931	average		71.70
20	14.0791	0.4388	5.2284	3.1413	49.00	136.00	0.70	122.7772	average		72.69

Sample ID: 07TS14

Catchment Name: Mekong

Grain #	U (ppm)	Th (ppm)	He (nmol/g)	mass (µg)	radius (µm)	length (µm)	F_T	Sm (ppm)	Grain Quality	Raw Age (Ma)	Corrected Age (Ma)
1	28.8157	98.1466	2.0365	6.6579	74.5	265	0.80	88.6531	pristine	7.20	9.00
2	25.9608	84.3122	1.6874	2.5573	65.5	116	0.73	133.1889	average	6.75	9.20
3	2.8374	45.8557	0.6151	5.6018	65.5	224	0.76	160.9995	pristine	8.19	10.68
4	41.6339	40.1118	2.3096	2.8992	59.5	182	0.75	66.0144	average	8.31	11.01
5	14.7696	206.7278	3.0156	4.2342	70	190	0.77	315.8708	average	8.69	11.32
6	9.3396	101.0086	1.6610	5.8701	74.5	221	0.79	201.8481	average	9.16	11.64
7	20.4349	318.2912	4.6744	2.9238	62.5	153	0.73	150.2422	round	9.00	12.26
8	25.1452	380.8136	5.5989	2.6378	51.5	171	0.70	168.8122	average	8.96	12.74

9	11.9287	127.7058	2.3219	4.9121	77	179	0.78	110.3489	average	10.14	13.00
10	3.8408	7.6622	0.3479	33.1371	56	134	0.72	27.4904	round	11.27	15.61
11	87.1347	212.2362	11.4308	1.4025	63	162	0.75	1971.3326	round	15.07	19.93
12	36.1667	83.1452	5.4827	4.8384	65	224	0.77	119.5099	average	18.04	23.29
13	6.4414	7.1824	0.8985	27.1498	50.5	220	0.73	111.5561	average	19.98	27.17
14	43.1734	84.0838	7.6636	1.9108	55	121	0.71	1452.7688	average	21.77	30.31
15	23.5621	69.4110	5.2847	5.3117	79	145	0.78	65.9155	average	24.29	31.14
16	26.0066	106.2234	6.7180	4.1930	69	153	0.76	117.3573	average	24.14	31.72
17	3.3998	6.7600	0.7858	12.2114	65	94	0.72	95.5716	pristine	28.27	39.03
18	3.8368	5.2911	1.0162	25.4150	68.5	195	0.78	77.4605	round	36.04	45.96
19	3.4438	8.0250	1.4129	2.9104	67.5	152	0.76	236.5066	round	46.16	59.71
20	24.6106	58.3531	12.2107	2.3883	62.5	138	0.74	699.1078	round	57.13	76.43

Sample ID: 07TS15

Catchment Name: Mekong(b)

Grain #	U (ppm)	Th (ppm)	He (nmol/g)	mass (µg)	radius (µm)	length (µm)	F_T	Sm (ppm)	Grain Quality	Raw Age (Ma)	Corrected Age (Ma)
1	15.6571	100.8851	1.5372	3.9607	52.5	93	0.67	260.8127	average	7.12	9.98
2	7.6707	51.2509	0.7874	2.9044	49	176	0.70	238.8135	average	7.24	10.28
3	10.6696	134.5581	2.5162	3.0760	68	125	0.74	144.1544	average	10.89	14.77
4	27.0025	96.8655	3.2711	2.6673	54	130	0.71	104.6158	average	12.05	17.03
5	41.2277	104.1914	5.4350	2.2798	48.5	155	0.70	228.9258	round	15.14	21.62
6	130.5468	29.8392	13.0511	2.9543	50.5	167	0.72	273.3221	average	17.39	24.03
7	5.4829	20.2690	1.2693	2.6968	57	110	0.70	448.9586	average	21.62	30.07
8	36.0447	23.0038	6.5298	1.3681	43	103	0.65	60.3420	round	28.87	44.06
9	35.9536	188.3094	16.1515	4.5735	59.5	206	0.75	203.9242	average	36.84	49.13
10	4.7421	25.6465	2.3339	2.1588	50	112	0.68	177.4162	average	39.00	57.12

Sample ID: 07TS20

Catchment Name: Salween

Grain #	U (ppm)	Th (ppm)	He (nmol/g)	mass (µg)	radius (µm)	length (µm)	F_T	Sm (ppm)	Grain Quality	Raw Age (Ma)	Corrected Age (Ma)
1	64.4747	6.7531	6.6833	2.3815	53	174	0.74	144.0794	round	18.54	25.16
2	38.9713	46.3386	4.8987	1.3800	40	121	0.64	229.8871	round	17.95	27.74
3	13.4300	19.4365	2.6784	4.1723	47.5	129	0.69	188.5154	average	26.99	38.99
4	48.0794	45.4076	9.1469	1.5390	44	148	0.68	429.7383	round	28.33	41.32
5	46.6652	71.3661	12.7811	4.4743	63	170	0.76	113.1370	round	36.89	48.61
6	17.5262	56.7699	5.7764	2.1609	48	148	0.69	101.5446	average	34.21	49.33
7	15.9084	2.6868	3.3048	1.9188	53	121	0.71	374.4474	average	35.68	49.44
8	43.7553	100.6685	12.4403	1.4873	42	108	0.64	253.5967	average	33.72	52.30
9	32.6223	33.3474	7.7669	1.5558	41.5	138	0.66	234.4965	round	34.98	52.48
10	49.9773	99.1887	14.9522	2.0871	51	142	0.71	312.3890	round	37.24	52.60
11	46.8217	136.9632	15.8793	1.3511	40	125	0.64	177.8191	average	36.78	57.36
12	20.6141	6.5838	5.1791	1.9000	50.5	126	0.71	369.2055	pristine	42.00	58.92
13	47.7163	118.1219	17.7601	2.2576	45	169	0.69	180.9813	average	43.03	62.46
14	38.3103	6.8779	10.3493	2.3804	53	157	0.73	349.6889	round	46.99	64.00
15	59.8811	75.0899	23.8918	4.1756	59	207	0.76	297.9166	round	56.18	73.96
16	23.6599	43.3610	10.2134	3.4309	52	191	0.73	271.2842	average	54.75	74.93
17	25.0248	16.7960	9.1549	2.0451	45	148	0.69	313.7619	round	57.11	82.22
18	46.1872	10.4622	19.0647	1.8514	54	120	0.72	271.1388	average	71.14	98.86
19	19.7156	17.3411	12.3909	1.2176	40	104	0.64	323.3736	average	93.52	145.12
20	45.0404	90.3515	404.1263	1.6250	45	126	0.67	213.6304	average	1007.82	1398.99

Sample ID: 07TS23

Catchment Name: Tsangpo

Grain #	U (ppm)	Th (ppm)	He (nmol/g)	mass (µg)	radius (µm)	length (µm)	F_T	Sm (ppm)	Grain Quality	Raw Age (Ma)	Corrected Age (Ma)
1	14.8218	18.5338	0.0890	4.5024	52.00	196.00	0.73	39.4658	pristine		1.17

2	14.7687	37.9730	0.1727	3.7374	50.50	189.00	0.72	202.3915	average	1.84
3	6.2658	23.1456	0.0857	3.3574	60.00	112.00	0.71	43.0452	pristine	1.87
4	25.5142	102.1384	0.5070	3.0295	58.50	122.00	0.72	144.3431	pristine	2.62
5	10.8506	23.7749	0.2319	2.5191	49.50	132.00	0.69	82.0506	average	3.70
6	21.7360	68.3201	0.5171	2.1955	53.50	84.00	0.67	22.9513	average	3.76
7	19.0982	103.9618	0.7180	3.8503	55.00	148.00	0.71	112.1843	average	4.22
8	11.4744	24.9288	0.2768	2.1942	57.00	74.00	0.67	144.5689	average	4.33
9	8.7454	37.0458	0.3060	3.1193	52.00	145.00	0.70	332.1489	average	4.43
10	24.5533	104.1293	0.8076	2.5178	50.50	103.00	0.67	50.9849	average	4.49
11	21.5402	29.5742	0.5060	3.3895	51.00	144.00	0.71	23.6411	average	4.60
12	5.7417	22.9342	0.2090	2.6368	49.50	92.00	0.66	255.7074	pristine	5.03
13	6.9216	6.1964	0.1503	3.8938	43.00	84.00	0.63	14.9493	average	5.19
14	7.7096	25.2187	0.2988	2.5930	52.00	123.00	0.70	271.7171	average	5.60
15	10.9138	41.2881	0.4715	2.8552	48.00	149.00	0.69	30.6151	average	6.07
16	17.6373	73.1992	0.8400	2.1443	43.00	125.00	0.65	37.0659	average	6.78
17	13.4025	73.9750	0.9193	2.9770	55.50	141.00	0.71	120.4198	average	7.64
18	9.3839	35.0452	0.4818	1.9496	48.50	84.00	0.65	27.5792	average	7.76
19	92.6564	25.4468	5.6925	3.9642	54.50	175.00	0.74	125.0901	average	14.29

Appendix Table A5.2. Apatite fission-track analyses

Sample ID: 07TS06

Catchment Name: Yellow

Grain #	N_s	Area (cm x cm)	$^{238}U/^{43}Ca$ (dmnls)	1 σ	^{43}Ca	^{238}U	^{232}Th	^{147}Sm	P(corr)	1 σ	*reported* FT Age (Ma)	*recalculated* FT Age (Ma)	Etch
1	18	2.91E-05	3.00E-02	1.44E-03	8.34E-03	7.14E-04	1.00E-01	7.62E-02	0.030045	0.0014422	118.82	121.36	4
2	22	4.85E-05	2.32E-02	1.15E-03	8.76E-03	2.62E-04	1.87E-02	2.21E-02	0.023247	0.0011518	112.67	114.66	4
3	19	3.88E-05	1.98E-02	9.52E-04	1.10E-02	4.09E-03	1.16E-02	1.72E-02	0.019788	9.52E-04	142.56	145.45	4
4	83	2.91E-05	1.34E-01	6.42E-03	1.23E-02	2.11E-04	3.04E-02	2.00E-01	0.13438	0.0064244	122.47	123.10	4
5	19	1.75E-05	1.33E-01	6.41E-03	1.27E-02	3.22E-03	1.37E-03	3.78E-02	0.13348	0.0064067	47.32	48.17	4
6	1	2.33E-05	4.52E-03	2.21E-04	1.26E-02	2.74E-02	1.70E-02	3.31E-02	0.0045152	2.21E-04	55.18	75.74	1
7	11	3.11E-05	1.11E-02	4.32E-04	1.80E-02	1.16E-02	5.37E-02	4.32E-01	0.011122	4.32E-04	182.98	188.91	4
8	29	2.91E-05	4.38E-02	1.89E-03	1.66E-02	6.13E-04	6.82E-02	5.44E-02	0.043799	0.0018864	131.2	132.97	4
9	63	4.85E-05	3.89E-02	1.55E-03	1.72E-02	9.75E-04	8.86E-03	2.02E-02	0.038892	0.0015533	191.68	192.94	4
10	72	2.91E-05	1.58E-01	6.76E-03	1.70E-02	3.28E-04	1.14E-02	1.76E-01	0.1582	0.006761	90.47	91.00	4
11	9	7.77E-06	3.15E-02	1.34E-03	1.78E-02	3.27E-03	9.09E-03	2.27E-02	0.031451	0.0013368	211.31	219.84	4
12	1	1.46E-05	2.60E-02	1.08E-03	1.99E-02	2.12E-03	1.20E-01	4.34E-02	0.02596	0.0010761	15.4	21.11	2
13	4	4.85E-05	4.10E-03	1.73E-04	1.75E-02	2.10E-02	5.41E-02	6.35E-02	0.0041034	1.73E-04	116.03	126.89	4
14	8	4.85E-05	8.98E-03	3.86E-04	1.70E-02	4.12E-03	2.84E-02	2.37E-02	0.0089798	0.0003863	106.12	111.13	4
15	6	3.11E-05	2.74E-02	1.31E-03	1.27E-02	1.68E-03	1.94E-03	1.46E-02	0.027364	0.001305	41.02	43.52	4
16	1	4.85E-05	2.47E-03	1.08E-04	1.66E-02	2.37E-02	7.67E-01	1.14E-01	0.0024663	1.08E-04	48.52	66.66	2
17	26	1.75E-05	5.42E-02	2.48E-03	1.79E-02	1.39E-03	7.32E-03	4.08E-02	0.054183	0.0024807	158.14	160.14	4
18	50	1.75E-05	9.72E-02	4.36E-03	1.41E-02	2.67E-04	5.50E-04	9.70E-03	0.097231	0.0043591	169.32	170.31	4
19	19	3.40E-05	5.92E-02	2.65E-03	1.56E-02	7.90E-04	1.69E-03	1.38E-02	0.059249	0.0026525	54.79	55.82	4
20	34	4.85E-05	3.69E-02	1.56E-03	1.61E-02	3.59E-03	1.41E-02	2.44E-02	0.036889	0.0015572	109.76	111.04	4
21	2	1.94E-05	1.45E-02	5.98E-04	1.70E-02	7.99E-03	2.26E-02	2.75E-02	0.014526	5.98E-04	41.21	48.94	2
22	25	2.43E-05	5.37E-02	2.29E-03	1.76E-02	5.81E-04	4.63E-02	9.67E-02	0.053686	0.002288	110.9	112.40	4

23	14	3.11E-05	7.88E-02	3.49E-03	1.60E-02	8.64E-04	4.26E-01	3.59E-02	0.07878	0.0034886	33.26	34.11	4
24	2	2.38E-05	4.47E-03	1.89E-04	1.68E-02	1.24E-02	1.97E	4.33E-02	0.0044686	0.0001886	108.78	128.88	2
25	22	2.43E-05	2.21E-02	9.80E-04	1.55E-02	2.18E-03	1.05E-02	8.77E-03	0.022111	9.80E-04	234.68	238.30	4
26	69	3.11E-05	1.92E-01	8.08E-03	1.56E-02	4.27E-04	2.72E-03	4.07E-02	0.19201	0.0080789	67.09	67.37	4
27	19	2.62E-05	2.67E-02	1.20E-03	1.74E-02	4.50E-03	1.70E-02	1.15E-02	0.02672	0.0011974	156.25	159.35	4
28	30	3.11E-05	4.94E-02	2.14E-03	1.53E-02	1.62E-03	5.61E-02	1.84E-02	0.049432	0.0021421	112.9	114.16	4
29	8	3.88E-05	9.38E-03	4.24E-04	1.52E-02	1.32E-02	1.99E-02	3.38E-02	0.009381	4.24E-04	126.78	132.75	4
30	13	4.85E-05	1.54E-02	7.51E-04	1.41E-02	1.99E-03	1.43E-02	9.24E-03	0.015412	7.51E-04	100.52	103.47	4
31	99	3.88E-05	1.31E-01	5.79E-03	1.51E-02	6.57E-04	2.27E-02	5.85E-03	0.13076	0.0057915	112.68	113.18	4
32	15	1.75E-05	3.38E-02	1.48E-03	1.64E-02	6.63E-04	6.73E-03	3.58E-02	0.033812	0.0014822	146.33	149.72	4
33	26	3.88E-05	3.57E-02	1.76E-03	1.51E-02	2.95E-03	1.37E-02	3.26E-02	0.03569	0.0017639	108.45	110.08	4
34	56	3.88E-05	5.64E-02	2.39E-03	1.78E-02	8.31E-04	6.64E-03	1.23E-02	0.056385	0.0023856	147.41	148.49	4
35	6	4.85E-05	1.28E-02	5.62E-04	1.88E-02	5.98E-03	3.06E-01	1.36E	0.01277	5.62E-04	56.19	59.72	4
36	20	3.88E-05	1.33E-01	5.42E-03	2.22E-02	3.20E-04	8.57E-03	4.03E-02	0.13294	0.0054166	22.55	22.99	4
37	48	4.85E-05	3.58E-01	1.45E-02	2.05E-02	1.45E-04	6.41E-03	1.71E-02	0.35752	0.014531	16.1	16.24	4
38	31	3.11E-05	8.18E-02	3.56E-03	2.23E-02	1.90E-04	1.29E-01	2.81E-02	0.081804	0.0035598	70.73	71.49	4
39	78	2.91E-05	9.57E-02	3.87E-03	2.01E-02	2.05E-03	1.21E-02	1.50E-01	0.095678	0.0038668	161.16	162.04	4
40	4	4.85E-05	5.18E-03	2.16E-04	2.24E-02	1.24E-02	1.09E	5.82E-02	0.0051803	2.16E-04	92.08	100.72	4

Dpar (µm)	**Dper**	**U (ppm)**	**Th (ppm)**	**Sm (ppm)**	**it Depth (µm)**
1.36	0.21	14.64	3.18	46.48	13.37
1.94	0.89	11.33	16.1	189.63	14.39
1.82	0.45	9.64	24.55	360.36	12.66
1.21	0.15	65.46	9.08	32.45	12.66
1.53	0.24	65.03	290.42	173.27	12.14
2.37	0.8	2.2	18.17	210.16	12.37
1.36	0.13	5.42	8.65	26.1	8.59
1.62	0.13	21.34	5.8	121.28	9.75
1.77	0.41	18.95	65.39	407.38	9.33
1.53	0.56	77.07	46.61	61.33	9.28

3.33	1.26	15.32	53.28	371.92	8.84
1.02	0.12	12.65	5.07	250.97	7.85
1.76	0.66	2	11.96	178.09	9.04
1.92	0.51	4.37	16.12	405.15	9.44
3.75	1.06	13.33	191.81	410.67	13.54
1.87	0.52	1.2	0.47	65.67	10.29
1.35	0.06	26.4	57.18	203.78	10.35
2.11	0.4	47.37	352.23	684.42	10.65
2.34	0.61	28.87	295.42	566.7	10.38
1.67	0.33	17.97	42.67	319.09	10.63
1.28	0.19	7.08	20.86	306.8	9.9
1.42	0.14	26.15	9.6	93.28	9.62
1.54	0.35	38.38	0.6	205.51	10.42
1.4	0.26	2.18	0.24	166.44	9.95
1.4	0.18	10.77	48.38	696.7	11.19
1.49	0.32	93.54	133.34	237.69	11.21
1.15	0.07	13.02	23.69	693.53	10.5
1.21	0.08	24.08	8.63	380.36	11
2.36	0.92	4.57	19.8	221.9	11.72
1.31	0.24	7.51	31.1	685.03	12.14
1.59	0.18	63.7	15.43	1282.7	11.45
1.83	0.39	16.47	67.32	243.07	10.69
1.67	0.34	17.39	35.83	235.99	11.32
1.39	0.1	27.47	70.61	804.23	10.08
1.66	0.5	6.22	1.55	3.95	10.74
1.35	0.09	64.77	75.16	286.34	8.15
1.56	0.19	174.17	88.74	634.68	8.01
1.29	0.09	39.85	5.48	410.69	7.65
2.49	0.92	46.61	37.99	54.29	9.29

1.55	0.58	2.52	0.02	171.42	7.89	

Sample ID: 07TS07

Catchment Name: Yellow_small

Grain #	N_s	Area (cm x cm)	$^{238}U/^{43}Ca$ (dmnls)	1 σ	^{43}Ca	^{238}U	^{232}Th	^{147}Sm	P(corr)	1 σ	*reported* FT Age (Ma)	*recalculated* FT Age (Ma)	Etch
1	5	2.91E-05	7.92E-03	2.94E-04	2.08E-02	1.30E-02	1.54E	1.03E-01	0.0079156	2.94E-04	128.41	138.04	3
2	9	4.85E-05	2.42E-02	9.15E-04	2.68E-02	3.78E-03	3.08E-02	6.11E-02	0.024213	9.15E-04	45.63	47.56	4
3	19	1.75E-05	2.33E-02	9.13E-04	2.20E-02	1.02E-02	5.51E-02	7.28E-02	0.023311	9.13E-04	273.06	277.91	4
4	59	4.85E-05	5.50E-02	2.11E-03	2.13E-02	2.44E-03	1.90E-01	1.33E-02	0.054969	0.0021106	130.89	131.81	4
5	35	3.88E-05	4.12E-02	1.72E-03	2.88E-02	1.97E-03	2.77E-02	5.01E-03	0.04124	0.0017175	129.39	130.86	4
6	3	3.88E-05	9.14E-03	3.50E-04	2.74E-02	1.83E-02	1.04E-01	1.35E-01	0.0091444	3.50E-04	50.32	56.63	2
7	12	4.85E-05	1.07E-02	4.14E-04	2.53E-02	1.52E-03	1.43E-01	1.15E-02	0.010714	4.14E-04	136.53	140.85	4
8	104	7.77E-06	6.88E-01	2.64E-02	1.94E-02	9.30E-05	2.00E-03	6.00E-03	0.68766	0.026359	115.41	115.76	4
9	10	3.88E-05	2.07E-02	7.69E-04	2.02E-02	1.10E-02	3.97E	7.56E-03	0.020662	0.0007694	74.1	76.92	4
10	8	4.85E-05	9.96E-03	4.18E-04	1.54E-02	4.68E-03	6.81E-03	1.11E-02	0.0099555	0.0004175	98.25	102.89	4
11	6	1.75E-05	2.32E-02	9.72E-04	1.85E-02	3.34E-03	7.01E-03	6.69E-03	0.023228	9.72E-04	87.8	93.10	4
12	7	2.33E-05	2.96E-02	1.14E-03	2.51E-02	1.31E-03	3.89E-03	8.86E-03	0.029594	0.0011406	60.43	63.64	4
13	18	4.85E-05	3.71E-02	1.68E-03	3.23E-02	3.24E-03	3.17E-01	1.13E-01	0.037074	0.001679	59.54	60.82	4
14	13	2.91E-05	4.27E-02	1.59E-03	2.45E-02	2.20E-03	1.58E-02	3.34E-02	0.042716	0.0015881	62.19	64.02	4
15	102	3.88E-05	2.45E-01	9.02E-03	2.32E-02	3.95E-04	1.72E-01	4.71E-03	0.24451	0.0090244	63.92	64.20	4
16	56	1.94E-05	1.68E-01	7.24E-03	1.77E-02	2.72E-04	4.04E-03	4.64E-03	0.16755	0.0072424	102.13	102.88	4
17	13	3.88E-05	2.39E-02	1.00E-03	2.02E-02	1.11E-02	1.78E	3.97E-02	0.023902	0.0010032	83.22	85.66	4
18	13	4.85E-05	1.49E-02	5.58E-04	2.09E-02	7.31E-03	5.21E-01	1.94E-02	0.014907	5.58E-04	106.55	109.68	4
19	114	1.46E-05	4.72E-01	1.98E-02	1.69E-02	7.71E-05	1.34E-01	5.35E-03	0.47155	0.019752	98.52	98.58	4
20	20	3.11E-05	2.03E-02	8.09E-04	1.77E-02	1.08E-02	5.83E-03	1.78E-02	0.02029	8.09E-04	187.01	190.24	4
21	4	4.85E-05	7.94E-03	3.26E-04	2.80E-02	3.37E-03	5.89E-02	2.86E-02	0.0079376	3.26E-04	61.79	67.60	4
22	4	4.37E-05	2.76E-02	1.08E-03	2.08E-02	1.80E-03	6.93E-03	2.65E-02	0.027589	0.001077	19.82	21.66	3

23	29	2.33E-05	8.56E-02	3.17E-03	2.43E-02	4.30E-04	5.89E-01	4.01E-03	0.085648	0.003172	86.32	87.42	4
24	36	1.94E-05	1.21E-01	4.84E-03	1.79E-02	1.04E-03	6.94E-03	2.56E-03	0.12119	0.0048364	90.85	91.85	4
25	7	1.94E-05	2.61E-02	1.03E-03	2.04E-02	2.56E-03	1.17E-02	2.32E-02	0.026093	0.001031	82.1	86.53	4
26	79	2.91E-05	1.80E-01	7.78E-03	1.60E-02	3.30E-04	7.86E-03	3.35E-02	0.18013	0.0077774	89.43	89.92	4
27	19	3.11E-05	4.28E-02	1.80E-03	1.95E-02	4.28E-03	8.54E-03	1.48E-02	0.042848	0.0018024	84.8	86.36	4
28	22	3.88E-05	1.82E-02	7.18E-04	2.80E-02	6.91E-03	1.02E-02	1.72E-02	0.018225	7.18E-04	183.27	186.48	4
29	12	4.37E-05	7.87E-03	3.04E-04	1.92E-02	1.18E-03	1.84E	1.17E-01	0.0078671	3.04E-04	205.49	211.72	4
30	0	3.11E-05	1.99E-03	8.75E-05	1.65E-02	5.14E-02	1.30E-01	6.77E-03	0.0019856	8.75E-05	0	36.21	1
31	93	3.88E-05	2.26E-01	8.84E-03	2.05E-02	2.95E-04	5.91E-03	3.56E-03	0.22592	0.0088431	63.08	63.38	4
32	31	2.43E-05	1.68E-01	6.21E-03	2.09E-02	4.04E-04	2.28E	1.45E-02	0.16772	0.0062122	45.38	45.87	4
33	1	3.88E-05	2.44E-03	1.23E-04	3.43E-02	2.02E-01	1.34E	1.37E-01	0.0024375	1.23E-04	62.87	86.35	1
34	40	2.43E-05	3.13E-01	1.14E-02	2.65E-02	3.18E-04	7.95E-04	4.80E-03	0.3132	0.011432	31.39	31.64	4
35	9	2.91E-05	1.94E-02	8.18E-04	1.73E-02	4.08E-03	2.67E-02	2.53E-02	0.019441	8.18E-04	94.36	98.33	2

Dpar (µm)	Dper	U (ppm)	Th (ppm)	Sm (ppm)	it Depth (µm)
1.21	0.38	3.77	0.11	33.25	8.61
1.45	0.1	11.53	22.04	73.59	8.17
2.21	0.88	11.1	9.29	64.91	8.85
1.51	0.12	26.18	1.86	221.18	9.23
1.66	0.19	19.64	14.36	829.37	7.15
1.43	0.51	4.35	4.26	38.93	7.72
1.78	0.45	5.1	2.63	214.32	7.67
1.6	0.13	327.46	73.6	517.53	9.78
1.93	0.3	9.84	0.01	488.47	9.31
1.9	0.32	4.74	49.05	272.88	12.08
1.47	0.44	11.06	55.65	402.94	10.88
2.45	0.66	14.09	123.64	443.57	7.74
1.98	0.21	17.66	1.89	40.39	6.45
1.53	0.28	20.34	30.22	114.26	7.76
1.94	0.42	116.44	4.04	872.51	8.26

1.73	0.08	79.79	103.34	429.53	10.99
1.62	0.3	11.38	0.07	107.94	10.31
1.88	0.31	7.1	0.7	241.57	9.15
1.55	0.07	224.55	1.64	490.58	11.58
1.71	0.34	9.66	66.67	175.61	10.69
2.19	0.37	3.78	12.18	134.33	6.78
1.46	0.33	13.14	75.23	119.5	9.85
1.47	0.15	40.79	0.92	956.36	8.54
1.22	0.54	57.71	54.84	1519.3	10.61
1.93	0.34	12.43	36.79	134.75	9.74
2.27	0.64	85.78	49.32	76.53	12.34
1.48	0.17	20.4	51.71	205.43	10.43
1.69	0.51	8.68	42.87	223.6	7.28
1.9	0.36	3.75	0.02	22.18	10.05
1.41	0.53	0.95	2.94	350.04	11.85
1.91	0.31	107.58	98.64	745.7	9.88
1.98	0.37	79.87	0.05	167.93	9.46
1.55	0.15	1.16	0.27	28.97	5.94
1.76	0.41	149.15	747.95	730.86	8.48
1.56	0.24	9.26	20.67	116.39	11.5

Sample ID: 07TS09

Catchment Name: Yalong

Grain #	N_s	Area (cm x cm)	$^{238}U/^{43}Ca$ (dmnls)	1 σ	^{43}Ca	^{238}U	^{232}Th	^{147}Sm	P(corr)	1 σ	*reported* FT Age (Ma)	*recalculated* FT Age (Ma)	Etch
1	20	9.71E-06	1.16E-01	5.78E-03	1.40E-02	7.07E-04	4.70E-03	1.19E-02	0.11553	0.0057839	104.03	105.93	4
2	19	4.85E-05	3.72E-02	1.53E-03	1.61E-02	2.65E-03	1.95E-02	9.55E-03	0.037248	0.0015308	61.51	62.76	4
3	15	4.85E-05	6.19E-02	2.58E-03	1.96E-02	2.30E-03	8.47E-03	2.16E-02	0.061875	0.0025805	29.31	30.06	4
4	38	2.91E-05	2.57E-01	1.10E-02	2.01E-02	3.56E-04	1.44E-01	2.63E-01	0.25655	0.01103	29.84	30.16	4

5	13	3.40E-05	3.16E-02	1.19E-03	2.00E-02	3.40E-03	2.93E-01	6.17E-02	0.03158	0.0011936	70.86	72.84	4
6	5	1.75E-05	3.70E-02	1.52E-03	1.92E-02	1.47E-03	6.12E-03	2.96E-02	0.036953	0.0015238	45.38	48.69	4
7	15	4.85E-05	2.53E-02	1.09E-03	1.68E-02	3.61E-03	8.59E-03	1.67E-01	0.025349	0.0010862	71.3	73.12	4
8	14	4.85E-05	9.26E-02	3.97E-03	1.62E-02	1.24E-03	3.14E-02	6.11E-02	0.092554	0.0039669	18.3	18.80	4
9	0	4.85E-05	5.45E-05	3.41E-06	1.76E-02	3.08E-01	1.65E	1.60E-01	5.45E-05	3.41E-06	0	784.22	1
10	38	3.88E-05	1.52E-01	5.95E-03	2.00E-02	6.69E-04	3.12E-03	2.99E-02	0.15177	0.0059515	37.81	38.21	4
11	46	3.88E-05	5.14E-02	1.97E-03	2.23E-02	1.77E-03	8.04E-03	7.23E-02	0.051385	0.0019705	134.17	135.35	4
12	58	2.91E-05	4.83E-01	1.84E-02	2.06E-02	2.70E-04	5.83E-03	2.66E-02	0.48331	0.018392	24.19	24.36	4
13	8	4.85E-05	2.45E-02	9.72E-04	2.12E-02	1.96E-02	3.59E-01	4.22E-01	0.024483	9.72E-04	39.47	41.34	4
14	23	2.91E-05	3.64E-02	1.46E-03	2.23E-02	7.00E-04	1.18E-02	5.09E-02	0.036427	0.0014577	126.26	128.38	4
15	92	3.64E-05	2.94E-01	1.23E-02	1.96E-02	6.09E-04	7.75E-02	2.92E-02	0.29363	0.012296	50.42	50.62	4
16	8	3.88E-05	2.23E-02	9.01E-04	1.70E-02	1.80E-03	1.64E-02	1.01E-01	0.022318	9.01E-04	54.06	56.62	4
17	16	3.11E-05	6.35E-02	2.69E-03	1.79E-02	1.14E-03	1.72E-01	4.00E-02	0.063496	0.0026864	47.53	48.58	3
18	32	1.55E-05	1.08E-01	4.58E-03	1.86E-02	7.65E-04	3.86E-03	1.08E-02	0.10787	0.0045824	111.35	112.87	4
19	0	2.91E-05	1.40E-02	6.03E-04	1.75E-02	5.31E-03	1.57E-02	7.15E-03	0.01398	6.03E-04	0	5.42	4
20	26	2.91E-05	6.43E-02	2.80E-03	1.82E-02	1.13E-03	2.51E-01	2.64E-02	0.064292	0.0027962	81.15	82.37	4
21	3	1.46E-05	3.36E-02	1.49E-03	1.57E-02	7.68E-04	9.61E-02	1.78E-01	0.033598	0.0014915	35.96	40.33	2
22	47	2.91E-05	1.82E-01	7.88E-03	1.82E-02	4.02E-04	3.99E-01	2.10E-02	0.1819	0.0078802	51.96	52.41	4
23	45	3.88E-05	1.03E-01	4.78E-03	1.48E-02	1.18E-03	4.60E-03	3.53E-02	0.10289	0.0047837	65.9	66.49	4
24	40	2.43E-05	1.54E-01	6.74E-03	1.88E-02	4.82E-04	7.68E-03	8.18E-03	0.15379	0.006739	62.72	63.22	4
25	54	1.75E-05	1.15E-01	5.01E-03	2.00E-02	1.13E-03	4.90E-03	1.66E-02	0.11547	0.0050091	155.5	156.32	4
26	24	3.88E-05	1.03E-01	4.23E-03	2.16E-02	1.66E-03	1.65E-02	2.28E-02	0.10278	0.0042271	35.27	35.84	4
27	3	2.91E-05	1.11E-02	4.92E-04	3.01E-02	1.57E-02	2.72E-02	1.10E-01	0.011109	4.92E-04	54.3	61.10	3
28	70	1.75E-05	1.43E-01	5.72E-03	2.52E-02	8.82E-04	7.53E-02	4.51E-01	0.14299	0.0057211	162.69	163.29	4
29	32	1.75E-05	1.88E-01	8.47E-03	2.89E-02	6.10E-04	1.30E-02	3.20E-02	0.18816	0.0084689	56.98	57.56	4
30	22	2.91E-05	5.97E-02	2.50E-03	2.83E-02	3.88E-03	3.26E-02	3.39E-02	0.059712	0.0025038	73.97	75.28	4
31	16	3.11E-05	3.89E-02	1.58E-03	2.62E-02	2.67E-03	1.50E-01	3.60E-02	0.038854	0.0015821	77.49	79.20	4
32	10	1.75E-05	4.29E-02	1.88E-03	1.67E-02	1.65E-03	2.86E-03	8.19E-03	0.042866	0.0018752	78.04	80.82	4
33	25	3.40E-05	3.72E-02	1.56E-03	2.10E-02	1.43E-03	4.18E-03	6.37E-03	0.037169	0.0015577	115.38	117.00	4

34	43	2.91E-05	6.45E-02	2.92E-03	1.69E-02	3.87E-04	1.14E-02	1.93E-02	0.064479	0.002921	133.28	134.52	4
35	23	1.75E-05	5.59E-02	2.42E-03	1.84E-02	1.03E-03	7.31E-03	1.54E-02	0.05594	0.0024159	136.91	138.90	4
36	242	3.88E-05	3.84E-01	1.69E-02	1.90E-02	2.82E-04	1.55E-02	1.21E-02	0.384	0.016919	94.74	94.96	4
37	58	2.91E-05	7.49E-02	3.23E-03	1.81E-02	3.10E-03	2.39E-01	2.03E-02	7.49E-02	0.003228	154.58	155.67	4
38	30	1.55E-05	1.13E-01	4.82E-03	1.78E-02	8.21E-04	4.39E-03	6.96E-03	0.11345	0.0048155	99.35	100.78	4
39	47	2.91E-05	8.15E-02	3.66E-03	1.67E-02	6.41E-04	6.13E-03	1.12E-02	0.081522	0.0036559	115.38	116.37	4
40	73	3.11E-05	1.03E-01	4.62E-03	1.79E-02	2.34E-04	3.76E-03	7.94E-03	0.10303	0.0046201	132.76	133.27	4

Dpar (µm)	**Dper**	**U (ppm)**	**Th (ppm)**	**Sm (ppm)**	**it Depth (µm)**
1.55	0.42	55.85	82.05	564.84	11.86
1.55	0.31	18.01	25.42	753.72	10.67
1.45	0.21	29.91	73.84	386.87	9.44
2	0.27	124.03	5.45	32.3	9.63
1.44	-0.01	15.27	1.27	156.29	8.68
1.81	0.37	17.86	72.36	212.57	10.22
1.57	0.19	12.25	42.35	39.41	10.45
1.33	0.07	44.74	9.36	112.47	10.81
1.53	0.2	0.03	0.07	39.08	10.89
1.35	0.18	73.37	159.93	245.2	9.41
1.84	0.48	24.84	50.13	134.68	8.49
1.86	0.37	233.65	92.52	272.62	8.32
1.67	0.04	11.84	1.07	19.2	9.4
1.81	0.34	17.61	43.76	136.8	8.9
1.78	0.52	141.95	7.4	250.35	9.84
1.6	0.4	10.79	33.51	75.78	10.31
1.56	0.34	30.7	3.6	171.88	10.57
2	0.37	52.15	93.35	578.16	10.12
1.52	0.22	6.76	33.12	826.84	10.92
1.71	0.34	31.08	1.28	241.58	11
1.24	0.14	16.24	4.2	33.61	11.42

1.52	0.26	87.94	0.64	295.15	10.66
1.58	0.31	49.74	74.79	156.43	12.41
1.42	0.29	74.35	48.23	808.08	10.31
1.71	0.26	55.82	109.99	450.44	9.73
1.59	0.45	49.69	38.53	344.38	8.81
1.43	0.28	5.37	26.61	105.95	6.69
1.44	0.37	69.12	8.39	17.18	7.79
1.66	0.18	90.96	46.93	347.65	6.6
1.86	0.42	28.87	16.97	247.35	7.31
1.6	0.18	18.78	4.42	255.74	7.48
1.85	0.28	20.72	155.03	589.9	11.65
1.76	0.36	17.97	92.11	920.54	9.61
1.72	0.48	31.17	46.35	293.8	10.89
1.48	0.25	27.04	65.84	420.05	10.47
1.81	0.45	185.64	26.36	440.6	10.45
1.41	0.28	36.19	0.9	208.93	11.06
1.57	0.45	54.85	109.93	606.66	10.43
1.87	0.21	39.41	70.42	474.42	11.51
1.75	0.41	49.81	110.78	486.99	11.37

Sample ID: 07TS12

Catchment Name: Yangtze

Grain #	N_s	Area (cm x cm)	$^{238}U/^{43}Ca$ (dmnls)	1 σ	^{43}Ca	^{238}U	^{232}Th	^{147}Sm	P(corr)	1 σ	*reported* FT Age (Ma)	*recalculated* FT Age (Ma)	Etch
1	178	3.88E-05	3.38E-01	1.57E-02	1.25E-02	2.22E-04	8.06E-02	4.39E-03	0.33774	0.015744	81.3	81.53	4

2	14	3.88E-05	6.64E-02	2.81E-03	1.32E-02	3.34E-04	2.92E-03	1.28E-02	0.066407	0.0028134	32.64	33.54	4
3	0	4.85E-05	1.55E-02	6.24E-04	1.58E-02	1.22E-03	5.22E-03	6.40E-03	0.015462	6.24E-04	0	3.01	1
4	81	2.33E-05	2.77E-01	1.20E-02	1.35E-02	2.98E-04	3.07E-03	6.07E-03	0.27703	0.011979	75.21	75.54	4
5	8	1.75E-05	1.58E-02	6.99E-04	1.32E-02	1.82E-03	6.87E-03	7.49E-03	0.015838	6.99E-04	171.93	179.60	4
6	119	2.91E-05	2.59E-01	1.03E-02	1.73E-02	1.70E-04	1.92E-02	1.71E-02	0.25865	0.010263	94.53	94.89	4
7	34	2.91E-05	3.16E-01	1.28E-02	1.72E-02	3.87E-04	2.73E-02	8.51E-03	0.31608	0.012763	22.23	22.49	4
8	7	4.85E-05	5.65E-02	2.05E-03	2.02E-02	9.04E-03	9.45E-03	9.34E-03	0.056544	0.002046	15.35	16.19	4
9	17	3.88E-05	1.79E-01	6.64E-03	1.89E-02	1.84E-04	2.39E-01	1.25E-02	0.17886	0.0066444	14.74	15.07	4
10	0	4.85E-05	2.13E-05	2.53E-06	3.23E-02	4.57E	1.11E	1.51E-02	2.13E-05	2.53E-06	0	1881.20	1
11	36	3.88E-05	2.09E-01	7.83E-03	2.24E-02	2.10E-04	2.09E	1.45E-02	0.20894	0.0078329	26.69	26.99	4
12	6	4.85E-05	7.54E-02	2.89E-03	2.29E-02	7.93E-03	8.20E-03	1.05E-02	0.075351	0.0028887	9.88	10.51	4
13	15	1.75E-05	7.87E-02	3.20E-03	1.67E-02	8.03E-04	1.41E-02	2.03E-02	0.078745	0.0031978	65.38	66.90	4
14	150	2.43E-05	4.84E-01	1.85E-02	1.63E-02	3.74E-04	2.00E-03	8.17E-03	0.48382	0.018469	76.55	76.64	4
15	14	3.88E-05	1.27E-02	5.68E-04	1.54E-02	2.05E-02	8.80E-03	1.41E-02	0.012746	5.68E-04	168.29	172.86	4
16	3	3.88E-05	6.90E-02	2.72E-03	2.44E-02	1.04E-03	4.08E	6.42E-03	0.068959	0.0027198	6.75	7.60	2
17	27	2.91E-05	2.91E-02	1.12E-03	2.13E-02	8.87E-04	1.62E-02	1.68E-02	0.029138	0.0011167	188.99	191.71	3
18	6	4.85E-05	7.58E-03	3.00E-04	1.53E-02	1.63E-02	1.63E-02	1.90E-02	0.0075812	0.0002995	97.54	103.66	4
19	14	3.88E-05	1.07E-02	4.37E-04	1.67E-02	1.56E-03	1.45E-02	2.52E-02	0.010686	4.37E-04	200.23	205.66	4
20	16	3.88E-05	1.16E-01	4.91E-03	1.68E-02	2.13E-04	7.04E-03	1.01E-02	0.11638	0.0049096	21.31	21.82	4
21	3	2.43E-05	1.12E-02	4.53E-04	1.76E-02	1.41E-02	2.44E-02	1.20E-02	0.011205	4.53E-04	66.16	74.28	2
22	69	2.33E-05	1.98E-01	8.07E-03	1.83E-02	4.09E-04	7.55E-03	1.01E-02	0.19815	0.0080682	89.47	89.94	4
23	34	1.75E-05	1.40E-01	5.21E-03	2.28E-02	3.87E-04	1.93E-03	7.91E-03	0.13997	0.0052144	83.25	84.04	4
24	22	4.85E-05	1.06E-01	3.99E-03	1.97E-02	1.09E-03	3.06E-03	1.48E-02	0.10612	0.0039896	25.69	26.15	4
25	4	3.88E-05	2.25E-02	8.54E-04	2.53E-02	4.68E-03	1.96E-02	1.53E-02	0.022464	8.54E-04	27.58	30.18	4
26	26	3.88E-05	1.56E-01	5.67E-03	2.28E-02	9.00E-04	1.58E-03	1.99E-02	0.15625	0.0056651	25.78	26.17	4
27	28	4.85E-05	1.33E-01	6.01E-03	3.11E-02	1.22E-03	1.67E-03	8.27E-03	0.13316	0.0060129	26.06	26.43	4
28	13	3.88E-05	1.48E-02	5.34E-04	2.29E-02	9.83E-03	1.11E-02	2.28E-02	0.014813	5.34E-04	134.81	138.76	4
29	3	4.85E-05	1.31E-01	6.19E-03	2.97E-02	6.59E-04	1.45E	4.49E-01	0.1312	0.0061915	2.84	3.20	2
30	11	4.85E-05	8.07E-03	2.80E-04	2.31E-02	2.13E-02	1.97E-02	1.93E-02	0.0080698	2.80E-04	167.09	172.84	4

31	22	4.85E-05	7.71E-02	2.99E-03	2.63E-02	6.56E-04	5.18E-03	3.90E-02	0.077092	0.0029877	35.34	35.97	4
32	24	4.85E-05	2.41E-01	9.23E-03	1.94E-02	1.49E-04	1.18E-01	1.21E-02	0.24054	0.0092267	12.38	12.58	4
33	31	4.85E-05	2.66E-02	9.98E-04	2.35E-02	2.42E-02	2.55E-03	6.63E-03	0.026613	9.98E-04	143.06	144.87	4
34	3	1.75E-05	1.06E-02	3.91E-04	2.62E-02	1.37E-02	1.83E-02	2.81E-02	0.010556	3.91E-04	97.3	109.19	2
35	9	3.11E-05	2.68E-01	1.21E-02	3.31E-02	5.74E-04	2.79E-01	2.10E-02	0.26786	0.012067	6.52	6.78	3
36	7	3.88E-05	8.13E-03	2.82E-04	2.40E-02	2.35E-02	2.79E-02	3.77E-02	0.0081261	2.82E-04	132.35	139.47	4
37	18	4.85E-05	8.45E-03	3.12E-04	2.38E-02	1.85E-03	2.18E-02	2.20E-02	8.45E-03	3.12E-04	259.18	264.66	4
38	66	3.88E-05	1.46E-01	5.47E-03	2.57E-02	2.95E-04	3.09E-03	9.84E-03	0.14578	0.0054657	69.9	70.34	4
39	5	3.88E-05	5.70E-02	2.08E-03	2.67E-02	4.76E-03	9.94E-04	1.47E-02	0.056982	0.002077	13.61	14.64	3
40	13	2.91E-05	1.44E-01	5.32E-03	2.76E-02	5.83E-04	4.34E-02	2.90E-02	0.14437	0.0053213	18.61	19.16	4

Dpar (µm)	**Dper**	**U (ppm)**	**Th (ppm)**	**Sm (ppm)**	**it Depth (µm)**
1.57	0.25	159.65	2.88	300.49	11.88
1.85	0.25	31.39	133.67	144.84	11.34
1.57	0.3	7.31	62.03	353.12	10.13
1.76	0.27	130.95	122.37	390.82	12.36
1.85	0.64	7.49	41.47	222.3	11.9
1.71	0.58	122.26	26.14	222.79	10.47
1.52	0.16	149.41	10.4	312.09	10.06
1.77	0.44	26.73	53.3	317.12	9.06
1.72	0.39	84.55	1.46	238.83	9.37
1.5	0.29	0.01	0.51	295.91	5.59
1.64	0.46	98.76	0.07	293.92	8.04
1.79	0.26	35.62	75.64	365.61	8.86
1.43	0.18	37.22	20.77	143.49	10.88
1.28	0.35	228.7	167.96	411.91	10.95
1.8	0.34	6.03	34.63	163.14	11.98
1.35	0.19	32.6	0.11	463.78	7.82
1.47	0.11	13.77	33.48	201.97	8.47
1.81	0.32	3.58	18.41	123.82	11.71

1.67	0.27	5.05	26.57	152.48	10.73
1.98	0.44	55.01	62.14	210.78	11.15
1.53	0.4	5.3	17.55	168.6	10.57
1.47	0.14	93.67	57.05	274.98	10.23
1.88	0.21	66.16	151.71	402.99	8.61
1.42	0.35	50.16	150.33	215.47	9.18
1.97	0.48	10.62	26.42	191.95	7.93
2.04	0.22	73.86	259.55	166.56	8.31
1.5	0.1	62.94	396.7	573.21	6.21
2.36	0.67	7	37.43	120.05	8.18
1.22	0.11	62.02	0.3	9.93	6.42
1.71	0.44	3.81	23.26	127.67	8.46
1.32	0.3	36.44	96.37	108.97	7.27
1.93	0.52	113.7	2.87	295.46	9.75
1.71	0.19	12.58	105.53	473.32	8.33
1.59	0.49	4.99	29.54	127.4	7.8
1.34	0.37	126.61	1.96	243.38	6.34
1.94	0.4	3.84	20.34	101.5	8.62
2.54	0.52	4	23.25	140.26	8.05
1.49	0.19	68.91	132.83	304.52	7.94
1.56	0.33	26.94	512.52	346.84	8.37
1.92	0.63	68.24	40.63	109.46	7.97

Sample ID: 07TS14

Catchment Name: Mekong

Grain #	N_s	Area (cm x cm)	$^{238}U/^{43}Ca$ (dmnls)	1 σ	^{43}Ca	^{238}U	^{232}Th	^{147}Sm	P(corr)	1 σ	*reported* FT Age (Ma)	*recalculated* FT Age (Ma)	Etch
1	20	3.88E-05	8.01E-02	3.23E-03	2.52E-02	1.28E-03	2.48E-03	1.60E-02	0.080088	0.0032252	38.98	39.73	4
2	32	2.91E-05	8.86E-02	3.40E-03	1.76E-02	5.72E-04	1.46E-03	5.30E-03	0.088625	0.0034004	74.93	75.86	4

3	16	2.91E-05	9.26E-02	3.39E-03	2.16E-02	7.36E-04	3.22E-03	1.14E-02	0.092587	0.0033913	35.97	36.84	4
4	13	3.88E-05	1.07E-01	3.91E-03	2.34E-02	2.26E-04	2.38E-03	2.32E-02	0.10659	0.0039097	19.06	19.63	4
5	19	2.43E-05	1.07E-01	3.96E-03	2.19E-02	1.35E-03	3.89E-03	1.41E-02	0.10739	0.0039571	44.16	44.97	4
6	1	4.37E-05	3.82E-03	1.52E-04	1.81E-02	1.75E-02	2.71E-02	1.78E-02	0.0038243	1.52E-04	36.28	49.82	2
7	14	4.85E-05	9.36E-03	3.23E-04	2.24E-02	0.00E	3.12E-02	2.01E-02	0.009358	3.23E-04	184.69	189.70	4
8	14	4.85E-05	2.75E-02	1.03E-03	2.49E-02	8.74E-04	8.64E-03	3.18E-02	0.027549	0.0010272	63.33	65.07	4
9	2	3.11E-05	9.75E-03	3.46E-04	2.06E-02	6.21E-03	2.34E-02	1.12E-02	0.00975	3.46E-04	40.02	47.43	4
10	17	4.85E-05	4.99E-02	1.88E-03	2.34E-02	1.57E-03	3.88E-03	8.55E-03	0.049855	0.0018763	42.56	43.53	4
11	30	2.91E-05	4.27E-02	1.68E-03	2.07E-02	1.22E-03	6.88E-03	8.37E-03	0.042681	0.0016759	145.07	146.97	4
12	3	2.33E-05	1.94E-02	9.61E-04	1.16E-02	2.35E-03	1.81E-03	3.49E-03	0.019427	9.61E-04	40.17	45.16	2
13	33	2.91E-05	1.30E-01	4.91E-03	2.30E-02	1.04E-03	1.32E-02	4.35E-02	0.12992	0.0049132	52.8	53.44	4
14	70	3.88E-05	1.24E-01	4.54E-03	2.05E-02	1.34E-03	2.23E-03	1.31E-02	0.12372	0.0045437	87.97	88.50	4
15	18	4.85E-05	4.60E-02	1.63E-03	2.40E-02	7.63E-03	5.97E-03	1.58E-02	0.046003	0.0016345	48.82	49.87	4
16	13	3.88E-05	6.82E-02	2.36E-03	2.42E-02	1.82E-03	4.17E-03	3.54E-02	0.068244	0.0023552	29.75	30.63	4
17	21	3.11E-05	1.38E-01	5.25E-03	2.23E-02	2.93E-04	5.00E-03	1.58E-02	0.13777	0.0052534	29.76	30.25	4
18	14	3.88E-05	6.08E-02	2.23E-03	2.42E-02	3.08E-03	2.79E-03	1.94E-02	0.06084	0.0022333	35.92	36.91	4
19	6	2.91E-05	1.99E-02	7.21E-04	2.01E-02	3.02E-03	1.64E-02	1.36E-02	0.019859	7.21E-04	62.76	66.71	4
20	25	3.88E-05	6.80E-02	2.54E-03	1.96E-02	1.68E-03	3.00E-03	2.09E-02	0.068016	0.0025433	57.28	58.18	4
21	12	4.85E-05	3.39E-02	1.27E-03	2.13E-02	4.94E-03	7.78E-03	1.01E-02	0.033862	0.0012657	44.23	45.64	4
22	6	2.91E-05	2.74E-02	9.73E-04	2.19E-02	1.48E-03	1.08E-02	2.47E-02	0.027363	9.73E-04	45.61	48.48	4
23	1	2.91E-05	4.93E-03	1.77E-04	2.14E-02	6.11E-03	4.83E-02	6.75E-03	0.0049306	1.77E-04	42.2	57.99	3
24	3	4.85E-05	6.07E-03	2.16E-04	2.36E-02	2.39E-03	4.63E-02	4.44E-02	0.0060693	2.16E-04	61.61	69.32	4
25	36	3.88E-05	5.72E-02	2.22E-03	2.72E-02	4.14E-04	4.31E-03	2.71E-02	0.05718	0.0022196	97.81	98.90	4
26	10	3.88E-05	7.12E-03	2.76E-04	2.14E-02	2.11E-02	3.60E-02	9.14E-03	0.0071221	2.76E-04	216.14	224.27	4
27	4	4.85E-05	5.88E-02	2.07E-03	2.41E-02	0.00E	6.88E-04	8.50E-03	0.058818	0.0020715	8.51	9.32	4
28	18	3.11E-05	3.16E-02	1.14E-03	2.31E-02	5.54E-03	1.81E-02	4.39E-03	0.031614	0.0011441	110.46	112.61	4
29	8	4.85E-05	3.94E-02	1.54E-03	2.85E-02	9.07E-04	4.86E-03	1.62E-02	0.039351	0.001538	25.41	26.62	4
30	12	4.85E-05	4.35E-02	1.68E-03	2.64E-02	2.73E-03	8.11E-03	2.71E-02	0.043451	0.0016782	34.49	35.60	4
31	19	3.88E-05	2.00E-02	7.04E-04	2.35E-02	2.17E-03	1.14E-02	7.45E-03	0.019986	7.04E-04	147.13	150.11	4

32	21	2.33E-05	7.51E-02	2.68E-03	2.71E-02	1.83E-03	4.99E-03	2.73E-02	7.51E-02	0.0026804	72.53	73.81	4
33	6	2.91E-05	7.51E-02	2.81E-03	2.61E-02	3.90E-03	3.06E-03	2.23E-02	0.075097	0.0028124	16.65	17.71	3
34	59	2.91E-05	8.06E-02	2.82E-03	2.52E-02	2.27E-03	4.42E-03	4.32E-02	0.080632	0.0028159	150.95	152.01	4
35	8	4.85E-05	3.73E-02	1.33E-03	2.84E-02	5.49E-03	1.05E-02	8.34E-03	0.037332	0.001326	26.78	28.05	4
36	3	4.85E-05	5.12E-03	1.79E-04	2.52E-02	8.70E-03	4.71E-02	1.28E-02	0.0051196	1.79E-04	72.97	82.10	4
37	10	3.11E-05	1.46E-02	5.21E-04	2.83E-02	3.41E-03	1.56E-02	1.51E-02	0.014612	5.21E-04	132.55	137.30	4
38	8	3.11E-05	1.03E-01	3.63E-03	2.68E-02	1.47E-03	3.57E-03	6.59E-03	0.10312	0.0036329	15.16	15.85	3
39	34	4.85E-05	2.02E-02	7.90E-04	2.44E-02	1.54E-02	1.45E-02	1.79E-02	0.020226	7.90E-04	207.16	209.56	4
40	32	3.11E-05	3.35E-02	1.25E-03	2.27E-02	3.09E-03	5.50E-03	1.29E-02	0.033451	0.0012536	184.53	186.44	4

Dpar (µm)	**Dper**	**U (ppm)**	**Th (ppm)**	**Sm (ppm)**	**it Depth (µm)**
1.8	0.41	37.56	233.4	198.04	7.45
2.56	1.05	41.56	210.88	551.56	10.58
1.33	0.37	43.42	188.53	352.14	8.92
1.56	0.48	49.99	217.45	138.64	8.04
1.76	0.62	50.36	122.94	184.39	8.98
2.21	0.61	1.79	14.72	168.87	10.56
2.66	0.55	4.39	12.85	237.91	8.61
1.72	0.19	12.92	49.66	123.64	7.74
2.11	0.57	4.57	21.37	276.37	9.11
1.71	0.15	23.38	141.8	365.27	8.24
3.02	0.84	20.02	93.95	291.95	9.54
1.96	0.87	9.11	98.86	448.32	17.36
1.81	0.47	60.93	49.98	95.91	8.69
2.42	0.96	58.02	212.14	262.41	9.26
1.65	0.24	21.57	108.63	201.51	8.5
1.92	0.78	32	106.72	140.08	8.62
1.43	0.27	64.61	95.62	169.76	9.34
1.93	0.45	28.53	124.52	162.37	8.72
1.76	0.47	9.31	27.55	194.07	9.51

1.34	0.14	31.9	96.68	99.56	10.41
1.58	0.03	15.88	72.92	250.44	9.8
1.79	0.5	12.83	42.56	117.93	8.95
1.67	0.34	2.31	9.6	425.48	9.05
2.73	1.02	2.85	9.49	99.4	8.58
1.78	0.46	26.82	124	134.64	7.76
1.45	0.34	3.34	10.28	285.7	9.8
1.87	0.25	27.58	522.02	313.08	8.48
1.3	0.21	14.83	40.64	599.87	9.38
2.32	0.39	18.45	93.86	239.39	7.65
1.88	0.27	20.38	64.73	129.52	7.68
2.2	0.58	9.37	47.17	311.9	8.74
1.95	0.41	35.23	107.95	119.71	8.27
1.5	0.29	35.22	131.19	118.16	7.62
1.29	0.35	37.81	106.88	37.35	8.54
2.21	0.35	17.51	93.48	295.42	8.22
1.18	0.13	2.4	7.77	241.5	8.48
3.21	1.01	6.85	30.46	223.79	8.32
1.59	0.31	48.36	114.27	419.63	8.3
3.29	1.36	9.49	43.5	245.06	10.9
2.81	1.07	15.69	81.24	249.84	10

Sample ID: 07TS20

Catchment Name: Salween

Grain #	N_s	Area (cm x cm)	$^{238}U/^{43}Ca$ (dmnls)	1 σ	^{43}Ca	^{238}U	^{232}Th	^{147}Sm	P(corr)	1 σ	*reported* FT Age (Ma)	*recalculated* FT Age (Ma)	Etch
1	45	3.88E-05	1.62E-01	7.35E-03	9.51E-03	8.64E-05	2.55E-03	2.13E-03	0.16248	0.0073486	42.17	42.55	4
2	7	3.88E-05	1.49E-02	6.98E-04	1.16E-02	1.03E-03	7.92E-02	6.62E-03	0.014872	6.98E-04	71.51	75.37	4
3	7	3.88E-05	7.64E-03	3.38E-04	1.27E-02	1.16E-02	8.98E-02	4.53E-03	0.0076359	3.38E-04	138.54	145.99	3

4	31	2.33E-05	1.70E-01	7.39E-03	1.28E-02	3.63E-04	1.27E-03	1.87E-02	0.16957	0.0073905	46.38	46.93	4
5	60	2.91E-05	1.95E-01	8.57E-03	1.22E-02	1.22E-04	9.36E-02	9.14E-03	0.1947	0.008572	62.46	62.90	4
6	32	3.88E-05	5.20E-02	2.24E-03	1.38E-02	1.30E-03	6.03E-03	9.07E-03	0.052	0.0022376	93.33	94.48	4
7	40	3.88E-05	1.10E-01	4.57E-03	1.65E-02	9.36E-04	3.51E-03	1.08E-02	0.10965	0.0045712	55.49	56.05	4
8	62	3.88E-05	1.91E-01	1.06E-02	1.45E-02	1.05E-04	1.53E-02	4.63E-03	0.19078	0.010565	49.45	49.79	4
9	25	4.85E-05	5.23E-02	2.07E-03	1.64E-02	4.43E-04	1.05E-02	1.86E-02	0.052331	0.0020731	58.12	59.03	4
10	34	3.88E-05	1.05E-01	4.40E-03	1.65E-02	4.47E-04	6.48E-03	6.76E-03	0.10526	0.0044004	49.16	49.73	4
11	60	3.88E-05	1.57E-01	6.39E-03	1.63E-02	1.33E-03	5.93E-03	5.80E-03	0.15716	0.0063935	58.06	58.46	4
12	6	3.88E-05	2.99E-02	1.21E-03	1.60E-02	3.46E-03	5.25E-02	1.54E-02	0.02989	0.001214	30.59	32.52	4
13	25	3.88E-05	1.05E-01	4.15E-03	1.75E-02	5.98E-04	5.08E-03	1.12E-02	0.10463	0.0041518	36.4	36.97	4
14	15	3.88E-05	8.44E-02	3.50E-03	1.73E-02	1.09E-03	3.00E-03	1.16E-02	0.084361	0.0034962	27.1	27.80	4
15	11	2.91E-05	2.92E-02	1.21E-03	1.75E-02	3.32E-03	1.04E-02	1.69E-02	0.029188	0.0012114	76.31	78.95	4
16	188	2.91E-05	5.54E-01	2.40E-02	1.57E-02	9.40E-05	2.48E-02	5.49E-03	0.55398	0.024032	68.76	68.94	4
17	33	4.85E-05	2.03E-01	7.62E-03	2.04E-02	1.76E-03	1.96E-03	8.09E-03	0.20268	0.0076227	19.87	20.11	4
18	16	2.91E-05	5.75E-02	2.33E-03	1.75E-02	1.66E-03	3.30E-03	1.30E-02	0.057513	0.0023341	56.42	57.78	4
19	86	2.91E-05	3.03E-01	1.29E-02	1.46E-02	0.00E	2.58E-02	5.78E-03	0.30335	0.01294	57.49	57.78	4
20	126	3.88E-05	2.72E-01	1.11E-02	1.86E-02	1.44E-04	1.99E-01	1.39E-02	0.27151	0.011088	70.51	70.77	4
21	27	3.88E-05	4.87E-02	1.94E-03	2.44E-02	5.53E-03	1.26E-02	2.21E-02	0.048666	0.0019443	84.2	85.42	4
22	40	3.88E-05	1.24E-01	5.73E-03	3.50E-02	1.85E-03	5.19E-03	1.95E-02	0.12361	0.0057256	49.25	49.74	4
23	17	3.11E-05	2.51E-01	1.18E-02	3.74E-02	2.51E-03	2.52E-02	9.55E-03	0.25063	0.011796	12.94	13.21	4
24	2	3.11E-05	6.29E-03	3.64E-04	4.26E-02	5.38E-02	5.31E-02	2.02E-02	0.006286	3.64E-04	60.47	71.66	2
25	29	3.88E-05	8.20E-02	3.19E-03	2.29E-02	8.22E-04	5.18E-01	1.79E-02	0.08201	0.0031928	53.79	54.53	4
26	105	3.88E-05	1.79E-01	7.86E-03	2.71E-02	7.18E-04	9.98E-03	1.17E-02	0.17868	0.0078591	89.15	89.53	4
27	33	3.11E-05	1.13E-01	4.84E-03	2.66E-02	1.19E-03	4.57E-03	1.39E-02	0.11297	0.0048442	55.54	56.10	4
28	12	3.88E-05	7.63E-02	2.82E-03	2.24E-02	7.61E-04	1.33E-02	2.24E-02	0.076331	0.0028231	23.97	24.74	4
29	13	4.85E-05	6.68E-02	2.70E-03	2.37E-02	3.55E-03	2.28E-01	2.97E-02	0.066846	0.0027042	23.72	24.42	4
30	21	2.91E-05	1.20E-01	4.65E-03	2.19E-02	5.67E-04	7.84E-03	1.76E-02	0.12013	0.0046517	35.51	36.17	4
31	34	2.91E-05	1.12E-01	4.51E-03	2.15E-02	2.61E-03	5.50E-02	1.04E-02	0.11168	0.0045088	61.71	62.44	2
32	25	3.88E-05	8.55E-02	3.26E-03	2.35E-02	7.63E-04	1.49E-02	6.35E-03	0.085516	0.0032623	44.51	45.20	4

33	77	1.94E-05	3.32E-01	1.26E-02	2.72E-02	4.92E-04	1.84E-03	4.74E-03	0.33236	0.012588	70.4	70.79	4
34	90	2.91E-05	2.43E-01	9.81E-03	2.07E-02	1.11E-03	7.34E	2.14E-02	0.24348	9.81E-03	74.85	75.22	4
35	114	2.91E-05	3.51E-01	1.33E-02	2.18E-02	1.20E-03	3.15E-03	6.48E-03	0.3508	0.013338	65.85	66.12	4
36	26	2.91E-05	6.23E-02	2.38E-03	2.00E-02	6.40E-03	1.33E-02	6.02E-03	0.062286	0.0023801	84.47	85.74	4
37	39	3.11E-05	2.29E-01	9.06E-03	2.68E-02	4.19E-04	4.30E-03	1.18E-02	0.22941	0.0090594	32.38	32.65	4
38	64	2.91E-05	2.95E-01	1.12E-02	2.60E-02	1.21E-03	2.55E-02	1.14E-02	0.29531	0.011185	43.99	44.28	4
39	53	3.88E-05	8.18E-02	3.15E-03	2.19E-02	9.61E-04	2.01E-01	8.99E-03	0.081764	0.0031538	98.27	99.03	4
40	46	2.91E-05	2.39E-01	9.66E-03	2.03E-02	6.99E-04	3.24E-02	9.14E-01	0.23932	0.0096566	39.03	39.38	4

Dpar (µm)	**Dper**	**U (ppm)**	**Th (ppm)**	**Sm (ppm)**	**it Depth (µm)**
1.9	0.35	77.94	96.69	867.58	12.95
1.47	0.31	7.13	4.22	332.65	12.33
1.29	0.12	3.66	2.27	494.91	11.68
1.73	0.4	81.34	165.47	164.6	11.91
1.39	0.34	93.4	4.9	384.1	12.34
1.47	0.19	24.95	54.69	458.44	11.63
1.6	0.52	52.6	107.91	471.43	11.27
1.18	0.33	91.52	22.12	803.88	11.51
1.41	0.33	25.1	34.84	222.67	10.16
1.02	0.2	50.49	68.89	749.61	10.35
1.42	0.2	75.39	64.72	769.4	10.85
1.31	0.33	14.34	5.66	265.33	10.56
1.53	0.27	50.19	79.99	409.3	9.91
1.33	0.13	40.47	88.7	342.11	10.19
1.27	0.08	14	23.47	237.14	10.36
1.8	0.34	265.75	13.44	492.49	11.41
1.66	0.26	97.22	232.64	553.97	9.4
1.57	0.15	27.59	94.58	298.41	10.6
1.93	0.44	145.52	18.54	618.71	11.98
1.76	0.33	130.24	1.94	317.94	9.47

1.61	0.29	23.35	52.81	251.23	7.43
1.76	0.29	59.3	149.51	336	6.34
1.62	0.5	120.23	56.87	864.5	6.04
1.56	0.29	3.02	14.87	535.21	4.62
1.96	0.44	39.34	1	228.76	7.99
1.78	0.39	85.71	65.67	452.21	6.76
1.64	0.31	54.19	94.2	406.93	7.01
1.58	0.42	36.62	51.3	208.14	8.29
1.63	0.25	32.07	2.74	144.77	7.56
1.28	0.12	57.63	58.06	164.42	8.72
1.44	0.14	53.57	9.58	456.94	9.45
1.87	0.17	41.02	38.56	593.91	8.37
1.37	0.38	159.43	296.06	1083	7.88
1.79	0.24	116.8	0	270.99	9.5
1.46	0.1	168.28	147.9	530.56	9.1
1.79	0.29	29.88	42.66	530.38	9.3
2.02	0.29	110.05	166.75	416.05	7.44
1.71	0.25	141.66	26.5	482.5	8.17
1.32	0.22	39.22	1.96	352.35	8.73
1.48	0.1	114.8	11.92	3.26	9.7

Sample ID: 07TS23

Catchment Name: Tsangpo

Grain #	N_s	Area (cm x cm)	$^{238}U/^{43}Ca$ (dmnls)	1 σ	^{43}Ca	^{238}U	^{232}Th	^{147}Sm	P(corr)	1 σ	*reported* FT Age (Ma)	*recalculated* FT Age (Ma)	Etch
1	1	3.88E-05	3.12E-02	1.15E-03	1.59E-02	3.09E-03	4.07E-03	2.66E-03	0.031184	0.00115	5.06	6.96	1
2	2	3.88E-05	1.75E-02	6.19E-04	2.11E-02	1.29E-02	1.05E-02	3.68E-02	0.017545	6.19E-04	17.97	21.35	1
3	2	3.88E-05	3.20E-02	1.08E-03	2.57E-02	2.68E-03	5.60E-03	1.42E-02	0.031989	0.0010841	9.86	11.72	1
4	5	4.37E-05	9.77E-02	3.22E-03	2.25E-02	1.20E-03	2.86E-03	1.45E-03	0.097745	0.0032163	7.17	7.71	2

5	0	4.85E-05	1.06E-03	5.96E-05	3.65E-02	1.23E-01	1.74E	5.99E-02	0.0010622	5.96E-05	0	44.46	1
6	1	4.85E-05	2.82E-02	9.49E-04	2.25E-02	1.05E-03	8.03E-03	3.68E-03	0.028232	9.49E-04	4.47	6.15	1
7	1	4.85E-05	2.26E-02	8.25E-04	2.66E-02	5.84E-03	1.28E-02	1.07E-02	0.022558	8.25E-04	5.6	7.70	1
8	2	4.85E-05	3.30E-02	1.18E-03	2.63E-02	3.74E-03	9.11E-03	4.57E-03	0.033043	0.0011827	7.64	9.08	2
9	11	4.85E-05	1.69E-01	5.95E-03	2.24E-02	4.02E-04	1.17E-01	1.43E-02	0.16871	0.0059525	8.23	8.52	3
10	4	4.85E-05	8.47E-02	3.37E-03	2.60E-02	4.51E-03	2.44E-02	3.01E-01	0.084651	0.0033675	5.97	6.53	2
11	4	4.85E-05	8.74E-02	3.09E-03	2.64E-02	2.85E-03	8.94E-03	2.97E-02	0.087412	0.003086	5.78	6.32	4
12	0	4.85E-05	1.37E-02	5.05E-04	2.83E-02	2.12E-02	3.30E-02	2.87E-01	0.013684	5.05E-04	0	3.46	1
13	4	3.88E-05	6.81E-02	2.47E-03	2.22E-02	4.11E-04	2.85E-03	1.08E-02	0.068125	0.0024669	9.26	10.14	4
14	2	4.85E-05	3.67E-02	1.26E-03	2.07E-02	2.01E-03	4.76E-03	6.73E-03	0.036724	0.0012564	6.87	8.17	1
15	2	4.85E-05	1.47E-02	5.48E-04	1.84E-02	5.58E-03	9.54E-03	3.77E-02	0.014746	5.48E-04	17.11	20.32	1
16	5	4.85E-05	7.81E-02	3.09E-03	2.05E-02	3.39E-04	2.56E-02	4.60E-03	0.07814	0.0030865	8.08	8.69	4
17	4	4.85E-05	4.12E-02	1.31E-03	2.18E-02	6.95E-04	4.10E-03	2.70E-03	0.041197	0.0013148	12.25	13.41	3
18	1	3.88E-05	2.08E-02	7.32E-04	2.03E-02	1.90E-03	1.03E-02	7.07E-03	0.020771	7.32E-04	7.6	10.45	2
19	1	4.85E-05	2.25E-02	7.73E-04	2.20E-02	1.01E-03	4.00E-01	1.92E-02	0.022465	0.0007727	5.62	7.73	1
20	1	4.85E-05	5.35E-02	1.92E-03	2.43E-02	1.42E-03	2.53E-03	1.12E-02	0.053506	0.0019178	2.36	3.25	1
21	5	4.85E-05	1.79E-01	6.41E-03	2.17E-02	4.18E-04	9.15E-01	1.85E-02	0.17937	0.0064145	3.52	3.79	2
22	2	4.85E-05	2.68E-02	9.76E-04	2.52E-02	5.74E-03	1.25E-02	1.28E-02	0.026809	9.76E-04	9.41	11.19	2
23	3	4.85E-05	3.47E-02	1.29E-03	2.88E-02	4.02E-03	1.58E-02	2.16E-02	0.034737	0.0012888	10.9	12.27	4
24	6	4.85E-05	1.36E-01	4.84E-03	2.66E-02	3.80E-04	1.28E-01	7.71E-03	0.13553	0.0048418	5.59	5.94	4
25	1	4.85E-05	1.17E-01	4.64E-03	2.84E-02	1.75E-03	3.57E-01	1.38E-02	0.11693	0.0046427	1.08	1.49	1
26	1	4.85E-05	5.60E-02	1.93E-03	2.42E-02	1.13E-03	2.20E-03	5.32E-03	0.056016	0.0019303	2.25	3.10	1
27	1	3.88E-05	1.33E-01	4.90E-03	2.49E-02	3.58E-04	2.51E-02	1.29E-02	0.13256	0.0049025	1.19	1.64	1
28	1	4.85E-05	2.56E-02	9.42E-04	2.62E-02	5.14E-03	8.19E-03	9.02E-03	0.025612	9.42E-04	4.93	6.78	1
29	1	4.85E-05	4.54E-02	1.64E-03	2.74E-02	1.12E-03	1.54E-02	5.62E-03	0.045405	0.0016352	2.78	3.83	1
30	2	4.85E-05	4.88E-02	1.77E-03	2.67E-02	2.88E-03	4.17E-03	1.51E-02	0.048844	0.0017698	5.17	6.14	3
31	1	4.85E-05	2.38E-02	8.77E-04	2.72E-02	4.21E-03	1.35E-02	6.17E-02	0.023781	0.0008771	5.31	7.30	1
32	1	4.85E-05	1.31E-01	4.49E-03	2.27E-02	6.70E-04	2.35E-02	4.44E-01	0.131	0.0044851	0.96	1.33	1
33	3	4.85E-05	3.13E-02	1.19E-03	3.08E-02	7.38E-03	6.05E-03	1.00E-02	0.031283	0.0011923	12.1	13.62	2

34	0	3.88E-05	2.78E-02	9.73E-04	2.70E-02	3.70E-03	9.66E-03	1.02E-02	0.027822	9.73E-04	0	2.13	1
35	2	4.85E-05	1.77E-02	6.34E-04	2.09E-02	1.02E-02	7.13E-01	2.33E-02	0.017653	6.34E-04	14.29	16.98	2
36	1	4.85E-05	1.33E-02	4.89E-04	2.62E-02	1.26E-02	1.03E-02	4.21E-02	0.013289	4.89E-04	9.5	13.06	1
37	3	4.37E-05	2.59E-02	8.79E-04	2.18E-02	1.52E-03	9.89E-03	3.56E-03	0.025875	8.79E-04	16.25	18.27	2
38	0	4.85E-05	2.55E-02	1.21E-03	3.86E-02	6.13E-03	6.27E-02	5.40E-01	0.025513	0.0012134	0	1.86	1
39	1	4.85E-05	2.33E-02	8.12E-04	2.54E-02	2.71E-03	9.66E-03	2.98E-03	0.023304	8.12E-04	5.42	7.45	1
40	5	4.85E-05	3.99E-02	1.40E-03	2.40E-02	5.85E-04	2.84E-03	1.26E-02	0.039925	0.0013989	15.8	16.99	4

Dpar (µm)	**Dper**	**U (ppm)**	**Th (ppm)**	**Sm (ppm)**	**it Depth (µm)**
1.19	0.12	14.51	87.6	665.44	9.55
1.55	0.51	8.16	42.83	69.54	8.76
1.65	0.28	14.88	101.89	138.15	8.45
1.6	0.42	45.47	215.78	1463.6	8.67
1.73	0.39	0.49	0.21	90.77	4.78
1.11	0.4	13.13	60.99	613.23	8.74
1.53	0.26	10.49	56.2	522.95	9.65
1.67	0.6	15.37	78.66	867.96	7.62
1.46	0.22	78.49	3.46	219.25	8.69
1.6	0.28	39.38	20.38	11.84	7.32
1.73	0.57	40.67	47.09	67.03	7.65
1.21	0.18	6.37	18.45	7.87	7.3
1.43	0.27	31.69	179.29	175.4	8.2
1.61	0.21	17.08	95.3	290.47	8.92
1.53	0.24	6.86	36.81	52.71	10.68
1.8	0.15	36.35	17.05	534.97	8.84
1.49	0.04	19.17	54.8	687.35	8.52
1.48	0.21	9.66	33.69	424.48	9.27
1.6	0.26	10.45	0.75	151.68	8.52
1.06	0.25	24.89	132.96	215.57	7.78
1.44	0.25	83.45	0.53	196.79	8.8

1.93	0.35	12.47	52.14	169.24	7.38
1.43	0.11	16.16	41.33	149.97	7.26
1.18	0.32	63.05	3.71	413.5	7.78
1.59	0.34	54.4	1.38	230.59	6.87
1.81	0.18	26.06	139.05	560.62	8.42
1.17	0.4	61.67	16.41	300.38	7.66
1.71	0.45	11.92	62.19	358.3	7.46
1.81	0.16	21.12	28.43	431.83	7.37
1.34	0.18	22.72	158.76	243.19	7.35
2.14	0.28	11.06	46.46	45.97	7.18
1.44	0.43	60.95	14.07	5.79	8.53
1.6	0.16	14.55	85.43	260.05	6.91
2.13	0.18	12.94	63.64	276.44	7.94
1.81	0.31	8.21	0.56	83.94	9.6
1.92	0.35	6.18	31.53	67.04	8
1.53	0.17	12.04	48.97	588.52	8.63
1.4	0.29	11.87	5.98	7.2	5.68
1.45	0.28	10.84	54.63	623.13	8.49
1.66	0.52	18.57	117.46	190.18	8.29

Appendix Table A5.3. U-Pb analyses

				Isotope ratios							Apparent ages (Ma)					
Analysis	U	$^{206}Pb/^{204}Pb$	U/Th	$^{206}Pb*/^{207}Pb*$	±	$^{207}Pb*/^{235}U*$	±	$^{206}Pb*/^{238}U*$	±	error	$^{206}Pb*/^{238}U*$	±	$^{207}Pb*/^{235}U*$	±	$^{206}Pb*/^{207}Pb*$	±
	(ppm)				(%)		(%)		(%)			(Ma)		(Ma)		(Ma)
09TS06																
Yellow River																
1	733	47843	4.0	14.354	0.8	1.442	3.0	0.150	2.9	0.97	901.694	24.0	906.599	17.7	918.588	15.7
2	753	154682	19.7	4.252	10.8	17.649	10.8	0.544	0.6	0.06	2801.395	13.5	2970.793	103.9	3087.566	172.2
3	286	66912	0.9	5.913	0.5	10.671	1.9	0.458	1.8	0.97	2429.186	37.1	2494.898	17.5	2548.824	7.6
4	367	4614	2.0	20.727	5.7	0.220	5.8	0.033	0.9	0.15	209.911	1.8	202.056	10.5	111.367	134.2
5	322	15978	1.8	13.843	1.5	1.585	2.5	0.159	2.0	0.81	951.988	18.1	964.377	15.7	992.737	29.7
6	448	21598	1.5	13.852	0.7	1.548	5.1	0.156	5.1	0.99	931.917	44.0	949.762	31.6	991.330	14.5
7	290	30260	2.0	8.700	0.5	5.127	0.9	0.324	0.7	0.85	1806.985	11.6	1840.647	7.4	1878.906	8.3
8	375	14395	1.5	15.573	1.2	1.080	2.4	0.122	2.1	0.87	741.787	14.7	743.504	12.8	748.658	25.7
9	229	15894	4.7	14.288	1.4	1.470	2.4	0.152	2.0	0.83	914.199	17.1	918.271	14.7	928.085	27.9
10	236	12822	3.0	8.828	1.6	5.017	5.4	0.321	5.2	0.96	1795.629	81.6	1822.140	46.1	1852.567	28.9
11	68	141	0.9	13.892	41.1	0.306	41.4	0.031	4.8	0.12	195.705	9.3	271.033	98.8	985.569	873.9
12	30	3922	2.1	9.788	1.9	4.029	2.2	0.286	1.1	0.49	1621.506	15.3	1640.061	17.6	1663.912	34.8
13	474	12853	4.3	13.728	1.1	1.381	1.4	0.138	0.9	0.63	830.599	6.9	880.935	8.2	1009.584	21.8
14	193	932	1.9	19.985	29.3	0.233	29.3	0.034	1.6	0.05	214.025	3.4	212.594	56.3	196.775	693.1
15	315	4902	2.1	21.465	5.9	0.225	5.9	0.035	0.5	0.08	222.165	1.0	206.257	11.0	28.122	140.6
16	264	39369	4.4	8.610	0.4	5.664	1.2	0.354	1.1	0.93	1952.050	18.1	1925.857	10.0	1897.763	7.9
17	122	10051	2.1	15.404	3.0	1.204	3.5	0.134	1.8	0.52	813.308	14.0	802.248	19.5	771.642	63.1
18	623	63651	1.3	6.139	0.2	10.014	1.7	0.446	1.7	0.99	2376.648	34.3	2436.041	16.1	2486.006	3.9
19	549	5764	7.3	14.426	1.8	1.394	2.3	0.146	1.4	0.59	877.453	11.1	886.230	13.5	908.186	37.8
20	355	7070	0.7	20.712	4.7	0.261	4.7	0.039	0.6	0.14	247.784	1.6	235.359	9.9	113.093	110.2
21	50	1245	1.7	30.602	23.4	0.219	23.6	0.049	3.3	0.14	305.906	9.7	201.045	43.1	-903.665	685.5

22	309	12833	2.8	16.149	1.9	0.918	2.3	0.107	1.2	0.54	657.970	7.8	661.039	11.2	671.502	41.7
23	137	3512	2.4	21.244	13.8	0.304	13.9	0.047	2.2	0.16	294.899	6.3	269.361	33.0	52.834	330.0
24	90	162	0.4	15.829	11.2	0.270	11.2	0.031	0.8	0.07	197.074	1.5	243.015	24.3	714.116	238.6
25	49	9501	1.6	8.312	1.7	6.209	3.0	0.374	2.5	0.82	2049.627	43.3	2005.740	26.3	1960.827	30.7
26	294	23963	2.0	9.852	1.8	2.998	4.6	0.214	4.2	0.92	1251.075	47.8	1406.995	34.7	1651.750	32.7
27	107	15555	2.7	7.851	0.7	6.378	1.2	0.363	1.0	0.82	1997.154	16.7	2029.207	10.4	2061.948	12.2
28	191	4884	1.3	18.730	3.2	0.379	3.3	0.051	0.7	0.22	323.421	2.3	326.117	9.1	345.400	72.0
29	40	6414	1.6	9.867	4.2	4.018	5.3	0.288	3.3	0.61	1629.039	47.2	1637.769	43.4	1648.979	78.1
30	136	4276	2.9	22.124	12.2	0.310	12.2	0.050	0.7	0.06	312.486	2.3	273.827	29.3	-44.836	297.4
31	204	5947	1.9	18.874	4.1	0.527	4.2	0.072	1.1	0.26	448.637	4.7	429.490	14.7	328.017	92.1
32	174	6316	4.2	19.302	5.4	0.493	5.6	0.069	1.6	0.28	429.833	6.6	406.634	18.9	276.942	124.1
33	371	3689	3.1	22.193	8.8	0.109	8.9	0.017	1.4	0.15	111.823	1.5	104.785	8.8	-52.440	214.0
34	120	29079	1.7	5.964	0.5	11.229	1.3	0.486	1.3	0.93	2551.902	26.4	2542.318	12.5	2534.667	8.3
35	133	22932	2.4	8.224	0.6	5.538	1.5	0.330	1.3	0.90	1840.144	20.9	1906.578	12.5	1979.645	11.6
36	12	3194	1.3	6.212	2.7	10.329	3.1	0.465	1.4	0.46	2463.100	28.8	2464.672	28.5	2465.957	46.3
37	164	5621	1.9	20.743	10.4	0.326	10.6	0.049	1.8	0.17	308.792	5.5	286.619	26.4	109.513	246.5
38	102	9086	2.7	14.044	2.9	1.534	3.0	0.156	1.0	0.33	935.976	8.7	944.177	18.6	963.373	58.5
39	377	9669	2.6	19.964	5.2	0.367	5.4	0.053	1.1	0.21	333.753	3.7	317.421	14.6	199.183	122.0
40	132	41800	1.1	5.929	0.3	11.825	1.6	0.508	1.6	0.98	2650.076	34.9	2590.673	15.4	2544.529	5.6
41	69	12581	0.9	8.113	1.2	6.066	1.7	0.357	1.2	0.73	1967.593	21.0	1985.360	14.9	2003.895	20.7
42	117	3200	2.5	19.449	10.6	0.337	10.9	0.047	2.4	0.22	299.011	7.1	294.579	27.9	259.565	244.6
43	354	9623	1.5	20.304	5.2	0.228	5.2	0.034	0.6	0.12	212.448	1.3	208.153	9.8	159.800	121.6
44	86	2756	0.9	21.356	16.0	0.324	16.0	0.050	1.3	0.08	315.678	4.0	284.995	39.8	40.330	383.8
45	79	17417	1.8	6.341	1.1	9.732	1.8	0.448	1.5	0.81	2384.379	29.7	2409.773	16.9	2431.283	18.0
46	84	1399	1.4	22.284	22.1	0.233	22.2	0.038	2.0	0.09	237.880	4.8	212.333	42.5	-62.385	543.8
47	192	4078	2.3	21.721	6.2	0.295	6.4	0.046	1.4	0.22	292.530	4.1	262.244	14.8	-0.348	150.5
48	133	26150	2.1	8.461	2.2	5.825	3.1	0.357	2.2	0.71	1970.109	37.1	1950.137	26.7	1928.979	39.0
49	149	1646	1.5	28.626	42.2	0.080	42.2	0.017	1.7	0.04	105.828	1.8	77.885	31.6	-713.959	1218.9
50	243	9620	9.2	18.343	4.8	0.516	6.5	0.069	4.3	0.67	428.347	18.0	422.769	22.5	392.440	108.8

51	450	12815	1.7	19.092	3.9	0.297	4.0	0.041	0.7	0.17	259.963	1.8	264.200	9.3	301.940	89.7
52	262	4424	1.5	18.867	7.1	0.317	7.3	0.043	1.9	0.26	274.079	5.1	279.906	17.9	328.882	161.0
53	193	4872	1.7	18.707	3.5	0.483	3.6	0.065	0.6	0.15	408.865	2.2	399.868	11.8	348.175	79.6
54	185	310	0.5	20.478	7.7	0.158	7.7	0.023	0.6	0.08	149.243	0.9	148.684	10.6	139.797	180.2
55	168	15163	1.4	15.745	2.1	1.154	2.3	0.132	1.1	0.45	798.040	7.9	779.171	12.7	725.473	44.2
56	705	2906	0.7	25.191	12.1	0.036	12.2	0.007	1.5	0.12	42.463	0.6	36.080	4.3	-370.623	315.8
57	323	8560	1.2	6.846	1.1	6.680	1.6	0.332	1.2	0.74	1846.445	19.1	2069.963	14.1	2300.433	18.4
58	163	3068	1.9	21.253	10.3	0.271	10.6	0.042	2.5	0.24	264.143	6.5	243.768	23.0	51.836	246.1
59	259	59943	2.3	6.118	0.2	10.654	1.2	0.473	1.2	0.98	2495.500	24.3	2493.405	11.1	2491.686	4.0
60	36	1465	2.3	25.013	26.6	0.348	26.6	0.063	1.6	0.06	394.740	6.0	303.280	69.9	-352.318	696.8
61	225	5187	2.2	18.690	7.8	0.293	7.9	0.040	1.4	0.18	250.677	3.5	260.542	18.1	350.240	175.5
62	409	6176	3.4	17.585	2.8	0.616	4.0	0.079	2.8	0.70	487.609	13.1	487.397	15.3	486.379	62.0
63	285	49388	6.3	8.663	0.4	5.584	0.9	0.351	0.8	0.91	1938.451	13.9	1913.568	7.9	1886.691	6.8
64	146	21747	1.9	9.076	0.9	3.909	1.6	0.257	1.4	0.83	1476.083	18.0	1615.556	13.3	1802.379	16.7
65	48	1340	0.9	23.172	36.7	0.246	36.7	0.041	1.2	0.03	260.687	3.1	222.957	73.7	-158.638	940.2
66	697	7583	1.5	19.814	3.4	0.267	4.3	0.038	2.6	0.61	242.499	6.3	240.092	9.2	216.621	78.5
67	70	6626	1.2	14.380	2.5	1.489	2.6	0.155	0.8	0.30	930.358	6.7	925.769	15.9	914.873	51.3
68	371	42769	1.0	8.778	0.5	4.985	1.1	0.317	1.0	0.89	1776.857	15.5	1816.743	9.5	1862.778	9.2
69	265	52209	2.4	8.679	0.6	5.506	0.6	0.347	0.3	0.42	1918.296	4.4	1901.583	5.4	1883.378	10.2
70	652	57964	1.4	9.421	0.9	4.179	1.1	0.286	0.6	0.53	1619.355	8.2	1669.971	8.9	1734.177	17.0
71	134	4979	2.0	18.904	4.4	0.503	4.7	0.069	1.6	0.34	430.069	6.7	413.858	16.0	324.442	100.2
72	200	17866	3.2	14.968	1.8	1.331	3.1	0.145	2.5	0.80	870.281	20.0	859.522	17.8	831.893	38.4
73	173	1905	1.1	35.382	33.6	0.060	33.6	0.015	1.2	0.03	98.368	1.1	59.089	19.3	-1346.027	1101.7
74	244	59282	2.4	6.090	0.4	10.604	2.2	0.468	2.2	0.98	2476.562	44.7	2489.067	20.5	2499.276	7.3
75	357	8841	2.9	20.196	4.9	0.289	5.2	0.042	1.7	0.32	267.569	4.3	258.032	11.8	172.231	114.5
76	129	5459	2.4	19.813	8.8	0.473	9.3	0.068	2.9	0.31	423.771	11.9	393.157	30.2	216.848	203.8
77	164	14197	1.4	14.958	1.5	1.307	1.8	0.142	1.0	0.54	855.005	7.7	848.954	10.2	833.177	31.2
78	460	75134	4.1	8.663	0.2	5.533	1.1	0.348	1.0	0.97	1923.283	17.1	1905.740	9.1	1886.680	4.3
79	201	19086	5.3	15.342	1.8	1.279	2.6	0.142	1.9	0.71	857.948	14.9	836.568	14.9	780.196	38.8

80	437	3479	1.8	22.089	8.9	0.104	9.0	0.017	0.4	0.04	106.267	0.4	100.233	8.5	-41.002	217.7
81	49	6701	1.1	9.666	2.2	3.690	2.4	0.259	0.9	0.37	1483.003	11.9	1569.147	19.4	1687.017	41.5
82	325	15203	2.0	18.356	3.1	0.520	3.8	0.069	2.3	0.60	431.561	9.6	425.195	13.3	390.805	68.9
83	231	5242	1.3	20.531	6.3	0.325	6.7	0.048	2.0	0.31	304.207	6.1	285.370	16.6	133.753	149.1
84	335	66755	6.4	8.801	0.3	5.261	1.6	0.336	1.6	0.98	1866.538	25.7	1862.577	13.9	1858.141	6.3
85	221	33625	2.5	7.903	0.5	6.624	1.4	0.380	1.3	0.92	2074.890	22.5	2062.586	12.1	2050.300	9.3
86	130	3843	1.3	20.577	4.1	0.451	4.2	0.067	1.1	0.26	420.214	4.4	378.217	13.3	128.502	96.1
87	403	14943	1.0	18.580	3.5	0.436	4.2	0.059	2.4	0.57	367.770	8.7	367.204	13.0	363.613	78.2
88	121	5168	2.1	19.605	10.3	0.491	10.4	0.070	1.0	0.10	435.190	4.2	405.707	34.8	241.140	239.0
89	145	1613	2.9	19.455	17.6	0.248	18.0	0.035	3.8	0.21	221.954	8.3	225.161	36.4	258.787	407.5
90	177	20701	4.9	8.738	0.5	5.176	0.6	0.328	0.3	0.49	1828.893	4.5	1848.746	4.9	1871.144	9.1

Best age (Ma)

Age	±
918.6	15.7
3087.6	172.2
2548.8	7.6
209.9	1.8
992.7	29.7
991.3	14.5
1878.9	8.3
741.8	14.7
928.1	27.9
1852.6	28.9
195.7	9.3
1663.9	34.8
1009.6	21.8
214.0	3.4
222.2	1.0
1897.8	7.9

813.3	14.0
2486.0	3.9
877.5	11.1
247.8	1.6
305.9	9.7
658.0	7.8
294.9	6.3
197.1	1.5
1960.8	30.7
1651.8	32.7
2061.9	12.2
323.4	2.3
1649.0	78.1
312.5	2.3
448.6	4.7
429.8	6.6
111.8	1.5
2534.7	8.3
1979.6	11.6
2466.0	46.3
308.8	5.5
963.4	58.5
333.8	3.7
2544.5	5.6
2003.9	20.7
299.0	7.1
212.4	1.3
315.7	4.0
2431.3	18.0

237.9	4.8
292.5	4.1
1929.0	39.0
105.8	1.8
428.3	18.0
260.0	1.8
274.1	5.1
408.9	2.2
149.2	0.9
798.0	7.9
42.5	0.6
2300.4	18.4
264.1	6.5
2491.7	4.0
394.7	6.0
250.7	3.5
487.6	13.1
1886.7	6.8
1802.4	16.7
260.7	3.1
242.5	6.3
914.9	51.3
1862.8	9.2
1883.4	10.2
1734.2	17.0
430.1	6.7
870.3	20.0
98.4	1.1
2499.3	7.3

267.6	4.3
423.8	11.9
855.0	7.7
1886.7	4.3
857.9	14.9
106.3	0.4
1687.0	41.5
431.6	9.6
304.2	6.1
1858.1	6.3
2050.3	9.3
420.2	4.4
367.8	8.7
435.2	4.2
222.0	8.3
1871.1	9.1

09TS12

Yangtze River

1	108	2342	4.9	23.945	15.6	0.231	15.7	0.040	1.8	0.12	253.902	4.6	211.290	30.0	-240.807	396.3
2	371	12766	12.8	16.407	2.4	0.542	2.7	0.065	1.2	0.44	403.264	4.7	440.069	9.7	637.471	52.6
3	321	36589	2.2	8.656	0.4	5.432	1.8	0.341	1.7	0.97	1891.511	28.3	1889.871	15.2	1888.056	7.3
4	153	4849	2.2	20.200	6.8	0.380	6.9	0.056	1.3	0.19	349.454	4.4	327.212	19.4	171.837	159.1
5	170	18482	1.3	13.252	0.9	2.000	1.6	0.192	1.4	0.85	1133.298	14.5	1115.410	11.2	1080.709	17.7
6	598	44540	3.9	13.828	0.3	1.669	0.6	0.167	0.5	0.82	997.732	4.3	996.832	3.6	994.873	6.7
7	366	6308	3.2	20.327	8.2	0.237	8.3	0.035	1.2	0.15	221.191	2.6	215.780	16.2	157.136	192.7
8	191	4153	2.9	22.699	6.9	0.216	7.0	0.036	1.3	0.18	225.725	2.9	198.964	12.7	-107.562	170.5
9	362	9922	2.6	19.327	3.2	0.278	3.7	0.039	1.9	0.52	246.155	4.6	248.820	8.2	274.006	72.7

10	163	13442	1.5	15.170	2.4	1.219	2.7	0.134	1.2	0.46	811.187	9.3	809.219	14.8	803.789	49.3
11	197	6048	2.5	20.037	5.2	0.273	6.3	0.040	3.6	0.58	250.352	9.0	244.694	13.8	190.775	120.3
12	232	51365	2.7	8.640	0.3	5.571	1.6	0.349	1.5	0.98	1930.446	25.4	1911.665	13.4	1891.331	5.5
13	866	227996	1.8	5.418	0.2	12.882	1.0	0.506	1.0	0.98	2640.423	21.8	2671.082	9.6	2694.360	3.0
14	118	1938	2.5	21.504	23.5	0.210	23.5	0.033	1.1	0.05	207.940	2.2	193.718	41.5	23.758	570.1
15	165	44061	1.0	6.215	2.7	10.814	5.7	0.487	5.0	0.88	2559.592	106.0	2507.294	52.9	2465.202	45.0
16	158	37351	1.5	6.577	0.9	8.658	2.9	0.413	2.7	0.95	2228.694	51.3	2302.656	26.1	2368.923	15.4
17	122	5904	1.5	18.982	5.2	0.527	5.6	0.073	2.0	0.36	451.655	8.8	429.924	19.6	315.065	118.6
18	919	17143	0.8	19.887	2.0	0.232	3.1	0.033	2.4	0.77	212.166	5.0	211.838	6.0	208.172	46.7
19	215	4742	2.4	19.764	7.3	0.234	7.6	0.034	2.4	0.31	213.088	4.9	213.868	14.7	222.444	168.2
20	210	26216	1.6	12.823	1.2	2.267	2.0	0.211	1.5	0.78	1233.092	17.3	1201.955	13.9	1146.416	24.6
21	214	4616	2.6	20.435	9.8	0.235	10.1	0.035	2.8	0.27	220.436	6.0	214.078	19.6	144.676	229.3
22	206	4007	2.8	19.866	9.0	0.272	9.1	0.039	1.2	0.14	247.652	3.0	244.150	19.8	210.609	209.4
23	293	42300	1.7	9.374	0.4	4.490	1.2	0.305	1.1	0.94	1717.119	16.5	1729.041	9.7	1743.481	7.3
24	269	5850	2.2	20.053	5.6	0.277	5.8	0.040	1.3	0.23	254.805	3.3	248.447	12.8	188.799	131.5
25	170	3746	2.5	20.359	8.6	0.220	8.7	0.032	1.5	0.17	205.964	3.0	201.805	15.9	153.485	201.1
26	199	3411	1.7	18.878	10.0	0.243	10.2	0.033	2.2	0.22	211.208	4.6	221.092	20.3	327.614	226.9
27	98	28618	1.6	6.031	0.4	10.506	2.3	0.460	2.3	0.98	2437.602	46.3	2480.472	21.5	2515.761	7.3
28	331	8305	2.6	19.509	5.1	0.282	6.2	0.040	3.4	0.55	252.078	8.4	252.118	13.7	252.510	117.9
29	193	7533	1.7	13.440	4.6	1.698	5.0	0.166	2.0	0.39	987.376	17.9	1007.817	31.8	1052.549	92.1
30	269	25688	4.2	14.069	1.0	1.571	2.8	0.160	2.6	0.93	958.254	23.1	958.702	17.2	959.711	20.1
31	475	13541	4.6	16.513	1.8	0.510	1.8	0.061	0.4	0.19	382.421	1.3	418.673	6.3	623.609	38.6
32	360	5085	2.6	19.546	6.8	0.241	7.0	0.034	1.5	0.22	216.753	3.3	219.421	13.7	248.144	156.2
33	489	7484	3.7	13.567	35.3	0.317	36.6	0.031	9.7	0.26	197.843	18.9	279.387	89.7	1033.440	736.8
34	326	8184	2.8	19.414	3.8	0.270	3.9	0.038	1.0	0.26	240.758	2.5	242.901	8.5	263.661	87.2
35	123	12306	1.4	14.711	2.4	1.323	3.0	0.141	1.7	0.57	850.957	13.5	855.641	17.1	867.796	50.1
36	361	2978	5.6	18.105	5.1	0.257	5.1	0.034	0.6	0.12	213.687	1.3	231.987	10.6	421.712	113.1
37	27	4647	0.6	8.389	3.7	5.103	4.8	0.310	3.1	0.65	1743.052	48.0	1836.633	41.1	1944.389	65.6
38	103	3081	2.3	19.694	7.8	0.371	8.1	0.053	2.3	0.29	332.920	7.6	320.450	22.3	230.743	179.4

39	197	4749	2.9	21.405	10.1	0.227	10.4	0.035	2.2	0.22	223.255	4.9	207.715	19.5	34.861	242.9
40	1185	103493	1.8	13.865	0.4	1.562	1.9	0.157	1.8	0.98	940.733	16.1	955.449	11.7	989.471	8.3
41	276	5112	2.0	19.640	7.8	0.277	8.0	0.039	1.7	0.21	249.335	4.1	248.160	17.7	237.040	181.1
42	724	72230	3.0	9.385	0.5	3.995	3.4	0.272	3.4	0.99	1550.664	46.7	1633.277	27.8	1741.343	9.0
43	296	42446	1.9	6.178	0.4	8.766	2.2	0.393	2.1	0.99	2135.541	38.5	2313.948	19.6	2475.339	6.2
44	1406	28224	2.6	16.565	0.8	0.687	1.3	0.083	1.1	0.82	511.090	5.4	530.869	5.5	616.796	16.5
45	334	19631	1.5	13.132	1.4	1.752	2.9	0.167	2.5	0.87	994.573	23.0	1027.741	18.5	1099.034	28.4
46	187	4032	3.7	21.163	15.9	0.228	16.0	0.035	1.7	0.10	222.047	3.6	208.810	30.2	61.950	380.6
47	445	13330	14.4	17.772	2.3	0.386	2.4	0.050	1.0	0.39	312.970	2.9	331.412	6.9	463.015	50.0
48	1450	89366	4.2	16.914	0.5	0.739	2.5	0.091	2.5	0.98	559.180	13.2	561.640	10.8	571.641	10.2
49	52	16762	3.0	4.535	1.8	16.359	3.6	0.538	3.1	0.86	2775.263	69.1	2898.018	34.0	2984.442	29.1
50	1025	43260	34.8	15.979	3.4	0.634	9.1	0.073	8.5	0.93	456.766	37.3	498.333	36.0	694.121	72.9
51	103	2450	1.6	14.923	11.5	0.629	11.6	0.068	1.8	0.15	424.475	7.4	495.384	45.7	838.072	240.4
52	41	4931	2.1	13.164	4.4	1.990	6.4	0.190	4.7	0.73	1121.315	48.2	1112.106	43.4	1094.167	87.9
53	534	56942	5.8	10.583	3.7	2.922	5.6	0.224	4.2	0.75	1304.517	49.0	1387.651	42.0	1517.885	69.5
54	286	13807	2.1	17.951	4.4	0.521	5.0	0.068	2.4	0.48	422.903	9.7	425.679	17.3	440.717	97.5
55	246	5854	2.7	19.295	8.8	0.235	9.0	0.033	2.2	0.25	208.504	4.6	214.245	17.5	277.847	200.9
56	278	23091	2.3	15.529	1.5	1.129	3.3	0.127	3.0	0.89	771.660	21.6	767.319	18.0	754.679	32.6
57	123	4990	2.4	17.093	6.3	0.562	6.3	0.070	0.8	0.13	433.903	3.4	452.592	23.2	548.700	137.5
58	619	55532	7.7	8.662	0.3	5.152	1.1	0.324	1.1	0.96	1807.528	17.1	1844.721	9.6	1886.918	5.4
59	338	54060	1.7	9.962	0.5	3.762	1.3	0.272	1.2	0.93	1550.192	16.2	1584.765	10.2	1631.063	8.8
60	152	4583	3.0	19.343	10.8	0.294	10.8	0.041	1.2	0.11	260.214	3.0	261.409	25.0	272.109	247.7
61	296	8545	3.8	20.683	4.7	0.218	5.1	0.033	1.9	0.38	207.847	4.0	200.615	9.3	116.398	111.0
62	77	16349	2.2	9.293	1.1	4.642	2.5	0.313	2.2	0.89	1754.751	33.5	1756.858	20.5	1759.348	20.6
63	716	16489	3.5	20.096	2.0	0.227	3.9	0.033	3.4	0.86	209.592	6.9	207.505	7.3	183.848	45.9
64	1362	123421	78.4	13.667	2.8	1.578	3.4	0.156	1.9	0.57	936.616	16.7	961.425	21.1	1018.589	56.5
65	540	49607	4.1	15.107	0.7	1.202	2.0	0.132	1.9	0.94	797.319	14.0	801.351	11.0	812.597	14.1
66	397	31734	20.5	15.272	1.5	1.155	2.7	0.128	2.2	0.83	775.985	16.4	779.569	14.7	789.823	31.5
67	518	13734	5.5	19.757	2.2	0.259	3.1	0.037	2.2	0.70	235.092	5.1	234.027	6.5	223.369	51.2

68	463	10709	3.1	20.398	5.2	0.223	5.8	0.033	2.5	0.43	209.486	5.2	204.625	10.7	148.973	122.7
69	491	11564	1.9	19.677	2.7	0.238	2.9	0.034	1.0	0.35	215.622	2.2	217.064	5.7	232.703	63.1
70	286	5688	1.8	18.597	5.6	0.300	5.8	0.041	1.2	0.21	255.947	3.1	266.625	13.6	361.482	127.4
71	560	164880	2.4	6.093	0.5	9.620	0.6	0.425	0.4	0.62	2283.717	7.0	2399.130	5.4	2498.595	7.8
72	386	13143	1.9	19.713	5.3	0.261	5.5	0.037	1.5	0.26	236.416	3.4	235.688	11.7	228.456	123.5
73	525	65947	2.9	12.298	2.5	1.979	7.1	0.177	6.6	0.94	1047.834	64.3	1108.349	47.9	1229.075	48.9
74	229	117412	2.7	3.127	2.8	28.407	3.8	0.644	2.5	0.66	3205.482	63.4	3433.259	37.1	3568.975	43.6
75	251	13455	1.6	15.979	3.1	0.625	3.6	0.072	1.8	0.50	450.474	7.7	492.692	13.9	694.074	65.8
76	318	39425	2.6	13.827	0.9	1.743	2.2	0.175	2.0	0.90	1038.614	18.7	1024.684	13.9	995.065	18.7
77	585	16633	3.5	19.915	3.5	0.230	3.8	0.033	1.4	0.38	210.289	3.0	209.844	7.2	204.877	82.2
78	280	28883	5.3	15.826	1.2	1.074	2.0	0.123	1.6	0.80	749.101	11.5	740.486	10.7	714.542	26.1
79	300	39398	11.6	13.140	0.8	2.147	1.4	0.205	1.1	0.82	1200.247	12.4	1164.200	9.6	1097.758	16.0
80	381	20138	2.0	12.652	0.9	2.210	2.7	0.203	2.5	0.94	1190.341	27.3	1184.244	18.7	1173.143	18.3
81	695	207284	3.3	5.744	1.4	11.284	1.4	0.470	0.5	0.32	2483.858	9.5	2546.842	13.5	2597.373	22.8
82	165	31884	1.5	8.837	0.7	5.072	1.2	0.325	1.0	0.83	1814.323	15.1	1831.379	9.8	1850.811	11.8

Best age (Ma)

Age	±
253.9	4.6
403.3	4.7
1888.1	7.3
349.5	4.4
1080.7	17.7
994.9	6.7
221.2	2.6
225.7	2.9
246.2	4.6
811.2	9.3
250.4	9.0
1891.3	5.5

2694.4	3.0
207.9	2.2
2465.2	45.0
2368.9	15.4
451.7	8.8
212.2	5.0
213.1	4.9
1146.4	24.6
220.4	6.0
247.7	3.0
1743.5	7.3
254.8	3.3
206.0	3.0
211.2	4.6
2515.8	7.3
252.1	8.4
1052.5	92.1
959.7	20.1
382.4	1.3
216.8	3.3
197.8	18.9
240.8	2.5
851.0	13.5
213.7	1.3
1944.4	65.6
332.9	7.6
223.3	4.9
989.5	8.3
249.3	4.1

1741.3	9.0
2475.3	6.2
511.1	5.4
1099.0	28.4
222.0	3.6
313.0	2.9
559.2	13.2
2984.4	29.1
456.8	37.3
424.5	7.4
1094.2	87.9
1517.9	69.5
422.9	9.7
208.5	4.6
771.7	21.6
433.9	3.4
1886.9	5.4
1631.1	8.8
260.2	3.0
207.8	4.0
1759.3	20.6
209.6	6.9
1018.6	56.5
797.3	14.0
776.0	16.4
235.1	5.1
209.5	5.2
215.6	2.2
255.9	3.1

2498.6	7.8
236.4	3.4
1229.1	48.9
3569.0	43.6
450.5	7.7
995.1	18.7
210.3	3.0
749.1	11.5
1097.8	16.0
1173.1	18.3
2597.4	22.8
1850.8	11.8

Chapter VI

Synopsis and Conclusions

6.1 Summary of primary dissertation results

This dissertation includes new results and interpretations with the aim of constraining the structural and topographic evolution of the Tibetan Plateau at two scales. Detailed studies along the northeastern margin of Tibet (Chapters II-IV) yield new timing of major faults, from which I interpret the kinematic framework for structures within this region. Integration of this work yields a comprehensive description of the deformation history of this part of the Tibetan orogen over the last 50 Ma. The broad-scale plateau-wide study presented in Chapter V offers a broader context for the work in Chapters II, III, and IV. New detrital low-temperature thermochronometry data coupled with a recently developed inverse-modeling approach provides estimates of long-term erosion rates and the timing of initiation of river incision from across the interior of the Tibetan Plateau (Chapter V). The results of this work have implications for validation of previously proposed geodynamic and mechanical models of plateau growth as well as climatic influences on erosion rates within Tibet.

6.1.1 Chapter II

Analysis of geodetic velocities, Quaternary fault slip rates, and structural patterns reveals the modern deformation field in the northeastern margin of the Tibetan Plateau. Results from this work demonstrate that fast slip on the left-lateral Kunlun fault (>10 mm/yr) is transferred northward, in the direction of plate convergence, rather than eastward. Specifically, deformation is partly accommodated by the left-lateral Haiyuan fault and intervening faults in a regional step-over, and partly by distributed extensional faults or block rotation farther north. This interpretation of slip dissipation explains both the distribution and sense of motion on faults that lie between the Kunlun and Haiyuan faults as well as extensional faulting in the northern plateau foreland. Furthermore, the transfer of Kunlun fault motion northward over 500 km suggests that a wide deforming zone develops in a region of weak lower crust. These findings do not support the notion of eastward extruding crustal blocks toward a lateral "free" boundary (Tapponnier et al., 1982).

6.1.2 Chapter III

Dating of illite in fault gouge from the West Qinling reverse fault in northern Tibet suggests fault motion was ongoing at 50 ± 8 Ma. This age, together with erosional constraints from adjacent hanging-wall rocks, indicates that faulting initiated near to the time of India-Eurasia collision and continued until at least the middle Miocene epoch. These findings offer definitive evidence for Eocene-age reverse faulting within the northeastern Tibetan Plateau and, along with reported ages on thrust faults near the Qaidam Basin (Clark et al., 2010; Yin et al., 2008), suggests that compressive

deformation across a significant portion of the northern margin of the plateau initiates within 10 myr of the initial plate collision.

This work demonstrates the advantages of pairing fault-gouge dating and low-temperature thermochronometry in order to elucidate a comprehensive and unambiguous interpretation of fault zone history difficult to infer from the erosion record or fault ages alone. Results from this study also have implications for the fault-gouge dating technique in general. Data demonstrate that the $^{40}Ar/^{39}Ar$ age of authigenic illite represents a single interval in West Qinling fault history rather than an amalgamation. These results also show that the fault-formed illite age does not always represent the latest phase in fault motion as has been proposed previously (Solum et al., 2005; Haines and van der Pluijm, 2008). Authigenic illite growth appears to be restricted to a thermal window during the fault history (108 +/- 10 °C), thus the stage of faulting recorded will vary among sample sites depending, at least in part, on thermal history.

The potential for temperature to control illite growth has implications for interpretation of authigenic illite ages and their relationship to deformation episodes within fault zones. The authigenic illite formation temperatures estimated in this study are similar to the thermal range of two of the most commonly applied thermochronometers, apatite helium (~ 60 – 70 °C) and apatite fission track (~ 110 °C). Thus, comparison among results from these techniques provides a powerful means to assess upper crustal deformation. Constraints on the relatively narrow temperatures of authigenic illite growth also permit targeted sampling of clays in fault gouge that correspond to particular periods of fault motion if the exhumation history of potential sample sites is reasonably well known.

6.1.3 Chapter IV

New low-temperature thermochronometry ages and geologic observations date periods of exhumation associated with transpressional deformation along the Kunlun and Haiyuan left-lateral faults, two major faults within the northeastern margin of the Tibetan Plateau. Results suggest that Kunlun fault motion initiated first along the central fault segment at approximately 20 Ma and then progressed to the west (12-8 Ma) and east (8-5 Ma) as the fault zone evolved. This history differs from earlier studies that proposed eastward fault propagation (Meyer et al., 1998; Metivier et al., 1998) and an Eocene onset of faulting along the western fault segment (Jolivet et al., 2003) or late Miocene initiation along the entire fault length (Kidd and Molnar, 1988; Fu and Awata, 2007).

Thermal histories from mountain ranges associated with the active Haiyuan Fault record primarily late Cretaceous cooling and suggest that total exhumation associated with Cenozoic motion is less than ~ 2-4 km. However, results also show that structures between the Kunlun and Haiyuan fault become active at 15-6 Ma, which I infer as the timing of simultaneous motion of both the Kunlun and Haiyuan faults that bound an ~250 km wide zone of associated transpressional shear. Strike-slip deformation along the eastern Haiyuan fault tip is kinematically linked with ~ E-W directed thrusting in the Liupan Shan (Zhang et al., 1991) which is thought to initiate by 10-8 Ma (Zheng et al., 2006; Wang et al., 2011; Lin et al., 2011). Thus, it appears that Haiyuan fault motion propagated to the east in time.

Collectively, data from this and previous studies indicate diachronous slip histories with left-lateral Kunlun motion initiating first along the central fault segment before expanding west and east along strike as well as to the north and then east along the

Haiyuan fault. Strike-slip fault initiation at ~20 Ma occurs earlier than most previous studies propose and this timing indicates that evolution of this fault system spans more than 15 Ma. Additionally, Miocene onset of Kunlun and Haiyuan faulting is also consistent with the age of initiation reported for other major Tibetan strike-slip faults (e.g., the Jiali, Karakorum, Xianshuihe, and Garze-Yushu faults) implying regional rather than local forcing drives lateral strain.

6.1.4 Chapter V

Low-temperature thermochronometry analysis of detrital apatites collected from modern river sands across the east-central Tibet interior places new constraints on patterns in erosion rates and timing of erosion-rate change that reflect the tectonic and geomorphic evolution of the Tibetan Plateau. Apatite-helium and Apatite-fission-track ages range widely (in most cases spanning the entire Cenozoic and late Mesozoic eras) within all but one of the large catchments studied, which suggests uniform catchment erosion histories spanning the width of the east-central Tibetan Plateau.

To first order, preservation of both old and young ages observed in each individual catchment suggests that regional slow erosion for much of the Cenozoic must be followed by a recent and widespread increase in erosion rate. Modeling using a recently developed methodology for inversion of detrital thermochronometric ages (Avdeev et al., 2011) confirms that data are poorly fit by a constant erosion rate model and instead require increases in erosion rate since the mid-to-late Miocene in order to adequately describe the data. A joint model with ages from all of the studied catchments modeled simultaneously indicates slow erosion until the late Cenozoic (11-4 Ma) when an abrupt increase to faster erosion rates (~0.2-0.6 mm/yr) occurred. An earlier erosion event at 60-

54 Ma, though of lesser magnitude than the late Miocene event, is also observed in one of the catchments and supported by model results.

Comparison of results from this sample transect within interior Tibet to bedrock studies along the same rivers farther east of the plateau margin show similar timing and rates of increased erosion. Bedrock studies record an onset of rapid fluvial incision into a regional low-relief surface between 15 and 5 Ma with a change in erosion rate from 0.01-0.06 to 0.25-5 mm/yr (Kirby et al., 2002; Clark et al., 2005; Godard et al., 2009; Ouimet et al., 2010; Wilson and Fowler, 2011) compared to between 11 and 4 Ma and catchment-wide increases in erosion rate from a slowly-eroding landscape (~0.005 mm/yr) to ~0.2-0.6 mm/yr from the detrital data of the central-eastern plateau presented in this dissertation. Commensurate erosion rates and timing of erosion rate increases along upstream and downstream sections of the major rivers draining Tibet, indicate that fluvial reaches within the Tibetan highlands are not isolated from base-level changes by a migrating knickpoint that has yet to drive into the headwaters regions, as has been thought previously (Ouimet et al., 2007; Korup and Montgomery, 2008; Whipple, 2010).

Although in some cases increased precipitation has been shown to drive enhanced erosion (e.g., Brozovic et al., 1997; Montgomery et al., 2001; Reiners et al., 2003; Theide et al., 2004), our results are consistent with other studies that suggest that there is not always a direct influence of precipitation on erosion rates (e.g., Riebe et al., 2001; Burbank et al., 2003; Finnegan et al., 2008; Binnie et al., 2010; Henck et al., 2011). Despite differences in precipitation, mean drainage-basin slope and relief, catchments spanning over 6º latitude share similar erosion histories. Nor were obvious correlations between erosion rate and precipitation evident when comparing interior Tibet to the

wetter eastern plateau perimeter. Although long-term erosion data were compared to modern mean annual precipitation (New et al., 2002), isotopic evidence supports that the northern plateau was arid by Neogene time (Kent-Corson et al., 2009) suggesting that modern trends in precipitation existed in the geologic past.

Erosion histories from the externally drained portion of the Tibetan Plateau have potential implications for the surface uplift history and climate conditions during orogen evolution, though erosion histories alone do not uniquely indicate a given tectonic or climatic scenario. Uniform, slow erosion across much of Tibet until the late Cenozoic does not support a steep propagating plateau migrating to the north from collision time, as is predicted for many geodynamic and mechanical descriptions of plateau evolution. Rather, results from this study are consistent with broad surface uplift as the main driver of late Cenozoic erosion rate increase. Such regional uplift potentially relates to flux of lower crustal material into this region (Clark and Royden, 2000), driving widespread and abrupt increases in erosion rate across the east-central Tibetan Plateau. In addition, the smaller-magnitude Eocene erosional event is likely related to local surface faulting associated with Indo-Asian plate collision.

6.2 Synthesis of Cenozoic deformation history of northern Tibet

A coherent history of Cenozoic deformation along the northern margin of the Tibetan Plateau emerges from the detailed work presented in part I of this dissertation (Figure 6.1a). All together, data indicate that earlier (prior to the Miocene epoch) deformation involved mainly contractional structures oriented favorably to accommodate NNE-SSW Indo-Eurasian plate convergence (Jolivet et al., 2001; Sobel et al., 2001; Yin et al., 2002;

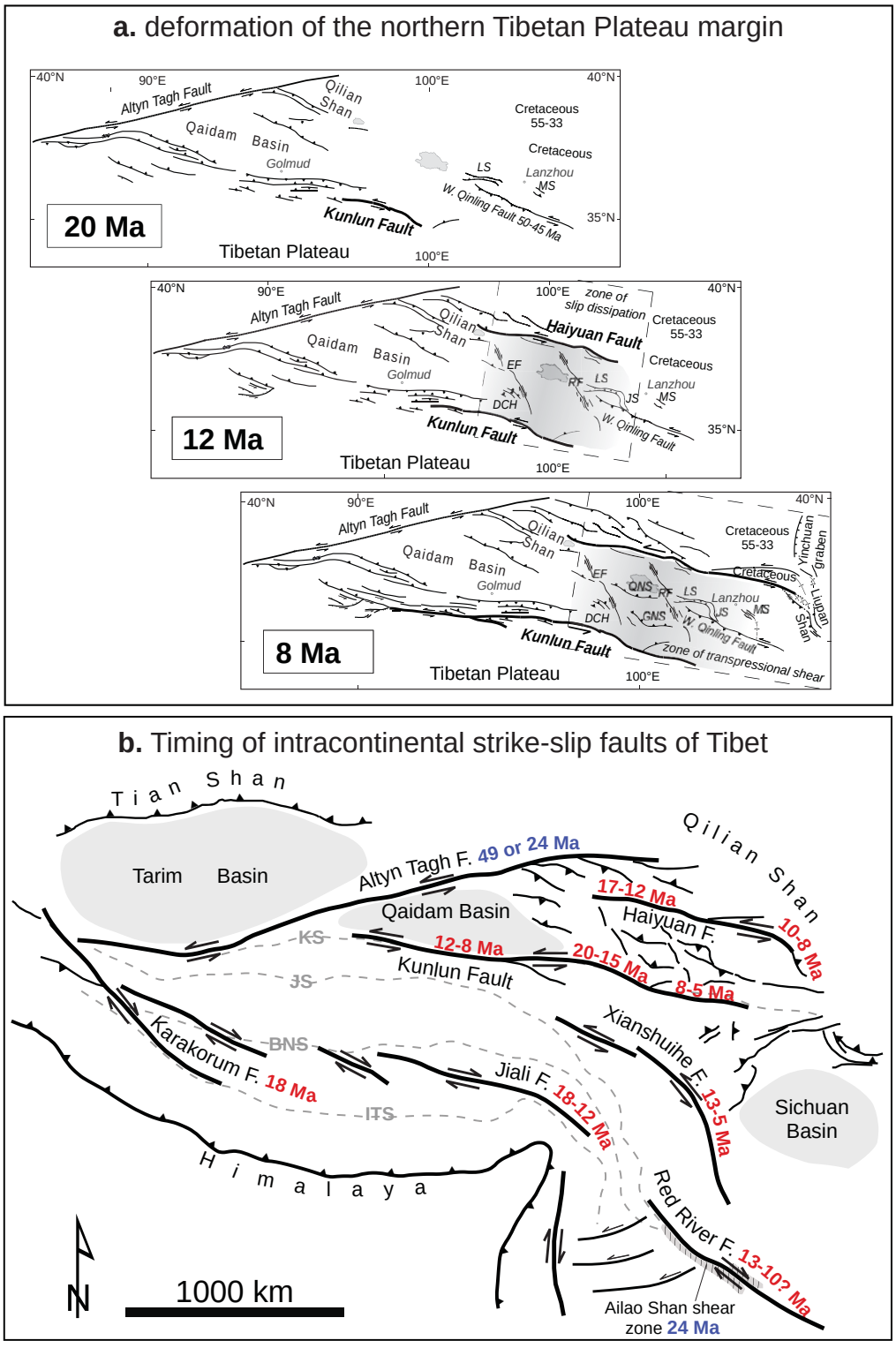

Figure 6.1. a. Proposed late Cenozoic deformation history of the northern Tibetan Plateau region through time (see chapter IV for details). b. Timing of initiation of intracontinental strike-slip faults of Tibet compiled from Searle et al., 2011 and this dissertation: blue (pre-Miocene) and red (Miocene and younger). Tibetan Plateau suture boundaries shown by dashed gray line: ITS Indus-Tsangpo suture, BNS Bangong Nujiang suture, JS Jingsha suture, KS Kunlun suture.

Horton et al., 2004; Dupont-Nivet et al., 2004; Dai et al., 2006; Yin et al., 2008; Dayem et al., 2009; Clark et al., 2010; Duvall et al., 2011; Lin et al., 2011; Huang et al., 2011), whereas later deformation (post middle-Miocene) involves faults of various orientations that accommodate both left and right lateral fault motion as well as thrusting. At approximately 20 Ma, Kunlun left-lateral faulting initiated along the central segment of the fault. By approximately 15 Ma, left-lateral faulting expanded northward to the western Haiyuan fault and by 12-5 Ma, Kunlun faulting expanded west and east along strike and Haiyuan faulting propagated eastward (Figure 6.1a).

Faulting, range growth, and basin deposition along many of the smaller structures (50-100 km in length) within the northeastern plateau margin (Zheng et al., 2003; Fang et al., 2005; Zheng et al., 2006; Yan et al., 2006; Zhao et al., 2007; Lease et al., 2007; 2011; Hough et al., 2011; Zhang et al., 2011; Yuan et al., 2011; Wang et al., 2011; Lin et al., 2011; Craddock et al., *in review*) interior were commensurate with or post-dated the onset timing of the bounding Kunlun and Haiyuan faults (Duvall et al., *in prep*). Based on this timing and the location and spatial orientation of these structures, I suggest the formation of a broad step-over zone of deformation resulting from concurrent Kunlun and Haiyuan strike-slip motion beginning ca. 15 Ma that continues through the present (Duvall and Clark, 2010). I further propose that the Kunlun and Haiyuan strike-slip faults control the structural landscape of northern Tibet beginning at the onset of concurrent fault activity at ca. 15 Ma. Thus, Miocene-Pliocene range growth and basin deposition within this region co-evolved with the growth of these two major fault systems and need not result from northward propagation of crustal thickening and upward growth of the Tibetan

Plateau into this region at this time (e.g., Meyer et al., 1998; Tapponnier et al., 2001; Royden et al., 2008).

6.3 Implications for the development of the Tibetan Plateau

The conclusions of this dissertation have important bearing on the mechanics of Tibetan Plateau evolution. Results from the West Qinling fault-gouge study (Duvall et al., 2011) add to a growing body of work that reveals long-lived faulting within the northern Tibet region that was located many thousands of kilometers north of the plate boundary at the time of initial plate convergence. Furthermore, plateau-wide erosion patterns across the eastern part of the interior Tibetan Plateau (Duvall et al., *in review*) show a uniform mid-Miocene increase in erosion rate rather than a northward propagating plateau front. Thus, these results are at odds with the long-standing view that Tibetan Plateau deformation began in the south and evolved northward in time. Widespread major strike-slip fault initiation during the mid-to-late stages of orogen development (Duvall et al., *in prep*) is also not predicted by the classic "continental-extrusion" (e.g., Molnar and Tapponnier, 1975; Tapponnier et al., 1982) or subsequent "step-wise growth" descriptions of Tibetan Plateau evolution (Tapponnier et al., 2001). Moreover, the notion of eastward extruding crustal blocks toward a lateral "free" boundary (Tapponnier et al., 1982) also lacks support from the Quaternary and modern deformation field in northern Tibet (Duvall and Clark, 2010).

Results from this dissertation and previous studies suggest an overlap in timing between lower-crustal flow and widespread intracontinental strike-slip faulting beginning approximately in the middle Miocene (Figure 6.1b). I propose that the development of

both of these crustal phenomena is part of the later-stage progression of the orogen as a result of long-term plate convergence rather than being tied to a specific event or abrupt change in orogen dynamics. Continued penetration of a strong Indian indentor northward into Eurasia and the increasing confinement of thickening Tibetan crust against rigid blocks to the north (Dayem et al., 2009; Clark, *in review*) may have eventually led to the funneling of deformation toward the unconfined eastern margin (Lease et al., 2011) facilitated by these two crustal processes. Geological offsets along the major strike-slip faults are generally limited (Searle et al., 2011), lateral motion does not always extend much beyond the plateau boundaries (Kirby et al., 2007; Duvall and Clark, 2010), and only minor Miocene expansion of marginal thrust faulting is observed (Clark et al., 2010). As a result, significant eastward expansion of the orogen likely occurred/occurs by flow in the deeper crust.

The connection between the tectonic evolution of the Tibetan Plateau and the Asian monsoon system is still highly speculative. The shift to increased erosion rates across east-central Tibet between 11-4 Ma (Duvall et al., *in review*) overlaps broadly with the timing of various purported climate changes in Asia at about 10 Ma, many of which have been linked with strengthening monsoon intensity (Molnar et al., 2010 and references therein). However, correlating specific climatic events with changes in erosion rates across the Tibetan Plateau is difficult. One complicating factor is the poorly-constrained relationship between erosion and precipitation. Although a case has been made that wetter climates lead to higher erosion rates (e.g., Reiners et al., 2003), results from the plateau-wide erosion study in this dissertation show no obvious correlation between erosion and precipitation rates (Duvall et al., *in prep*). Relating erosion rate changes to

climatic events is further complicated by complex moisture source interactions in this region (e.g., Hren et al., 2009), particularly with respect to the monsoonal systems. Thus, although documenting the tectonic and erosion history of Tibet helps to inform the roles of climate change in tectonics and vice versa, perhaps our greatest research need toward resolving this issue is better understanding of the complex monsoonal system and its evolution in time along the eastern plateau, the region of Tibet where the monsoon is predicted to be most sensitive to its uplift (Molnar et al., 2010).

6.4 References

Avdeev, B., Niemi, N.A., and Clark, M.K., 2011, Doing more with less: Bayesian estimation of erosion models with detrital thermochronometric data: Earth Planet Sci Lett., v. 305(3-4), p. 385-395.

Binnie, S. A., Phillips, W.M., Summerfield, M.A., Fifield, L,K., and Spotila, J.A., 2010, Tectonic and climatic controls of denudation rates in active orogens: The San Bernardino Mountains, California: Geomorphology, v. 118(3-4), p. 249-261.

Brozovic, N., Burbank, D.W., and Meigs, A.J., 1997, Climatic limits on landscape development in the northwestern Himalaya: Science, v. 276(5312), p. 571-574.

Burbank, D. W., Blythe, A.E., Putkonen, J., Pratt-Sitaula, B., Gabet, E., Oskin, M., Barros, A., and Ojha, T.P., 2003, Decoupling of erosion and precipitation in the Himalayas: Nature, v. 426(6967), p. 652-655.

Clark, M. K., Farley, K.A., Zheng, D.W., Wang, Z.C., and Duvall, A.R., 2010, Early Cenozoic faulting of the northern Tibetan Plateau margin from apatite (U-Th)/He ages: Earth Planet Sci Lett, v. 296(1-2), p. 78-88.

Clark, M. K., House, M.A., Royden, L.H., Whipple, K.X., Burchfiel, B.C., Zhang, X., and Tang, W., 2005, Late Cenozoic uplift of southeastern Tibet: Geology, v. 33(6), p. 525-528.

Craddock, W.H., Kirby, E., and Zhang, H., Late Miocene-Pliocene growth of the interior of the northeastern Tibetan Plateau: Lithosphere, *in review*.

Dai, S., Fang, X., Dupont-Nivet, G., Song, S., Gao, J., Krijgsman, W., Langereis, C., Zhang, W., 2006, Magnetostratigraphy of Cenozoic sediments from the Xining Basin: Tectonic Implications for the northeastern Tibetan Plateau: J. Geophys. Res., v. 111, doi:10.1029/2005JB004187.

Dayem, K.E., Molnar, P., Clark, M.K., and Houseman, G.A., 2009, Far-field lithospheric deformation in Tibet during continental collision: Tectonics, v. 28, doi:10.1029/2008TC002344.

Dupont-Nivet, G., Horton, B.K., Butler, R.F., Wang, J., Zhou, J., and Waanders, G.L., 2004, Paleogene clockwise tectonic rotation of the Xining-Lanzhou region, northeastern Tibetan Plateau: J. Geophys. Res., v. 109, doi: 10.1029/2003JB002620.

Duvall, A. R. and Clark, M. K., 2010, Dissipation of fast strike-slip faulting within and beyond northeastern Tibet: Geology, v. 38, p. 223-226.

Duvall, A. R., Clark, M.K., van der Pluijm, B.A., and Li, C., 2011, Direct dating of Eocene reverse faulting in northeastern Tibet using Ar-dating of fault clays and low-temperature thermochronometry: Earth Planet Sci Lett., v. 304(3-4), p. 520-526.

Duvall, A.R., Clark, M.K., Avdeev, B., Farley, K.A., and Chen, Z., *in review*, Widespread Late Cenozoic increase in erosion rates across the interior of eastern Tibet constrained by detrital low-temperature thermochronometry: Tectonics.

Duvall, A.R., Clark, M.K., Kirby, E., Farley, K.A., Craddock, W.H., Li, C., and Yuan, D.-Y., *in prep*, Timing of Kunlun and Haiyuan strike-slip faulting, northeastern margin of the Tibetan Plateau.

Finnegan, N. J., Hallet, B., Montgomery, D.R., Zeitler, P.K., Stone, J.O., Anders, A.M., and Yuping, L., 2008, Coupling of rock uplift and river incision in the Namche Barwa-Gyala Peri massif, Tibet: Geol Soc Am Bull, v. 120(1-2), p. 142-155.

Fu, B. H., and Awata, Y., 2007, Displacement and timing of left-lateral faulting in the Kunlun Fault Zone, northern Tibet, inferred from geologic and geomorphic features: Journal of Eurasian Earth Sciences, v. 29, p. 253-265.

Godard, V., Pik, R., Lave, J., Cattin, R., Tibari, B., de Sigoyer, J., Pubellier, M., and Zhu, J., 2009, Late Cenozoic evolution of the central Longmen Shan, eastern Tibet: Insight from (U-Th)/He thermochronometry: Tectonics, v. 28, p. doi:10.1029/2008TC002407.

Haines, S.H., and van der Pluijm, B.A., 2008, Clay quantification and Ar–Ar dating of synthetic and natural gouge: Application to the Miocene Sierra Mazatán detachment fault, Sonora, Mexico: Joural of Structural Geology, v. 30, p. 525-538.

Henck, A. C., Huntington, K.W., Stone, J.O., Montgomery, D.R., and Hallet, B., 2011, Spatial controls on erosion in the Three Rivers Region, southeastern Tibet and southwestern China: Earth Planet Sci Lett: v. 303, p.71-83.

Horton, B. K., Yin, A., Spurlin, M.S., Zhou, J., and Wang, J., 2002, Paleocene–Eocene syncontractional sedimentation in narrow, lacustrine-dominated basins of east-central Tibet: Geol Soc Am Bull, v. 114(7), p. 771-786.

Hough, B. G., Garzione, C. N., Wang, Z., Lease, R. O., Burbank, D. W., and Yuan, D., 2011, Stable isotope evidence for topographic growth and basin segmentation: Implications for the evolution of the NE Tibetan Plateau: Bulletin of the Geological Society of America, v. 123, p. 168.

Hren, M. T., Bookhagen, B., Blisniuk, P.M., Booth, A.L., and Chamberlain, C.P., 2009, (delta) 18O and (delta) D of streamwaters across the Himalaya and Tibetan Plateau: Implications for moisture sources and paleoelevation reconstructions: Earth Planet Sci Lett, v. 288(1-2), p. 20-32.

Huang, G., Hourigan, J.K., Ritts, B.Z., and Kent-Corson, M.L., 2011, Cenozoic multiple-phase tectonic evolution of the northern Tibetan Plateau: Constaints from sedimentary records from Qaidam Basin, Hexi Corridor, and Subei Basin, northwest China: American Journal of Science, v. 311, p. 116-152.

Jolivet, M., Brunel, M., Seward, D., Xu, Z., Yang, J., Malavieille, J., Roger, F., Leyreloup, A., Arnaud, N., and Wu, C., 2003, Neogene extension and volcanism in the Kunlun Fault Zone, northern Tibet: New constraints on the age of the Kunlun Fault: Tectonics, v. 22.

Jolivet, M., Brunel, M., Seward, D., Xu, Z., Yang, J., Roger, F., Tapponnier, P., Malavieille, J., Arnaud, N., and Wu, C., 2001, Mesozoic and Cenozoic tectonics of the northern edge of the Tibetan plateau: fission-track constraints: Tectonophysics, v. 343, p. 111-134.

Kidd, W. S. F., and Molnar, P., 1988, Quaternary and Active Faulting Observed on the 1985 Academia Sinica--Royal Society Geotraverse of Tibet: Philosophical

Transactions of the Royal Society of London. Series A, Mathematical and Physical Sciences, v. 327vp. 337-363.

Kirby, E., Reiners, P.W., Krol, M.A., Whipple, K. X., Hodges, K. V., Farley, K.A., Tang, W.Q., and Chen, Z.L., 2002, Late Cenozoic evolution of the eastern margin of the Tibetan Plateau: Inferences from Ar-40/Ar-39 and (U-Th)/He thermochronology: Tectonics, v.21(1), 10.1029/2000TC001246.

Korup, O., and Montgomery, D., 2008, Tibetan plateau river incision inhibited by glacial stabilization of the Tsangpo gorge: Nature, v. 455, p. 786-789.

Lease, R. O., Burbank, D. W., Clark, M. K., Farley, K. A., Zheng, D., and Zhang, H., 2011, Middle Miocene reorganization of deformation along the northeastern Tibetan Plateau: Geology, v. 39, p. 359-362.

Lease, R. O., Burbank, D. W., Gehrels, G. E., Wang, Z. C., and Yuan, D. Y., 2007, Signatures of mountain building: Detrital zircon U/Pb ages from northeastern Tibet: Geology, v. 35, p. 239-242.

Lin, X., Chen, H., and Wyrwoll, K.H., Batt, G.E., Liao, L., and Xiao, J., 2011, The Uplift History of the Haiyuan-Liupan Shan region northeast of the present Tibetan Plateau: Integrated constraint from stratigraphy and thermochronology: The Journal of Geology, v.119(4), p. 372-393.

Metivier, F., Gaudemer, Y., Tapponnier, P., and Meyer, B., 1998, Northeastward growth of the Tibet plateau deduced from balanced reconstruction of two depositional areas: The Qaidam and Hexi Corridor basins, China: Tectonics, v. 17, p. 823-842.

Meyer, B., Tapponnier, P., Bourjot, L., Metivier, F., Gaudemer, Y., Peltzer, G. Shunmin, G., Zhitai, C., 1998, Crustal thickening in Gansu-Qinghai, lithospheric mantle

subduction, and oblique, strike-slip controlled growth of the Tibet plateau: Geophysics Journal International, v. 135, p. 1-47.

Molnar, P., and Tapponnier, P., 1975, Cenozoic tectonics of Eurasia: effects of a continental collision: Science, v. 189, p. 419-426.

Molnar, P., Boos, W.R., and Battisti, D.S., 2010, Orographic Controls on Climate and Paleoclimate of Asia: Thermal and Mechanical Roles for the Tibetan Plateau: Annu Rev Earth Pl Sc, v. 38, p. 77-102.

Montgomery, D. R., Balco, G., and Willett, S.D., 2001, Climate, tectonics, and the morphology of the Andes: Geology, v. 29(7), p. 579-582.

New, M., Lister, D., Hulme, M., and Makin, I., 2002, A high-resolution data set of surface climate over global land areas: Climate Res, v. 21(1), p. 1-25.

Ouimet, W., Whipple, K., Royden, L., Sun, Z., and Chen, Z., 2007, The influence of large landslides on river incision in a transient landscape: Eastern margin of the Tibetan Plateau (Sichuan, China): Geological Society of America Bulletin, v. 119(11), p. 1462– 1476.

Ouimet, W., K. Whipple, L. Royden, P. Reiners, K. Hodges, and M. Pringle, 2010, Regional incision of the eastern margin of the Tibetan Plateau: Lithosphere, v. 2(1), p. 50-63.

Reiners, P. W., Ehlers, T.A., Mitchell, S.G., and Montgomery, D.R., 2003, Coupled spatial variations in precipitation and long-term erosion rates across the Washington Cascades: Nature, v. 426(6967), p. 645-647.

Riebe, C. S., Kirchner, J.W., Granger, D.E., and Finkel, R.C., 2001, Minimal climatic control on erosion rates in the Sierra Nevada, California: Geology, v. 29(5), p. 447-450.

Royden, L. H., Burchfiel, B.C., and van der Hilst, R.D., 2008, The geological evolution of the Tibetan plateau: Science, v. 321(5892), p. 1054-1058.

Searle, M., Elliott, J., Phillips, R., and Chung, S. L., 2011, Crustal-lithospheric structure and continental extrusion of Tibet: Journal of the Geological Society, v. 168, p. 633.

Sobel, E.R., Arnaud, N., Jolivet, M., Ritts, B.D., and Brunel, M., 2001, Jurassic to Cenozoic exhumation history of the Altyn Tagh range, northwest China constrained by 40Ar/39Ar and apatite fission track thermochronology, *in* Hendrix, M.S., and Davis, G.A., ed., Paleozoic and Mesozoic tectonic evolution of central and eastern Eurasia: From continental assembly to intracontinental deformation: Geological Society of America Memoir 194, p. 247-268.

Solum, J.G., van der Pluijm, B.A., and Peacor, D.R., 2005, Neocrystallization, fabrics and age of clay minerals from an exposure of the Moab Fault, Utah: J. Struct. Geol., v. 27, p. 1563-1576.

Tapponnier, P., Peltzer, G., Ledain, A.Y., Armijo, R., and Cobbold, P., 1982, Propagating Extrusion Tectonics in Asia - New Insights from Simple Experiments with Plasticine: Geology, v. 10(12), p. 611-616.

Tapponnier, P., Xu, Z.Q., Roger, F., Meyer, B., Arnaud, N., Wittlinger, G., and Yang, J.S., 2001, Oblique stepwise rise and growth of the Tibet plateau: Science, v. 294(5547), p. 1671-1677.

Thiede, R. C., Bookhagen, B., Arrowsmith, J.R., Sobel, E.R., and Strecker, M.R., 2004, Climatic control on rapid exhumation along the Southern Himalayan Front: Earth Planet Sci Lett, v. 222(3-4), p. 791-806.

Wang, W., Zhang, P. Z., Kirby, E., Wang, L. H., Zhang, G. L., Zheng, D. W., and Chai, C. Z., 2011, A revised chronology for Tertiary sedimentation in the Sikouzi basin: Implications for the tectonic evolution of the northeastern corner of the Tibetan Plateau: Tectonophysics.

Whipple, K.X., 2010, Transient landscapes: Recorders of history and engines of discovery, Abstract EP51G-02, presented at 2010 Fall Meeting, AGU, San Francisco, Calif., 13-17 Dec.

Wilson, C.J.L., and Fowler, A.P., 2011, Denudational response to surface uplift in east Tibet: Evidence from apatite fission-track thermochronology: Bulletin of the Geological Society of America, doi:10.1130/B30331.1.

Yan, M., VanderVoo, R., Fang, X., Parés, J. M., and Rea, D. K., 2006, Paleomagnetic evidence for a mid-Miocene clockwise rotation of about 25 of the Guide Basin area in NE Tibet: Earth and Planetary Science Letters, v. 241, p. 234-247.

Yin, A., Rumelhart, P. E., Butler, R., Cowgill, E., Harrison, T. M., Foster, D. A., Ingersoll, R. V., Zhang, Q., Zhou, X. Q., Wang, X. F., Hanson, A., and Raza, A., 2002, Tectonic history of the Altyn Tagh fault system in northern Tibet inferred from Cenozoic sedimentation: Geological Society of America Bulletin, v. 114, p. 1257-1295.

Yin, A., Dang, Y.Q., Wang, L.C., Jiang, W.M., Zhou, S.P., Chen, X.H., Gehrels, G.E., and McRivette, M.W., 2008, Cenozoic tectonic evolution of Qaidam basin and its surrounding regions (Part 1): The southern Qilian Shan-Nan Shan thrust belt and northern Qaidam basin: Geol Soc Am Bull, v. 120(7-8), p. 813-846.

Yuan, D.Y., Champagnac, J.D., Ge, W.P., Molnar, P., Zhang, P.Z., Zheng, W.J., Zhang, H.P., and Liu, X.W., 2011, Late Quaternary right-lateral slip rates of faults adjacent to the lake Qinghai, northeastern margin of the Tibetan Plateau: Geological Society of America Bulletin, doi:10.1130/B30315.1.

Zhang, P. Z., Burchfiel, B. C., Molnar, P., Zhang, W. Q., Jiao, D. C., Deng, Q. D., Wang, Y. P., Royden, L., and Song, F. M., 1991, Amount and style of Late Cenozoic deformation in the Liupan Shan area, Ningxia Autonomous region, China: Tectonics, v. 10, p. 1111-1129.

Zhang, H.P., Craddock, W.H., Lease, R.O., Wang, W., Yuan, D.Y., Zhang, P.Z., Molnar, P., Zheng, D.W., and Zheng, W.J., 2011, Magnetostratigraphy of the Neogene Chaka basin and its implications for mountain building processes in the north-eastern Tibetan Plateau: Basin Research, doi:10.1111/j.1365-2117.2011.00512.x.

Zhao, H.G., Liu, C.Y., Wang, F., Wang, J.Q., Li, Q., and Yao, Y.M., 2007, Uplift and evolution of Helan Mountain: Science in China Series D: Earth Sciences, v.50, p.217-226.

Zheng, D. W., Zhang, P.Z., Wan, J.L., Yuan, D.Y., Li, C.Y., Yin, G.M., Zhang, G.L., Wang, Z.C., Min, M., and Chen, J., 2006, Rapid exhumation at similar to 8 Ma on the Liupan Shan thrust fault from apatite fission-track thermochronology: Implications for growth of the northeastern Tibetan Plateau margin: Earth and Planetary Science Letters, v. 248(1-2), p. 198-208.

Zheng, D. W., Zhang, P.Z., Wan, J.L., Li, C.Y., and Cao, J.X., 2003, Late Cenozoic deformation subsequence in northeastern margin of Tibet - Detrital AFT records from Linxia Basin: Sci China Ser D, v. 46, p. 266-275.

Appendix

This appendix includes a preliminary original geologic map resulting from three field seasons of work (August 2006; July 2007; September 2010) within the greater Maxian Shan region of northeastern Tibet. Three generalized stratigraphic columns rom this area are also included.

Geology of the Maxian Shan Region, northeastern Tibetan Plateau margin

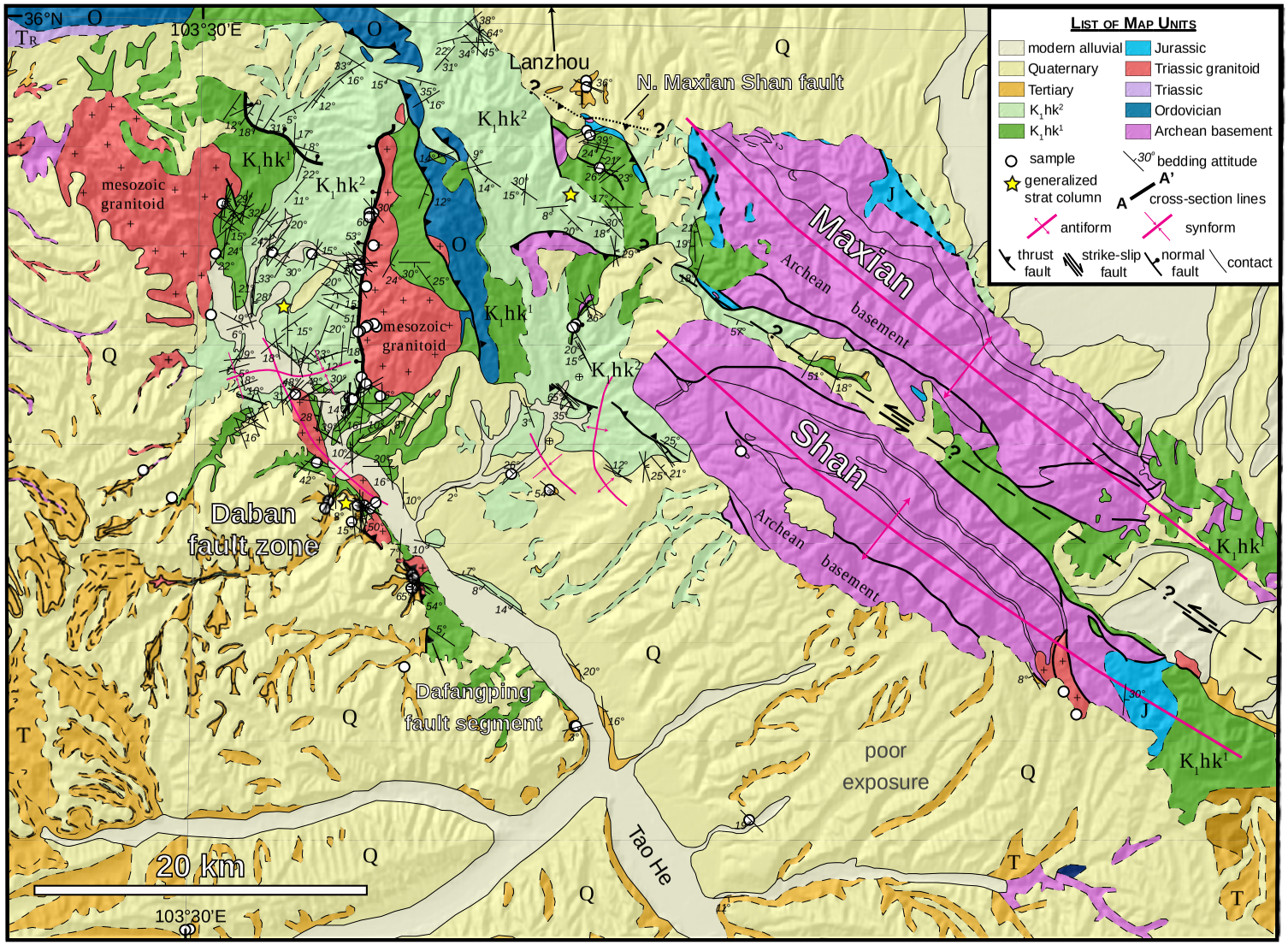

Generalized Stratigraphic Column: Cretaceous Hekou formation
Old Maxian Shan highway

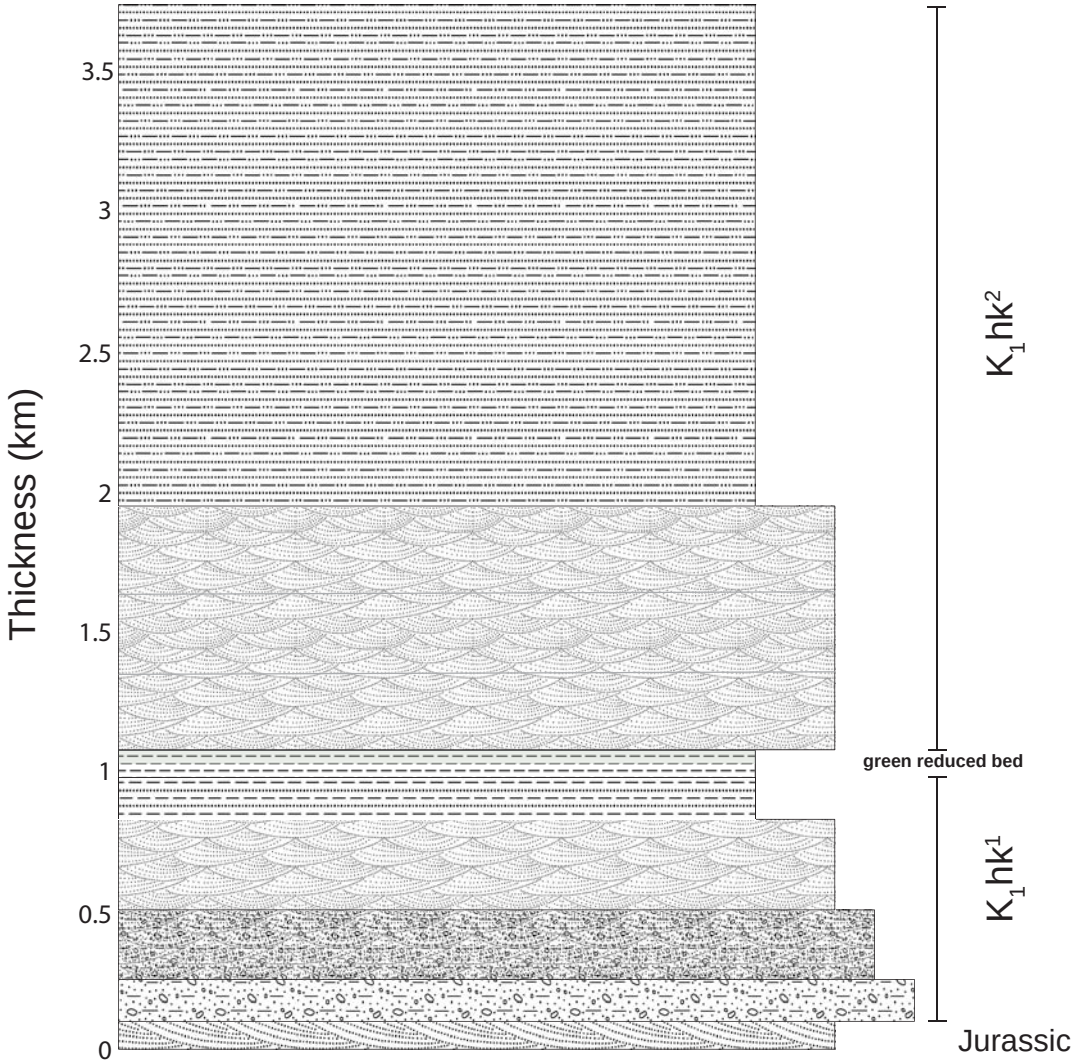

Generalized Stratigraphic Column: Cretaceous Hekou formation
West Maxian Shan

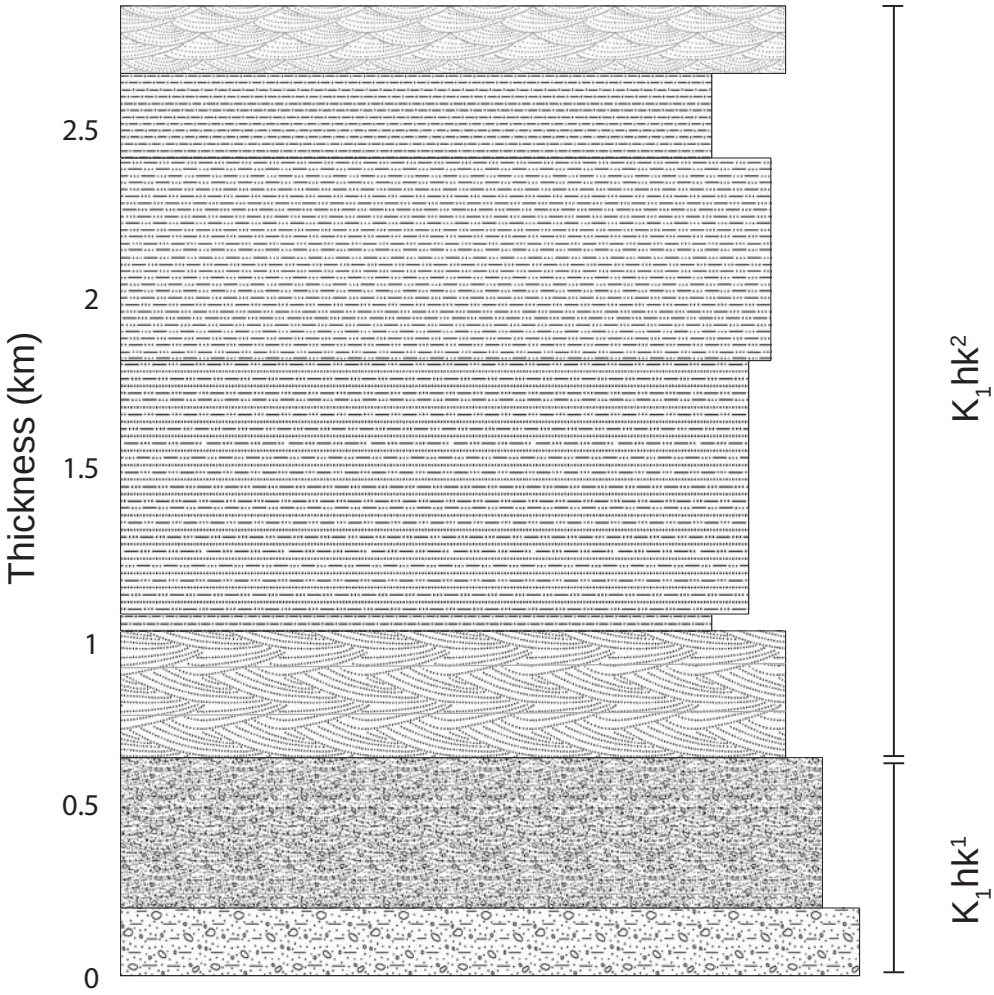

Generalized Stratigraphic Column: Tertiary clastics
Daban Overlook